Applications of
Boundary Integral Methods to
Rising and Bursting Bubbles

By

Jeremy Michael Boulton-Stone

A thesis submitted to the
Faculty of Science
of the
University of Birmingham
for the degree of
DOCTOR OF PHILOSOPHY

School of Mathematics
and Statistics
University of Birmingham
B15 2TT
England

March 1993

Synopsis.

Direct and indirect boundary integral methods are introduced and compared for the problem of a two-dimensional, constant volume bubble rising under the action of buoyancy in an inviscid liquid. It is found that the vortex, dipole and Green's formula approaches produce good results in agreement with previous theoretical studies and with experimental evidence, with the source distribution method breaking down after only a short time. The Green's formula method is found to be less stable to perturbed initial conditions. An analytic stability analysis indicates that a bubble rising with zero surface tension is unstable, but that the one inch bubble of Walters and Davidson (1962) is stable to small, short wavelength perturbations. By using a conformal map, the theory is extended to the case of a two-dimensional bubble near to a free surface, the numerical results of which compare well with an analytic expression for the surface elevation due to a deeply submerged dipole.

The motions of three-dimensional gas bubbles, modelled using the equivalent boundary element method for the axisymmetric geometry, are found to be similar to those of their two-dimensional counterparts. Important differences in behaviour, mainly of a quantitative nature, are highlighted, and discussed. Bubble size, though the action of surface tension, is found to have a marked effect on the motion, determining whether the bubble will eventually split up into one or two smaller bubbles. The interaction of two bubbles is also considered, again the differences from the equivalent two-dimensional case are explored.

Finally, using numerical techniques developed in the previous chapters, bubble bursting is considered in detail. By assuming suitable initial conditions for the interface shape immediately after film rupture, the effect of bubble volume on the following motion is examined. The findings, that the smallest bubbles burst the most violently resulting in greater pressures and energy dissipation rates, are broadly in agreement with the experimental evidence for cell damage by bubbles in bioreactors. A method for including a boundary layer into the calculations is developed. This allows an approximation of the vorticity distribution in the region below the bubble. The effects of including a boundary layer are found to be small, and the magnitude of the vorticity in the downward jet region suggests shear rates to be insignificant compared to strain rates predicted by the irrotational flow model.

To

My wife, Susan Bernadette.

Acknowledgments.

Contents.

Chapter 1.

INTRODUCTION.

1.1 Aims.

Bubbles present us with a startling variety of fluid dynamical problems. Although many aspects of bubble dynamics can be examined analytically, it is only recently, with the advent of sophisticated numerical methods and high speed computers, that we have been able to inspect in detail complicated unsteady moving boundary problems. The highly non-linear nature of the equations of motion make futile most attempts to find neat mathematical solutions in closed form. Having said this, there are methods — based on a global conservation principle such as energy integrals or virial theorems (Longuet-Higgins, 1983; Oguz and Prosperetti, 1990a) or the Kelvin impulse (Blake, 1988) — that one can often use in order to obtain an idea of the motions involved.

Boundary integral methods rely on the writing a partial differential equation, in this case Laplace's equation, in terms of an integral equation. In the problems dealt with here, the integration is carried out over the gas/liquid interface so that the dimension of the problem is effectively reduced by one: finite element and finite difference techniques require discretisation of the whole flow domain. In many 'three-dimensional' situations one can further simplify calculations by assuming axisymmetry. In terms of computational effort, such an approach is thus relatively cheap. For problems where the accurate determination of the position of an interface is an essential requirement, boundary integral methods can be very effective. Using such techniques, the motion of points along the interfaces can be explicitly tracked. Piecewise continuous elements are often employed to interpolate between these nodes in order to calculate the surface integrations. High order surface representations such as cubic splines (Best and Kucera, 1992) parametrised by arc-length can afford greater accuracy.

Boundary integral methods have been employed to solve a wide variety of free boundary problems in fluid mechanics, including a number in bubble dynamics. One of the most successful applications is to the field of cavitation bubble dynamics. A Green's formula approach was used by Guerri, Lucca and Prosperetti (1981), Blake, Taib and Doherty (1986, 1987) and Taib (1985) to study cavitation bubbles near boundaries. Blake and Kucera (1988) tackled the problem of water-coning, a phenomenon occurring in oil reservoirs, using a steady boundary integral technique. Longuet-Higgins and Cokelet (1976) used a boundary integral scheme in conjunction with a conformal map to study the overturning of large amplitude surface waves.

The aim of this thesis is to present various aspects of bubble dynamics from a largely numerical viewpoint with the aid of boundary integral methods. The first chapters deal exclusively with the modelling, using a variety of boundary integral techniques, of two-dimensional bubbles both rising in an infinite fluid and then near to a free-surface. Although two-dimensional bubbles are unrealistic, they have similar properties to 'real' bubbles. This work also provides an introduction to the most commonly used boundary integral techniques for problems in potential flow theory, paving the way for the consideration of axisymmetric problems in later chapters.

1.2 Motivation.

The long-term aims of the project are to study and gain an understanding of the physics involved in mammalian cell damage in aerated bioreactors. The production of mammalian cells in culture vessels is important for several reasons. The biochemicals produced by cells such as monoclonal antibodies, hormones and enzymes have many uses in medicine. The cells themselves may be used in future for transplantation and diagnostic purposes.

Bioreactor induced cell damage has been studied experimentally for several years by many researchers: indeed it was a team working in this field in the School of Chemical Engineering at the University of Birmingham, who suggested this mathematical study.

Through the data collected, a number of possible damage mechanisms have been proposed. It has been claimed (e.g. Tramper et al, 1986) that the high agitation rates, used to circulate nutrients through the medium, are detrimental to cells. However, many now believe an overwhelming proportion of the damage observed to be due to the cells' interactions with bubbles sparged through the medium to provide oxygen to the cell culture.

Experiments have often involved actual, scaled down bioreactors (figure 1.1, below), but there have been some where cells have been placed in controlled hydrodynamic environments. McQueen and Bailey (1989) pumped cells in a medium through capillary tubes which had either smooth or sudden constrictions to produce laminar or turbulent flows respectively. They found that the viscosity of the fluid did not effect the cell death rates, even though the associated Kolmogorov eddy lengths changed. By using different sized tubes with viscosities adjusted so that the wall shear stresses remained constant, they concluded that there are other factors affecting cell death as well as just wall shear stresses. However, both they and Kunas and Papoutsakis (1989) who used an agitated bioreactor, found that an increase in serum concentration decreased the death rate, these latter authors claiming the change to be due to some physical factor other than viscosity.
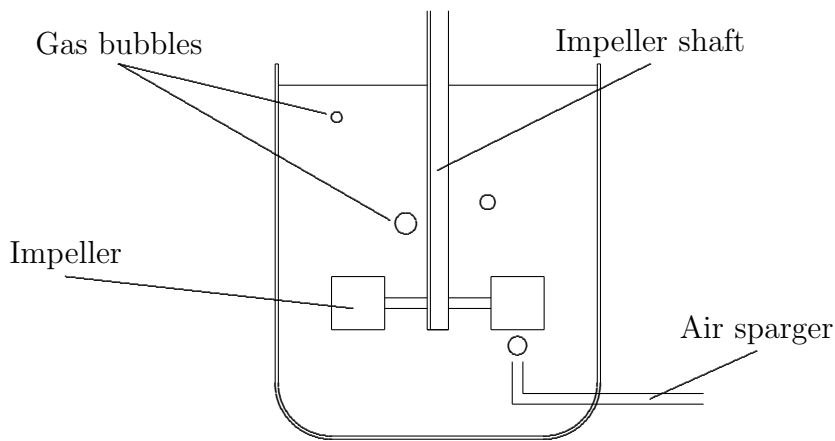

Figure 1.1. Components of a bioreactor, with the air sparger placed beneath the agitator.

Using simple bubble columns, with no agitation, Handa, Emery and Spier (1987) and Handa (1986) showed a direct relationship between the presence of bubbles and cell death

rate. Death rates, per bubble, were found to be higher for small bubbles than for large ones. It was also found that Pluronic (a co-polymer of propylene oxide and ethylene oxide; a product of BASF, UK) which allows a stable, slowly draining foam, with the bursting of bubbles mainly restricted to its upper surface, resulted in lower death rates. They claimed that the presence of an anti-foam causes cell damage as a consequence of shock waves produced by many bubbles bursting at the free-surface, and that without anti-foam, rapid draining in unstable foams causes high shear stresses that can cause damage. By showing cell death to be independent of the air sparger position and hence bubble residence time, Kioukia (1990) was able to conclude that, at least for the bubble column case, this damage occurs in a region near to the free-surface.

Al-Rubeai, Chalder and Emery (1990) used laser flow cytometry to study the morphology of damaged cells. They discovered that damage caused by agitation alone was less severe than that occurring when air bubbles were being sparged through in which case cells were seen to have been torn apart. In another recent paper, Oh, Nienow, Al-Rubeai and Emery (1989), it was shown that, under solely surface aeration, cell growth and viability does not depend on hydrodynamic conditions, even at very high agitation rates. However with sparging, the growth rates become lower and reduce as agitation intensity increases.

A possible cause of damage in stirred reactors was suggested by Yang et al (1990). They claimed that a bubble stretched until breakup in the trailing vortex near to the tip of the agitator impeller blade will release the built-up surface energy in a potentially damaging shock wave as it bursts into many smaller bubbles. Recent experiments by Oh, Nienow, Al-Rubeai and Emery (1992) suggest that cell damage is increased by positioning the air sparger beneath the impeller. The effects of this are however two-fold as it will increase the number of bubble/impeller interactions but will also split large bubbles into smaller ones which are known to be more lethal at the free-surface.

In the experiments of Kunas and Papoutsakis (1990), bubbles are seen to be en-

trained at the gas/liquid interface of a vortex produced in an agitated reactor. The death rate was found to be directly related to the size of the surface indentation, namely less damage was recorded if the reactor volume was increased or if the head-space above it was removed altogether. In this latter case cell growth, though slower, occurred even at high agitation rates. If, in addition, tiny bubbles, moving around at high speeds were present, the death rates were still very small compared to the situation where there was a free-surface. Significant agitation damage was only found when Kolmogorov eddy lengths became comparable to the dimensions of the cells.

It has been speculated (Chalmers and Bavarian, 1991) that the high acceleration at the rim of a rupturing film, such as occurs when a bubble bursts, is a possible cause of cell damage. Along similar lines, Kowalski (1991) by concentrating on the bursting of a single, large bubble manufactured by placing a pipette into a cell culture medium, claimed that cells trapped in the rupturing film may be killed by large compressional forces which occur when the retreating rim breaks into threads which in turn split into droplets. The walls of the experimental vessel were found to be littered with cell debris, indicating a secondary effect of the burst as a means of removing cells from the reactor. He also found that Pluronic allowed the cells to drain away with the fluid in the film, and thus escape the regions where high stresses may be experienced.

It is therefore apparent, given the above overview of just some of the recent literature, that there is no complete agreement as to the precise mechanisms responsible, but there is a growing inclination to view the role of bubbles and their interaction with the free-surface as the prime cause of cell damage in aerated bioreactors.

1.3 Summary.

In Chapter 2, an inviscid model of a two-dimensional bubble is introduced. Boundary integral techniques, which have had much success previously in bubble dynamics, are then employed to solve for the bubble motion. The results obtained are almost identical to those of Baker and Moore (1989) and close to the experimental findings of Walters

and Davidson (1962). Several different boundary integral techniques are employed and compared.

In Chapter 3, the theory is extended to look at the problem of a two-dimensional bubble as it approaches a free-surface. A conformal map technique, similar to that of Longuet-Higgins and Cokelet (1976), is used to enable integration over the infinite free-surface. This is compared against an asymptotic solution valid for bubbles at large depths.

In Chapter 4, the motion of axisymmetric gas bubbles is examined via a boundary integral method. Two example problems are examined. The first, as in Chapter 2, looks at the case of bubbles rising from rest in an infinite fluid. This time we allow for bubble-bubble interaction by including a second bubble into the calculations. The second problem uses an inviscid boundary integral together with modified boundary conditions to include some effects of viscosity and thus obtain an approximate solution to the steady state of a rising bubble when the drag and buoyancy are in balance.

The thesis culminates in Chapter 5, with the development of a model for bubbles bursting at a free-surface with a view to developing a greater understanding of cell damage in bubble aerated bioreactors. A method, based on that of Lundgren and Mansour (1988), for including viscous forces via a boundary layer is developed. This allows an approximation of the shedding of vorticity as the boundary layer separates when a high speed liquid jet rises above the fluid.

Finally, in Chapter 6, we summarise the important results and conclusions and indicate briefly possible directions for future research into the cell damage problem.

Chapter 2.

A TWO-DIMENSIONAL BUBBLE
IN AN INFINITE FLUID.

2.1 Introduction.

Two-dimensional bubbles are less physically realistic than their three-dimensional counterparts. Nevertheless their study provides a useful introduction to the mathematical concepts involved in potential theory and boundary integral equations.

Two-dimensional bubbles have been the subject of the mathematical attention of a number of researchers. Walters and Davidson (1962) found an analytic expression for the initial motion. They also conducted experimental studies and, in their paper, they include photographs of a bubble rising in the narrow gap between two sheets of glass.

A complex-variable technique was used by Baumel et al (1982) to compute the bubble motion. They developed a series solution which they summed using a variant of Padé approximants. This approach successfully predicted the position of the top and bottom of the bubble through time. However because of singularities in the complex plane, their series does not have a very large radius of convergence, thus they could only use it to give information for small times.

Baker and Moore (1989) successfully used numerical techniques to model the motion of the bubble. Their methods hinge on finding equations describing the evolution of the strengths of vortex or dipole singularities distributed over the gas/liquid interface. The dipole method is given in detail in Baker, Meiron and Orszag (1982), and works by deriving a second-kind Fredholm equation for the rate of change of the dipole strength, which may be solved iteratively. Vortex methods have been used extensively in other problems, for example in the modelling of large amplitude surface waves (Baker, Meiron and Orszag, 1982), and in studying the surface water waves induced by a submerged body

(Soh, 1987).

2.2 Mathematical preliminaries.

2.2.1 Formulation of the problem.

Incompressible fluid fills the infinite region of the (x, y)-plane, Ω_-. The fluid is bounded internally by the closed curve, C, representing the bubble's surface. Denote the interior of C by Ω_+. It is assumed that the fluid is inviscid and that the flow is irrotational since it is initially at rest. Incompressibility leads to $\nabla \cdot \boldsymbol{u} = 0$ and irrotationality to $\nabla \times \boldsymbol{u} = \boldsymbol{0}$ so that the velocity field, $\boldsymbol{u}$, may be expressed as the gradient of a potential, φ, which satisfies the Laplace equation, $\nabla^2 \varphi = 0$. Initially, the fluid is at rest so that the potential, φ, is constant throughout the domain of solution, Ω_-. Particles on the boundary of the bubble, for this two-dimensional problem given by the Lagrangian description $\boldsymbol{q}(\eta, t)$, $\eta \in [0, 1)$ say, must remain there. This gives us the kinematic condition

$$\frac{\partial \boldsymbol{q}}{\partial t}(\eta, t) = \nabla \varphi(\boldsymbol{q}(\eta, t), t), \quad \forall \eta \in [0, 1), t \geq 0. \tag{2.2.1}$$

The dynamic boundary condition takes the form of the Bernoulli theorem, namely

$$\frac{p_\infty}{\rho} = \frac{p}{\rho} + \frac{1}{2}|\boldsymbol{u}|^2 + \frac{\partial \varphi}{\partial t} + \Phi, \tag{2.2.2}$$

where p_∞ is the ambient pressure and Φ is the gravitational potential $(= gy)$. Due to the relatively low density of the gas inside the bubble, we assume that the pressure inside the bubble is a function of time only.

Lengths are scaled with respect to the radius of the initially circular bubble, a, times with respect to $(a/g)^{1/2}$ and pressures with respect to $\rho g a$. Evaluating (2.2.2) at the bubble surface and using the substantial derivative,

$$\frac{D\varphi}{Dt} = \frac{\partial \varphi}{\partial t} + |\boldsymbol{u}|^2,$$

yields an equation describing the evolution of the potential of fluid particles on the bubble. In terms of dimensionless variables,

$$\frac{D\varphi}{Dt} = \frac{1}{2}|\boldsymbol{u}|^2 - y + p_\infty - p_b(t),$$

$$- 8 -$$

where $p_b(t)$ is the bubble's internal pressure.

The total volume change for a bubble containing an ideal gas at fixed temperature, is given by

$$\frac{V}{V_0} \simeq (1 - \rho g a \Delta y/p_\infty)^{-1}.$$

If p_∞ is taken to be atmospheric pressure of the order of $10^6 dyn/cm^2$, and we assume that the total translation of the bubble before it splits up (see Walters and Davidson, 1962), Δy, is only a few bubble radii, then $\rho g a \Delta y/p_\infty \ll 1$ and we may assume that the bubble volume remains constant. This agrees with the experimental findings of Walters and Davidson (1962). To conserve bubble volume, we insist that the total flux of fluid through the bubble's surface vanishes, i.e.

$$\int_C \frac{\partial \phi}{\partial n} ds = 0.$$

As a far-field condition for the potential, we may assume in this case that $\varphi(\boldsymbol{x}) \to 0$ as $|\boldsymbol{x}| \to \infty$. As will be seen presently, this condition provides us with a means of calculating the unknown value of $p_\infty - p_b(t)$.

To remove the $p_\infty - p_b(t)$ term from the dynamic condition, we define a new potential, ϕ, by

$$\phi = \varphi + \int_0^t (p_b(t') - p_\infty)dt', \tag{2.2.3}$$

(see also Lundgren and Mansour, 1991), thus yielding

$$\frac{D\phi}{Dt} = \frac{1}{2}|\boldsymbol{u}|^2 - y, \tag{2.2.4}$$

for ϕ on the bubble.

2.2.2 Green's Theorem.

In a similar manner to the three-dimensional case, Green's formula may be used in the plane, namely

$$\int_A \left(G\nabla^2\phi(\boldsymbol{x}') - \phi(\boldsymbol{x}')\nabla'^2 G \right) dA' = \int_{C \cup \Sigma_R} \left(G\frac{\partial \phi}{\partial n}(\boldsymbol{x}') - \phi(\boldsymbol{x}')\frac{\partial G}{\partial n'} \right) ds', \tag{2.2.5}$$

$$- 9 -$$

where here A is a finite region of Ω_-, bounded internally by C and externally by Σ_R. Here,

$$G(\boldsymbol{x}, \boldsymbol{x}') = \frac{1}{2\pi} \log \frac{1}{|\boldsymbol{x} - \boldsymbol{x}'|}$$

is the free-space Green's function for the two-dimensional Laplace equation, i.e.

$$\nabla'^2 G(\boldsymbol{x}, \boldsymbol{x}') = -\delta(\boldsymbol{x} - \boldsymbol{x}').$$

To resolve any ambiguity with functions of two space variables, $\boldsymbol{x}$ and $\boldsymbol{x}'$, differentiations and integrations with respect to $\boldsymbol{x}'$ are indicated by a prime: so that for example $\{\nabla'\}_i \equiv \partial/\partial x_i'$.

If $\nabla^2 \phi = 0, \forall \boldsymbol{x} \in A$, we get

$$c(\boldsymbol{x})\phi(\boldsymbol{x}) = \int_{C \cup \Sigma_R} \left(G \frac{\partial \phi}{\partial n}(\boldsymbol{x}') - \phi(\boldsymbol{x}') \frac{\partial G}{\partial n'} \right) ds', \qquad (2.2.6)$$

where

$$c(\boldsymbol{x}) = \begin{cases} 1, & \boldsymbol{x} \in A \subset \Omega_-, \\ \frac{1}{2}, & \boldsymbol{x} \in C \cup \Sigma_R, \\ 0, & \boldsymbol{x} \in \Omega_+. \end{cases}$$

These values for $c(\boldsymbol{x})$ come about as a result of the fact that in two dimensions, Green's formula can be derived as the real part of a Cauchy integral. The factor of a half for the case where the field point is on the contour, represents the Cauchy principal value.

The integral over Σ_R in (2.2.6) can be significantly simplified. Following Batchelor (1967), this is perhaps best seen if Σ_R is taken to be a circle of radius R around the point $\boldsymbol{y} \in A$ which coincides with the field point, $\boldsymbol{x}$. In this case the integral can be written as

$$\frac{1}{2\pi} \left(\log \frac{1}{R} \int_{\Sigma_R} \frac{\partial \phi}{\partial R} ds + \frac{1}{R} \int_{\Sigma_R} \phi ds \right). \qquad (2.2.7)$$

The second integral in (2.2.7) over Σ_R is just

$$\int_0^{2\pi} \phi d\theta.$$

In the general case, when

$$\frac{1}{2\pi} \int_S \frac{\partial \phi}{\partial n} ds = -m_S, \qquad (2.2.8)$$

over any curve, S, enclosing the bubble, we have by the divergence theorem that $m_S = m$ is independent of the particular contour, S, since $\nabla^2 \phi = 0$ in A. Thus m is the rate of expansion of the bubble. So taking S to be Σ_R and writing (2.2.8) in terms of an angular variable, θ, as above, we have

$$\frac{R}{2\pi} \int_0^{2\pi} \frac{\partial \phi}{\partial R} d\theta = -m. \tag{2.2.9}$$

Integrating (2.2.9) with respect to R gives

$$\frac{1}{2\pi} \int_0^{2\pi} \phi d\theta = m \log \frac{1}{R} + k. \tag{2.2.10}$$

Moreover k is independent of $\boldsymbol{y}$, the centre of Σ_R, since differentiating (2.2.10) with respect to y_i gives

$$\frac{\partial k}{\partial y_i} = \frac{1}{2\pi} \int_0^{2\pi} \frac{\partial \phi}{\partial y_i} d\theta, \tag{2.2.11}$$

where this expression is independent of R and, in the limit $R \to \infty$, the right-hand-side is seen to be zero, since the fluid is at rest at infinity.

Thus combining (2.2.6), (2.2.7), (2.2.9) and (2.2.10), we get the final form of Green's theorem which can be used as a basis for boundary integral methods in the unbounded domain, Ω_-, viz

$$c(\boldsymbol{x})\phi(\boldsymbol{x}) = k + \int_C \left(G \frac{\partial \phi}{\partial n}(\boldsymbol{x}') - \phi(\boldsymbol{x}') \frac{\partial G}{\partial n'} \right) ds'. \tag{2.2.12}$$

Information as to the form of ϕ given by (2.2.12) can be found by expanding in a Taylor series (Batchelor,t 1967; Lighthill, 1986) for points $\boldsymbol{x} \in \Omega_-$ with $r = |\boldsymbol{x}| \gg |\boldsymbol{x}'|$. On doing this, we find

$$\phi(\boldsymbol{x}) = k - \frac{m}{2\pi} \log \frac{1}{r} - \frac{\boldsymbol{x}}{2\pi r^2} \cdot \left(\frac{d(\boldsymbol{c}V)}{dt} + \frac{\boldsymbol{I}}{\rho} \right) + O(r^{-2}). \tag{2.2.13}$$

Here m, the strength of the source term, is the expansion rate of (2.2.9). The second term represents a dipole and is made up of two components. The first is related to the centroid velocity, where $\boldsymbol{c}$ is the centroid position and V is the volume of the bubble. The second part is related to the Kelvin impulse defined by

$$\boldsymbol{I} = \int_C \rho \phi \hat{\boldsymbol{n}} ds.$$

It was suggested by Lamb (1932) that the Kelvin impulse can be thought of as an impulsive wrench which induces the motion on a fluid initially at rest, analogous to the notion of impulse in the theory of particle mechanics.

It is clear from (2.2.13) that, if we take ϕ to be the modified potential defined in section 2.2.1, k is the limiting value of ϕ as $r \to \infty$ and so, from the far-field condition on the original potential, φ, we have that

$$k = \int_0^t (p_b(t') - p_\infty) dt'. \tag{2.2.14}$$

2.2.3 Indirect formulations.

From Green's theorem, the potential may be written as a simple source or dipole distribution which can then give rise to two so-called 'indirect' boundary integral methods (see also Brebbia and Walker, 1980 and Jaswon and Symm, 1977). If, in (2.2.5), we had chosen A to be the internal region, Ω_+, we would have immediately had

$$\tilde{c}(\boldsymbol{x})\tilde{\phi}(\boldsymbol{x}) = -\int_C \left(G \frac{\partial \tilde{\phi}}{\partial n}(\boldsymbol{x}') - \tilde{\phi}(\boldsymbol{x}') \frac{\partial G}{\partial n'} \right) ds', \tag{2.2.15}$$

(the '$-$' sign is because we are taking normal derivatives in the same direction as in (2.2.6), i.e. into Ω_+) where

$$\tilde{c}(\boldsymbol{x}) = \begin{cases} 1, & \boldsymbol{x} \in \Omega_+, \\ \frac{1}{2}, & \boldsymbol{x} \in C, \\ 0, & \boldsymbol{x} \in \Omega_-. \end{cases}$$

Hence adding (2.2.15) to (2.2.12) gives, for all $\boldsymbol{x}$,

$$\phi(\boldsymbol{x}) = k + \int_C \left\{ \left(\frac{\partial \phi}{\partial n}(\boldsymbol{x}') - \frac{\partial \tilde{\phi}}{\partial n}(\boldsymbol{x}') \right) G - \left(\phi(\boldsymbol{x}') - \tilde{\phi}(\boldsymbol{x}') \right) \frac{\partial G}{\partial n'} \right\} ds'.$$

If we assert that the potential is to be continuous across C then

$$\phi(\boldsymbol{x}) = k + \frac{1}{2\pi} \int_C \sigma(\boldsymbol{x}') \log \frac{1}{|\boldsymbol{x}' - \boldsymbol{x}|} ds', \tag{2.2.16}$$

where $\sigma(\boldsymbol{x}') = \left(\partial\phi/\partial n - \partial\tilde{\phi}/\partial n \right)$ and if the normal derivative is continuous across C,

$$\phi(\boldsymbol{x}) = k - \frac{1}{2\pi} \int_C \mu(\boldsymbol{x}') \frac{\partial}{\partial n'} \log \frac{1}{|\boldsymbol{x}' - \boldsymbol{x}|} ds', \tag{2.2.17}$$

where $\mu(\boldsymbol{x}') = (\phi - \tilde{\phi})$.

2.3 Source distribution method.

2.3.1 Formulation.

The source formulation, given by (2.2.16), may be derived from the Green's formula as shown above or may be thought of as a Poisson integral for the solution of $\nabla^2 \phi = - \int_C \sigma(\boldsymbol{q}(s)) \delta(\boldsymbol{x} - \boldsymbol{q}(s)) ds$, where $\boldsymbol{q}(s)$ is an arc-length parametrisation of the bubble surface.

Consider the integral of the normal derivative of the potential (by re-writing (A3)) for the cases where the field point $\boldsymbol{x}^\star$ approaches $\boldsymbol{x}$ from Ω_+ and from Ω_-,

$$\int_C \frac{\partial \phi}{\partial n} ds = \int_C \left(\frac{1}{2\pi} \int_C \sigma(\boldsymbol{x}') \frac{\partial}{\partial n} \log \frac{1}{|\boldsymbol{x}' - \boldsymbol{x}|} ds' \mp \frac{1}{2} \sigma(\boldsymbol{x}) \right) ds, \quad \boldsymbol{x}^\star \to \boldsymbol{x}_\pm. \tag{2.3.1}$$

Here $\boldsymbol{x}_\pm$ is shorthand for the two limiting cases. Note that, for $\boldsymbol{x}' \in C$, the Cauchy-Riemann relations with inward facing normals, applied to the complex logarithm, give us

$$\int_C \frac{\partial}{\partial n} \log \frac{1}{|\boldsymbol{x}' - \boldsymbol{x}|} ds = \int_C \frac{\partial \theta}{\partial s} ds = \pi, \tag{2.3.2}$$

where $\partial/\partial s$ represents a tangential derivative and θ is the angle between $\boldsymbol{x}$ and $\boldsymbol{x}'$. So we have, on reversing the order of integration in (2.3.1) and applying (2.3.2), that

$$\int_C \frac{\partial \phi}{\partial n} ds = \begin{cases} \int_C \sigma(\boldsymbol{x}') ds', & \boldsymbol{x}^\star \to \boldsymbol{x}_-, \\ 0, & \boldsymbol{x}^\star \to \boldsymbol{x}_+. \end{cases} \tag{2.3.3}$$

So in the case considered here, we need to explicitly constrain the integral of source strengths over the surface to be zero, in order that the volume remains constant. To show that this can be done, consider the problem of finding a potential in an internal domain, D, with constant Dirichlet boundary conditions. If we are given that $\phi = 1$ on ∂D, then we have the following Fredholm equation to solve for λ on ∂D:

$$\frac{1}{2\pi} \int_{\partial D} \lambda(\boldsymbol{x}') \log \frac{1}{|\boldsymbol{x}' - \boldsymbol{x}|} ds' = 1, \quad \forall \boldsymbol{x} \in \partial D, \tag{2.3.4}$$

(see for example Jaswon and Symm, 1963). By the Dirichlet existence theorems, $\phi = 1$ throughout D, and so taking the derivative of (2.3.4) normal to ∂D, into D yields (as in

(2.3.1))

$$\frac{1}{2\pi}\int_{\partial D}\lambda(\boldsymbol{x}')\frac{\partial}{\partial n}\log\frac{1}{|\boldsymbol{x}'-\boldsymbol{x}|}ds'-\frac{1}{2}\lambda(\boldsymbol{x})=0,\quad\forall\boldsymbol{x}\in\partial D.$$

This has non-trivial solutions since application of (2.3.2) shows that its adjoint,

$$\frac{1}{2\pi}\int_{\partial D}\mu(\boldsymbol{x}')\frac{\partial}{\partial n'}\log\frac{1}{|\boldsymbol{x}-\boldsymbol{x}'|}ds'-\frac{1}{2}\mu(\boldsymbol{x})=0,\quad\forall\boldsymbol{x}\in\partial D,$$

certainly has non-trivial solutions for μ — namely $\mu = const$. Multiplying (2.2.16) by $\lambda(\boldsymbol{x})$, integrating over C, interchanging the order of integration and using (2.3.4), for the case $\partial D = C$, it is evident that the volume remains fixed, according to (2.3.3), when

$$k=\frac{\int_C\lambda(\boldsymbol{x})\phi(\boldsymbol{x})ds}{\int_C\lambda(\boldsymbol{x})ds}.$$

In practice we do not need to find λ in order to determine the correct constant, k, as we can use (2.2.16) in conjunction with a volume constraint. Thus, from (2.3.3), we need to solve the system:

$$\phi(\boldsymbol{x})=k+\frac{1}{2\pi}\int_C\sigma(\boldsymbol{x}')\log\frac{1}{|\boldsymbol{x}'-\boldsymbol{x}|}ds',\tag{2.3.5}$$

$$0=\int_C\sigma(\boldsymbol{x}')ds'.\tag{2.3.6}$$

2.3.2 Discretisation.

In order to solve the problem of the two-dimensional bubble computationally, the surface shape and functions defined on the surface need to be represented; in this case, discrete forms are used. The symmetry of the problem means that only half of the bubble need be followed through time, but a more general code not requiring symmetry was written. Only the repositioning routine assumes symmetry (see section 2.3.3), but modification for the general case is straightforward. The program should therefore be able to handle other problems such as finding the motion of many bubbles in arbitrary arrangements (see Robinson, 1992; Robinson, Boulton-Stone and Blake, 1993) or, by using an appropriate Green's function, a bubble rising under an inclined plane. In this particular case, the whole of the bubble's surface was represented at N discrete points.

It was found that in order to maintain stability for those methods which produced good results, it was necessary to place points either side of the central axis at the top and bottom of the bubble, rather than on this axis. Since a linear representation for the bubble shape was used here, this is the same as insisting that the tangents to the top and bottom of the bubble are horizontal as required physically due to the symmetry of the problem.

An isoparametric representation was used, for both the bubble surface and the source strength, σ, namely that on the ith element $(i = 1, 2, \ldots, N)$,

$$\boldsymbol{q}(\epsilon) = (1 - \epsilon)\boldsymbol{x}_i + \epsilon\boldsymbol{x}_{i+1},$$

$$\sigma(\epsilon) = (1 - \epsilon)\sigma_i + \epsilon\sigma_{i+1},$$

(2.3.7)

for $\epsilon \in [0, 1]$, where $\boldsymbol{x}_{N+1} \equiv \boldsymbol{x}_1$ and $\sigma_{N+1} \equiv \sigma_1$. Thus equation (2.3.5) becomes

$$\phi_i \equiv \phi(\boldsymbol{x}_i) = \frac{1}{2\pi} \sum_{j=1}^{N} \int_0^1 \left(((1 - \epsilon)\sigma_j + \epsilon\sigma_{j+1}) \log \frac{1}{|\boldsymbol{q}(\epsilon) - \boldsymbol{x}_i|} \right) d_j d\epsilon + k, \qquad (2.3.8)$$

where $d_j = |\boldsymbol{x}_{j+1} - \boldsymbol{x}_j|$, is the length of the jth element The coefficients of the σ_i in the integrals (2.3.8) can be placed in a matrix, $G \in R_{N+1 \times N+1}$, with ones in the $N + 1^{st}$ column to represent the constant, k. The $N + 1^{st}$ equation is the volume constraint (2.3.6) which discretises to

$$0 = \sum_{j=1}^{N} \frac{d_j}{2}(\sigma_j + \sigma_{j+1}),$$

so that $G_{N+1,j} = (d_j + d_{j-1})/2$.

A 4-point Gauss quadrature scheme is used to calculate the integrals in (2.3.8) except in the case where $\boldsymbol{q}$ lies on an element adjacent to the node $\boldsymbol{x}_i$, in which case it is a simple matter to calculate them analytically. Once G is found, the equation $G\underset{\sim}{\sigma} = \underset{\sim}{\phi}$ where $\underset{\sim}{\sigma} = (\sigma_1, \sigma_2, \ldots, \sigma_N, k)^T$ and $\underset{\sim}{\phi} = (\phi_1, \phi_2, \ldots, \phi_N, 0)^T$ can be solved using Gauss elimination.

In order to update the positions of the nodes on the bubble, the derivatives of the potential in the normal and tangential directions are required. Differentiating (2.2.16), the expression for the potential, gives (see A3)

$$\frac{\partial \phi}{\partial n}(\boldsymbol{x}) = \frac{1}{2\pi} \int_C (\sigma(\boldsymbol{x}')\hat{\boldsymbol{n}}(\boldsymbol{x}) - \sigma(\boldsymbol{x})\hat{\boldsymbol{n}}(\boldsymbol{x}')) \cdot \frac{\boldsymbol{x}' - \boldsymbol{x}}{|\boldsymbol{x}' - \boldsymbol{x}|^2} ds', \quad \boldsymbol{x} \in C, \qquad (2.3.9)$$

where $\hat{\boldsymbol{n}}$ is the normal to the bubble surface at $\boldsymbol{x}$ or $\boldsymbol{x}'$ as indicated. The knowledge of σ on C can be employed to find $\partial\phi/\partial n$ at all points on C. This integral is calculated using the discretisation scheme of (2.3.7), thus yielding an expression similar to (2.3.8). We take the normal at $\boldsymbol{x}'$ to be in the direction perpendicular to the line joining the ends of each segment of integration. However since $\boldsymbol{x}$, the observation point, is situated on a node rather than along an element, it is necessary to use a quadratic fit to the curve through the point and its two neighbours to get a good approximation for the direction of the normal. The exception to this rule is in the case where $\boldsymbol{x}'$ lies on the intervals adjacent to the node at $\boldsymbol{x}$. Here, the normal at $\boldsymbol{x}'$ is also taken to be the normal to a quadratic through three points, and we use quadratic interpolation for the integration (see Appendix B). If this is not done, then as $\boldsymbol{x}'$ approaches $\boldsymbol{x}$ the normals do not become parallel and thus the expression $\sigma(\boldsymbol{x}')\hat{\boldsymbol{n}}(\boldsymbol{x}) - \sigma(\boldsymbol{x})\hat{\boldsymbol{n}}(\boldsymbol{x}')$ of (2.3.9) does not vanish as it clearly should. A 4-point Gauss rule is again used for all the integrals. Placing the coefficients of the σ_j in the integrals corresponding to (2.3.9) into a matrix, $H \in R_{N \times N}$, and defining

$$\psi_i \equiv \left.\frac{\partial\phi}{\partial n}\right|_{\boldsymbol{x}_i},$$

we have $\underset{\sim}{\psi} = H\underset{\sim}{\sigma}$, which can then be used to calculate the normal velocities.

The tangential derivatives of ϕ and hence the tangential velocities are calculated by fitting a quadratic to each set of potentials at three adjacent nodes (Taib, 1985). The boundary conditions (2.2.1) and (2.2.4) allow us to update the nodal positions and potentials respectively, integrating with a simple iterative trapezium rule (see below). Once a single step of the method has been completed, the initial conditions for the next step — the potentials at and positions of the nodes — are known. Thus repeating this process, the motion of the bubble can be followed through time.

2.3.3 Time-stepping and repositioning.

To move the position of the bubble and the potential at its surface through time, an iterative trapezium rule is used for each $\boldsymbol{x}_i(t)$ and $\phi_i(t)$, $i = 1, 2, \ldots, N$. Firstly, a new value

is predicted using Euler's rule; for instance, for $\phi_i(t)$

$$\phi_i^{(0)}(t + \delta t) = \phi_i(t) + \delta t \frac{D\phi_i}{Dt}(t),$$

where $D\phi/Dt$ is given by the right-hand side of (2.2.4). The trapezium rule,

$$\phi_i^{(j+1)}(t + \delta t) = \phi_i(t) + \frac{\delta t}{2} \left\{ \frac{D\phi_i}{Dt}(t) + \frac{D\phi_i^{(j)}}{Dt}(t + \delta t) \right\},$$

is then used repeatedly. The same scheme is used, in parallel, for $\boldsymbol{x}_i(t)$, with the velocities given by (2.2.1). (For simplicity, the velocities are resolved into cartesian coordinates, when updating the position vectors). Notice that the integral equations need to be re-formulated and solved for the velocities at time $t + \delta t$ after the first Euler and each trapezium step, until convergence, thus making the time-stepping process computationally expensive.

The time-step is chosen so that

$$\delta t = \min_{i=1,\ldots,N} \left\{ \left| \frac{\Delta\phi}{D\phi_i/Dt} \right| \right\},$$

where $\Delta\phi$ has a prescribed value. This time-step is calculated immediately before the first Euler step, and fixed until the time-step has been completed. Convergence is assumed when the position of the bubble does not change between iterations, according to the criterion

$$\frac{\max_{i=1,\ldots,N} \left\{ \left| \boldsymbol{x}_i^{(j+1)}(t + \delta t) - \boldsymbol{x}_i^{(j)}(t + \delta t) \right| \right\}}{\max_{i=1,\ldots,N} \{ |\boldsymbol{x}_i(t)| \}} < \epsilon.$$

Typically, $\epsilon = 10^{-4}$. If the method fails to converge after j_{max} steps, or starts to diverge after j_{min} steps the time-step, δt, is halved and the procedure repeated.

If, after any of the time-steps, the nodes become too close, i.e. if for any j

$$kd_j < \frac{1}{N} \sum_{i=1}^{N} d_i,$$

then the original nodes are repositioned. Typically, $k = 2$ gives good results. Repositioning is carried out by stepping around the bubble and placing new nodes equally spaced according to the linear arc-lengths of the old positions. The new positions and potentials

can be found by quadratic interpolation to three points. Note that there is an arbitrariness here, since the new point is generally on an old element, and thus a choice needs to be made as to which of the two points at the ends of the adjacent elements to take for the third interpolation point. Since the problem is symmetrical, we fix the side from which the final node is taken and only reposition half of the surface after which we reflect the data in the y-axis. This reflection is also required on the grounds that it is not the exact arc-length being used above to find the new positions of the nodes, so it is likely that there would, otherwise, be a different distribution of points on either side of the bubble, after repositioning. The reason for using quadratic interpolation is that with linear interpolation, the bubble tends to flatten off and corners begin to appear after many repositionings.

2.4 Dipole distribution method.

Returning to Green's theorem and noticing that, for a fixed volume bubble, the source term is identically zero in the far-field expansion (2.2.13), it is reasonable to expect a double-layer distribution to represent well the behaviour of the bubble. If we know the potential initially then, in principle, we may use (2.2.17) to find the dipole strength, μ. However as $\boldsymbol{x} \to C_-$, we get the boundary problem

$$\phi(\boldsymbol{x}) - k = -\frac{1}{2\pi} \int_C \mu(\boldsymbol{x}') \frac{\partial}{\partial n'} \log \frac{1}{|\boldsymbol{x}' - \boldsymbol{x}|} ds' + \frac{1}{2}\mu(\boldsymbol{x}), \quad \boldsymbol{x} \in C, \qquad (2.4.1)$$

and from (2.3.2), the right-hand side vanishes if $\mu = const$. One way to get round this problem is to add a vortex term to the integrand. This was studied by Kreβ and Spassov (1983) for the Helmholtz and Laplace equations, with a view to minimising the condition number of the corresponding integral operators. However in order to keep this method as a pure dipole method, the following resolution, detailed in Mikhlin (1957), is used here.

Consider the complex form of (2.2.17), namely

$$W(z) = k - \frac{1}{2\pi i} \int_C \frac{\mu(z')}{z' - z} dz', \quad z \in \Omega_-,$$

and set k to be the real constant,

$$k = -\frac{1}{2\pi} \int_C \mu(z')ds'.$$

As z approaches C, the real part of the potential is given by (2.4.1). If the homogeneous problem, i.e. $\phi \equiv \Re[W] = 0$ on C, has solution $\mu_0(z)$, then for $z \in \Omega_-$, define the function

$$W_0(z) = -\frac{1}{2\pi i} \int_C \frac{\mu_0(z')}{z' - z}dz' - \frac{1}{2\pi} \int_C \mu_0(z')ds'. \qquad (2.4.2)$$

Since W_0 is analytic with $\Re[W_0] = 0$ on C, it must be an imaginary constant, i.e. $W_0 = ia$. As $z \to \infty$ in (2.4.2), the first integral vanishes and so we have

$$ia = -\frac{1}{2\pi} \int_C \mu_0(z')ds'. \qquad (2.4.3)$$

As μ_0 is real, $a = 0$ and so $W_0(z) = 0, \forall z \in \Omega_-$, so that (see Muskhelishvili, 1953), μ_0 is the boundary value of a function, Ψ, continuous on $C \cup \Omega_-$, analytic on Ω_-. Again as μ_0 is real, $\Im[\Psi(z)] = 0$ and as Ψ is analytic, it must be a real constant, c, i.e. $\mu_0 = c$, but as $a = 0$, (by virtue of 2.4.3), $c = 0$ and thus there are no non-trivial solutions to the boundary problem.

Hence the dipole method used is based on the integral equation

$$\phi(\boldsymbol{x}) = \frac{1}{2\pi} \int_C (\mu(\boldsymbol{x}') - \mu(\boldsymbol{x})) \hat{\boldsymbol{n}}(\boldsymbol{x}') \cdot \frac{\boldsymbol{x}' - \boldsymbol{x}}{|\boldsymbol{x}' - \boldsymbol{x}|^2} ds' - \frac{1}{2\pi} \int_C \mu(\boldsymbol{x}')ds', \quad \boldsymbol{x} \in C, \qquad (2.4.4)$$

(see A5). The method is, from now on, very similar to the source method, except that no volume constraint is required: this is implicit.

Discretising the first integral of (2.4.4) according to (2.3.7) gives

$$\frac{1}{2\pi} \sum_{j=1}^N \int_0^1 ((1-\epsilon)\mu_j + \epsilon\mu_{j+1} - \mu_i) \hat{\boldsymbol{n}}(\boldsymbol{q}(\epsilon)) \cdot \frac{\boldsymbol{q}(\epsilon) - \boldsymbol{x}_i}{|\boldsymbol{q}(\epsilon) - \boldsymbol{x}_i|^2} d_j d\epsilon. \qquad (2.4.5)$$

If G is the matrix of coefficients of the μ's of (2.4.4), of which a contribution $\tilde{G}$ is from (2.4.5), with $\tilde{G}^1$ and $\tilde{G}^2$ coming from the first and second terms of the integrals of (2.4.5), then

$$\tilde{G}_{ij} = \begin{cases} \tilde{G}_{ij}^1 + \tilde{G}_{ij}^2, & j \neq i, \\ \tilde{G}_{ii}^1 + \tilde{G}_{ii}^2 + \tilde{G}_i^3, & j = i, \end{cases}$$

$$- 19 -$$

where $\tilde{G}^3$ is the coefficient of the dipole strength at the observation node in each of the integrals of (2.4.5). It is clear that for the linear, isoparametric interpolation used,

$$\tilde{G}_i^3 = -\sum_{j=1}^{N}(\tilde{G}_{ij}^1 + \tilde{G}_{ij+1}^2)$$

$$= -\left(\sum_{j\neq i}\tilde{G}_{ij} + \tilde{G}_{ii}^1 + \tilde{G}_{ii}^2\right).$$

This gives

$$\tilde{G}_{ii} = -\sum_{j\neq i}\tilde{G}_{ij}, \qquad (2.4.6)$$

thus removing the need to explicitly calculate the integrals for the diagonal terms of G.

Taking the normal at $\boldsymbol{q}$ as the linear normal, the integrand of (2.4.5) vanishes when $\boldsymbol{q}$ is adjacent to $\boldsymbol{x}_i$. The constant term in the second integral of (2.4.4) gives a contribution to G_{ij} of $-(d_j + d_{j-1})/4\pi$.

As before, we get a linear algebraic system, $\underset{\sim}{\phi} = G\underset{\sim}{\mu}$, to solve, this time for the dipole strength at each node. The normal derivative of (2.2.17) (see A6) is

$$\frac{\partial\phi}{\partial n}(\boldsymbol{x}) = -\frac{1}{2\pi}\int_C\left(\frac{d\mu}{ds}(\boldsymbol{x}')\hat{\boldsymbol{t}}(\boldsymbol{x}) - \frac{d\mu}{ds}(\boldsymbol{x})\hat{\boldsymbol{t}}(\boldsymbol{x}')\right)\cdot\frac{\boldsymbol{x}' - \boldsymbol{x}}{|\boldsymbol{x}' - \boldsymbol{x}|^2}ds', \quad \boldsymbol{x} \in C, \qquad (2.4.7)$$

where $\hat{\boldsymbol{t}}$ is the tangent to the bubble.

The tangent at $\boldsymbol{x}'$ is taken to be the linear tangent, whereas the tangent at $\boldsymbol{x}$ is taken to be the quadratic-fit tangent (compare with source method). Again, the exception is when $\boldsymbol{x}$ and $\boldsymbol{x}'$ are adjacent, when the quadratic integration has to be used, so that the integrand is non-singular as $\boldsymbol{x}' \to \boldsymbol{x}$. The tangential derivatives of the dipole strength are also found by a quadratic fit to three points. Thus the coefficient matrix for the discretisation of (2.4.7) allows us to calculate the normal velocities on the bubble surface. The tangential velocities can be calculated, as before, from the tangential derivatives of the potentials. The positions and potentials are then updated (see §2.3.3), thus completing a single time step.

2.5 Green's formula method.

A very common approach to solving potential problems by boundary integral methods is to use Green's formula (2.2.12) directly. The Green's formula method may be thought of as a distribution of both single and double layer potentials on the surface of the bubble. However the strengths of these distributions are the physically significant potential and its normal derivative, rather than the jumps of these values across the surface of the bubble, as is the case in the indirect methods described in the last two sections.

Analogous to (A5) we may express the second integral of (2.2.12) in a regular form so that Green's formula may be written as

$$\phi(\boldsymbol{x}) = \frac{1}{2\pi} \int_C \frac{\partial \phi}{\partial n}(\boldsymbol{x}') \log \frac{1}{|\boldsymbol{x}' - \boldsymbol{x}|} ds' + \frac{1}{2\pi} \int_C (\phi(\boldsymbol{x}') - \phi(\boldsymbol{x})) \hat{\boldsymbol{n}}(\boldsymbol{x}') \cdot \frac{\boldsymbol{x}' - \boldsymbol{x}}{|\boldsymbol{x}' - \boldsymbol{x}|^2} ds' + k, \qquad (2.5.1)$$

for $\boldsymbol{x} \in C$. As, initially at least, we know the potential, ϕ, at each of the points on the bubble's surface, we can in principle solve (2.5.1) as a Fredholm integral equation of the first kind for $\partial \phi / \partial n$ on C.

Since the method allows for a source-like behaviour, it is necessary to apply the constraint

$$\int_C \frac{\partial \phi}{\partial n} ds = 0, \qquad (2.5.2)$$

to ensure a constant volume and determine the unknown constant, k. Proceeding in a similar manner to previously, we discretise the integrals using linear representations for the surface, the potential and its normal derivative.

Define $G \in R_{N+1 \times N+1}$ and $H \in R_{N+1 \times N}$ to be the coefficient matrices of the normal derivative and potential respectively. Placing the second integral on the left-hand side and using (2.4.6) we have

$$H_{ii} = 1 - \sum_{j \neq i} H_{ij}.$$

The $N + 1^{st}$ row of H contains zeros and the volume constraint equation (2.5.2) gives $G_{N+1,j} = (d_j + d_{j-1})/2$. The $N + 1^{st}$ column of G contains all ones — the coefficients of the constant, k.

The linear system $G\underset{\sim}{\psi} = H\underset{\sim}{\phi}$, can then be solved for $\underset{\sim}{\psi}$, the vector of normal velocities. Note that the integrals are exactly those which appear for the potentials in the source and dipole formulations and are calculated in the same way. Once the normal derivatives and the tangential derivatives are found, the potential and positions can be updated, thus completing a step of the method.

2.6 Vorticity distribution method.

It is possible to solve the problem using a distribution of point vortices around the bubble's surface. As the fluid is incompressible, we may write $\boldsymbol{u} = \nabla \times \boldsymbol{B}$ for a vector field, $\boldsymbol{B}$. If $\underset{\sim}{\omega}$ is a vorticity distribution, we have that

$$\underset{\sim}{\omega} = \nabla \times \boldsymbol{u} = \nabla(\nabla \cdot \boldsymbol{B}) - \nabla^2 \boldsymbol{B}. \tag{2.6.1}$$

If (2.6.1) were simply $\nabla^2 \boldsymbol{B} = -\underset{\sim}{\omega}$, it would have the solution given by the Poisson integral,

$$\boldsymbol{B}(\boldsymbol{x}) = \frac{1}{2\pi} \int_A \underset{\sim}{\omega}(\boldsymbol{x}') \log \frac{1}{|\boldsymbol{x}' - \boldsymbol{x}|} dA'. \tag{2.6.2}$$

It can be shown, by an application of the divergence theorem (Batchelor, 1967), that $\nabla \cdot \boldsymbol{B} = 0$ if the region, A, extends to infinity where the fluid is at rest or if A is extended to a region with a boundary that is everywhere tangent to the vorticity, $\underset{\sim}{\omega}$.

For a distribution of vorticity $\underset{\sim}{\Gamma}(\boldsymbol{x}') = \underset{\sim}{\omega}(\boldsymbol{x}')dn$ on the bubble, where dn is an element normal to the surface, the vector potential (2.6.2) may be written

$$\boldsymbol{B}(\boldsymbol{x}) = \frac{1}{2\pi} \int_C \underset{\sim}{\Gamma}(\boldsymbol{x}') \log \frac{1}{|\boldsymbol{x}' - \boldsymbol{x}|} ds'. \tag{2.6.3}$$

We may be able to invert this integral equation to find the vorticity distribution, given the vector potential. In order to find the velocity with which the bubble's surface moves, we consider the complex potentials. As $\boldsymbol{u} = \nabla \times \boldsymbol{B}$, for a two-dimensional velocity field, $\boldsymbol{u}$, it must be that $\boldsymbol{B} = (0, 0, \psi)^T$, where ψ is the stream function of the flow, and $\underset{\sim}{\Gamma} = (0, 0, \Gamma)^T$. Thus from (2.6.3) the complex potential, $W = \phi + i\psi$, is given by

$$W(z) = -\frac{1}{2\pi i} \int_C \frac{\Gamma(z')}{\tau(z')} \log \frac{1}{z' - z} dz', \tag{2.6.4}$$

$$- 22 -$$

with $\tau(z) = dz/ds$ the tangent to C. The derivative of (2.6.4) forms the basis of the vortex method used by Soh (1987). Here, we use the normal and tangential velocity components which, for the external problem, (see (A8-9)) are given by

$$\frac{\partial \phi}{\partial n} = -\frac{1}{2\pi} \int_C \left(\Gamma(\boldsymbol{x}')\hat{\boldsymbol{t}}(\boldsymbol{x}) - \Gamma(\boldsymbol{x})\hat{\boldsymbol{t}}(\boldsymbol{x}') \right) \cdot \frac{\boldsymbol{x}' - \boldsymbol{x}}{|\boldsymbol{x}' - \boldsymbol{x}|^2} ds', \qquad (2.6.5)$$

and

$$\frac{\partial \phi}{\partial s} = \frac{1}{2\pi} \int_C \left(\Gamma(\boldsymbol{x}')\hat{\boldsymbol{n}}(\boldsymbol{x}) - \Gamma(\boldsymbol{x})\hat{\boldsymbol{n}}(\boldsymbol{x}') \right) \cdot \frac{\boldsymbol{x}' - \boldsymbol{x}}{|\boldsymbol{x}' - \boldsymbol{x}|^2} ds', \qquad (2.6.6)$$

for $\boldsymbol{x} \in C$.

The computational scheme here is slightly different from previously. Once the integrals (2.6.5) and (2.6.6) have been calculated, in the same manner as the normal derivatives of the source and dipole integrals, two matrix equations are obtained

$$\underset{\sim}{\phi}_n = H \underset{\sim}{\gamma}, \qquad (2.6.7)$$

and

$$\underset{\sim}{\phi}_s = G \underset{\sim}{\gamma}, \qquad (2.6.8)$$

respectively, with $\underset{\sim}{\phi}_n$, $\underset{\sim}{\phi}_s$ and $\underset{\sim}{\gamma}$ denoting vectors of R^N containing nodal values of normal velocities, tangential velocities and vortex strengths respectively; $G, H \in R_{N \times N}$ are coefficient matrices. Thus given a potential distribution on the bubble (initially constant), its tangential derivatives are first calculated by a quadratic fit. Equation (2.6.8) is then solved for the vortex strengths $\underset{\sim}{\gamma}$ and this substituted into (2.6.7) to find the normal velocities. In this way the bubble can be stepped through time exactly as before.

2.7 Results and discussion.

The following pages show examples of the output from the four codes described above. Calculations shown are based on a standard set-up with $N = 50$ points, the repositioning parameter $k = 2$, the time-step parameter $\Delta \phi = 0.1$ and the convergence parameter $\epsilon = 10^{-4}$ (see §2.3.3). In order to get insight into the effect of changing some of the parameters, other runs were also carried out. For the dipole, vortex and Green's methods the results

are visually identical and sample output for the vortex method only is included in figure 2.1. The number of time-steps required to reach $t = 4.0$ was 82 for these three methods, in addition to which 8, 7 and 7 time-steps respectively were abandoned in order to reposition points. An estimate of the average convergence rates in the time-stepping routine can be calculated from the ratio of the number of iterations required in the trapezium rule routine to the number of time-steps. The dipole, vortex and Green's methods gave values of 2.86, 2.82 and 2.83 iterations per time-step respectively. Thus, based on this data so far there is nothing to distinguish these three methods.

The results in figure 2.1 closely match those of Baker and Moore (1989), who went on to examine the discrepancies between calculation and experiment. The main difference, which can be clearly seen in the photographs of Walters and Davidson (1962), is that the jet in the experiment widens out when it is further away from the top of the bubble. This was shown to be as a result of a greater computed jet speed. This discrepancy was not removed by including surface tension forces into the calculations. Possible reasons for differences were put forward. These relate to the fact that in the experiments, a two-dimensional bubble is approximated by injecting gas into the narrow gap between two sheets of glass which is filled with liquid. Thus, three-dimensional effects such as the formation of a meniscus or a thin film separating the bubble from the glass may be important.

Figure 2.2 shows the poor performance of the source method. This was as far as we could manage to get it to run. There seems to be an inherent instability on the lower part of the surface, near the indent. We attempted to smooth this out using the Longuet-Higgins and Cokelet (1976) 5-point formula, but this made little difference. We also used a modified source distribution technique (Muskhelishvili, 1953), by integrating (2.2.16) by parts to give, for $\boldsymbol{x} \in C$,

$$\phi(\boldsymbol{x}) = \frac{1}{2\pi} \int_C \left(\nu(\boldsymbol{x}') - \nu(\boldsymbol{x})\right) \hat{\boldsymbol{t}}(\boldsymbol{x}') \cdot \frac{\boldsymbol{x}' - \boldsymbol{x}}{|\boldsymbol{x}' - \boldsymbol{x}|^2} ds' + k,$$

where

$$\left.\frac{d\nu}{ds}\right|_{\boldsymbol{x}} \equiv \sigma(\boldsymbol{x}).$$

As in the dipole method, k was chosen to be

$$k = \frac{1}{2\pi} \int_C \nu(\boldsymbol{x}')ds',$$

to ensure solvability of the corresponding Dirichlet problem and thus preserve bubble volume. The normal velocities are again given by equation (2.3.9). Results from this method were also very disappointing, with only a small improvement over the original source method.

A routine to calculate the total energy in the fluid was included in all codes. As in Baker and Moore (1989) the quantity $|T + V|/V$ was output at several times throughout the runs. However, for all methods these values range from about 10^{-3} up to 10^{-2} with no difference between the dipole and Green's methods of magnitude significantly larger than the variation with time. However for the vortex method the energy ratios remain of the order of 10^{-3} throughout most of the latter part of the run, through to $t = 4.0$, whereas the other two methods that completed the run have figures higher than this by a factor of 10.

To investigate the stability of the various codes, an initial perturbation was applied to the bubble. Specifically, the initial radius was taken as

$$r = 1 + e\cos(f\theta).$$

For the case of a perturbation amplitude of 0.01 and a wave number of 18, a clear initial amplification of the perturbation is apparent for the Green's method (figure 2.3), suggesting that it is significantly less stable than the other methods which ran to completion by sweeping the perturbation to the underside of the bubble (figure 2.4). For a lower wave number of 5, both the dipole and vortex methods are relatively untouched whereas the Green's method reaches $t = 4.0$ visibly perturbed. For a wave number of 9, a jagged region develops on the jet in the vortex method causing the code to break down. It is

however clear that the results for initially large wave numbers are somewhat restricted by the point resolution on the bubble so that the actual wave number imposed numerically may be much less than this and irregular in apparent amplitude.

The 1-norm condition numbers for the various methods were also examined. The average values for a complete run starting with the unperturbed bubble were 1.2×10^2, 6.1×10^1 and 4.6×10^2 for the dipole, vortex and Green's methods were respectively. This may explain the initial amplification of the perturbation for the Green's method as opposed to the other methods, but work needs to be done on how stable a two dimensional bubble really is (see section 2.8), as in all of the methods the repositioning will damp out perturbations to a certain extent (Moore, 1981). The greater success of the vortex and dipole methods may have been anticipated on the grounds that they hinge on solving second-kind rather than first-kind equations.

It is interesting to note that the average condition numbers for the source and modified source methods were 4.2×10^4 and 5.8×10^2 respectively, which suggests that it is not the stability of the modified source method that hinders its progress, although this may contribute to the lack of success with the source method.

The coloured plots of figures 2.5 and 2.6 show the pressure in the fluid at times $t = 1.5$ and $t = 3.5$ respectively. The pressures are calculated from (2.2.2) by working out, at two successive time-steps, the potential, φ, at a large number of points in the fluid using (2.2.12), viz for $\boldsymbol{x} \in \Omega_-$,

$$\varphi(\boldsymbol{x}) = \int_C \left(G \frac{\partial \phi}{\partial n}(\boldsymbol{x}') - \phi(\boldsymbol{x}') \frac{\partial G}{\partial n'} \right) ds'.$$

In this case, a 30×30 grid of points is used. Derivatives of the potential are calculated by a finite difference scheme. Figures 2.5 and 2.6 also show the streamlines at the corresponding times. These are calculated by taking the conjugate harmonic function to (2.2.12) which gives the stream function in the fluid in terms of the boundary values of the potential and its normal derivative, namely for $\boldsymbol{x} \in \Omega_-$,

$$\psi(\boldsymbol{x}) = \frac{1}{2\pi} \int_C \left(-\theta(\boldsymbol{x}' - \boldsymbol{x}) \frac{\partial \phi}{\partial n}(\boldsymbol{x}') + \phi(\boldsymbol{x}') \hat{\boldsymbol{t}}(\boldsymbol{x}') \cdot \frac{\boldsymbol{x}' - \boldsymbol{x}}{|\boldsymbol{x}' - \boldsymbol{x}|^2} \right) ds',$$

where $\theta(\boldsymbol{x}' - \boldsymbol{x})$ is the angle between the vector $\boldsymbol{x}' - \boldsymbol{x}$ and the x-axis, in the sense defined in Jaswon and Symm (1977, p 155), so that the function is continuous as $\boldsymbol{x}'$ traverses the bubble surface for any fixed $\boldsymbol{x} \in \Omega_-$. The pressure plots (figures 2.5 (a) and (c)) show the pressure near the centre of the underside of the bubble to be slightly greater than the pressure beneath the outer parts; this helps to accelerate the jet through the bubble. At the later time, this high pressure is seen to extend into the middle of the jet causing the subsequent broadening. The streamlines (figures 2.5 (b) and (d)) show the bubble to exhibit the essential behaviour of a dipole, as predicted by equation (2.2.13).

If no repositioning is performed, all of the successful methods break down just before the jet starts to broaden out. Due to the translation of the bubble, the points move rapidly around to the lower part of the bubble as it moves up through the fluid, thus resolution is soon lost on the upper part. This can be clearly seen in figure 2.6(b) where the paths taken by particles on the bubble's surface are followed through time. Even points that start near the top of the bubble end up well into the jet by $t = 4.0$. Repositioning was not used in some of the calculations that have been done for cavitation bubbles, for example Blake et al (1986), where translating velocities are much smaller than jet velocities.

The programs were also run with reduced time-step convergence parameters, so that the stepping routine converged with just one pass through the trapezium rule. All three working methods ran through to t=4.0, thus indicating that the higher accuracy in the time-stepping routine may be superfluous.

2.8 Stability analysis.

2.8.1 Formulation of the equations.

In this section, we examine the growth of small perturbations to a two-dimensional bubble. This is done by utilising the analytic solution of Walters and Davidson (1962) which is valid for small times. Initially, the bubble has acceleration g and thus the analysis is slightly different from that of Batchelor (1987) who examined the stability of a spherical

cap bubble which had reached a steady state. It may be possible to adapt Batchelor's results for a two-dimensional bubble that has almost reached a terminal velocity and, on the upper surface at least, is changing shape very slowly. This could be used in conjunction with this analysis to judge its long-term stability.

For convenience, place the co-ordinate origin at the centre of the accelerating bubble. If this centre rises at a speed $U(t)$ then, as in Walters and Davidson (1962), Bernoulli's theorem becomes

$$\frac{p_\infty}{\rho} = \frac{p}{\rho} + \frac{1}{2}|\boldsymbol{u}|^2 + \frac{\partial \phi}{\partial t} + g\left(\int_0^t U(t')dt' + r\cos\theta\right), \tag{2.8.1}$$

where $\boldsymbol{u}$ and ϕ are the velocity and corresponding potential, taken with respect to the fluid which is at rest at infinity, and (r,θ) represent polar co-ordinates from the moving centre with $\theta = 0$ in the direction of travel. If the bubble has internal pressure $p_b(t)$, we have the pressure balance at the bubble surface

$$p = p_b - \sigma\kappa, \tag{2.8.2}$$

where σ is the surface tension, and κ is the curvature. Thus using (2.8.1) and (2.8.2) gives

$$\frac{1}{2}|\boldsymbol{u}|^2 + \frac{\partial \phi}{\partial t}\bigg|_{\substack{\text{fixed in} \\ \text{space}}} + g\left(\int_0^t U(t')dt' + R\cos\theta\right) - \sigma\kappa = P(t), \tag{2.8.3}$$

on the bubble surface, given by $r = R(\theta,t)$, where $P(t) = (p_\infty - p_b(t))/\rho$.

For the corresponding kinematic condition, as before, use the fact that particles of fluid on the bubble surface must remain there. In order to determine this condition, first define the potential for the bubble at rest with the fluid moving around it by $f = \phi - Ur\cos\theta$. Thus the kinematic condition is

$$\frac{\partial R}{\partial t} + \frac{1}{R^2}\frac{\partial f}{\partial \theta}\bigg|_{r=R}\frac{\partial R}{\partial \theta} = \frac{\partial f}{\partial r}\bigg|_{r=R}. \tag{2.8.4}$$

In terms of ϕ, (2.8.4) becomes

$$\frac{\partial R}{\partial t} + \frac{1}{R}\left(\frac{1}{R}\frac{\partial \phi}{\partial \theta}\bigg|_{r=R} + U\sin\theta\right)\frac{\partial R}{\partial \theta} = \frac{\partial \phi}{\partial r}\bigg|_{r=R} - U\cos\theta. \tag{2.8.5}$$

Now introduce perturbations $\eta(\theta,t)$ to the bubble surface and ψ to the potential. Substitute these into (2.8.3) and (2.8.5), expand about $r = R$, neglecting squares of small

terms, and subtract the corresponding unperturbed equations. This gives, for the dynamic condition,

$$\eta u_\theta \frac{\partial u_\theta}{\partial r} + \frac{u_\theta}{R} \frac{\partial \psi}{\partial \theta} + \eta u_r \frac{\partial u_r}{\partial \theta} + u_r \frac{\partial \psi}{\partial r} + \eta \frac{\partial^2 \phi}{\partial r \partial t} + \frac{\partial \psi}{\partial t} + g\eta \cos\theta - \sigma\kappa' = 0, \qquad (2.8.6)$$

and, for the kinematic condition,

$$\frac{\partial \eta}{\partial t} + \frac{1}{R^2} \left\{ \frac{\partial R}{\partial \theta} \left(\eta \frac{\partial^2 \phi}{\partial r \partial \theta} + \frac{\partial \psi}{\partial \theta} - U\eta\sin\theta - 2\frac{\eta}{R} \frac{\partial \phi}{\partial \theta} \right) + \frac{\partial \eta}{\partial \theta} \left(\frac{\partial \phi}{\partial \theta} + UR\sin\theta \right) \right\} = \eta \frac{\partial^2 \phi}{\partial r^2} + \frac{\partial \psi}{\partial r}. \quad (2.8.7)$$

Here $u_\theta = \partial\phi/R\partial\theta$, $u_r = \partial\phi/\partial r$ and κ' is the small change in curvature.

In order to solve these equations and determine the evolution of the perturbation, it is necessary to know the unperturbed quantities appearing in (2.8.6) and (2.8.7). For this, we refer to the work of Walters and Davidson (1962). They derived an approximate solution for the motion of the bubble, correct for small times. Here we use the highest order terms in their expansion for the undisturbed potential. They assumed a general potential of the form

$$\phi = \sum_{n=1}^{\infty} \beta_n(t) \frac{\cos n\theta}{r^n}, \qquad (2.8.8)$$

which they substituted into the Bernoulli equation (2.8.1), ignoring the effects of surface tension and assumed the pressure to be uniform throughout the bubble, since the density of the gas contents is small compared to that of the surrounding fluid. This gave them a first approximation to the unknown β's, ignoring non-linear terms, of

$$\beta_1^{(1)} = -U^{(1)}a^2 = -gta^2,$$
$$\beta_n^{(1)} = \frac{(-1)^n(n-1)!n!2^n a^2}{(2n)!t}(gt^2)^n. \qquad (2.8.9)$$

The first two terms of the potential give

$$\phi \sim -gt\frac{a^2}{r}\cos\theta + \frac{1}{3}g^2t^3\frac{a^2}{r^2}\cos 2\theta, \quad t \to 0. \qquad (2.8.10)$$

The unperturbed surface elevation can be obtained from the kinematic condition (2.8.5). If the surface elevation is $R = a(1 + \zeta)$, $\zeta \ll 1$, then since $R \sim a$ as $t \to 0$, the first term of the power series in t for R must be a, and thus independent of θ. Hence by considering

– 29 –

the second term in the series, we see that $\partial R/\partial\theta = O(t\partial R/\partial t)$ as $t \to 0$, for almost all θ: the coefficient of the second term may vanish for some values of θ, with its derivative non-zero. Thus the terms of (2.8.5) in $\partial R/\partial\theta$ are of order $t^2\partial R/\partial t$ as $t \to 0$, and so may be neglected for small times. This leaves us with a first order ordinary differential equation for ζ,

$$a\frac{\partial\zeta}{\partial t} = \frac{\partial\phi}{\partial r} - U\cos\theta. \tag{2.8.11}$$

On substituting (2.8.10) into (2.8.11), using $U = gt$ and linearising with respect to ζ, we find the solution, retaining just the first term in t, for ζ is

$$R \sim a\left(1 - \frac{g^2t^4}{6a^2}\cos 2\theta\right), \quad t \to 0. \tag{2.8.12}$$

Now with (2.8.10) and (2.8.12) and their respective derivatives substituted into (2.8.6), we find

$$2\eta g\cos\theta + \frac{\partial\psi}{\partial\theta}\frac{gt}{a}\sin\theta + \frac{\partial\psi}{\partial r}gt\cos\theta + \frac{\sigma}{\rho a^2}\frac{\partial^2\eta}{\partial\theta^2} + \frac{\partial\psi}{\partial t} = 0, \tag{2.8.13}$$

where a term proportional to $\eta g^2t^2/a$ has been neglected in comparison to the $\eta g\cos\theta$ term. This is true for $t \ll (a/g\cos\theta)^{1/2}$, or if $\theta \ll 1$ for $t \ll (a/g)^{1/2}$. Similarly, we get for (2.8.7),

$$\frac{\partial\eta}{\partial t} + 2\eta\frac{gt}{a}\cos\theta + \frac{1}{3}\frac{\partial\psi}{\partial\theta}\frac{g^2t^4}{a^3}\sin 2\theta - \frac{\partial\psi}{\partial r} + 2\frac{\partial\eta}{\partial\theta}\frac{gt}{a}\sin\theta = 0. \tag{2.8.14}$$

Again terms of order t^5 have been neglected in comparison to terms of order t, when $t \ll (a/g)^{1/2}$.

Next, follow Batchelor (1987) by confining ourselves to $\theta \ll 1$. Near the top, the interface is almost flat, so introduce non-dimensional, cartesian co-ordinates defined by $x = \theta, z = r/a - 1, \tau = (g/a)^{1/2}t$. Thus at $z = 0$, (2.8.13) and (2.8.14) become

$$2\eta + \frac{\partial\psi}{\partial x}\tau x + \frac{\partial\psi}{\partial z}\tau + k\frac{\partial^2\eta}{\partial x^2} + \frac{\partial\psi}{\partial\tau} = 0, \tag{2.8.15}$$

and

$$\frac{\partial\eta}{\partial\tau} + 2\eta\tau + \frac{2}{3}\frac{\partial\psi}{\partial x}\tau^4x - \frac{\partial\psi}{\partial z} + 2\frac{\partial\eta}{\partial x}\tau x = 0, \tag{2.8.16}$$

where $k = \sigma/\rho ga^2$.

In order to solve these equations, try a solution of the form

$$\psi = A(\tau) \exp[n(\tau)(ix - z)],$$

$$\eta = B(\tau) \exp[in(\tau)x].$$

(2.8.17)

These are substituted into (2.8.15) and (2.8.16), bearing in mind that

$$\frac{\partial \phi}{\partial t}\Big|_{\substack{\text{fixed in} \\ \text{space}}} = \frac{\partial \phi}{\partial t}\Big|_{\substack{\text{fixed} \\ r, \theta}} + \frac{\partial \phi}{\partial r}\frac{dr}{dt} + \frac{\partial \phi}{\partial \theta}\frac{d\theta}{dt},$$

where the first term on the right is taken in the accelerating frame of reference.

Neglecting the τ^4 term as $\tau \ll 1$, the imaginary parts of (2.8.15) and (2.8.16) give $dn/d\tau + 2n\tau = 0$, thus

$$n = n_0 \exp(-\tau^2),$$

(2.8.18)

whereas the real parts give

$$\frac{dA}{d\tau} = B(kn^2 - 2),$$

$$\frac{dB}{d\tau} = -2B\tau - An.$$

(2.8.19)

The form of equations (2.8.18) and (2.8.19) are in many ways similar to those found by Batchelor (1987). A couple of differences are worth mentioning. In both this problem and that considered by Batchelor as one moves around the bubble from a position above the upper stagnation point to the equatorial region, the flow speed relative to a frame where the bubble is stationary increases and so the corresponding streamlines become closer together. Consequently any waves propagated along the bubble surface will become elongated and attenuated. The effect of this straining flow around the bubble is seen here for a single Fourier component of a travelling wave. In the case of an accelerating bubble the decay of the wave number is also dependent upon time. For small times, when the bubble is not rising very fast, (2.8.18) shows that the increase in wavelength is not as rapid as for the steadily rising bubble. The other notable feature of these equations is that, from (2.8.19), the critical nondimensional wavelength, above which disturbances would be expected to grow, is $2\pi/(\sqrt{2/k}) = 2\pi/\sqrt{2g\rho a^2/\sigma}$. This is due to the destabilising effect of the upward acceleration in addition to that of gravity; hence $2g$ rather than g as is the

case of steady rise. The meaning of the terms in equations (2.8.19) becomes slightly more transparent if we eliminate A to give

$$\frac{d^2B}{d\tau^2} + 4\tau \frac{dB}{d\tau} + B\left\{2 + 4\tau^2 - 2n\left(1 - \frac{n^2}{n_c^2}\right)\right\} = 0, \qquad (2.8.20)$$

where, as in Batchelor (1987), n_c is the critical wave number, in this case in non-dimensional form and equal to $\sqrt{2/k}$.

2.8.2 Solutions and discussion.

Equations (2.8.19) are solved numerically, using NAG routine D02BBF, and the results are given in figures 2.7(a)-(c). For initial conditions it is assumed that the bubble shape is perfectly circular, but that the initial velocity on the bubble is perturbed slightly from zero. Thus we take $B(0) = 0$ and $dB/d\tau(0) = \delta$, and hence $A(0) = -\delta/n_0$. As the equations are linear, δ is taken to be 0.01, in all cases. These initial conditions are similar to those used by Batchelor (1987) for a spherical cap bubble, rising steadily.

Figure 2.7(a) shows the effect of surface tension on the amplitude of the perturbation, B, on the bubble, as a function of time, for $n_0 = 6$ and $k = 0$, 0.076, 0.15, 0.23 and 0.30. This value of n_0 is the critical wavenumber if $k = 0.056$, so that only the smallest two values for k exhibit continued growth. The other curves, which are beginning to show oscillatory behaviour are higher values of the surface tension parameter, k, thus confirming the stabilising effect of surface tension. Note that as the physical validity of the results is confined to $\tau \ll 1$ the attenuation due to the vertical contraction of the fluid moving around the bubble is not apparent in these calculations, although (2.8.20) shows that the amplitude would eventually approach zero were they continued beyond $\tau = 1$. Figure 2.7(b) shows the effect of changing the initial wave number, for a value of $k = 74/(980 \times 2.54^2)$ corresponding to a one inch bubble in water (this value was chosen to allow a comparison with the Walters and Davidson (1962) and Baker and Moore (1989)). Here we take $n_0 = 5$, 15, 25 and 35. A higher initial wavenumber results in higher frequency waves, which, as the initial velocity is fixed at 0.01, therefore have lower peak amplitudes. Again growth is

only observed when n_0 is (approximately) less than n_c. The lowest wave number plotted does not reach a high enough amplitude for small times for us to say that such a case is unstable. This leads us to comment that the analysis as given is limited by the fact that it can only predict instability if it occurs very early on (i.e. for $\tau \ll 1$), and cannot really predict long-term stability at all. For this, further, more detailed calculations are required.

The analysis given becomes more interesting if we examine figure 2.7(c) where the results of different initial wave numbers for zero surface tension are given, with the same set of values of n_0. The fastest growing curves are those with highest wave numbers as the coefficient of the B term in (2.8.20) is now initially negative for $n_0 > 1$. For the largest wave number, provided that the results still hold close to $\tau = 1$, the amplitude of the surface perturbation may be sufficient to induce bubble break-up. This indicates that the results given in figure 2.3, where the Green's method is applied to a perturbed bubble are what would happen in reality with zero surface tension. However if we look back at figure 2.7(b) for a one inch bubble with a short wave length perturbation, and thus correspondingly high curvatures, surface tension induces large restoring forces to produce small amplitude oscillations. Thus on the basis of this analysis, bearing in mind the above caveat, one may expect such a bubble to be stable to small surface perturbations.

To conclude, we mention that for a one inch bubble, where according to Baker and Moore (1989) surface tension has little effect on the unperturbed motion, figures 2.7(b) and (c) show that this small amount of surface tension affects the perturbed motion tremendously. The initial growth of the amplitude is unchecked in the case of zero surface tension with the result that such bubbles are unstable.
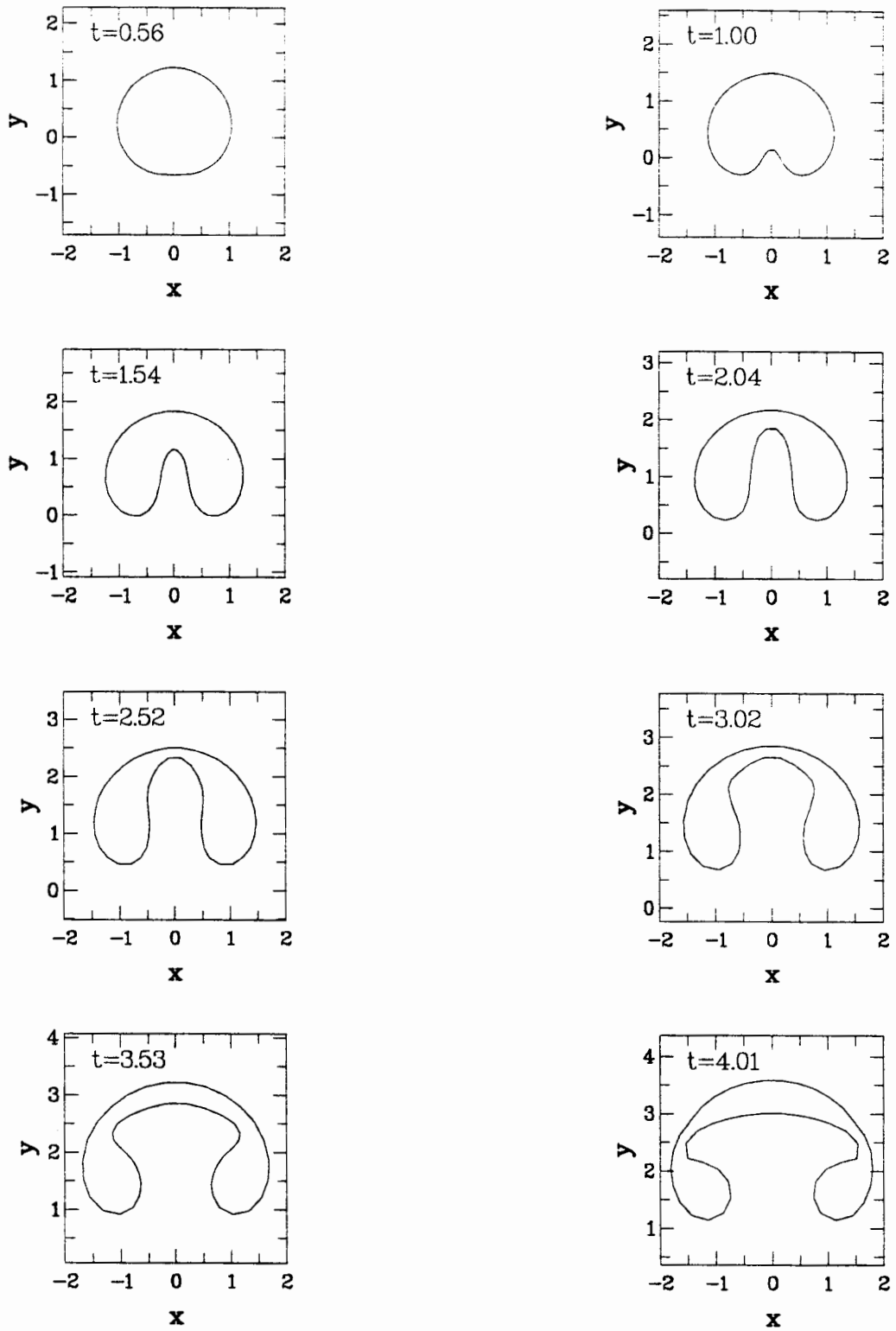
Figure 2.1. The time evolution of a two–dimensional bubble moving through an infinite fluid calculated using the vortex method, with N=50, $\Delta\phi$=0.1, k=2 and ε=10^{-4}. The dipole and Green's formula methods give results graphically identical to these. See Baker and Moore (1982) for comparison with a previous computational study.
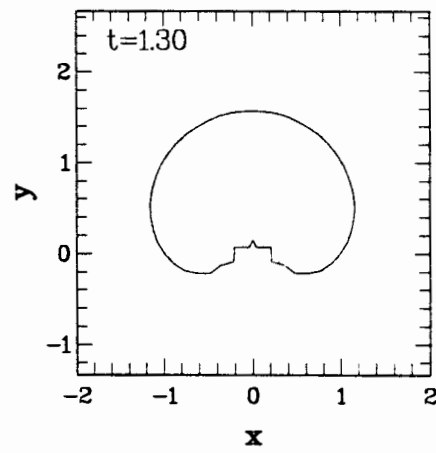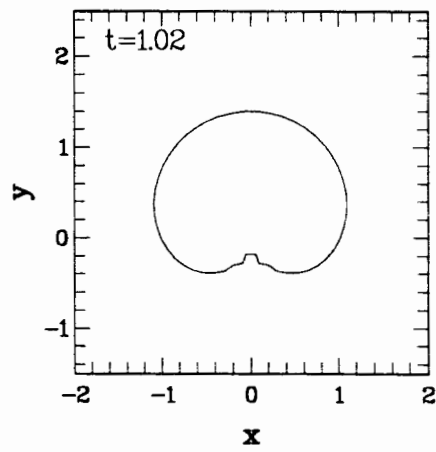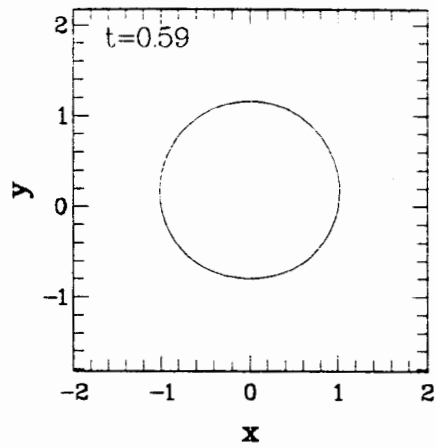
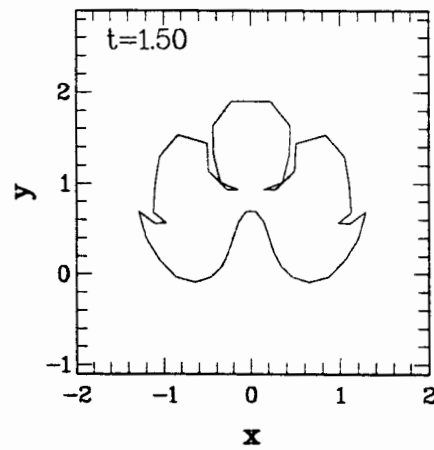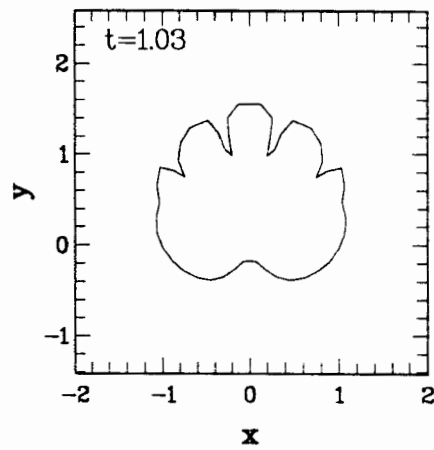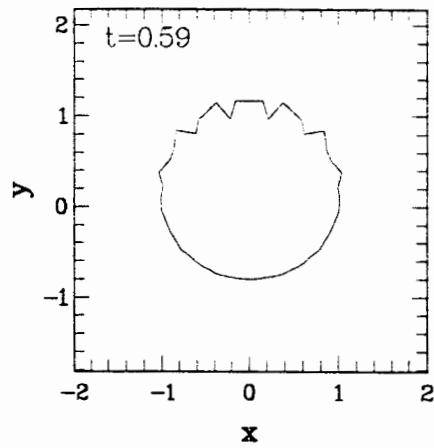Figure 2.2. As figure 2.1 but using the source distribution method. A numerical instability occurs as the jet begins to form and the method soon breaks down.

Figure 2.3. The Green's formula method applied to a two–dimensional bubble with an initial surface perturbation (e=0.01, f=18). An apparent Rayleigh–Taylor instability occurs splitting the bubble into a number of parts, as the method breaks down.
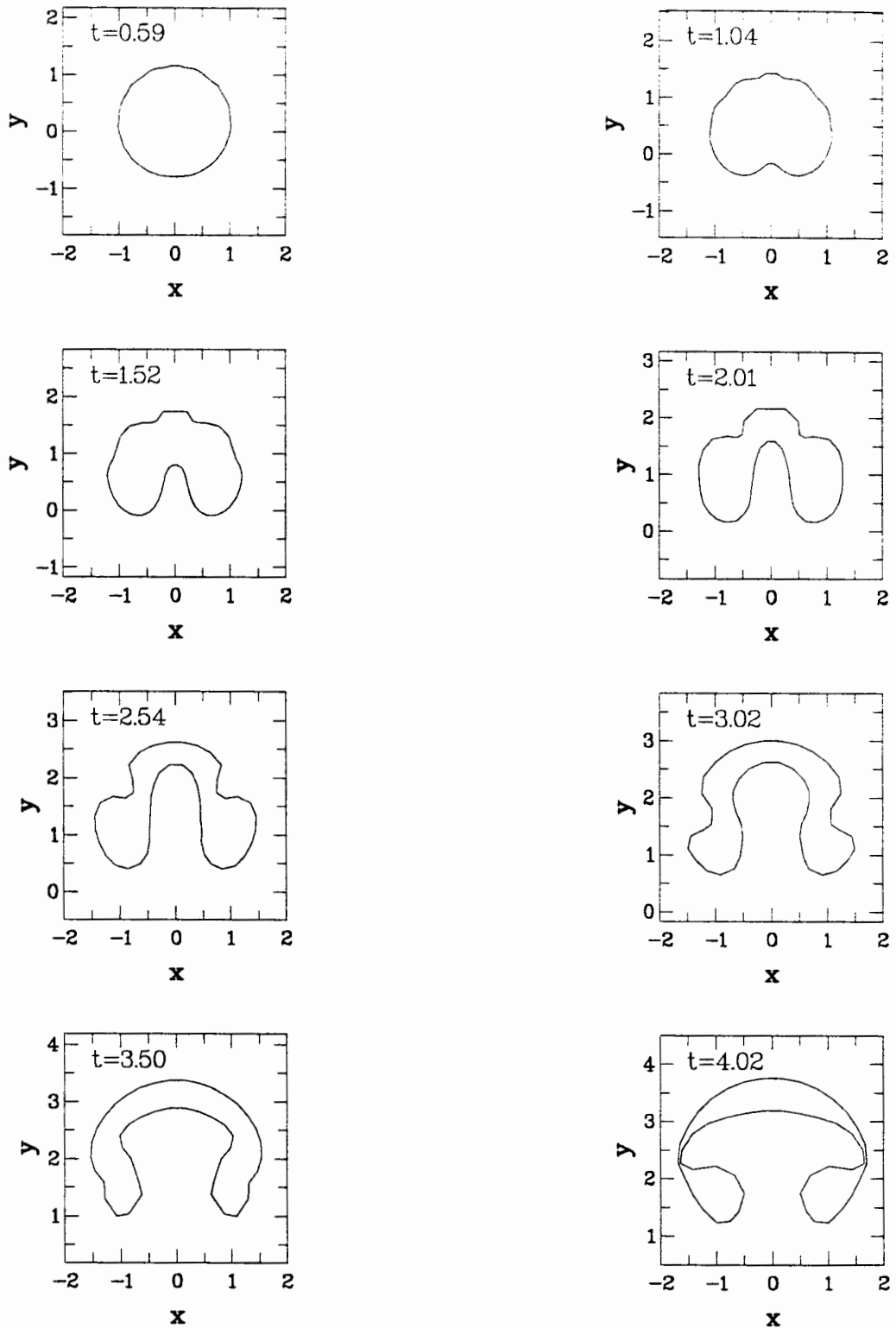
Figure 2.4. The motion of the perturbed bubble of figure 2.3, followed using the dipole method. The initial amplification of the disturbance is noticably less and a similar shape to that in figure 2.1 is eventually reached. Similar results are found for the vortex method.
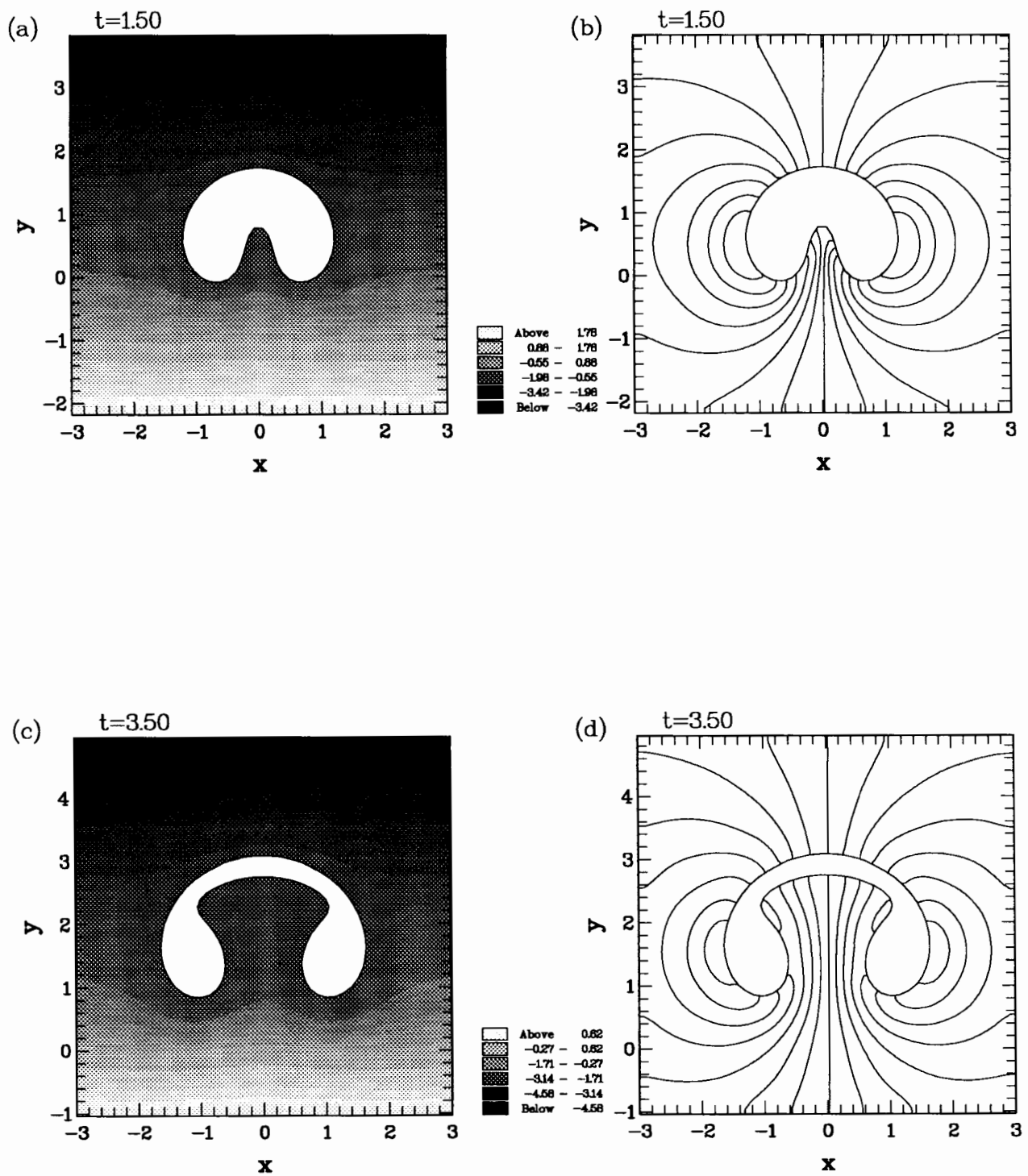
Figure 2.5. Pressure contours ((a) and (c)) and Streamlines ((b) and (d)) plotted for a two-dimensional gas bubble at different times during the rise, calculated using the Green's formula method.
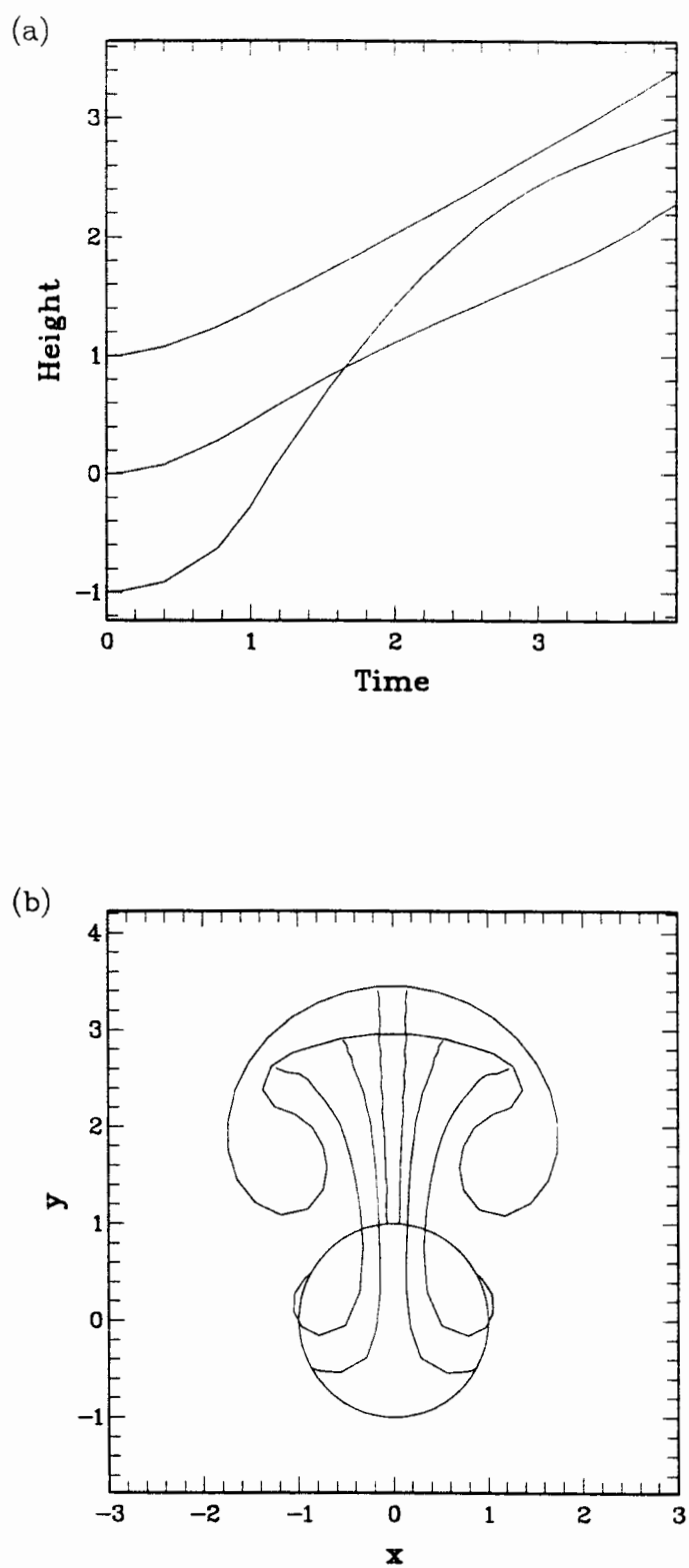
Figure 2.6. (a) Shows the evolution of the heights of the top, bottom and centroid of a two-dimensional bubble. (b) Shows the paths taken by some some particles in moving from the initial to the final configuration.

(a)

*10^{-2}

(b)

(c)
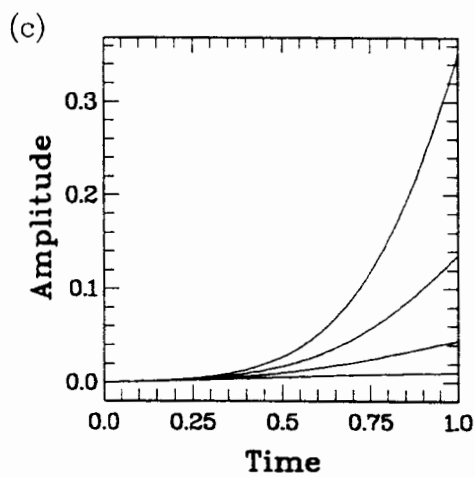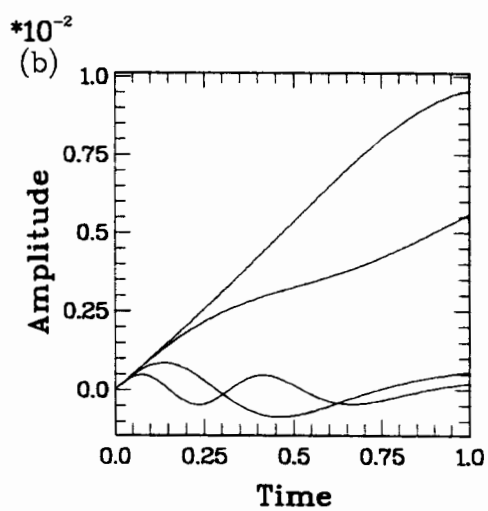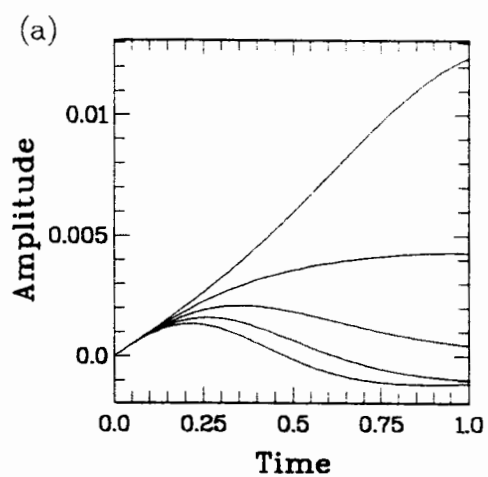
Figure 2.7. The amplitude of surface perturbation is plotted against time. (a) shows the effect of changing the surface tension parameter, k; (b) and (c) show the effect on the behaviour of altering the initial wave number, n_ϕ (b) is for a one inch bubble in water, and frame (c) is with zero surface tension. See text for details.

Chapter 3.

A TWO-DIMENSIONAL BUBBLE
NEAR A FREE-SURFACE.

3.1 Introduction.

This chapter considers the motion of a two-dimensional bubble below a free gas/liquid interface. Free-boundary problems of this nature may be dealt with using boundary integral techniques similar to those described in the previous chapter. The situation is, however, complicated slightly by the need to evaluate line integrals over the infinite free-surface.

There are many examples of numerical solutions to free-surface problems in the literature. An early use of the Green's formula boundary integral method was by Longuet-Higgins and Cokelet (1976). They made a significant advance in the problem of the computation of breaking waves by being able, for the first time, to calculate the motion well after the interface had become vertical. Later, Baker, Meiron and Orszag (1982) developed vortex and dipole distribution methods which they used to tackle the same problem. Using a vortex method similar to that of Baker et al (1982), Oguz and Prosperetti (1990b) were able to obtain some beautiful pictures of the jet formed after a drop had impacted on a free-surface.

Vortex methods can be employed to calculate the rolling up of a vortex sheet (Moore, 1973; Fink and Soh, 1978). These ideas can then be extended to study the response of a free-surface to a vortex sheet below it (Tryggvason, 1988).

There have also been a number of studies in the field of cavitation bubble dynamics. Blake and Gibson (1981) used a discrete ring-source distribution to approximately represent the cavitation bubble and adjacent free-surface and follow the bubble's growth and collapse. They were able to predict motions that compare well with the experimental

results given in their paper. More recently, Blake, Taib and Doherty (1987) used a full boundary integral technique to solve the same problem.

In order to solve for the motion of the bubble using a boundary integral method, it is necessary to discretise the integral equations into a set of algebraic equations. To do this, the relevant quantities such as position and potential have to be known at a finite number of points along the bounding surfaces of the solution domain. Thus it can be appreciated that, as mentioned above, difficulties arise when one wishes to integrate over the free-surface. If the bubble is situated in a finite container, it is possible to integrate over the container walls and finite free-surface, thus simplifying the task significantly. One way of overcoming the problem of an infinite free-surface was used for the axisymmetric case by Oguz and Prosperetti (1989) by integrating out for a finite radius and then matching on to a simple first-order expansion for the potential and surface elevation. If the velocities at the free-surface are small then a linearised boundary condition, namely that the potential vanishes there, may be used. This was one of the approaches taken by Blake and Gibson (1981), and was achieved by using the appropriate image of the free-space Green's function in the $z = 0$ plane. For problems with periodic boundary conditions on the free-surface, the integration can be simplified analytically by summing over all identical parts (Baker et al, 1982). Alternatively a conformal map may be used as in Longuet-Higgins and Cokelet (1976), to transform all periodic parts onto a closed contour.

The method described here is a conformal mapping technique that maps the bubble beneath the flat free-surface onto a bubble within the unit circle. The results obtained are compared with a first order perturbation expansion for the problem of a submerged dipole.

3.2 Numerical approach.

3.2.1 Problem formulation.

Unlike the study of the growth and collapse of cavitation bubbles where a bubble can just appear in the fluid near to the surface, in the case of bioreactors described in the introductory chapter, the bubbles rise a large distance from a sparger before reacting with the interface. Since the two-dimensional bubble considered in the previous chapter breaks up after a time of the order of $t = 4(a/g)^{1/2}$ seconds (where a is the initial radius of the bubble) and takes about $(a/g)^{1/2}$ seconds to rise one bubble radius (Baker and Moore, 1989), a bubble that starts much further away from the free-surface than about 4 bubble radii will split up before getting close. Bearing this in mind, some of the example results given at the end of the chapter for larger bubbles are somewhat unphysical. However for the purposes of studying the behaviour of bubbles in bioreactors where the bubble sizes are of the order of a millimeter, surface tension will act so as to keep the bubble shape roughly elliptical and will prevent jetting and breakup; thus the example for a bubble with a radius of one millimeter, is more realistic. It is for this reason that it was deemed necessary to include surface tension into the model in this chapter.

As for the bubble in an infinite fluid, we wish to solve for the velocity field as the gradient of a potential, ϕ. The kinematic condition is as before, namely that particles on the bubble and free-surface remain there throughout the motion. The dynamic condition is again from Bernoulli's theorem

$$p_\infty = p + \frac{1}{2}\rho|\boldsymbol{u}|^2 + \rho\frac{\partial\phi}{\partial t} + \rho gy, \qquad (3.2.1)$$

where p_∞ is the fluid pressure at infinity just below the gas/liquid interface. The surface tension introduces a discontinuity into the pressure field, dependent on the curvature of an interface. For the case considered here, a two-dimensional bubble may be thought of as being between two sheets of glass, thus at a point on the plane midway between the sheets there is curvature in two directions: κ tangential to the 2-D representation and $\kappa^\star$

normal to the glass. The latter value is assumed constant. Both curvatures are taken as positive if the corresponding surface is concave on the gas side. So the pressure just below the free-surface is given by

$$p = p_{atm} - \sigma(\kappa + \kappa^\star), \tag{3.2.2}$$

where σ is the surface tension coefficient of the gas/liquid interface, and p_{atm} is atmospheric pressure. Since $\kappa = 0$ at infinity, (3.2.2) evaluated at the free-surface gives

$$p_\infty = p_{atm} - \sigma\kappa^\star. \tag{3.2.3}$$

Using (3.2.2) and (3.2.3) in (3.2.1), the Bernoulli pressure condition at the free-surface can be written as

$$\frac{1}{2}\rho|\boldsymbol{u}|^2 + \rho\frac{\partial\phi}{\partial t} + \rho g y - \sigma\kappa = 0. \tag{3.2.4}$$

The pressure balance at the bubble surface is

$$p = p_b(t) - \sigma(\kappa + \kappa^\star), \tag{3.2.5}$$

where $p_b(t)$ is the pressure inside the bubble. Assume that the bubble is initially circular with radius a, at rest and at a distance h below the liquid surface. Evaluating (3.2.5) and (3.2.1) at $t = 0, y = -h$ (where use is made of the Walters and Davidson (1962) expression for the potential for small times, (2.8.10)) and eliminating p we find that the pressure inside the bubble is initially given by

$$p_b(0) = p_\infty + \rho g h + \sigma\left(\frac{1}{a} + \kappa^\star\right). \tag{3.2.6}$$

Substituting for p and p_∞ in (3.2.1) using (3.2.5) and (3.2.6) gives the pressure condition at the bubble surface,

$$\frac{1}{2}\rho|\boldsymbol{u}|^2 + \rho\frac{\partial\phi}{\partial t} + \rho g(y + h) + \sigma\left(\frac{1}{a} - \kappa\right) + p_b(t) - p_b(0) = 0. \tag{3.2.7}$$

It is convenient to scale lengths with respect to a, times with respect to $(a/g)^{1/2}$ and pressures with respect to $\rho g a$. On applying the substantial derivative to (3.2.4) and (3.2.7), we get for the free-surface,

$$\frac{D\phi}{Dt} = \frac{1}{2}|\boldsymbol{u}|^2 - y + \frac{4\kappa}{E_o}, \tag{3.2.8}$$

and for the bubble,

$$\frac{D\phi}{Dt} = \frac{1}{2}|\boldsymbol{u}|^2 - (y + \gamma_1) + \frac{4}{E_o}(\kappa - 1) + p_b(0) - p_b(t), \qquad (3.2.9)$$

where $\gamma_1 = h/a$ is the initial dimensionless distance beneath the surface and we introduce the Eötvos number, $E_o = 4\rho g a^2/\sigma$. Note that κ is now the non-dimensional curvature in the plane of the bubble. Writing the dynamic boundary condition in terms of the initial conditions, ensures that changes of the potential for each surface will be initially centred on zero, thus reducing round-off errors, especially for very small or deeply submerged bubbles.

The solution domain of the problem is the semi-infinite region of the complex z-plane below the free-surface, S, that is initially the real axis. The domain is bounded internally by the closed curve, B, representing the bubble. This region represents the area covered by the liquid and is denoted by Ω_-. Its complement in the complex plane is the gas of the atmosphere and bubble and is denoted Ω_+. For convenience, write $C = S \cup B$. Normals to C are taken into Ω_+.

3.2.2 Solution by boundary integral method.

The conformal mapping

$$\zeta = -\left(\frac{z + i\gamma_1}{z - i\gamma_1}\right), \qquad (3.2.10)$$

transforms the unbounded region, Ω_-, of the z-plane onto a finite region, $\tilde{\Omega}_-$, in the ζ-plane, bounded externally by the closed contour, $\tilde{S}$, initially the unit circle centred on the origin, $\tilde{O}$, and internally by the image of the bubble, $\tilde{B}$.

If $z = x + iy$ and $\zeta = \xi + i\eta$, then (3.2.10) gives the following expressions transforming co-ordinates:

$$y = \gamma_1 \frac{\xi^2 - 1 + \eta^2}{(\xi + 1)^2 + \eta^2}; \qquad x = \frac{-2\gamma_1 \eta}{(\xi + 1)^2 + \eta^2}$$

and

$$\xi = -\frac{y^2 - \gamma_1^2 + x^2}{(y - \gamma_1)^2 + x^2}; \qquad \eta = \frac{-2\gamma_1 x}{(y - \gamma_1)^2 + x^2}.$$

$$- 45 -$$

If we denote the complex potential in the ζ-plane by $\tilde{W}$, then we have the relationship $\tilde{W}(\zeta, t) = W(z(\zeta), t)$, and as the map is conformal in the solution domain, $\nabla^2\tilde{\phi} = 0$, where $\tilde{\phi} = \Re[\tilde{W}]$. Hence we may apply Green's formula to $\tilde{\phi}$.

In order to determine the value of the $p_b(0) - p_b(t)$ term of (3.2.9), we introduce the quantity, $k(t) = \int_0^t (p_b(t') - p_b(0))dt'$, and write the boundary values of the potential as

$$\tilde{f}(\zeta, t) = \tilde{\phi}(\zeta, t) + \begin{cases} k(t), & \zeta \in \tilde{B}, \\ 0, & \zeta \in \tilde{S}. \end{cases}$$

Once we insist that the bubble is to remain of constant volume, the problem becomes equivalent to a modified Dirichlet boundary value problem. This is one in which the potential on each disconnected surface is known only up to a constant which may depend on the particular surface; we are free to choose one of the constants to be zero (see for example Muskhelishvili, 1953). The constants are determined by the side condition that the potential is the real part of a complex function analytic in the solution domain. In a fluid dynamics context, this implies that the flow field has no circulation or expansion due to a multivalued potential or stream function respectively.

Evaluating Green's formula (2.2.6), where the integration is carried out over the surface $\tilde{C} = \tilde{S} \cup \tilde{B}$, for $\zeta^\star \in \tilde{\Omega}_-$, $\zeta \in \tilde{C}$ gives

$$\tilde{\phi}(\zeta^\star) = \int_{\tilde{C}} \left(G(\zeta^\star, \zeta')\frac{\partial\tilde{\phi}}{\partial n}(\zeta') - (\tilde{\phi}(\zeta') - \tilde{\phi}(\zeta))\frac{\partial G}{\partial n'}(\zeta^\star, \zeta') \right) ds' - \tilde{\phi}(\zeta)\int_{\tilde{C}}\frac{\partial G}{\partial n'}(\zeta^\star, \zeta')ds', \qquad (3.2.11)$$

where, as in the previous chapter, G is the free-space Green's function for Laplace's equation. The last integral of (3.2.11) is equal to the angle subtended at $\zeta^\star$, by $\tilde{S}$ divided by 2π, and is thus equal to -1.

In practice, we use the boundary values of the potential in terms of the function $\tilde{f}$, defined above, and work with $\tilde{f}$ entirely. Taking the limit of (3.2.11) as $\zeta^\star \to \zeta$ and writing in terms of $\tilde{f}$ gives

$$\int_{\tilde{C}} \left(G\frac{\partial\tilde{\phi}}{\partial n}(\zeta') - (\tilde{f}(\zeta') - \tilde{f}(\zeta))\frac{\partial G}{\partial n'} \right) ds' + \begin{cases} k, & \zeta \in \tilde{B}, \\ 0, & \zeta \in \tilde{S}, \end{cases} = 0. \qquad (3.2.12)$$

The side condition that the complex potential is analytic manifests itself, as suggested above, in the form of an integral requiring that the total flow out of the bubble vanishes

$$\int_{\tilde{B}} \frac{\partial \phi}{\partial n} ds = 0. \tag{3.2.13}$$

The dynamic conditions for $\tilde{f}$, from (3.2.8) and (3.2.9) are: for the free-surface

$$\frac{D\tilde{f}}{Dt} = \frac{1}{2}|\boldsymbol{u}|^2 - y + \frac{4\kappa}{E_o}, \tag{3.2.14}$$

and for the bubble

$$\frac{D\tilde{f}}{Dt} = \frac{1}{2}|\boldsymbol{u}|^2 - (y + \gamma_1) + \frac{4}{E_o}(\kappa - 1). \tag{3.2.15}$$

In order to update the position of a discrete set of Lagrangian points taken on $\tilde{C}$, the velocities are required in the ζ-plane. Consider the identity

$$\frac{D\zeta}{Dt} = \frac{d\zeta}{dz}\frac{Dz}{Dt}.$$

As the second factor on the right-hand side is just the Lagrangian velocity of points in the z-plane, which is simply the gradient of the potential, we have

$$\begin{aligned}
\frac{D\zeta}{Dt} &= \frac{d\zeta}{dz}\left(\frac{dW}{dz}\right)^* \\
&= \left|\frac{d\zeta}{dz}\right|^2 \left(\frac{d\tilde{W}}{d\zeta}\right)^*,
\end{aligned} \tag{3.2.16}$$

where an asterisk denotes a complex conjugate. Hence using (3.2.10) to evaluate the first factor of (3.2.16) and taking components, it is easily seen that the normal and tangential particle velocities in the ζ-plane are

$$\frac{1}{4\gamma_1^2}|\zeta + 1|^4 \frac{\partial \tilde{\phi}}{\partial n} \tag{3.2.17}$$

and

$$\frac{1}{4\gamma_1^2}|\zeta + 1|^4 \frac{\partial \tilde{\phi}}{\partial s} \tag{3.2.18}$$

respectively, where here $\partial/\partial n$ and $\partial/\partial s$ represent derivatives taken normally and tangentially in the ζ-plane. The normal, n, and tangent, τ, are oriented relative to each other in the sense $n = i\tau$.

– 47 –

In order to evaluate the Bernoulli pressure condition, it is necessary to determine the value of the $|\boldsymbol{u}|^2/2$ term. Here we make use of the fact that

$$\left|\frac{dW}{dz}\right|^2 = \left|\frac{d\zeta}{dz}\right|^2 \left|\frac{d\tilde{W}}{d\zeta}\right|^2,$$

and so from (3.2.10) above,

$$|\boldsymbol{u}|^2 = \frac{4\gamma_1^2}{|\zeta+1|^4} \left|\frac{D\zeta}{Dt}\right|^2. \tag{3.2.19}$$

Computationally, the method used here is essentially the same as that described in section 2.5. The surfaces in the ζ-plane are discretised using N_B and N_S nodes on the images of the bubble and free-surface respectively. The only major difference is that when updating positions of nodal points and values of potentials in the ζ-plane, (3.2.17), (3.2.18) and (3.2.19) are used to ensure that the correct kinematic and dynamic conditions are obeyed by the z-plane values. By fitting quadratics to three adjacent points on the surfaces in the z-plane, arc-length derivatives can be found which give in turn tangents and hence the curvatures for use in the dynamic conditions (3.2.14) and (3.2.15). This '5-point' method for finding curvatures gives reasonable results provided that there are not surface oscillations on the scale of the segment lengths, which may be avoided by using a sufficient number of nodes together with frequent application of the Longuet-Higgins and Cokelet (1976) smoothing formula.

Due to the conformal mapping, repositioning is done in a slightly different way to that in Chapter 2. Here, points on the free-surface are spaced out evenly with respect to the ζ-plane, whereas the repositioning of the bubble surface is done in the z-plane. This ensures that the resolution of the free-surface is not lost for the purposes of the calculations, but also has the effect that the output bubble shapes have points evenly spaced. Similar comments apply to the initial nodal spacings.

3.3 Perturbation expansion approximation.

Analytical solutions have been developed for many free-surface problems. One of the most well-known examples being the simple but successful solution of the linearised equations for small amplitude gravity waves. Many more complicated problems have been studied, for instance Havelock (1927) considered the problem of a circular cylinder submerged in a uniform stream and its effect on the surface elevation. He did this by first using a dipole and its image in the flat, surface, together with a distribution of dipoles behind this image. For the case of a horizontal dipole, he reflected this image system back in the cylinder to yield a second approximation, reinforcing the boundary condition at the cylinder itself.

Many free-stream problems in two-dimensional potential flow can be greatly simplified by considering an inverse problem formulation. That is, by writing the position in space as a function of a complex potential, $W = \phi + i\psi$, rather than the other way around. With this scheme, steady free-surfaces become the straight lines $\psi = const$. Problems such as the free-stream flow past a finite, flat plate or flow out of an orifice which would otherwise be very difficult, may be tackled in a straightforward manner by using appropriate conformal maps. For example the hodograph transformation, $w = \log(dz/dW)$, can be used to map steady, free-surfaces onto lines $\Re[w] = const$ and straight, rigid surfaces onto lines $\Im[w] = const$. Following this by a Schwartz-Cristoffel transformation to map the resulting straight-sided figure onto the upper half-plane, yields a problem that can be easily solved. By considering the steady Bernoulli equation, written in terms of inverse variables, evaluated at $\psi = 0$, Vanden Broeck, Schwartz and Tuck (1978), developed a power series, in the square of a Froude number, for position as a function of potential. In this way they were able to generate terms in the asymptotic expansions far more easily than with more direct methods. They considered some examples of free-surface flows one of which is the response of a gas/liquid interface to a submerged source or sink. The results obtained show a stagnation point above the source. However for somewhat larger Froude numbers,

such solutions do not exist. Tuck and Vanden Broeck (1984) and King and Bloor (1988) found solutions with a downward pointing cusps for larger Froude numbers. Forbes and Hocking (1990) considered the same problem and compared the results from a regular expansion in terms of the square of a Froude number with a steady, boundary integral solution.

In order to approximate the effect of a rising bubble on a free-surface, consider the problem of finding the surface elevation as a function of time due to a dipole moving far below the surface. We may expect this to give reasonable agreement with the numerical result since for a bubble of constant volume, the dipole term is dominant in the far field (see (2.2.13)).

With the same scalings as in section 3.2, assume that the dipole accelerates from rest from a point a distance $\gamma_1 = 1/\epsilon$ below the surface, for $\epsilon \ll 1$ and let $\gamma(t) > 0$ be the distance of the dipole below the x–axis as a function of time. Re-defining Ω_- to be the whole of the semi-infinite region below the surface, the problem can be formulated as follows. Laplace's equation must be satisfied by the potential everywhere except at the dipole, namely

$$\nabla^2 \phi = 0, \quad \text{in} \quad \Omega_- \setminus \{(0, -\gamma(t))\}, \tag{3.3.1}$$

with

$$\phi(\boldsymbol{r}) \sim -U(t) \frac{y + \gamma(t)}{x^2 + (y + \gamma(t))^2}, \quad \text{as} \quad \boldsymbol{r} \to (0, -\gamma(t)), \tag{3.3.2}$$

where $U(t) = -d\gamma/dt$ is the dipole's rise speed and $U(0) = 0$. Initially, the surface, given by the curve $y = \eta(x, t)$, is flat and the fluid occupying Ω_- is stationary.

The first boundary condition is the usual kinematic condition, this time in the Eulerian form

$$\frac{D\eta}{Dt} = \hat{\boldsymbol{j}} \cdot \nabla \phi \Big|_{y=\eta},$$

where $\hat{\boldsymbol{j}}$ is the unit vector in the y direction. This can be written more conveniently as

$$\frac{\partial \eta}{\partial t} + \frac{\partial \phi}{\partial x}\Big|_{y=\eta} \frac{\partial \eta}{\partial x} = \frac{\partial \phi}{\partial y}\Big|_{y=\eta}. \tag{3.3.3}$$

If we assume that the curvatures on the surface remain small, the pressures across this interface can be assumed to be continuous and the dynamic condition (3.2.4) gives, in dimensionless variables,

$$\left(\frac{1}{2}|\nabla\phi|^2 + \frac{\partial\phi}{\partial t}\right)\Big|_{y=\eta} + \eta = 0. \tag{3.3.4}$$

Since $\gamma = O(\epsilon^{-1})$, $(y+\gamma)/[x^2 + (y+\gamma)^2] = O(\epsilon)$, as $\epsilon \to 0$ for fixed x and y, and so we expect to be able to expand the potential and surface elevation in the form

$$\phi(x,y,t) = \epsilon\phi_1(x,y,t) + \epsilon^2\phi_2(x,y,t) + O(\epsilon^3), \tag{3.3.5}$$

$$\eta(x,t) = \epsilon\eta_1(x,t) + \epsilon^2\eta_2(x,t) + O(\epsilon^3), \tag{3.3.6}$$

with the first order potential given by the solution to

$$\nabla^2\phi_1 = 0, \quad \text{in} \quad \Omega_- \setminus \{(0,-\gamma(t))\}, \tag{3.3.7}$$

and

$$\phi_1(\boldsymbol{r}) \sim -\frac{U(t)}{\epsilon}\frac{y+\gamma(t)}{x^2 + (y+\gamma(t))^2}, \quad \text{as} \quad \boldsymbol{r} \to (0,-\gamma(t)), \tag{3.3.8}$$

and higher orders satisfying

$$\nabla^2\phi_i = 0, \quad \text{in} \quad \Omega_-, \quad i \geq 2. \tag{3.3.9}$$

Since this is a free-boundary perturbation problem, Taylor expand each of the terms in (3.3.5) about $y = 0$, and substitute for η as defined in (3.3.6). This gives

$$\phi(x,\eta,t) = \epsilon\phi_1\Big|_{y=0} + \epsilon^2\left(\eta_1\frac{\partial\phi_1}{\partial y} + \phi_2\right)\Big|_{y=0} + O(\epsilon^3). \tag{3.3.10}$$

By differentiating (3.3.5) it is clear that we can write down similar expressions for $\partial\phi/\partial t$, $\partial\phi/\partial x$ and $\partial\phi/\partial y$ at the surface. Substituting (3.3.6) and (3.3.10) into the kinematic and dynamic conditions (3.3.3) and (3.3.4), produces the first order, linearised boundary conditions

$$\frac{\partial\phi_1}{\partial t}\Big|_{y=0} + \eta_1 = 0, \tag{3.3.11}$$

and

$$\frac{\partial\eta_1}{\partial t} = \frac{\partial\phi_1}{\partial y}\Big|_{y=0}. \tag{3.3.12}$$

The second order boundary conditions are given by

$$\left\{ \left(\frac{\partial\phi_1}{\partial x}\right)^2 + \left(\frac{\partial\phi_1}{\partial y}\right)^2 + 2\left(\eta_1\frac{\partial^2\phi_1}{\partial y\partial t} + \frac{\partial\phi_2}{\partial t}\right)\right\}\Bigg|_{y=0} + 2\eta_2 = 0,$$

and

$$\frac{\partial\eta_2}{\partial t} + \frac{\partial\phi_1}{\partial x}\bigg|_{y=0}\frac{\partial\eta_1}{\partial x} = \eta_1\frac{\partial^2\phi_1}{\partial y^2}\bigg|_{y=0} + \frac{\partial\phi_2}{\partial y}\bigg|_{y=0},$$

but here, we restrict ourselves to solving only the first order problem.

Combining equations (3.3.11) and (3.3.12) gives a condition for the first order potential

$$\left(\frac{\partial^2\phi_1}{\partial t^2} + \frac{\partial\phi_1}{\partial y}\right)\bigg|_{y=0} = 0. \tag{3.3.13}$$

To solve the first order problem posed by equations (3.3.7), (3.3.8) and (3.3.13), apply a technique analogous to that used by Havelock (1927) for a similar problem by writing ϕ_1 as the sum of a singular part,

$$\phi_S(x,y,t) = -\frac{U(t)}{\epsilon}\left(\frac{y+\gamma(t)}{x^2 + (y+\gamma(t))^2} + \frac{y-\gamma(t)}{x^2 + (y-\gamma(t))^2}\right), \tag{3.3.14}$$

and an unknown harmonic part, ϕ_H. The same approach can be employed to find the response of a free-surface to the fundamental singularity of the Laplace equation and hence determine the Green's function; see for example Wehausen and Laitone (1960), where many surface wave problems are examined in detail. Note that the second term in (3.3.14) makes the analysis slightly simpler by anticipating the form of the final solution: in fact, from (3.3.11), ϕ_S does not contribute to the surface elevation since $\phi_S\big|_{y=0} = 0$.

We now take the Fourier transform with respect to x, $\mathcal{F}_x$, and the Laplace transform with respect to t, $\mathcal{L}_t$, of the singular potential, ϕ_S, given by (3.3.14). By consulting tables of transforms or using a simple application of the calculus of residues for an appropriate complex contour, it can be seen that for $|y| < \gamma$

$$\hat{\phi}_S(q,y,t) \equiv \mathcal{F}_x[\phi_S] = -\sqrt{\frac{\pi}{2}}\frac{U(t)}{\epsilon}\left(\exp\left(-|q|(y+\gamma(t))\right) - \exp\left(-|q|(\gamma(t)-y)\right)\right). \tag{3.3.15}$$

Thus

$$\frac{\partial\hat{\phi}_S}{\partial y}\bigg|_{y=0} = \sqrt{2\pi}\frac{U(t)}{\epsilon}|q|e^{-|q|\gamma(t)}. \tag{3.3.16}$$

$$- 52 -$$

If $\bar{\phi}_S(q, y, s) \equiv \mathcal{L}_t[\hat{\phi}_S]$ and we define $\bar{h}(q, s) = \mathcal{L}_t[U(t)e^{-|q|\gamma(t)}]$, then we have

$$\frac{\partial \bar{\phi}_S}{\partial y}\bigg|_{y=0} = \frac{\sqrt{2\pi}}{\epsilon}|q|\bar{h}(q, s). \qquad (3.3.17)$$

Similarly, transforming Laplace's equation, satisfied by ϕ_H throughout Ω_-, gives

$$\frac{\partial^2 \bar{\phi}_H}{\partial y^2} - q^2 \bar{\phi}_H = 0, \qquad (3.3.18)$$

from which we may deduce that

$$\bar{\phi}_H = \bar{A}(q, s)e^{|q|y}, \qquad (3.3.19)$$

so that $\bar{\phi}_H \to 0$ as $y \to -\infty$, for all $q \neq 0$. Transform the boundary conditions (3.3.13) to give

$$\left(s^2 \bar{\phi}_1 + \frac{\partial \bar{\phi}_1}{\partial y} \right)\bigg|_{y=0} = 0. \qquad (3.3.20)$$

In calculating the time transform we have assumed that, since the fluid starts at rest, the potential is initially zero and, on using (3.3.11), we have taken $\partial \phi_1/\partial t(x, 0, 0) = 0$ since the surface is initially flat.

Substituting $\bar{\phi}_1 = \bar{\phi}_S + \bar{\phi}_H$ into (3.3.20) and using (3.3.17) and (3.3.19) immediately gives us

$$\bar{A}(q, s) = -\frac{\sqrt{2\pi}}{\epsilon}\frac{|q|}{s^2 + |q|}\bar{h}(q, s). \qquad (3.3.21)$$

We may now use the convolution theorem for Laplace transforms which, together with the definition of the function $\bar{h}$, allows us to invert the time transform for the harmonic potential given by (3.3.19), to yield

$$\hat{\phi}_H(q, y, t) = -\frac{\sqrt{2|q|\pi}}{\epsilon}e^{|q|y}\int_0^t U(t')e^{-|q|\gamma(t')}\sin(\sqrt{|q|}(t - t'))dt'. \qquad (3.3.22)$$

Proceeding with a direct inversion of the Fourier transform gives

$$\phi_H(x, y, t) = -\int_{-\infty}^{\infty} e^{iqx}\frac{\sqrt{|q|}}{\epsilon}e^{|q|y}\left(\int_0^t U(t')e^{-|q|\gamma(t')}\sin(\sqrt{|q|}(t - t'))dt' \right)dq. \qquad (3.3.23)$$

In order to simplify the appearance of (3.3.23) slightly, we separate the intervals $(-\infty, 0)$ and $[0, \infty)$ of the q integral and interchange the order of integration to give, finally,

$$\phi_H(x, y, t) = -2\int_0^t \frac{U(t')}{\epsilon}\left(\int_0^{\infty} \sqrt{q}\exp(-q(\gamma(t') - y))\sin(\sqrt{q}(t - t'))\cos(qx)dq \right)dt'. \qquad (3.3.24)$$

With the potential written in this form, we can easily use (3.3.11) to get an expression for the first order surface elevation, namely

$$\eta(x,t) = 2 \int_0^t U(t') \left(\int_0^\infty q e^{-q\gamma(t')} \cos(\sqrt{q}(t-t')) \cos(qx) dq \right) dt' + O(\epsilon^2). \qquad (3.3.25)$$

Once the dipole speed $U(t)$ and hence depth $\gamma(t)$ are known, the integrals in (3.3.25) can be calculated accurately numerically and the assumption that the bubble rises with unit acceleration so that $U = t$ and $\gamma = \gamma_1 - t^2/2$, will give good results for small times. However a small bubble flattens as it rises (see section 3.4 below) and so its added mass increases and its acceleration decreases leading to inaccuracies in the surface elevation. Bearing this in mind, it is instructive to consider the expansion of the inner integral of (3.3.25) for large γ. Since, in this case, the integral will be dominated by the contribution from a small region around $q = 0$, substitute $q' = \gamma(t')q$ and expand the cosine term on the assumption that $t \ll \gamma^{1/2}$. Retaining only the first term, and using the fact that $U(t')dt' = -d\gamma$, we find that the surface elevation is

$$\eta(x,t) = 2 \left[\frac{\gamma'}{x^2 + \gamma'^2} \right]_{\gamma'=1/\epsilon}^{\gamma(t)} + O(\epsilon^2). \qquad (3.3.26)$$

We thus can use (3.3.26) to approximate the surface elevation without knowing the history of the dipole's motion, simply by using the initial and current bubble centroid positions. Equation (3.3.26) is also the result of substituting ϕ_S, given by (3.3.14) into (3.3.12).

3.4 Results and discussion.

The boundary integral code described in section 3.2 was used to solve the problem for various different Eötvos numbers and initial distances from the free-surface. The first two figures show results for a bubble with $E_o = 53$, equivalent to a $1cm$ bubble in water. Figure 3.1 is a bubble that starts at rest with $\gamma_1 = 2$ bubble radii from the surface, whereas figure 3.2 is with $\gamma_1 = 10$. The latter figure is a test case where it is clear that for large distances from the interface, the bubble moves as if it were in an infinite fluid. This also shows the effect of surface tension for this bubble is very small (compare with figure 2.1). The effect

of the free-surface for $\gamma_1 = 2$ is not very strong, but the jet broadens out earlier since the flow around the bubble is slightly slower. This is due to gravity acting on the free-surface thus preventing, to a certain extent, flow from above the bubble which is unhindered in the infinite fluid case. Figure 3.3 shows a time sequence for a bubble with $E_o = 0.53$, $\gamma_1 = 10$. Here the surface tension effect is much larger and acts so as to keep the bubble almost elliptical, without any jet formation. This figure is more relevant to the long-term studies of bubbles in bioreactors.

Pressures are calculated in the same manner as in Chapter 2. The potentials for a grid of points in the z-plane are calculated for each equivalent ζ-plane position using

$$\tilde{\phi}(\zeta) = \int_{\tilde{C}} \left(G \frac{\partial \tilde{\phi}}{\partial n}(\zeta') - \tilde{f}(\zeta') \frac{\partial G}{\partial n'} \right) ds'. \tag{3.4.1}$$

In order to improve resolution around the bubble and free-surface, the pressure at these surfaces is calculated explicitly using

$$p(\zeta, t) = p_\infty + \begin{cases} dk/dt - 4(\kappa - 1)/E_o + \gamma_1, & \zeta \in \tilde{B}, \\ -4\kappa/E_o, & \zeta \in \tilde{S}. \end{cases} \tag{3.4.2}$$

Streamlines are calculated by using the stream function, given by

$$\tilde{\psi}(\zeta) = \int_{\tilde{C}} \left(-\theta(\zeta' - \zeta) \frac{\partial \tilde{\phi}}{\partial n}(\zeta') + \tilde{f}(\zeta') \frac{\partial G}{\partial s'}(\zeta, \zeta') \right) ds', \tag{3.4.3}$$

where $2\pi\theta(\zeta' - \zeta)$ is the angle between $\zeta' - \zeta$ and the ξ-axis.

Figure 3.4 shows pressure and streamline plots corresponding to the bubble in figure 3.3 at time $t = 5.5$. The lower pressures around the sides of the bubble, as a result of faster flow than at the top, can be seen. To reach an equilibrium, the bubble has moved into an elliptical shape so that the curvatures at the sides allow for the correct jump between the fluid pressure and the uniform bubble pressure. It is also clear from the pressure plot that there is a higher pressure region directly above the bubble. This acts to push the free-surface up as the bubble approaches. The streamlines indicate that the free-surface is moving up above the bubble and down and outwards to the left and right of the bubble.

In order to investigate the convergence of the solution of the discretised form of the integral equation (3.2.12) as the number of nodal points increases, we consider an example problem where the exact solution is known. This problem is

$$\nabla^2 \phi = 0, \quad \text{in} \quad \Omega_-, \tag{3.4.4}$$

with Dirichlet boundary conditions,

$$\phi = 0, \quad \text{on} \quad S,$$

$$\phi = -\left\{ y + \gamma + \frac{y - \gamma}{1 - 4y\gamma} \right\}, \quad \text{on} \quad B. \tag{3.4.5}$$

As before, S is the free-surface, taken here to be the x-axis, and B is the bubble, taken to be the unit circle centred at $(0, -\gamma)$. The exact solution is given by

$$\phi(x, y) = -\left\{ \frac{y + \gamma}{x^2 + (y + \gamma)^2} + \frac{y - \gamma}{x^2 + (y - \gamma)^2} \right\}, \tag{3.4.6}$$

which is clearly just a dipole, representing the bubble's translation, together with its image in S. On the basis of the analysis in Section 3.3, equation (3.3.14) in particular, we would expect this to be typical of the type of boundary value problem solved by the numerical code when calculating the bubble motion, and hence it should give us a practical estimate for the rate-of-convergence.

To measure convergence, the normal derivative estimated on the transformed free-surface by the boundary integral method with $N_S = N_B = N$ nodes, denoted $\tilde{\psi}_N$, is compared with that from the exact solution. The exact normal derivative in the z-plane is, from (3.4.6),

$$\psi \Big|_S \equiv \frac{\partial \phi}{\partial n} \Big|_S = \frac{4\gamma^2}{(x^2 + \gamma^2)^2} - \frac{2}{x^2 + \gamma^2}, \tag{3.4.7}$$

and is related to that in the ζ-plane, $\tilde{\psi}$, by the expression

$$\tilde{\psi} = \left| \frac{dz}{d\zeta} \right| \psi. \tag{3.4.8}$$

We define the error, E_N, by

$$E_N = \max_{i=1,\dots,N} \{ \tilde{\psi}_N(x_i) - \tilde{\psi}(x_i) \}. \tag{3.4.9}$$

Inspection of figure 3.5 shows that the error falls off as N^{-2}, as is the case for a corresponding second-kind integral equation using a piecewise linear collocation method (see for example Atkinson et al, 1983). It was found in Chapter 2 that the 1-norm condition numbers for the discretised first-kind formulation, such as the Green's formula method used here, are significantly larger than for second-kind vortex or dipole distribution methods. Thus small errors introduced at each time-step may be amplified faster using this method. A source of such errors is the integration of (3.2.14) and (3.2.15), particularly because of the difficulty involved in accurately differentiating the surface shape twice to find the curvatures. Indeed, it is the inclusion of surface tension that necessitates the use of smoothing.

Problems can occur when solving integral equations with weakly singular kernels if elements become very close to nodes on other parts of the surface. If this happens on parts of the surfaces where the distances between adjacent nodes are relatively large, so that few quadrature points are used, the integrals along the elements closest to the observation node will not be calculated accurately. In the context of problems considered here, this typically occurs in the cases when a small, circular bubble gets very close to the free-surface or when a large bubble has developed a jet which is about to pinch off smaller bubbles. We find that the problem tends to manifest itself by causing excessively large values for the normal derivatives as solutions to the integral equation. The time-step is chosen in the manner described in Chapter 2, so that the maximum change in potential is restricted for each step. From the dynamic conditions (3.2.14) and (3.2.15), we see that large velocities result in correspondingly large rates-of-change of potential, and thus a small time-step, eventually causing the calculation to grind to a halt. It is, however, important to note that for this particular application, these problems occur in situations where one may expect viscous effects to be important, namely in the drainage of thin films. Thus the method will give good results to physical problems provided that small enough elements are used to ensure accuracy up to the point where the underlying

assumptions of the model cease to be valid.

Figure 3.6 shows the results of the asymptotic expansion described in section 3.3, for the case $\gamma_1 = 10$. The solid lines represent the surface elevations according to the analytic solution (3.3.26) and the broken lines the solution from the boundary integral method. As expected, the curves compare best for small times when the bubble is further from the free-surface and when the surface elevation and velocity are small. As the bubble moves closer, the comparison is less satisfactory. There are several reasons for inaccuracy at later times. One factor is the fact that in the above analysis we assume that the bubble is represented by a dipole, and make no other attempt to ensure that the kinematic boundary conditions at the bubble are satisfied. Thus as it deforms from circular or becomes much closer to the free-surface the simple dipole model starts to break down. To get a better approximation, one could use the method of images to reinforce the boundary condition at the bubble on the assumption that it is a rigid cylinder (Havelock, 1927). One may also consider taking more terms in the asymptotic expansion. This should improve the comparison, however it should be emphasised that this would only yield a better approximation to the solution of the problem of a *dipole's* effect on a free-surface and so could not predict accurately the situation when the bubble becomes much closer to the surface, for the reason pointed out above.

Figure 3.7 shows an example of the possible motion when a $1mm$ two-dimensional gas bubble bursts at a free-surface. Unlike the corresponding calculation of Chapter 5, where a high speed jet is seen to form, only a small bump can be observed here. Much of the energy from the burst seems to propagate outwards in the form of surface waves. Part of the reason for the lack of jet is that, in two-dimensions, there is no component of the surface tension force that in the axisymmetric case acts radially to thin and lengthen a straight jet. For the same reason, the cavity formed by the bubble collapses in a completely different way to the three-dimensional case where it is rapidly pulled inwards near to the base by surface tension.
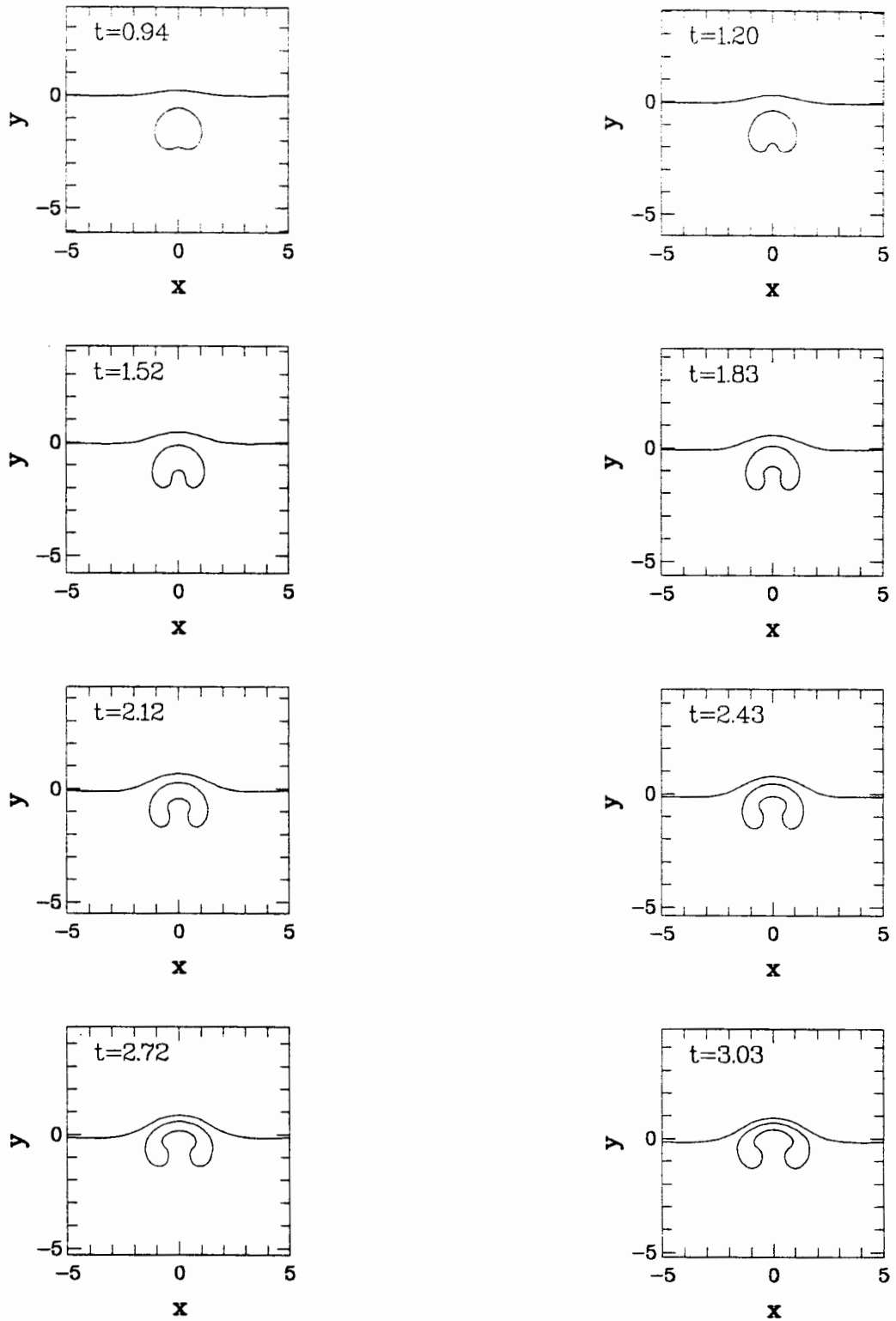
Figure 3.1. Here the motion of a two–dimensional bubble rising near a free surface is shown. ($N_B=N_S=50$, $\gamma_1=2$). In this case $E_o=53$ corresponding to a 1cm bubble in water. The results are similar to those of figure 2.1 for a bubble in an infinite fluid.
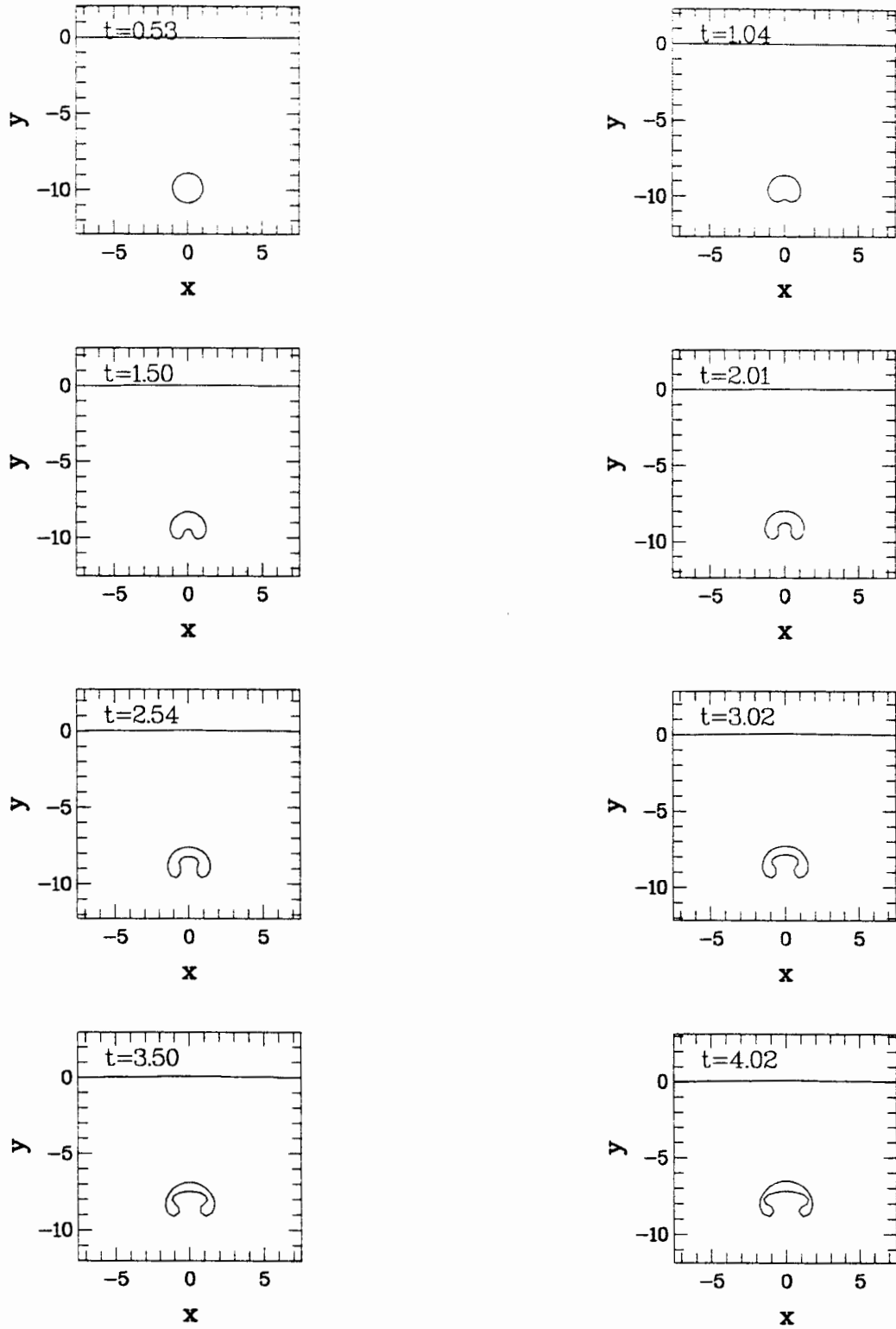
Figure 3.2. As figure 3.1, but with $\gamma_1=10$, $N_2=N_3=30$. This case shows that the numerical method produces the same results as in the infinite fluid case when the bubble is far removed from the free surface.
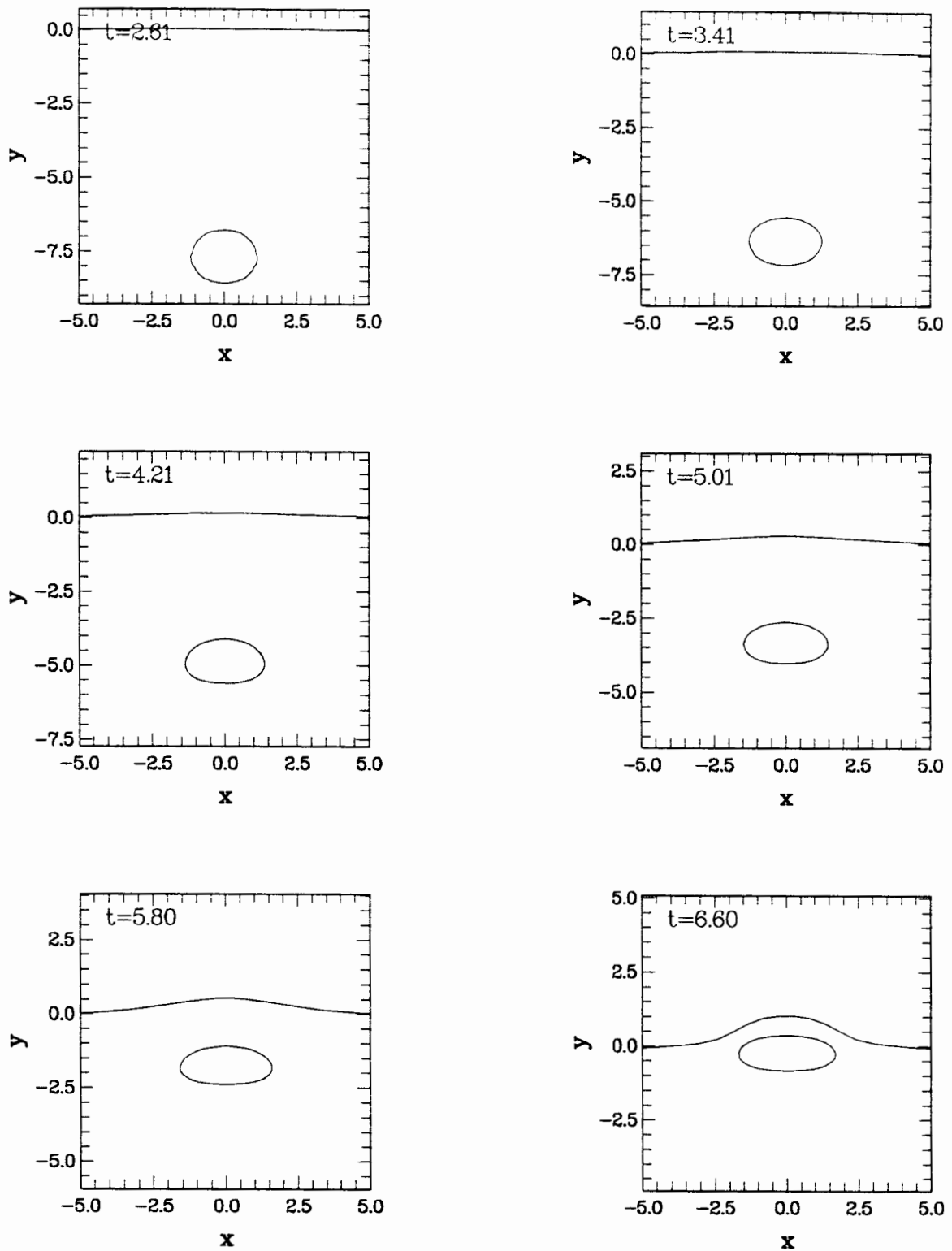
Figure 3.3. The motion for a smaller 1mm bubble, $E_o=0.53$ with $\gamma_1=10$. This is a more realistic example of the motion of a bubble towards a free surface. Near the end of the calculation, the bubble has become quite flattened due to the lower pressure at the sides of the where the fluid is moving faster.
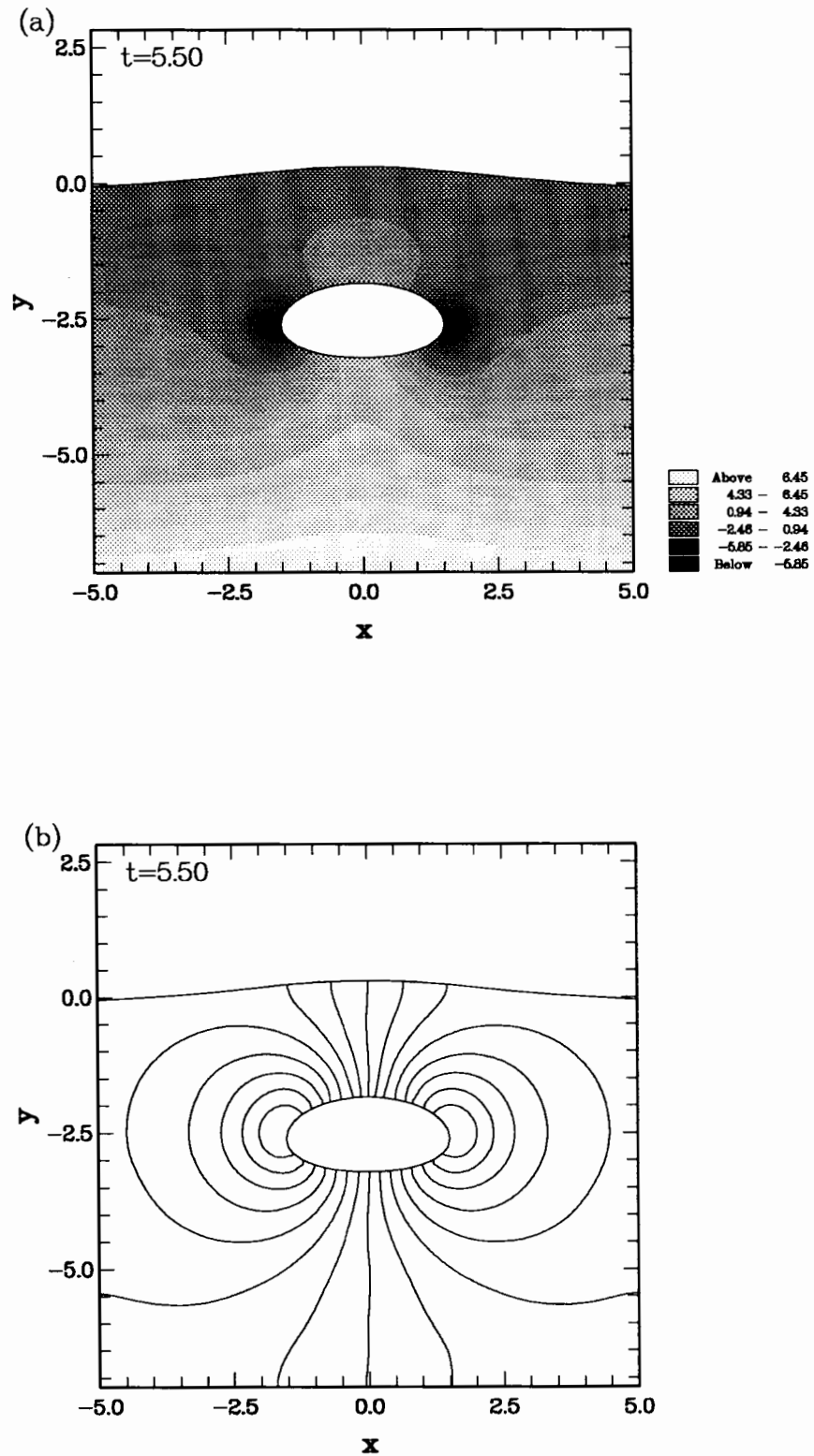
Figure 3.4. (a) Pressure contours and (b) Streamlines are plotted for the two–dimensional bubble and free surface of figure 3.3 at time t=5.5. The pressures around the sides of the the bubble are clearly lower than at the top and bottom and so it has become almost elliptical. Notice the high pressure above the bubble that pushes the free surface up.
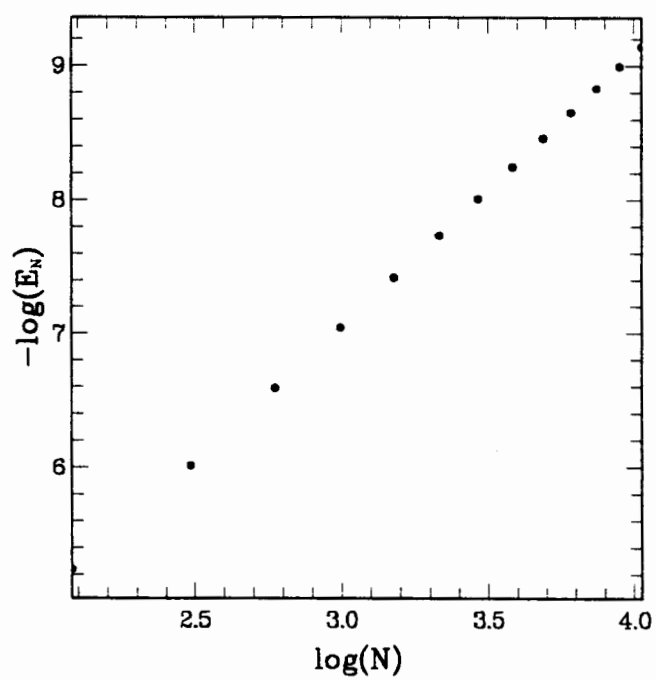
Figure. 3.5. The error in the normal derivative for a single inversion of the boundary integral equation, related to the number of nodes on each surface.
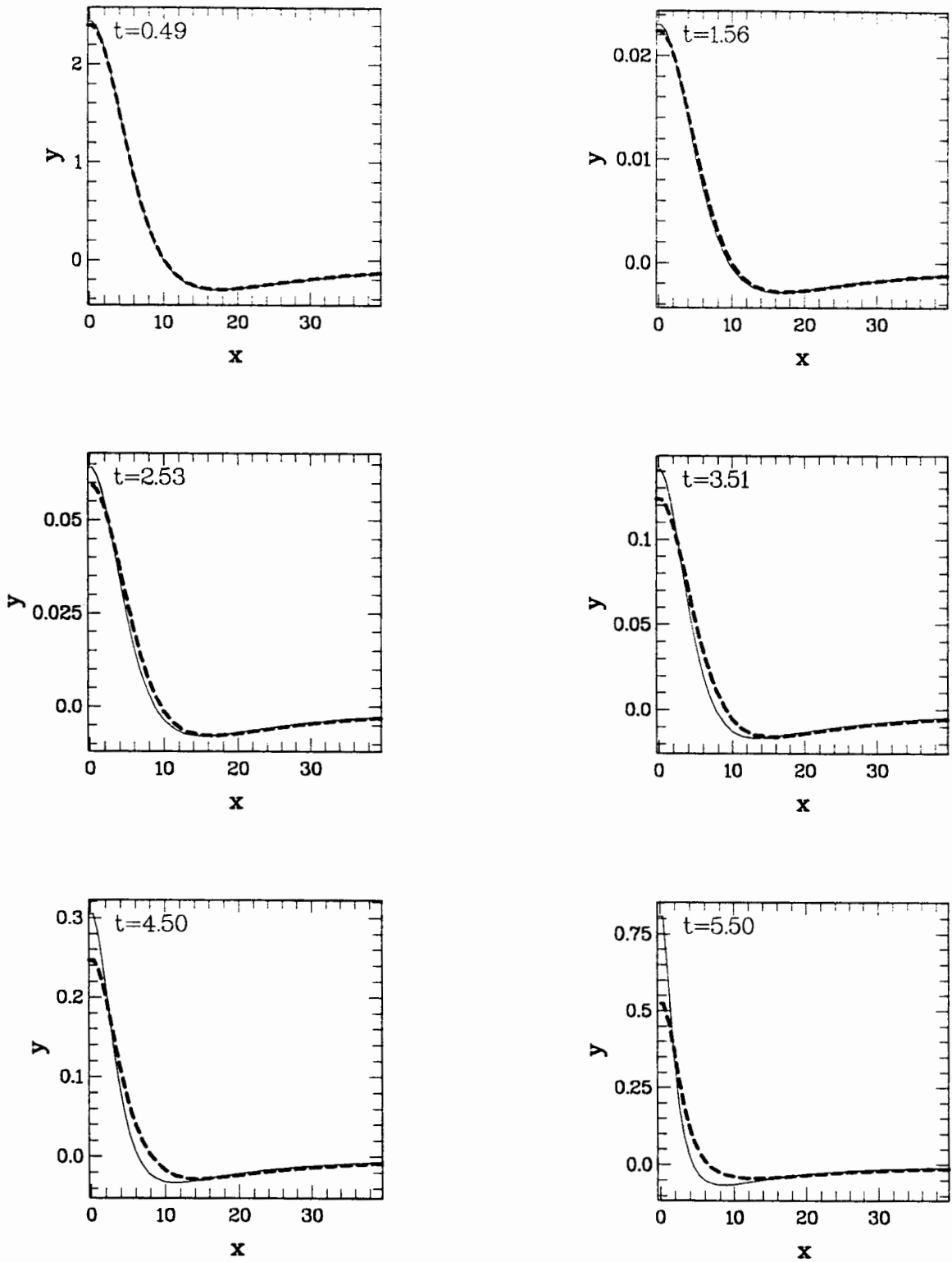
Figure 3.6. Surface elevations for the numerical method of section 3.2 (- - -) compared with those given by the first term of the asymptotic expansion of section 3.3 (———) for the effect of a submerged dipole on a free surface. The case $\gamma_1=10$ is shown here.
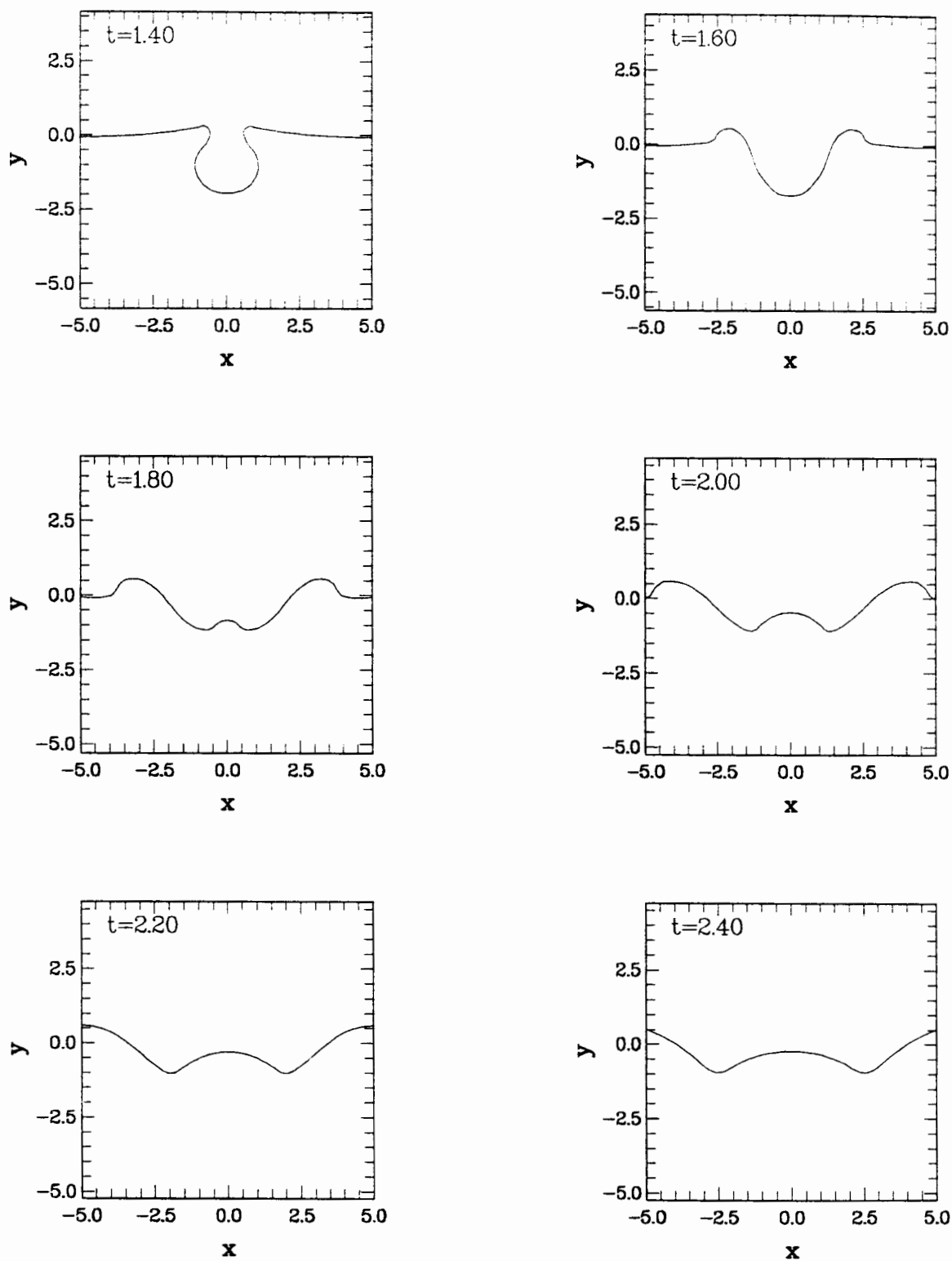
Figure 3.7. The figure shows the motion of a free surface subsequent to the bursting of a 1mm radius two–dimensional bubble in water. Compare this with the calculations of Chapter 5, where the axisymmetric converging flow causes a liquid jet to form.

Chapter 4.

RISING AXISYMMETRIC GAS BUBBLES.

4.1 Introduction.

The rise of air bubbles in water is one of the most common examples of two-phase flow experienced in everyday life. It is not surprising, therefore that a significant effort has been focused on trying to understand some of the associated phenomena. From a mathematical point of view, the complexity of the problem is due to the fact that the bubble shape is itself an unknown. Even for the steady state problem of a bubble rising at its terminal velocity it is difficult to get accurate solutions to the general case except by using sophisticated numerical techniques. There are, however, several known results and approximations for certain special cases. These and other topics are covered in detail in, for instance, Clift, Grace and Weber (1978). As an introduction, we give some of the more fundamental models here, before going on to consider the numerical techniques used in this chapter.

4.1.1 Analytical results.

For very small bubbles, with Reynolds number, $Re = 2Ua/\nu$ (U being the rise speed, a the bubble radius and ν the kinematic viscosity), much smaller than unity, viscous forces will dominate inertial forces and we can get a good picture of the flow field by assuming that it can be represented by the Stokes flow equations. In the case when inertia is completely neglected, the gas bubble (or liquid drop) takes on a spherical shape (see for example Taylor and Acrivos, 1964).

We may easily solve for the flow field around a spherical bubble. As the density and dynamic viscosity of the gas are substantially less than those of surrounding liquid, we may ignore the internal dynamics of the bubble itself. For boundary conditions, assume that

there is no flow across the bubble surface, that normal stresses are continuous, apart from a contribution due to surface tension, and that tangential stresses vanish. Were we dealing with a drop, we would have to take into consideration the effect of its internal circulation, driven by a non-zero tangential stress at the interface. In fact, it is straightforward to generalise the Stokes flow solution to a drop of arbitrary density and viscosity for which the rigid sphere and bubble are the extreme cases.

To solve the problem, introduce a Stokes' stream function, ψ, and consider the equation $D^4\psi = 0$ where

$$D^2 = \frac{\partial^2}{\partial r^2} + \frac{\sin\theta}{r^2}\frac{\partial}{\partial\theta}\left(\frac{1}{\sin\theta}\frac{\partial}{\partial\theta}\right), \tag{4.1.1}$$

subject to the conditions above and the far-field condition $\psi \sim -(Ur^2/2)\sin^2\theta$ as $r \to \infty$. The solution obtained, it should be noted, is not valid in the far field, where it can be shown that if $r = O(aRe^{-1})$, the neglected inertia terms in the equations of motion contribute to the same order as the retained viscous terms.

The drag, D, on the bubble can be determined directly by integrating the stress over the bubble surface, namely

$$D = k_i \int_C \sigma_{ij} n_j dS, \tag{4.1.2}$$

where σ_{ij} is the stress tensor, n_j is the inward normal to C, the bubble surface, and k_i is the unit vector in the direction of motion. This immediately gives the result $D = 4\pi\mu Ua$. Often, the drag coefficient, C_D, is quoted in text books on the subject. This is defined as the ratio of the drag to the dynamic pressure multiplied by the projected area of the bubble in the direction of motion. In practice, for non-spherical objects, this projected area is taken to be that of a sphere of equal volume. Thus

$$C_D = \frac{4\pi\mu Ua}{\frac{1}{2}\rho U^2 \pi a^2} = \frac{16}{Re}. \tag{4.1.3}$$

For an early account see, for example, Levich (1962).

The drag can also be used to estimate the terminal velocity, U_0, by equating it to the buoyancy force $4\pi a^3 \rho g/3$, giving a value of $U_0 = a^2 g/3\nu$. These results agree well with

experimental data for bubbles in water which are of less than about $0.01cm$ in diameter. The tendency for bubbles to deform slightly from spherical is due to the effect of inertia (see for example Taylor and Acrivos, 1964). By matching a low Reynolds number inner expansion to an Oseen outer solution, for the general case of a drop, Taylor and Acrivos (1964) derived expressions for the drag and the shape deformation. They found an expression for the ellipticity, the ratio of cross-stream to with-stream axes, χ. This turns out to be an expression in terms of the Weber number, $W = 2a\rho U^2/\sigma$, which is based on the ratio of inertial pressure variations to the pressure jump due to surface tension. This is surprising since inertial effects are only small, and one would expect the shape to depend on a ratio of the viscous stress to the surface tension pressure jump, in terms of a capillary number, $Ca = \mu U/\sigma$. If, however, as pointed out by Harper (1972), the ellipticity of a bubble or drop with fore and aft symmetry depended on the capillary number at first order, the axis ratio would not be invariant under replacement of U by $-U$. Taylor and Acrivos' (1964) expression for the ellipticity is given by $\chi = 1 + 5W/32 + O(W^2/Re) + O(WRe)$.

For large Reynolds numbers, Levich (1949) estimated the boundary layer thickness, δ, around a spherical bubble to be of order $(\nu a/U)^{1/2} = a/Re^{1/2}$ — as is the case for a solid sphere. Thus it is appropriate to model such high Reynolds number flows in the usual way, by considering all vorticity to be confined to a thin boundary layer at the bubble's surface. Levich (1949) also showed that as the surface is stress free, the normal derivative of the velocity must change by $O(U/a)$, so that the velocity change due to the boundary layer is $O(\delta U/a)$, as opposed to $O(U)$ in the solid sphere case. As $\delta/a \ll 1$ the boundary layer perturbation to the velocity is much smaller than the irrotational velocity, whereas velocity gradients are of the same order. As the volume of the boundary layer is much smaller than the volume of the region surrounding the bubble where these gradients are of the same order, the first order energy dissipation rates for the potential flow and the exact flow for large Reynolds number are equal. The drag can thus be calculated by considering the energy dissipation rate for the potential flow case.

Solving Laplace's equation for a sphere moving at speed U through a fluid at rest at infinity, we get the well-known result $\phi = -(a^3/2r^2)U\cos\theta$. Since for irrotational flow $\nabla\boldsymbol{u}$ is already symmetric, this is just the rate-of-strain tensor and the energy dissipation rate, integrated over an infinite volume, V, bounded internally by the bubble, can be written as

$$
\begin{aligned}
\Phi &= 2\mu \int_V \frac{\partial u_i}{\partial x_j}\frac{\partial u_i}{\partial x_j}\,dV, \\
&= \mu \int_{\partial V} \frac{\partial q^2}{\partial n}\,dS,
\end{aligned}
\tag{4.1.4}
$$

on using the divergence theorem, where $q = |\boldsymbol{u}|$. Equating Φ, given by (4.1.4), to UD, where D is the drag, and substituting $\boldsymbol{u} = \nabla\phi$ gives

$$
D = 12\pi\mu U a,
\tag{4.1.5}
$$

so that, rather than (4.1.3), in this case we get

$$
C_D = \frac{48}{Re},
\tag{4.1.6}
$$

a result first calculated by Levich (1949). It is interesting to note that integrating the normal stress for the potential flow over the bubble, gives a drag coefficient of $32/Re$. The reason for this discrepancy, as was pointed out by Moore (1963), is that the neglected pressure perturbation due to the boundary layer also contributes to the drag at the same order.

By taking into account energy dissipated in the boundary layer and wake, Moore (1963) found the first order correction to the drag coefficient (4.1.6) for spherical bubbles. His value is

$$
C_D = \frac{48}{Re}\left(1 - \frac{2.21}{Re^{1/2}} + \dots\right).
\tag{4.1.7}
$$

For larger bubbles, the Weber number will not be so small and so the bubble shape will deviate from that of a sphere. For large Reynolds numbers, the ellipticity is given by $\chi = 1 + 9W/64 + O(W^2)$. It is possible to form the corresponding expression for the drag coefficient for $W \ll 1$ (see Moore, 1965), when the bubble is assumed to be ellipsoidal.

4.1.2 Numerical methods.

Many fundamental free-boundary problems, particularly those in bubble dynamics, exhibit a symmetry about a central axis. It is therefore not surprising that boundary element techniques similar to those described in earlier chapters have been developed to exploit this feature of axisymmetry. Indeed, there are many difficulties associated with a fully three-dimensional method, not the least being the increased computational times involved with the number of nodes required to maintain a reasonable resolution on a two-dimensional surface mesh. Examples of 3D codes have however been successfully used by, for instance, Chahine (1991) and Harris (1992). This highlights the beauty of two-dimensional problems where symmetry has very little effect on the method that has to be used. In effect, the axisymmetric method reduces a three-dimensional problem to a two-dimensional one. This is done in the obvious way by representing the bubble as a curve in a half-plane containing the axis of symmetry. The azimuthal integration in the Green's formula can then be carried out analytically and written in terms of complete elliptic integrals.

There are many examples of uses of axisymmetric boundary element methods in the literature. The analogue of the techniques introduced in Chapter 2 were used for cavitation bubbles by Guerri et al (1981), Blake et al (1986, 1987) and Taib (1985). An alternative integral equation approach was used by Miksis, Vanden Broeck and Keller (1981) to find steady-state solutions for a bubble in a constant velocity stream. In this article they also calculate the energy dissipation and hence the drag coefficient and terminal velocity, which compare well with the values of Moore (1965). In a later paper — Miksis et al (1982) — the same authors considered a bubble rising under gravity and included the effects of normal viscous stresses in their pressure balance (see §4.4). More sophisticated, finite difference techniques have also been developed. Ryskin and Leal (1984) used an orthogonal mapping technique to solve the steadily rising bubble problem. Unsteady viscous flows with a free-surface can also be treated accurately using front tracking finite

difference codes (see Unverdi and Tryggvason, 1992)

4.2 The axisymmetric boundary integral method.

We now give a brief overview of the differences between the two-dimensional Green's formula method of Section 2.5 and the method used here to solve axisymmetric problems. Green's formula is given by (2.2.12) where in this case

$$G(\boldsymbol{x}, \boldsymbol{x}') = \frac{1}{4\pi|\boldsymbol{x} - \boldsymbol{x}'|}, \tag{4.2.1}$$

is the free-space Green's function for the three-dimensional Laplace equation and C is the bubble surface. In the examples given here, modified versions of the code of Best and Kucera (1992) were used. The routines use cubic splines to interpolate $N + 1$ nodes, $\boldsymbol{x}_i$, $i = 0, \ldots, N$, which are given in cylindrical polar coordinates by $(r_i, 0, z_i)$. Note that nodes 0 and N lie on the central axis at the bottom and top respectively. The splines take the form

$$\boldsymbol{q}(s, \theta)\big|_{\theta=0} = (r(s), 0, z(s)) = \boldsymbol{q}_{0i} + \boldsymbol{q}_{1i}(s - s_i) + \boldsymbol{q}_{2i}(s - s_i)^2 + \boldsymbol{q}_{3i}(s - s_i)^3, \tag{4.2.2}$$

and

$$\phi(s) = \phi_{0i} + \phi_{1i}(s - s_i) + \phi_{2i}(s - s_i)^2 + \phi_{3i}(s - s_i)^3, \tag{4.2.3}$$

for $s_i \leq s \leq s_{i+1}$, $i = 0, \ldots, N - 1$. Here, ϕ represents the potential along the surface and s_i is the cumulative arc-length from node 0 to node i.

In order to obtain an accurate arc-length, Best and Kucera (1992) use an iterative scheme. Define $\delta s_i \equiv s_i - s_{i-1}$ and set

$$\delta s_i^{(0)} = |\boldsymbol{x}_i - \boldsymbol{x}_{i-1}|, \tag{4.2.4}$$

and

$$\delta s_i^{(j+1)} = \int_{s_{i-1}^{(j)}}^{s_i^{(j)}} \left|\frac{\partial \boldsymbol{q}}{\partial s}\right| ds, \quad j = 0, 1, \ldots. \tag{4.2.5}$$

After each approximation, the spline coefficients for **q** are calculated to ensure that it runs through the $N + 1$ nodes with continuous first and second derivatives. The end

– 71 –

conditions used are that the top and bottom of the bubble are horizontal as is required physically. The method converges very quickly, at which point the corresponding spline for the potentials can be constructed, with end conditions dictated by symmetry, that $\partial \phi / \partial s = 0$ at $s = 0$ and $s = s_N$.

The unknown potential derivatives, ψ_i, are parametrised linearly by arc-length, namely

$$\psi(s) = \psi_{i-1} \frac{(s_i - s)}{\delta s_i} + \psi_i \frac{(s - s_{i-1})}{\delta s_i}, \tag{4.2.6}$$

for $s_{i-1} \le s \le s_i, i = 1, \ldots, N$.

In the axisymmetric case, it is necessary to deal with the azimuthal integrations separately. We may write the three dimensional form of Green's formula, analogous to (2.2.12), evaluated on the bubble as

$$\begin{aligned}
\frac{1}{2} \phi(\boldsymbol{x}_i) = k &+ \int_0^{s_N} \frac{\partial \phi}{\partial n}(\boldsymbol{q}(s,0)) \left\{ \int_0^{2\pi} G(\boldsymbol{x}_i, \boldsymbol{q}(s,\theta)) r(s) d\theta \right\} ds \\
&- \int_0^{s_N} \phi(\boldsymbol{q}(s,0)) \left\{ \int_0^{2\pi} \frac{\partial G}{\partial n_q}(\boldsymbol{x}_i, \boldsymbol{q}(s,\theta)) r(s) d\theta \right\} ds.
\end{aligned} \tag{4.2.7}$$

Here the functions $\boldsymbol{q}(s,\theta)$ are given in terms of the splines by $(r(s), \theta, z(s))$, in cylindrical polar co-ordinates. As the Green's function vanishes at infinity, the constant, k, is the limiting value of the potential there.

The inner integrals of (4.2.7) over the angle θ can be expressed in closed form (see Taib (1985)) as follows

$$\begin{aligned}
\int_0^{2\pi} \frac{\partial G}{\partial n_q}(\boldsymbol{x}_i, \boldsymbol{q}(s,\theta)) r(s) d\theta = &\frac{1}{\pi} \frac{r(s)}{\left((r(s) + r_i)^2 + (z(s) - z_i)^2\right)^{3/2}} \left\{ \frac{2}{k^2(s)} \frac{dz}{ds} r_i K(k(s)) \right. \\
&\left. + \left[\frac{dz}{ds}(r(s) + r_i) - \frac{dr}{ds}(z(s) - z_i) - \frac{2}{k^2(s)} \frac{dz}{ds} r_i \right] \frac{E(k(s))}{1 - k^2(s)} \right\},
\end{aligned} \tag{4.2.8}$$

and

$$\int_0^{2\pi} G(\boldsymbol{x}_i, \boldsymbol{q}(s,\theta)) r(s) d\theta = \frac{1}{\pi} \frac{K(k(s)) r(s)}{\left((r(s) + r_i)^2 + (z(s) - z_i)^2\right)^{1/2}}, \tag{4.2.9}$$

Here

$$k^2(s) = \frac{4 r(s) r_i}{(r(s) + r_i)^2 + (z(s) - z_i)^2}, \tag{4.2.10}$$

$$- 72 -$$

and $K(k)$ and $E(k)$ are complete elliptic integrals of the first and second kind respectively. These are calculated from the approximate formulae

$$K(k) = P(1 - k^2) - Q(1 - k^2)\log(1 - k^2),$$
$$E(k) = R(1 - k^2) - S(1 - k^2)\log(1 - k^2),$$

$$(4.2.11)$$

where P, Q, R and S are polynomials tabulated in Hastings (1955).

In an analogous manner to that explained in Chapter 2, we can substitute (4.2.6) into (4.2.7) to obtain a system of $N + 1$ algebraic equations,

$$\frac{1}{2}\phi_i + A_i = k + \sum_{j=1}^{N}(B_{ij}\psi_{j-1} + C_{ij}\psi_j), \quad i = 0, \ldots, N, \tag{4.2.12}$$

where, if we denote the azimuthal integrals (4.2.8) and (4.2.9) by $\alpha_i(s)$ and $\beta_i(s)$ respectively,

$$A_i = \int_0^{s_N} \phi(s)\alpha_i(s)ds, \tag{4.2.13}$$

$$B_{ij} = \int_{s_{j-1}}^{s_j} \left(\frac{s_j - s}{\delta s_j}\right)\beta_i(s)ds, \tag{4.2.14}$$

and

$$C_{ij} = \int_{s_{j-1}}^{s_j} \left(\frac{s - s_{j-1}}{\delta s_j}\right)\beta_i(s)ds. \tag{4.2.15}$$

Numerical integration is done via Gauss quadrature, and the weak singularity is dealt with by using a logarithmic Gauss-type scheme.

Two problems are considered here. The first is a simple extension of Chapter 2, that is modelling a constant volume bubble rising through an infinite fluid under gravity. The second problem is that of finding the steady state of a rising bubble — the problem considered in detail by Miksis et al (1982).

4.3 The rise of constant volume bubbles.

This section is the axisymmetric analogue of the Chapter 2 problem. The only difference being the inclusion of surface tension effects. It is a straightforward extension to allow more than one bubble positioned on the central axis, so we formulate the problem

for the more general case of M bubbles. In this way, the interaction of several bubbles can be examined.

The solution domain, Ω_-, is defined to be the infinite region bounded internally by each of the bubbles C_m, $(m = 1, \ldots, M)$. Normals, as previously, are taken as pointing outwards from Ω_-, into the gaseous phase. Initially, bubbles are spherical with non-dimensional radii r_m, lengths being scaled with respect to the radius of bubble 1, which we denote by a. Bubble m is initially positioned on the z−axis at a distance $\gamma_m (> 0)$ below the centre of bubble 1 which is situated at the origin. At the start of the calculations, the fluid is assumed at rest so we take $\phi \equiv 0$ at $t = 0$ and the constant, k, of equations (4.2.7) and (4.2.12) is chosen to be zero. As before we scale times with respect to $(a/g)^{1/2}$ and pressures by the factor $\rho g a$.

For air bubbles larger than about $1mm$ in radius, rising at terminal velocity in water, the corresponding Reynolds numbers are of the order of 700 (see Levich, 1962; Clift, Grace and Weber, 1978). We can therefore assume that the potential flow model of the previous chapters will give realistic results when applied to the problem of axisymmetric bubble rise.

With the above scalings, the Bernoulli equation becomes

$$p_\infty = p + \frac{1}{2}|\boldsymbol{u}|^2 + \frac{\partial \phi}{\partial t} + z, \qquad (4.3.1)$$

where p_∞ is the fluid pressure at infinity at $z = 0$.

If viscous stresses in the thin boundary layers are ignored, a pressure balance may be used across each interface. The pressure just outside the surface C_m $(m = 1, \ldots, M)$ is given by

$$p = p_m(t) - \frac{4\kappa}{E_o}, \qquad (4.3.2)$$

where κ is twice the mean curvature and again $E_o = 4\rho g a^2/\sigma$ is the Eötvos number. Here, $p_m(t)$ $(m = 1, \ldots, M)$ is the pressure inside the mth bubble.

Combining (4.3.1) and (4.3.2), evaluated initially and at a general time, and employing

the substantial derivative gives an equation for the time evolution of the potential on C_m,

$$\left.\frac{D\phi}{Dt}\right|_{C_m} = \frac{1}{2}|\boldsymbol{u}|^2 - z - \gamma_m + \frac{4}{E_o}(\kappa - \kappa_m) + p_m(0) - p_m(t). \qquad (4.3.3)$$

In (4.3.3), $\kappa_m(= 2/r_m)$ is the initial curvature for bubble m. Note that, by definition, $\kappa_1 = 2$ and $\gamma_1 = 0$.

In order to eliminate the unknown pressure terms in (4.3.3) we introduce, as in the previous chapter, a function f defined on $\partial\Omega$ by

$$\left.f\right|_{C_m} = \left.\phi\right|_{C_m} + k_m, \qquad (4.3.4)$$

where

$$k_m(t) = \int_0^t (p_m(t') - p_m(0))dt', \qquad (4.3.5)$$

for $m = 1,\ldots,M$, and again we work with f rather than ϕ. With this definition, the dynamic condition (4.3.3) becomes

$$\left.\frac{Df}{Dt}\right|_{C_m} = \frac{1}{2}|\boldsymbol{u}|^2 - z - \gamma_m + \frac{4}{E_o}(\kappa - \kappa_m), \quad m = 1,\ldots,M. \qquad (4.3.6)$$

Each surface C_m is now represented parametrically by the function $\boldsymbol{q}_m(s,\theta,t)$. The kinematic condition expresses the assumption that there is no mass transfer across interfaces, so that particles that lie on a surface will remain there and move with its local velocity. Hence for the time dependent surface parametrisation, we have

$$\frac{\partial \boldsymbol{q}_m}{\partial t}(s,\theta,t) = \nabla\phi(\boldsymbol{q}_m(s,\theta,t),t), \quad m = 0,\ldots,M. \qquad (4.3.7)$$

The surface B_m, the projection of C_m into the half-plane $\theta = 0$, is discretised using $N_m + 1$ nodes interpolated by cubic splines as described in section 4.2. The curvature of B_m, required in the boundary condition (4.3.6), is obtained directly from the splines.

To keep the bubble volumes constant, constraint equations in the form of the line integrals

$$\int_{B_m} \frac{\partial\phi}{\partial n} r ds = 0, \quad m = 1,\ldots,M \qquad (4.3.8)$$

are used.

The calculation of the integrals that make up the boundary integral method is essentially as described in section 4.2 except that all of the surfaces must now be integrated over for each observation point. At each time-step, equations analogous to (4.2.12) and the discrete form of (4.3.8) are solved to yield the normal velocities and the constants, k_m. The bubble is then stepped through time using the boundary conditions (4.3.6) and (4.3.7). A trapezium rule is used for the time integrations.

4.4 Steady rise of a bubble through a viscous fluid.

Consider a bubble rising in a viscous fluid at high Reynolds number. Below, we describe a method similar to that of Miksis, Vanden-Broeck and Keller (1982), to find the steady-state shape reached. They assumed that the bubble remains at a fixed height, otherwise its volume would increase and no steady state could be reached. Viscous forces were included in their model in as much as viscous stresses were incorporated into the normal stress balance across the bubble surface. There is also a pressure drop due to the thin boundary layer that exists in the real high Reynolds number flow, but Miksis et al (1982) showed this to be negligible compared with the normal stress component, σ_{rr}, on the upper part of the bubble surface. On the lower part of the bubble, this pressure drop is not negligible and this, together with the turbulent wake, it was argued, reduces confidence in the shape of this part of the bubble as predicted by their calculations.

The formulation of the model used here is slightly different from that used by Miksis et al (1982). The method described below was used because it was reasonably straightforward to adapt the existing boundary integral program of Best and Kucera (1992), although unfortunately it uses more equations. In common with their method however it is equally applicable to drops falling as to bubbles rising.

Assume that the fluid around the bubble is incompressible with density, ρ, and kinematic viscosity, ν. The bubble is moving upward through the fluid at a steady speed, U. As explained in section 4.1.1, the change in velocity due to a viscous free-surface boundary

layer is $o(U)$. We may therefore assume that the flow can be represented by a velocity potential, ϕ, so that $\nabla^2 \phi = 0$ outside the bubble which, as usual, we denote by Ω_-. Denote the bubble surface itself by C. At infinity, the fluid is taken to be at rest and the potential assumed to vanish there. On the bubble there is no normal component of velocity relative to C, so we must have that, on C,

$$\frac{\partial \phi}{\partial n} = U n_z, \tag{4.4.1}$$

where n_z is the z-component of the unit normal to the bubble.

A normal stress balance on C, taking into account the density of gas (or liquid), ρ_b, inside the bubble gives

$$p_b - \rho_b g z = p - 2\rho\nu \frac{\partial u_n}{\partial n} + \sigma\kappa, \tag{4.4.2}$$

where p_b is the ambient pressure within the bubble, κ is the sum of the curvatures, σ is the surface tension and p is the pressure on the outside of the interface. If, as in Miksis et al (1982), we take the pressure jump across the boundary layer as being insignificant, then we may equate p to the pressure outside the boundary layer and use Bernoulli's theorem for the potential flow region. First, we introduce a frame of reference where the bubble is at rest by defining the potential $\psi = \phi - Uz$, so that $\psi \sim -Uz$ at infinity. This transformation alleviates the need to calculate $\partial\phi/\partial t$ in the moving frame. Hence we may write down Bernoulli's equation as

$$\frac{p_\infty}{\rho} + \frac{1}{2}U^2 = \frac{p}{\rho} + \frac{1}{2}|\nabla\phi - U\hat{\boldsymbol{k}}|^2 + gz. \tag{4.4.3}$$

If we now eliminate the pressure, p, from (4.4.2) and (4.4.3) we get

$$\frac{p_\infty - p_b + \frac{1}{2}\rho U^2}{\rho} = gz\left(1 - \frac{\rho_b}{\rho}\right) + 2\nu\frac{\partial u_n}{\partial n} - \frac{\sigma\kappa}{\rho} + \frac{1}{2}|\boldsymbol{u}|^2 - U\frac{\partial\phi}{\partial z} + \frac{1}{2}U^2. \tag{4.4.4}$$

Following Miksis et al (1982), scale velocities with respect to U and lengths with respect to an equivalent radius, r_e, defined from the volume, $V = 4\pi r_e^3/3$. This reduces (4.4.4) to

$$1 + \gamma + \frac{3}{4}C_D z + \frac{8}{Re}\frac{\partial^2 \phi}{\partial n^2} - \frac{4}{W}\kappa + |\boldsymbol{u}|^2 - 2\frac{\partial\phi}{\partial z} = 0, \tag{4.4.5}$$

where the parameters are defined by

$$Re = \frac{2Ur_e}{\nu}, \qquad C_D = \frac{8}{3}\left(1 - \frac{\rho_b}{\rho}\right)\frac{gr_e}{U^2},$$
$$W = \frac{2U^2 r_e \rho}{\sigma}, \qquad \gamma = \frac{p_b - p_\infty - \frac{1}{2}\rho U^2}{\frac{1}{2}\rho U^2}.$$

(4.4.6)

To solve for the shape of the bubble and the potential on the bubble, the intersection of the bubble surface, C, with the half-plane containing the axis of symmetry can be discretised and represented using an even number of nodes $N = 2K$ interpolated using cubic splines as defined above by (4.2.2) to (4.2.5). The linear interpolant (4.2.6) gives the normal derivative of the potential in terms of its nodal values. To describe the properties of the fluid itself, we use the Morton number,

$$M = \left(1 - \frac{\rho_b}{\rho}\right)\frac{g\rho^3\nu^4}{\sigma^3},$$

(4.4.7)

and to describe the flow, the Miksis et al 'cavitation' number, γ. The unknown parameters are the Reynolds number, Re, the Weber number, W, and the drag coefficient, C_D. As the problem is axisymmetric, the end nodes are explicitly placed on the central axis but at unknown heights. We fix the height of the bubble by insisting that it is at its widest at $z = 0$, and explicitly set $z_K = 0$. Bearing this in mind, we see that there are a total of $3N + 3$ unknowns. The effect of a different choice for the bubble height, for example setting z_0 to zero, would be to introduce a constant into equation (4.4.5) and so alter the effective value of γ. The physical requirements that $dz/ds = 0$ and $\partial\phi/\partial s = 0$ on the axis are also explicit in view of the spline end conditions given in section 4.2.

It is more convenient to write the term in (4.4.5) involving a second normal derivative of the potential in terms of tangential derivatives which are readily calculated numerically from the splines. As ϕ is harmonic,

$$\frac{\partial^2\phi}{\partial n^2} = -\left(\frac{\partial u_t}{\partial s} - \kappa^{(t)}u_n + \frac{\boldsymbol{u}\cdot\hat{\boldsymbol{r}}}{r}\right),$$

(4.4.8)

where $\kappa^{(t)}$ is the curvature of the surface in the plane $\theta = 0$.

In order to determine the unknowns, Green's formula (2.2.12) with G given by (4.2.1) and $k = 0$, is employed to relate the potential and its normal derivative, the latter of

which is given by the condition (4.4.1). This is discretised as described in section 4.2 and, written in the form of (4.2.12), it represents $N + 1$ equations.

The Bernoulli condition (4.4.5), likewise gives $N + 1$ equations. The volume of the bubble is also known: in non-dimensional variables, it is

$$V = \frac{4}{3}\pi. \tag{4.4.9}$$

Since r and z are discretised separately, whereas Miksis et al (1982), in principle, use $z_i = z(r_i)$ for a known set of values r_i, we need to fix which one of the infinite number of solutions to take. To do this, we set the spacing between all the nodes on the upper surface equal and, separately, all spacings on the lower surface are set equal, namely

$$\delta s_1 = \delta s_2 = \ldots = \delta s_K, \quad \text{and} \quad \delta s_{K+1} = \ldots = \delta s_N. \tag{4.4.10}$$

This gives another $N - 2$ equations and allows us to choose node K to coincide with the maximum bubble radius expressed by the equation

$$\hat{\boldsymbol{n}}_K \cdot \hat{\boldsymbol{k}} = 0. \tag{4.4.11}$$

Finally, we use the fact that the Reynolds number may be calculated explicitly in terms of the other parameters

$$Re = \left(\frac{3C_D W^3}{4M}\right)^{\frac{1}{4}}. \tag{4.4.12}$$

We now have sufficiently many independent equations to solve the problem. However, as was pointed out above, the drag calculated from the inviscid flow, and therefore which would be produced by a solution of these equations, does not take into account the pressure perturbation of the boundary layer which contributes to the drag at the lowest order. In order to compensate for this (Miksis et al, 1982) we can replace the Reynolds number in (4.4.12) by the value given by Levich's (1949) expression for the drag (see §4.1.1). This gives the Morton number as

$$M = \frac{3\pi^4 C_D^5 W^3}{1024 I^4}, \tag{4.4.13}$$

where I is the non-dimensional form of the energy dissipation rate

$$I = \int_C \frac{\partial}{\partial n} |\nabla \phi|^2 dS. \tag{4.4.14}$$

Using (4.4.13) in place of (4.4.12) allows a more accurate results in the light of the above. After the solution has been found, (4.4.12) can then be used to determine a better value for the Reynolds number.

For computational purposes the integrand of (4.4.14) is written as

$$2\left(u_n \frac{\partial^2 \phi}{\partial n^2} + u_t \frac{\partial u_n}{\partial s} + u_t^2 \kappa^{(t)}\right). \tag{4.4.15}$$

The system of non-linear equations (4.4.5), (4.4.8), (4.4.9), (4.4.10), (4.4.11) and (4.4.12) can then be solved using a modified version of Newton's method, where derivatives for the Jacobian are approximated by a simple finite-difference scheme. As a starting point, the asymptotic solutions for large γ, given in Miksis et al (1982), are used. In order to get convergence for other values of γ the procedure is run repeatedly with smaller and smaller values. As the Morton number is typically much less than unity, (4.4.13) is divided by M in order to allow unbiased determination of the error for this equation.

4.5 Results.

The following pages show examples of output for the two problems considered in sections 4.3 and 4.4. Figures 4.1(a)-(d) show the time evolution for single bubbles accelerating from rest at $t = 0$. In 4.1(a) the largest bubble, with an Eötvos number of 212, is considered, so that buoyancy forces are much stronger than surface tension. Consequently, a narrow jet of fluid forms below the bubble, eventually impacting on the upper surface, at which point the calculations break down. In reality, the bubble would evolve into a toroidal vortex ring bubble similar to those modelled by Lundgren and Mansour (1991). As the Eötvos number decreases, corresponding to smaller bubbles and higher values of surface tension, the jet becomes slower and less pointed. In figure 4.1(b), where $E_o = 29.8$, the jet only just reaches the far side of the bubble before widening and forming

a jet directed radially outwards, ultimately pinching off a toroidal bubble and leaving behind a spherical cap.

As the Eötvos number decreases further, the size of the toroidal bubble that splits off decreases as the jet becomes shorter and wider. For the case $E_o = 13.2$, shown in figure 4.1(c), the bubble eventually evolves into a shape resembling a skirted bubble. Experimentally observed skirted bubbles (Bhaga and Weber, 1981) rising steadily in viscous fluids are only observed for intermediate Reynolds numbers (between about 10 and 100), with large Eötvos numbers (between about 300 and 1000). As the jet broadens, the skirt thins and the curvature at its rim increases until surface tension forces pull it back up to the position shown in the final frame. This particular bubble seems to be close to the limiting size whereby bubbles larger than this develop a jet which pinches off a thin ring and bubbles smaller than this form a jet so wide that the bubble forms a crescent shape when viewed in profile.

Figure 4.1(d), a slightly smaller bubble, $E_o = 4.8$ is shown. Here the effect of surface tension is again exhibited pulling back the rim, this time just as a very slow jet starts to form. As the bubble accelerates and thins due to the increasing pressure difference across its surface, it begins to develop a secondary jet or dimple on its underside.

As the bubble becomes thinner and the acceleration decreases, the pressure difference between the upper and lower surfaces due to the hydrostatic gradient and the time rate of change of the velocity potential becomes less. The curvature of the upper and lower surfaces thus become equal and the lower dimple is matched by an upper one. Eventually these meet, transforming the bubble into a toroidal geometry.

In summary, there seem to be two clear cut-off points which, although we have made no attempt to locate them accurately, seem to occur around $E_o = 30$ and $E_o = 13$. The first of these corresponds to the change from the jet impacting at a single point — or at least over some simply connected region — of the upper surface, to the jet impacting on a ring — or doubly connected region — thus breaking the bubble up into a single

toroidal bubble or a toroidal bubble together with a spherical cap respectively. The other bifurcation point is when the impact ring reaches the rim of the bubble, so that the bubble remains intact, although the resulting high curvature at the rim subsequently pulls it back towards the centre of the bubble. We should point out that continuing these calculations indefinitely to ascertain the long-term behaviour of the bubbles that remain in one piece can be seen as somewhat unrealistic in that we are ignoring the drag on the bubble which would ensure that they would reach a terminal rise speed, rather than keep on accelerating, albeit slower as the added mass increases.

The similarity between figure 4.1 and the results of Chapter 2 are clear, showing the value of the study of two-dimensional bubbles as an indication of the behaviour in the axisymmetric case. The major difference between this and the two-dimensional case is that due to the greater mobility of the fluid moving in a three dimensional geometry, liquid is more easily drawn in to form a jet. Consequently for large bubbles jets may penetrate the bubble and impinge on its upper surface. For the two-dimensional case, this is not so: even for effectively infinite Eötvos numbers the jet broadens out due to the downward pull of gravity before being able to reach the far side. The broadening jet in the axisymmetric case is a result of surface tension acting so as to prevent the sharpening of the jet, rather than of gravity alone.

In figures 4.2(a) and (b), the interaction of two identical bubbles is examined. In each case, $\gamma_1 = 0$ and $\gamma_2 = -2.5$. In 4.2(a), $E_o = 212$ and we find that the jet of the upper bubble is noticeably broader than that of the lower bubble, and slightly broader than the case of a single bubble of the same size (see figure 4.1(a)). However the increased pressure at the top of the lower bubble, as compared to case when this second bubble is not there, (see figure 4.5(a)) has the effect of making the tip speed of the jet on the upper bubble slightly faster than for a single bubble of equal size. This can be seen by comparing figures 4.1(a) and 4.2(a) at $t = 0.91$ and $t = 1.2$. Although the upper part of the lower bubble is pulled upwards slightly with the jet of fluid into the upper bubble, this effect is not as great

as in the two-dimensional case (Robinson, 1992; Robinson et al, 1993). The volume flow rate across a normal to a sphere, radius a, placed in a uniform stream, $\phi \sim Uz$ at infinity is $U\pi a \sin^2 \theta$, per unit length of normal. The corresponding rate for a cylinder is $Ul \sin \theta$, where l is the length of the cylinder. Since for small θ the expression for the spherical case is an order of magnitude smaller, we may expect that the fluid in the jet of the axisymmetric bubble to originate mainly from the sides rather than from the underneath. Comparing figures 2.1 and 4.1(a) — both for large bubbles with buoyancy dominant — seems to bear this out: the initial jet is much narrower for the case of the cylindrical bubble. The result of this when a second bubble obstructs the flow beneath the upper bubble is that the jet speed in the top one is largely unaffected as the bulk of the volume is drawn from the sides, so that the lower bubble is not drawn into the jet as much as it is in the two-dimensional case. The lower jet differs little from the jet of a single bubble except that careful comparison with figure 4.1(a) shows it to be slightly faster. This can be seen as a result of the lower bubble becoming thinner due to the flow around the upper bubble, and therefore rising faster — a similar 'slipstreaming' behaviour was reported for the two-dimensional case (Robinson, 1992; Robinson et al, 1993).

For smaller bubbles, $E_o = 13.2$, shown in figure 4.2(b), the interaction is less strong due to the bubbles widening as very broad jets form, thus increasing their separation. However ring bubbles at the bottom of both bubbles are now seen to split off rather than be pulled back by surface tension as in the case of the single bubble. This is likely to be as a result of slightly faster jets as in figure 4.2(a). In general, the effect of the following bubble is the same as for the larger bubbles in the previous figure, for instance in the final frames of both figures the lower bubble is taller and wider than the upper one.

Figure 4.3(a) shows how the high pressure due to surface tension on the concave sections of the bubble of figure 4.1(c) acts against further lengthening of the jet. The low pressure around the ring tip (figure 4.3(b)) of the bubble intensifies as the jet broadens. Here unlike the two bubble case of figure 4.5 (corresponding to figure 4.2(b)), the high

pressure below the bubble does not extend far into the broad jet, so that the low pressure is able to pull back the rim before the jet pinches it off. Figure 4.4 shows the pressure distribution for the two bubbles shown in figure 4.2(a)

The bubble shapes for the steady-state problem of section 4.4 are shown in figure 4.6(a) and (b) for the cases $M = 1.75 \times 10^{-7}$, and $M = 10^{-5}$ respectively. In each case γ decreases in successive frames. These compare well with the results of Miksis et al (1982). As one may expect, as γ is reduced due to the pressure difference between the points on the axis and at the edge of the bubble increasing, the Weber number, W, which relates this pressure difference to the pressure drop due to surface tension increases and the bubble thus becomes more elliptical (see §4.1.1). A smaller Morton number has the effect of decreasing the buoyancy and viscosity and increasing surface tension. One effect of decreasing buoyancy is to lessen the pressure difference on the upper and lower surfaces thus increasing fore and aft symmetry of the bubble. The case for the larger Morton number shows that the lower surface has become slightly concave for $\gamma = 0$, while the upper surface is strongly curved in the opposite direction.

Figure 4.7(a) shows the relationship between the drag coefficient and the Reynolds number. This agrees with the calculations of Miksis et al (1982). For much larger Morton numbers (above about 4×10^{-3}), the curve relating the drag to the Reynolds number does not have a minimum value as it does here (Harper, 1972; Bhaga and Weber, 1981).

Figure 4.7(b) shows the effect of the bubble ellipticity, $\chi = 2r_K/(z_N - z_0)$, on the Weber number. The case for $M = 0$, which is calculated using the method described in section 4.4 by neglecting the viscous and the buoyancy terms from equation (4.4.5), is also included. This reduces the number of unknowns by 2. In addition, equation (4.4.13) was dropped as was (4.4.11) which is redundant due to the symmetry of the new problem. The results show a maximum value for the Weber number, as identified by Moore (1965), at about 3.59. Miksis et al (1981) found this value to be 3.23.
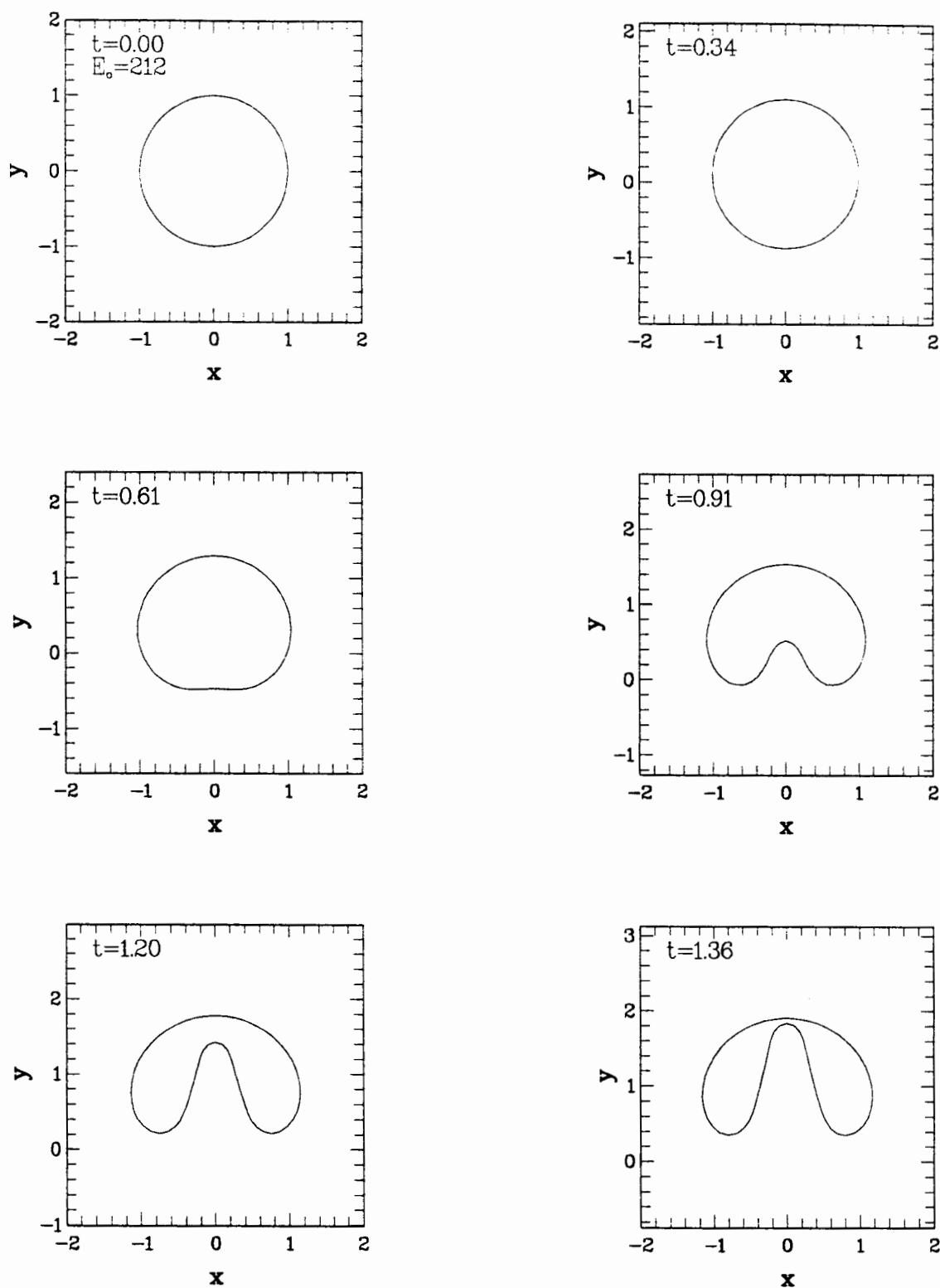
Figure 4.1. The calculated motion of axisymmetric gas bubbles of various sizes. Smaller values of the Eötvos numbers correspond to smaller bubbles, and thus a greater effect of surface tension. E_o takes the values (a) 212, (b) 29.8, (c) 13.2 and (d) 4.8, equivalent to air bubbles in water of radii 2cm, 7.5mm, 5mm and 3mm.
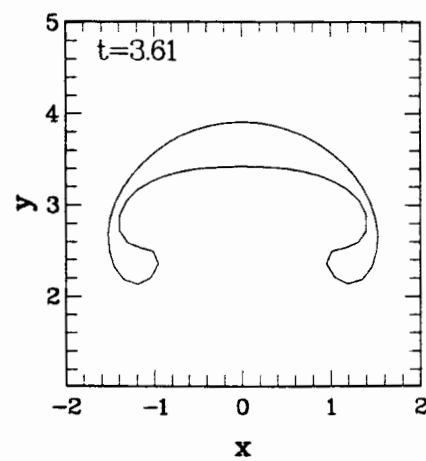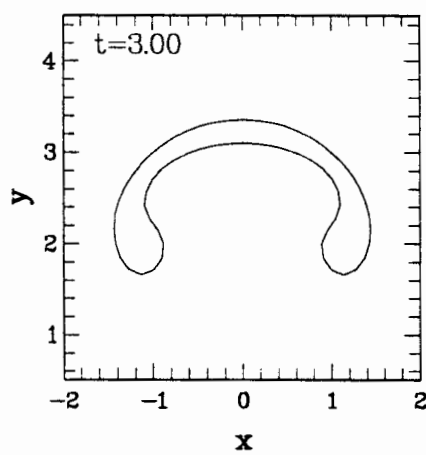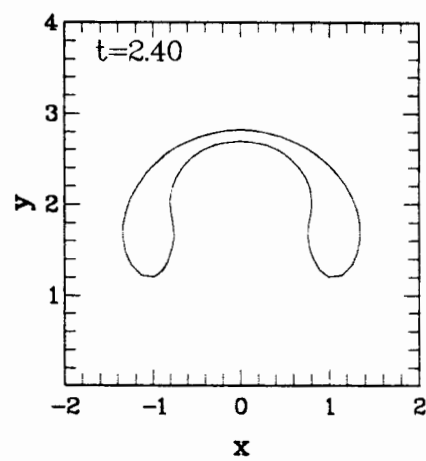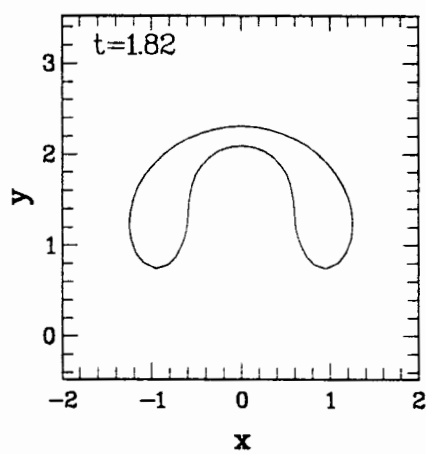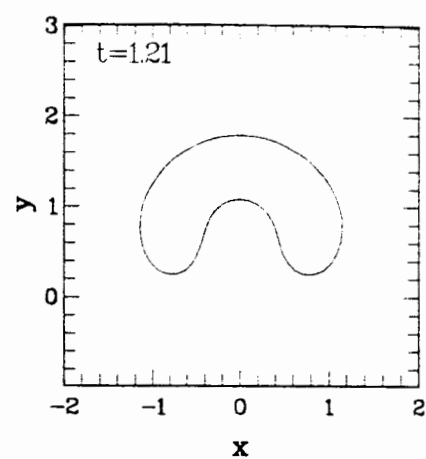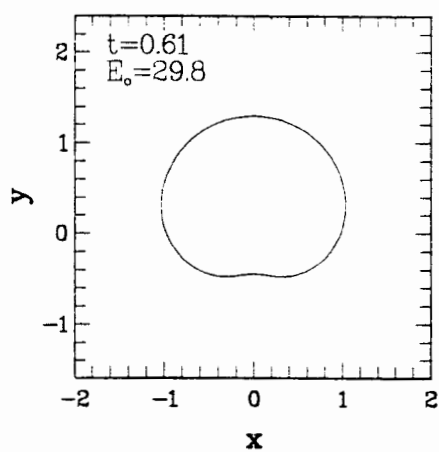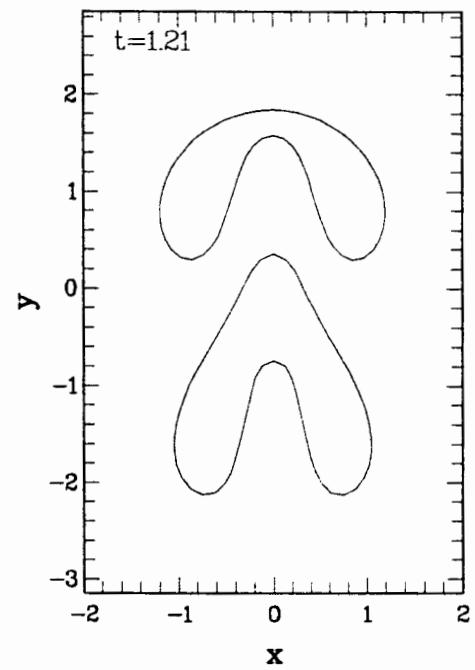
Figure 4.1(b)
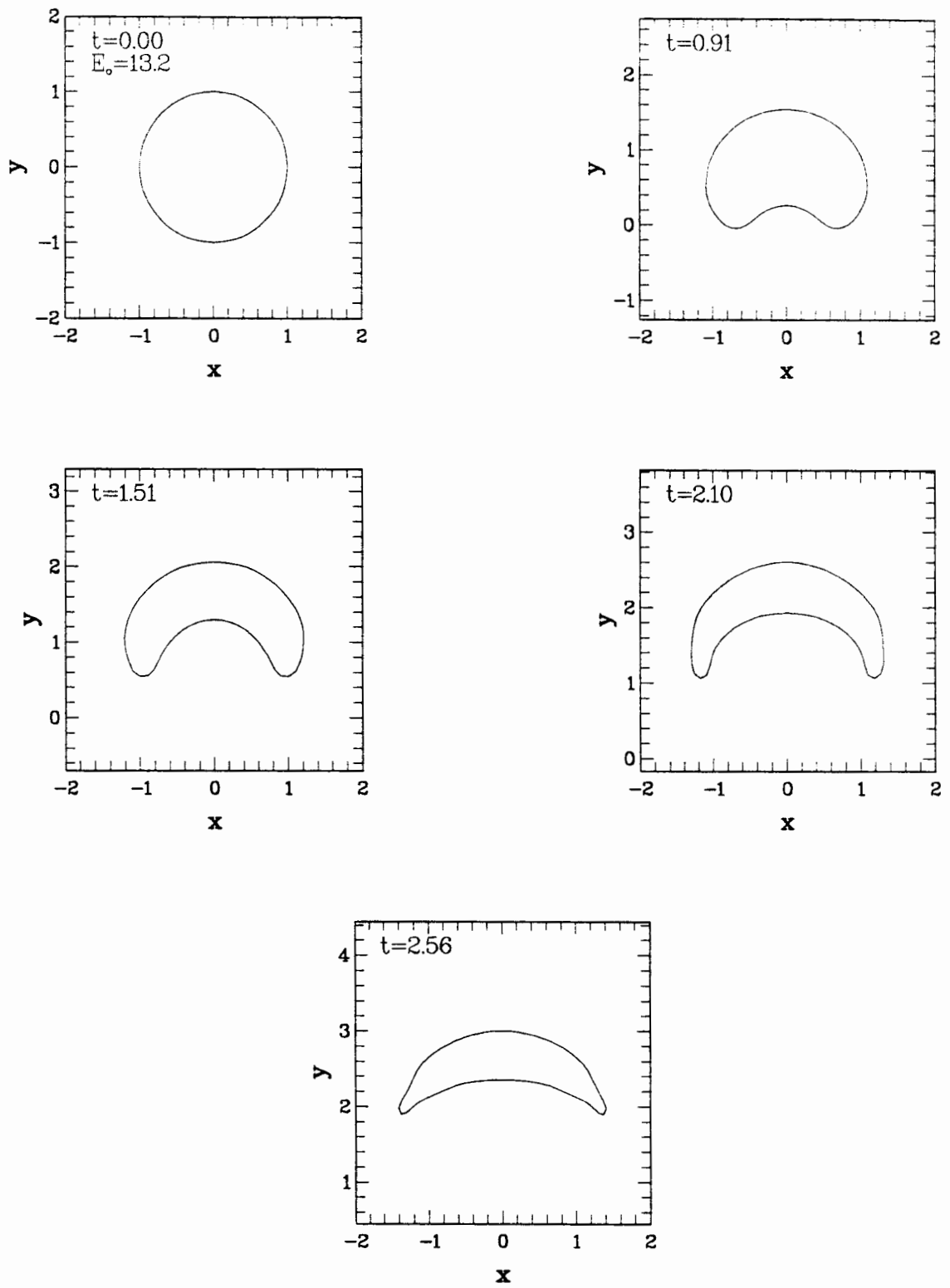
Figure 4.1(c)
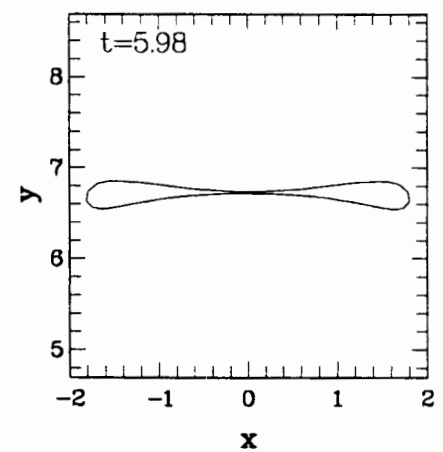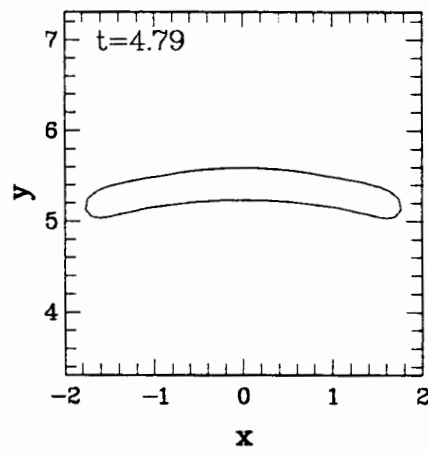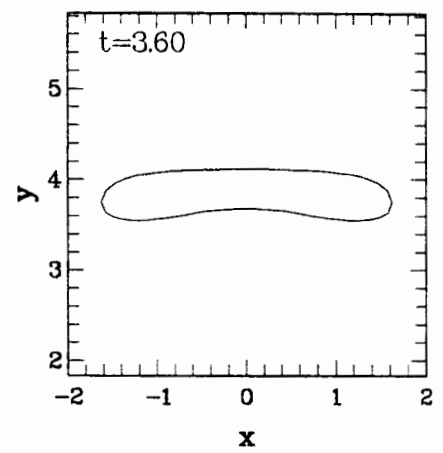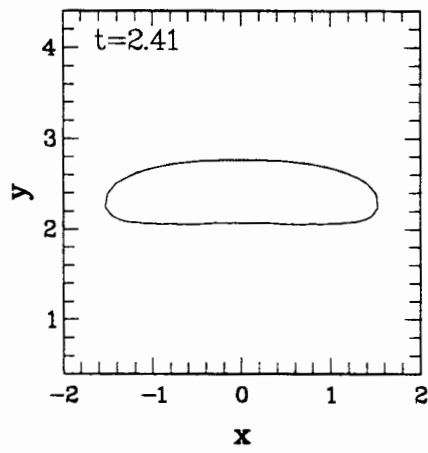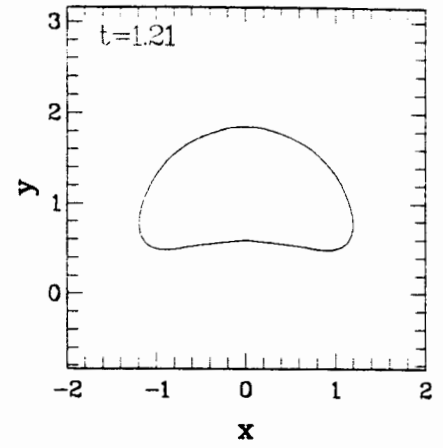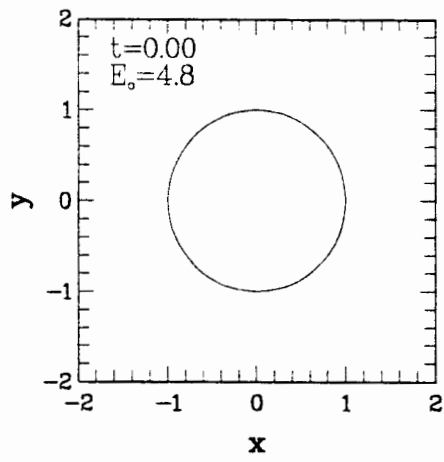
Figure 4.1(d)
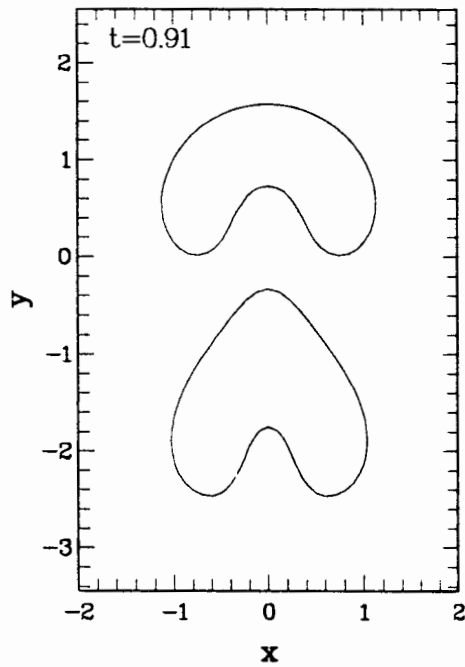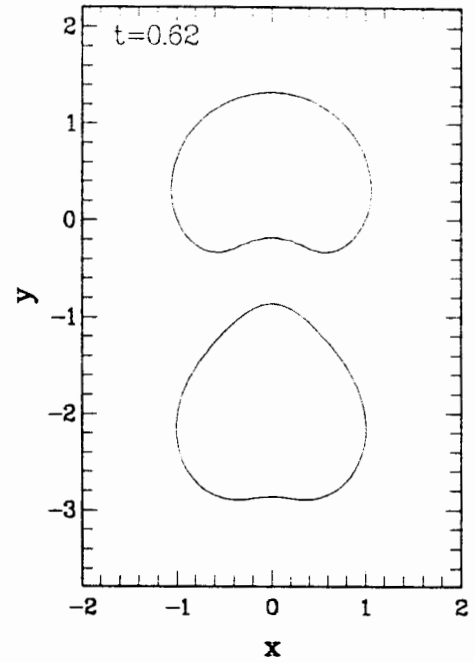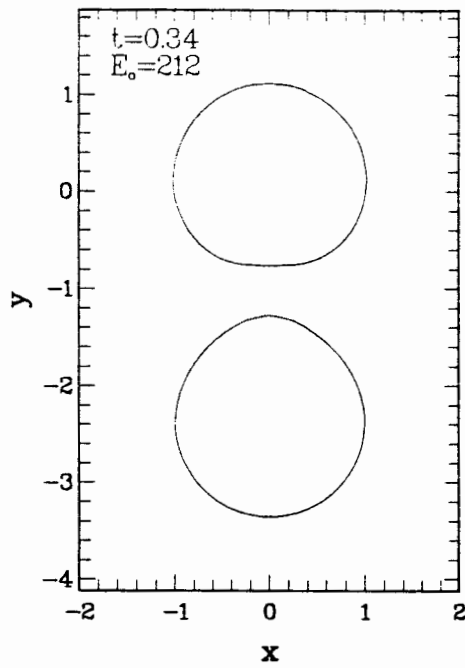
Figure 4.2. The calculated motion of two identical axisymmetric gas bubbles of various sizes, separated by a distance of 2.5 non-dimensional units. E_o takes the values (a) 212 and (b) 13.2, corresponding to air bubbles in water of radii 2cm and 5mm.

Figure 4.2(b)

(a)   t=1.22

(b)   t=2.41
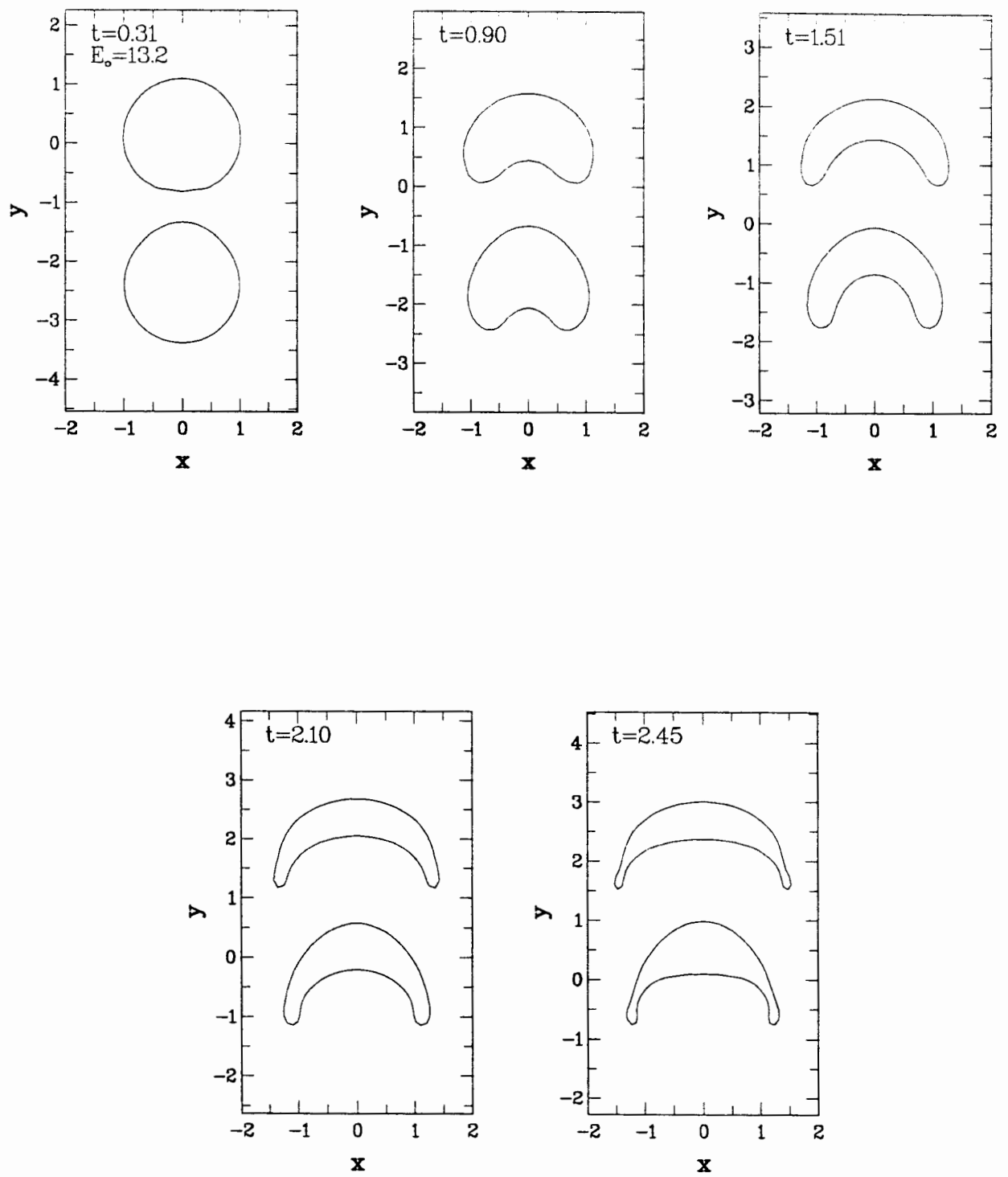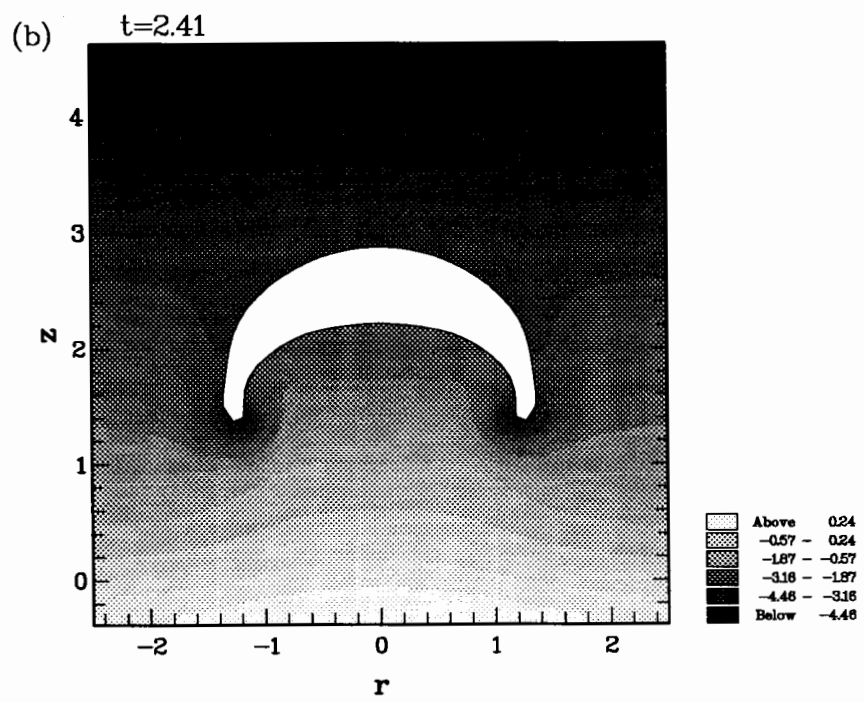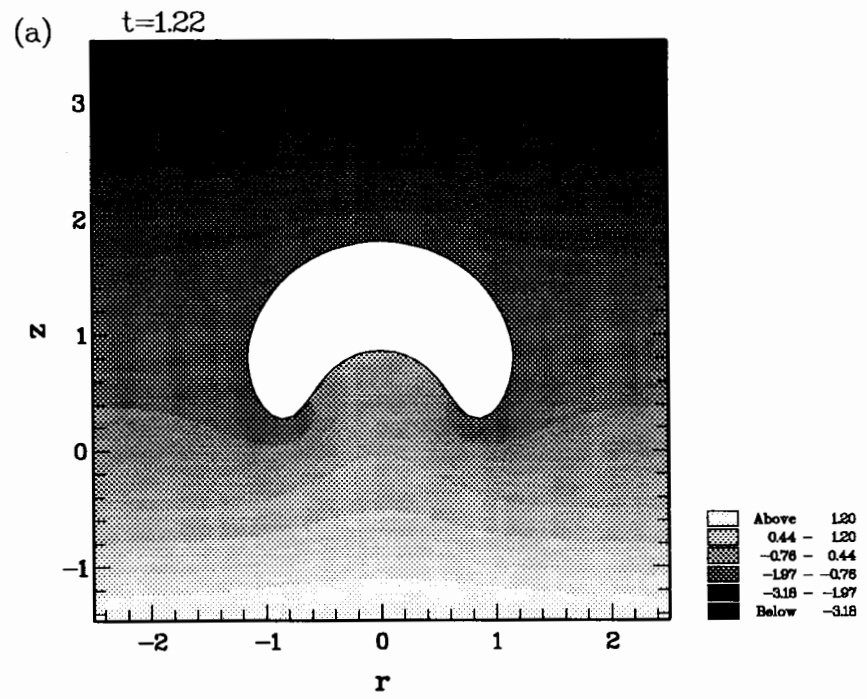
Figure 4.3. Pressure plots corresponding to figure 4.1(c).
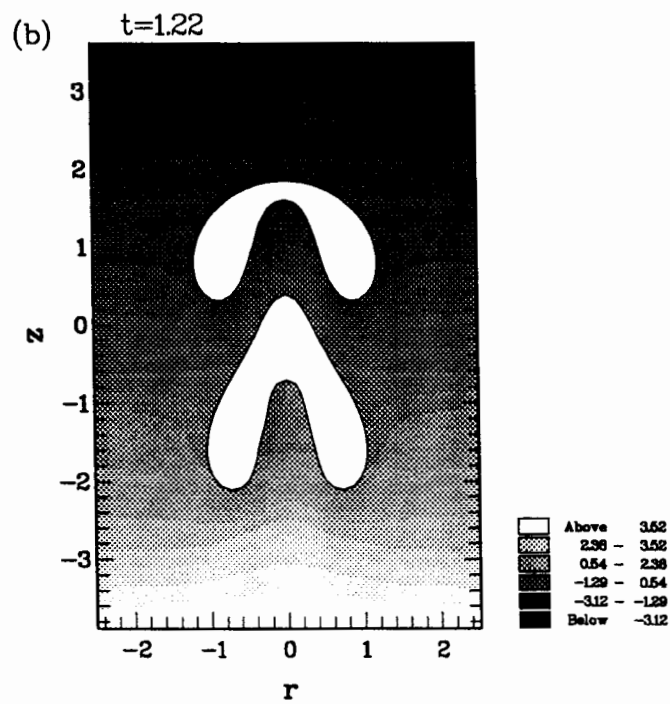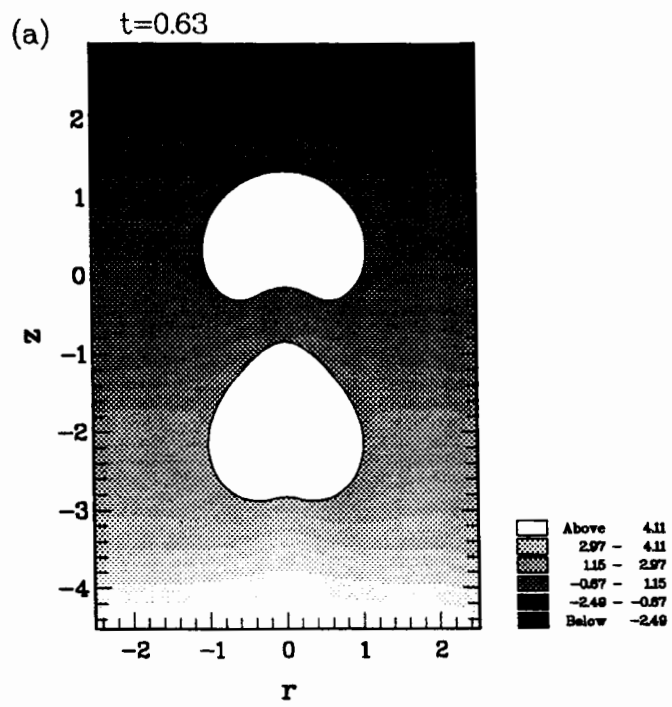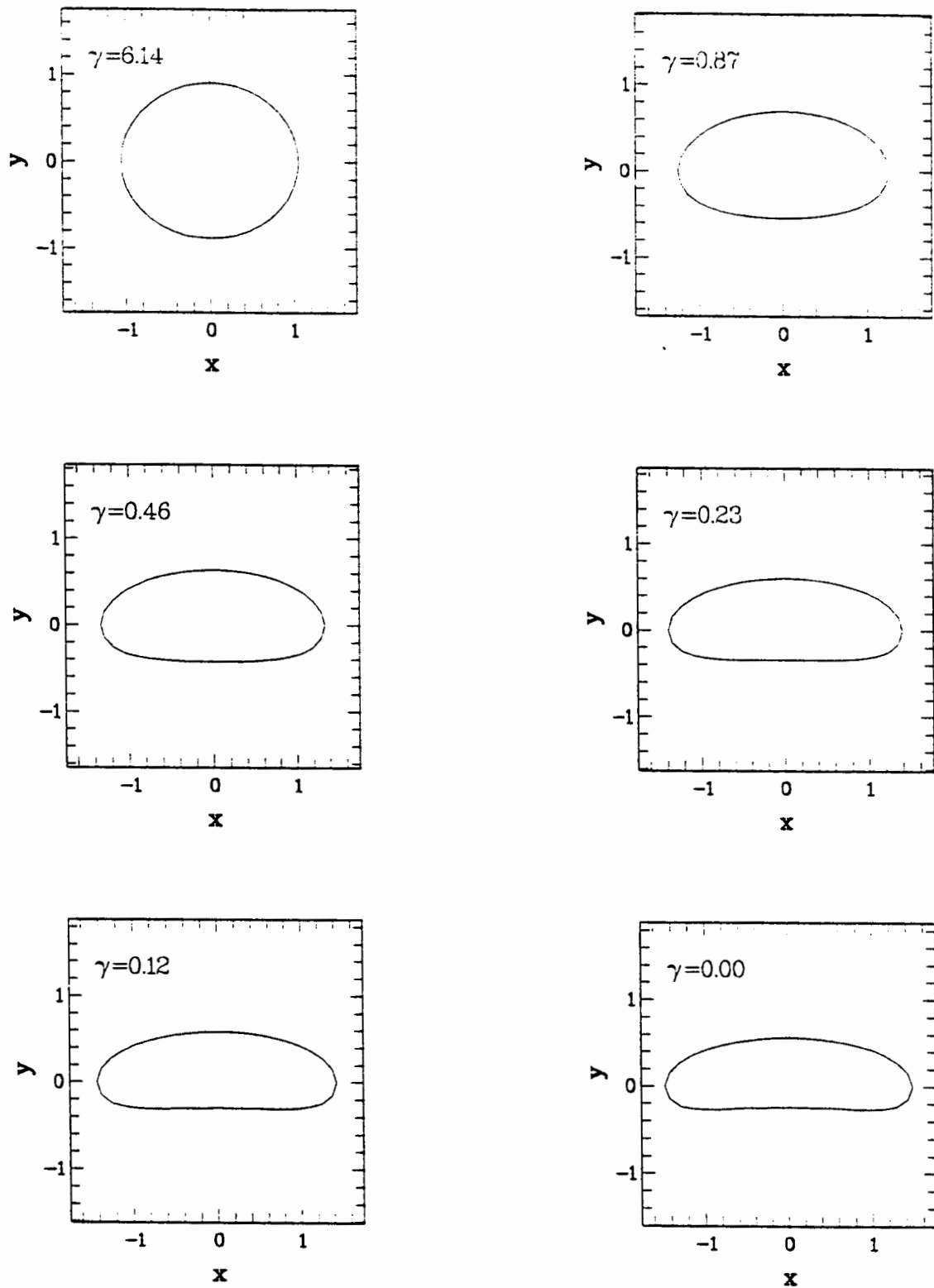
Figure 4.4. Pressure plots corresponding to figure 4.2(a).

(a)   t=1.81

(b)   t=2.43
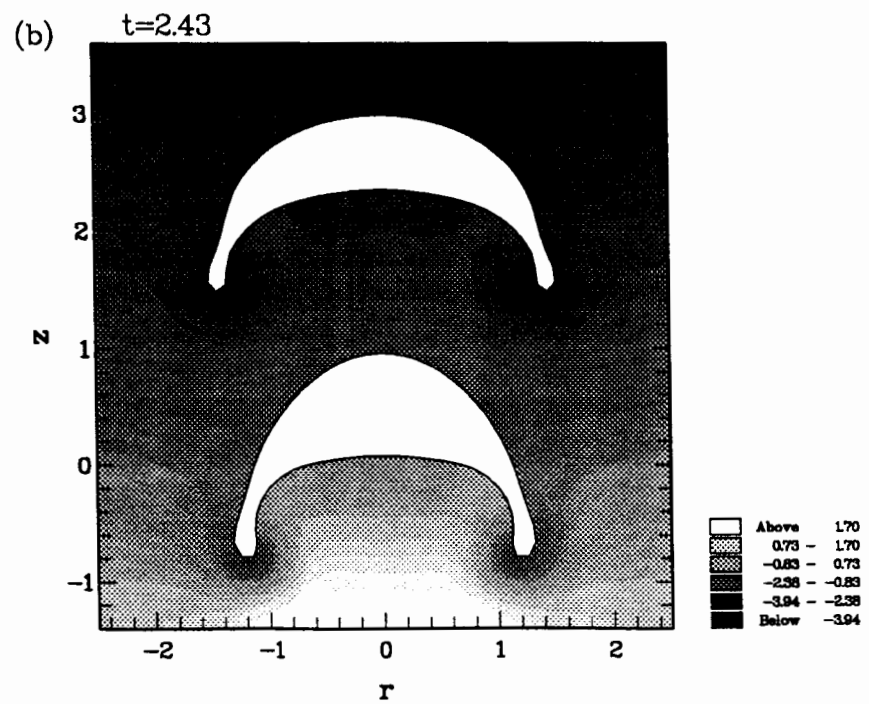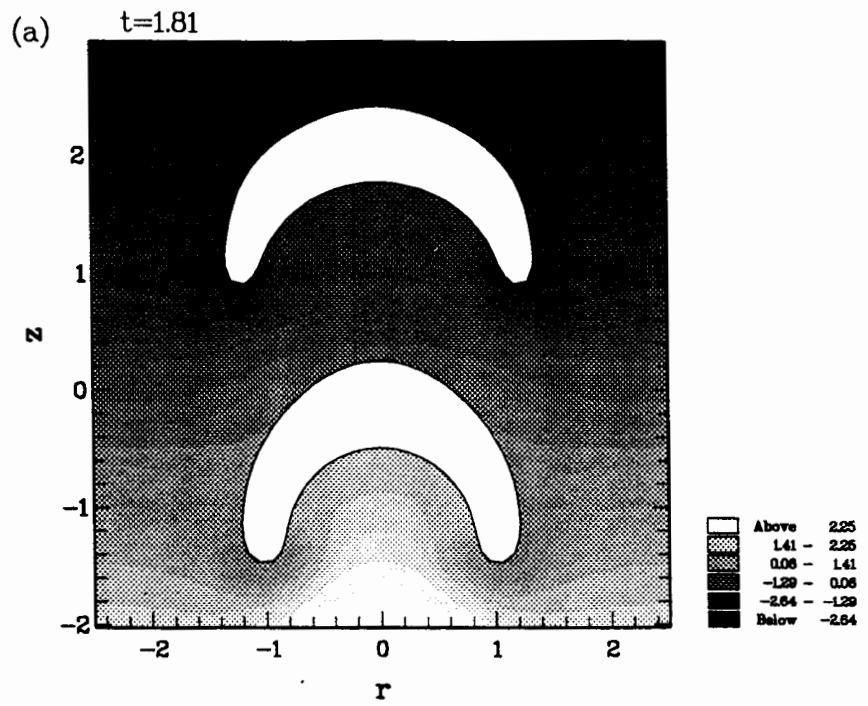
Figure 4.5. Pressure plots corresponding to figure 4.2(b).

Figure 4.6(a). Steady state profiles for decreasing values of the cavitation number, γ, for the case (a) $M=1.75 \times 10^{-7}$ and (b) $M=10^{-6}$.
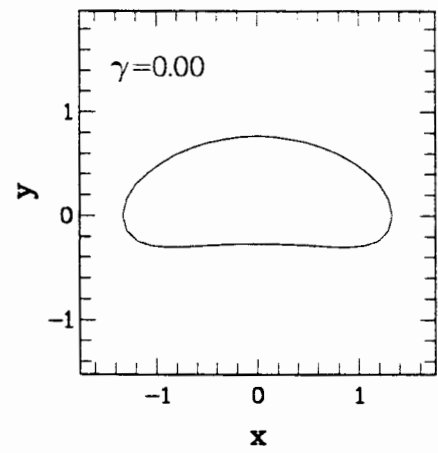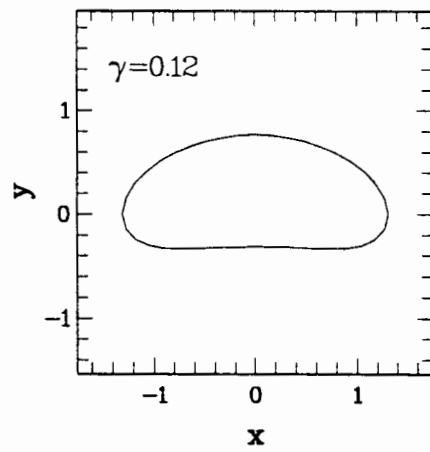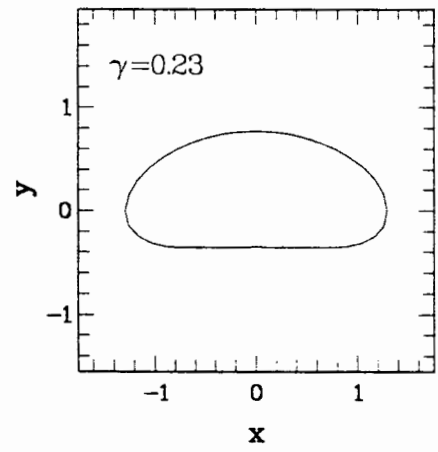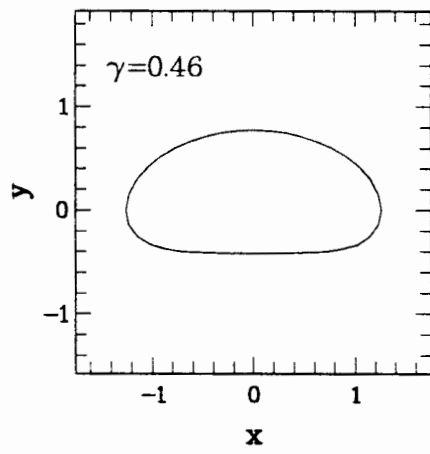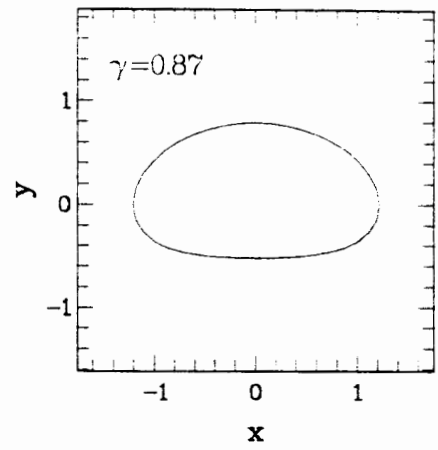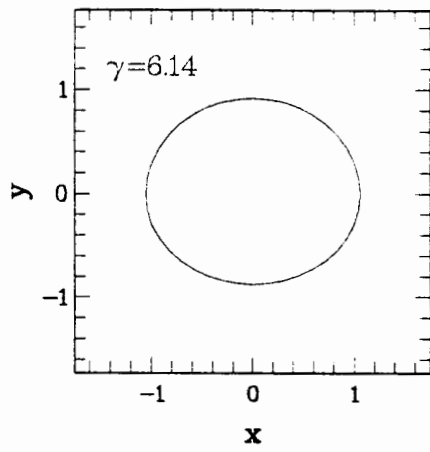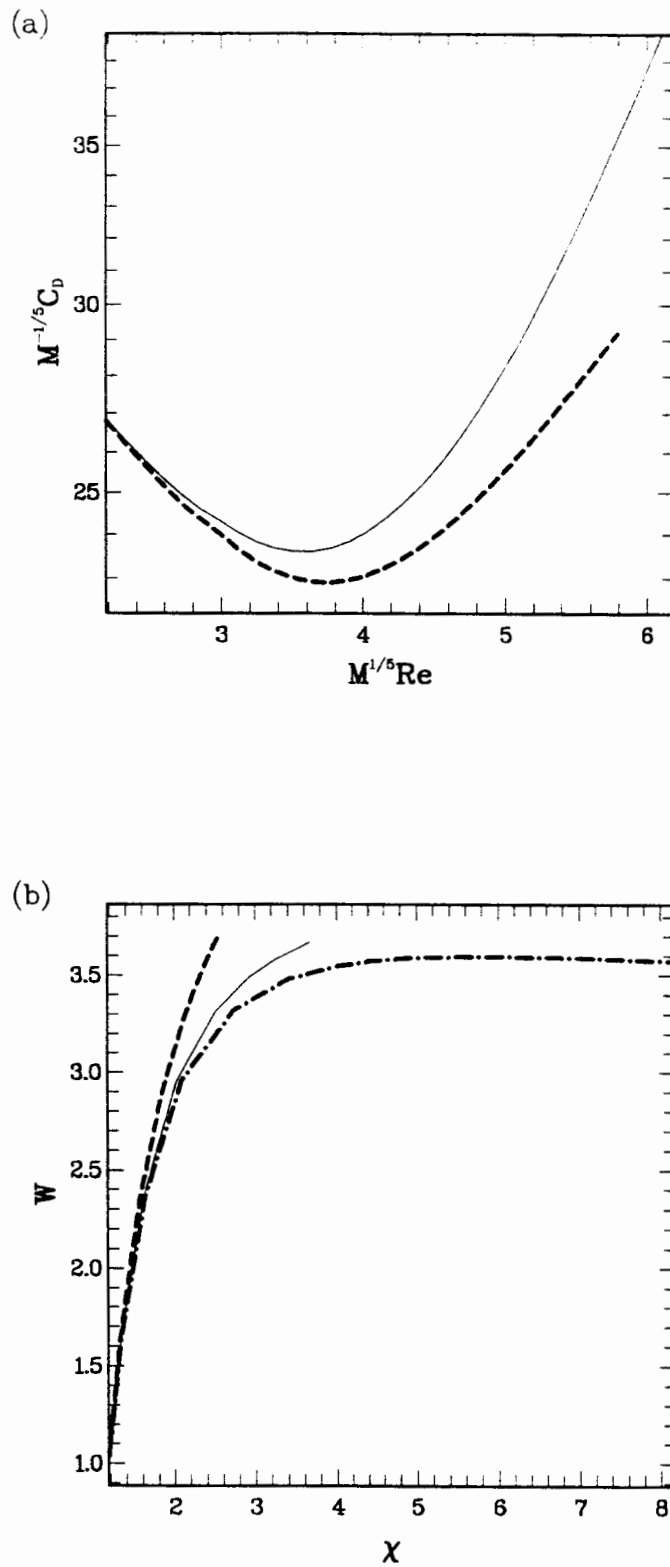
Figure 4.6(b)

Figure 4.7. In (a) the drag coefficient is plotted against the Reynolds number and in (b) the Weber number is plotted against the aspect ratio of the bubble for different Morton numbers: $M=1.75 \times 10^{-7}$ (———), $M=10^{-6}$ (– – –) and in (b) $M=0$ (– · –).
In both graphs the cavitation number decreases on moving to the right.

Chapter 5.

BURSTING BUBBLES.

5.1 Introduction.

5.1.1 Summary.

When a small bubble bursts at a gas/liquid interface, the fluid motion subsequent to film rupture is driven by surface tension. The high curvature at the rim of intersection of the bubble with the free-surface creates a large pressure difference which rapidly pulls it outward and downward. At the same time, the base is drawn inwards as the cavity wall straightens. Eventually, the converging flow near the base causes a liquid jet to be thrown upward at high speed, often several metres per second. The jet, as it rises, may break up into a number of drops. The corresponding downward jet may be expected to advect vorticity from the boundary layer around the bubble cavity into the region below. Various aspects of this motion have been studied experimentally by a number of researchers — Kientzler, Arons, Blanchard and Woodcock (1954), Newitt, Dombrowski and Knelman (1954), Garner, Ellis and Lacey (1954) and MacIntyre (1972). A numerical model based on an inviscid boundary integral scheme is used in this chapter to model these bursting processes. Viscous effects are included in an attempt to model the boundary layer and the subsequent distribution of vorticity in the downward jet region.

5.1.2 Background.

The first event occurring when a bubble bursts is the rupture of the thin lamella that separates the bubble from the atmosphere above the free-surface. There is a substantial body of literature relating to films and film drainage. The assumptions that must be made when dealing with thin films are completely different from those used below for a bubble in a high Reynolds number flow. Here, viscosity plays an important role in determining

the drainage and stability properties of lamellae. Film stability has three main causes (see for example Bikerman, 1973). The first of these is surface viscosity, whereby the presence of surfactants causes the film surfaces to have a higher viscosity than the central parts. This viscosity can be non-Newtonian and may also give the surfaces of the film crust-like properties which can, like a solid, resist stresses up to a certain yield point. Another stability mechanism is the Marangoni effect — a kind of restoring property for contaminated surfaces. If a film thins over a small region, the surface area will increase locally thus decreasing the surfactant concentration there. The resulting surface tension gradient can pull the surrounding surface towards the thin region. The fluid beneath the surface flows with it because of viscosity, thus thickening the film. Repulsion of the opposite sides of the surface due to electrical dipoles is the third cause of stability. Acting against these electrostatic forces there are London-van der Waals forces that tend to pull the two sides of the film together, thus increasing the tendency to rupture. However both of these forces act over a very short range (of the order of $100nm$) and have an effect in only the latter stages of thinning. Early on, while the film is thicker, there are two main mechanisms for drainage. Obviously, one is gravity. The second is due to Plateau borders (see Bikerman, 1973). These are regions of high surface curvature, particularly in foams, causing low pressures at the 'corners' of a bubble. This mechanism is not so important when applied to a single bubble, where the curvature is almost constant before it bursts.

With respect to bubbles approaching a free-surface, experimental and theoretical aspects are considered in a number of papers. Allan, Charles and Mason (1961) measured the thickness of the film above a bubble. They found that the thinnest part of the film moves out from the centre to a circular rim. The radius of this rim, c, which remains almost constant, was found to agree well with the expression $c = \sqrt{E_o/6}$, based on a balance of surface tension and buoyancy forces, where E_o is the Eötvos number. The thinning rates found also match theoretical estimates based on a pair of parallel discs or on the film between a rigid sphere and a free-surface. They also observed that the presence of

surfactants markedly reduced the thinning rates.

Hahn, Chen and Slattery (1985) used a lubrication theory approximation including the effects of London-van der Waals forces to model the draining of a film above a bubble. In this way they were able to obtain estimates for the rupture time, taken as the time for the rim thickness to become zero. However, they mentioned that the geometry used, which prevents any asymmetric instabilities, and the assumption that there is no tangential motion on the surfaces due to the presence of surfactants, means that the model gives only an upper bound for the rupture time. Electrostatic repulsion was also neglected.

The effect of the approach speed of a bubble towards a free-surface was investigated by Kirkpatrick and Lockett (1974). They found that for larger velocities (above about $1cm/sec$ for $2.5mm$ radius bubbles in water), the thinning process does not have time to complete before the bubble is decelerated to rest by surface tension, which may then push it back into the fluid. In contrast, a bubble that is released just below the surface and so does not have time to accelerate to its terminal velocity is found to burst almost immediately, without bouncing. A simple mathematical model, based on the fact that the rate of thinning is inversely related to the area of the film was developed, leading to the same general conclusion. Minor impurities in the water were found to be insignificant, but with a larger amount of surfactant (0.6 molar sodium chloride) the coalescence times became longer, with little to distinguish between low and high approach velocities.

A film is said to be unstable (Scheludko, 1962), if there is some critical thickness at which point small perturbations on the surface will grow causing a hole to appear (Vrij, 1966) which, provided that it is big enough (Taylor and Michael, 1973), then expands due to surface tension, thus rupturing the film. One of the earliest investigations of film rupturing was by Lord Rayleigh (1891), who applied high-speed photography to view the bursting of soap films. Newitt et al (1954) show a photograph which exhibits clearly the breakup of a liquid film into a 'lace-like' structure of liquid threads, each of which breaks up into a number of tiny droplets. The fluid in the film gathers up into a toroidal rim

which often breaks irregularly into a number of threads (Rayleigh, 1891; Ranz, 1959) which then break into more tiny droplets. This rim itself is expanding too rapidly to be broken up by capillary ripples, as in the case of the jet (MacIntyre, 1972). Instead, this breakup is due to the effects of variations of surface tension and film thickness and, in the case of bubble burst, this is coupled with the effect of turbulence from the escaping air. The droplets formed in the film are much smaller than the jet drops mentioned below (Newitt et al, 1954; Garner et al 1954) and are projected sideways by the expansion of the bursting film and upwards by the rush of gas as the pressure in the bubble is released. Droplet speeds may be as high as $10m\,s^{-1}$ (Resch et al, 1986). By exploiting a simple energy balance argument, Culick (1960) showed that the speed of the retreat of the film is given approximately by $v = \sqrt{2\sigma/h\rho}$ where h is the film thickness, usually just a few microns. By comparing the portion of the energy used in the inelastic acceleration of fluid entering the rim with the viscous energy dissipation, he showed that the length of fluid being accelerated is about $h\mu v/\sigma$, which is typically of the order of the film thickness.

The subsequent bubble bursting motion which takes place on a longer time-scale — a few milliseconds as opposed to times of the order of $100\mu s$ for the film rupture (Resch et al, 1986) — is better suited to study by high-speed photographic methods. After film rupture, what remains of the toroidal film rim was observed by MacIntyre (1972) to follow a ripple down the sides of the bubble. This flow converges at the base of the bubble and a high-speed jet is thrown upwards. By using dyes in the fluid, it was shown by MacIntyre that the liquid in the jet originates in a thin layer surrounding the bubble crater. Very little mixing of the dye with surrounding fluid during jet formation indicated that the flow at the base of the jet is irrotational. MacIntyre was also able to observe the corresponding downward jet of fluid that must occur on grounds of momentum conservation by its effect of propelling tiny bubbles into the fluid beneath the bursting bubble. Kientzler et al (1954) also show clear pictures of the complete bursting process from immediately after the film rupture up to and including the formation and breakup of the high-speed liquid

jet.

The fact that a narrow jet breaks up into a number of drops is well known. Rayleigh (1878), by considering the change in surface area of a jet subjected to a symmetric disturbance, showed it to be stable provided that the wavelength of the perturbation is shorter than the circumference of the jet. The most destructive mode was shown to have wavelength $\lambda \approx 4.508 \times 2a$ where a is the jet radius.

The evidence above relating to the origin of the material in the jet is significant in the study of cell damage by bubbles, since it has been reported by Blanchard and Syzdek (1972) that bacteria tend to become adsorbed onto bubble surfaces. Similar results have been found for insect cells by Bavarian, Fan and Chalmers (1991). This was followed up by Chalmers and Bavarian (1991) who claimed that the hydrodynamic forces due to the shear in the boundary layer around the walls of the bubble cavity are sufficiently large to kill cells. They also postulated a second mechanism based on Culick's (1960) finding of the small length of fluid accelerating as the rupturing film recedes. Cells may be struck by the advancing toroidal rim as they sit on a stationary part of the bursting lamella. Experiments by Kowalski (1991) also highlight this as a likely cause of cell damage.

5.1.3 Aims.

The primary aim of this chapter is to produce a numerical model of a bursting bubble, which agrees with the experimental results indicated above. In particular, the model should predict the high-speed liquid jet, together with the corresponding downward jet. Calculations can then be made of the stresses imposed on a particle in the vicinity of a bursting bubble. The effects of viscosity, leading to a boundary layer and high shear rates, are also of interest as they may further increase the damaging potential of the burst. An estimate of the contribution to the stress on a cell due to shear in the downward jet region is also sought. Such information may provide useful evidence for or against particular proposed cell damage mechanisms.

We do not address a numerical study of the film rupturing process itself, nor do we

discuss here the stresses on a particle resting on the film as it breaks: this will be left for the future. We will use the term 'burst' to refer to the events that occur after the completion of the film rupturing process. Although we neglect the dynamics of the film rupture it is important to consider the effect that the film has on the position of a bubble at a free-surface. Since it is clear that the burst will be driven by the potential energy stored in the initial bubble configuration, both in terms of surface energy and buoyancy, the starting shape and height of the bubble with respect to the free-surface is critical in determining the consequent flow.

5.2 Problem statement.

5.2.1 Inviscid formulation.

The photographic evidence of Kientzler et al (1954) indicates that Reynolds numbers for a bubble bursting, from the time just after film rupture to the rise of the jet, are of the order of 1000. We may therefore assume that, up until the formation of the jet, any vorticity is limited to thin boundary layers around the air/water interfaces, so that the velocity distribution may be reasonably represented by potential flow, $\boldsymbol{u} = \nabla\phi$. Again, as we are only interested in bubbles in close proximity to the free-surface, we assume that any rising bubbles remain of fixed volume.

The solution domain, Ω_- (see figure 5.1), is defined to be the semi-infinite region bounded above by the free-surface, C_0, and internally by the bubbles C_m, $(m = 1, \ldots, M)$. The free-surface coincides with the (x, y)-plane at infinity.

Formally, this problem is a simple extension of that in section 4.3 with a free-surface included. Here bubble m is situated on the $z-$axis at a distance $\gamma_m (> 0)$ below C_0. As the bursting phenomenon is dominated by surface tension forces, especially for the smaller bubbles, we scale times with respect to $(\rho a^3/\sigma)^{1/2}$ and pressures by the factor σ/a, σ being the surface tension and a the radius of bubble 1.

The code was written to allow bubbles to either rise up to an initially flat free-surface

and burst as they reach it, or so that a bubble will have just burst at $t = 0^-$, when the calculation is started. The latter option allows us to include more physical reality into the problem without worrying too much about surface drainage. The method for finding the initial surface shape in this case is discussed in section 5.2.2.

The Eötvos number, $E_o = 4\rho g a^2/\sigma$, again enters as an explicit parameter in the boundary conditions. It measures the bubble size and represents the square of the ratio of the two time-scales associated with the collapse, due to surface tension, of a spherical cavity whose contents remain fixed at the ambient pressure of the fluid and with the rise of a bubble due to gravity. During bubble burst, this parameter therefore measures the relative importance of bubble rise and bubble collapse. For the smallest bubbles, the effect of buoyancy will clearly be secondary to surface tension forces.
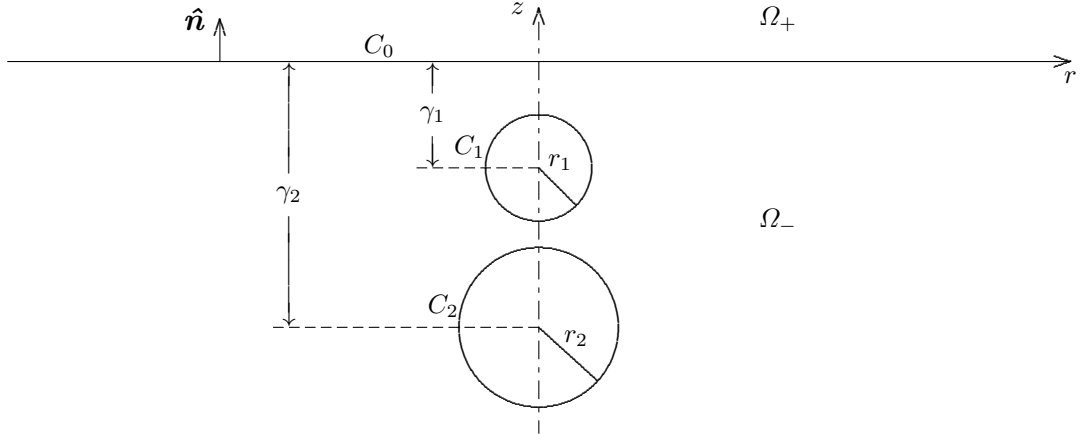

Figure 5.1. The initial position of bubbles C_1 and C_2 below the free-surface, C_0. In most calculations presented, the free-surface is not flat as depicted, but takes the shape of a bubble for which the film cap has just ruptured, together with a meniscus extending to infinity (see also figure 5.2).

If we again define

$$f\Big|_{C_m} = \phi\Big|_{C_m} + k_m,$$

(5.2.1)

with k_m given by (4.3.5) for $m = 0, \ldots, M$ (note that $k_0 = 0$ for all times), the dynamic condition for updating f on the boundaries is

$$\frac{Df}{Dt}\Big|_{C_m} = \frac{1}{2}|\boldsymbol{u}|^2 - \frac{E_o}{4}(z + \gamma_m) + \kappa - \kappa_m, \quad m = 0, \ldots, M.$$

(5.2.2)

We again use the constraint equations (4.3.8) to fix the bubble volumes as they rise.

5.2.2 Initial configuration.

Certain questions have to be addressed in order to produce a good model of the bursting process. As the film above the bubble will be very thin, we assume for the purposes of this chapter that the film itself will have no significant effect on the subsequent motion. The rupture of the film may have dire consequences for cells adsorbed onto the upper surface of the bubble, but this is neglected in this investigation.

If we can ignore the film, then when a bubble is 'burst' numerically, a decision still has to be made as to the amount of film above the bubble to remove before reconnecting the bubble cavity to the free-surface. This will invariably be greater than the total amount of fluid in an actual film because of the difficulty in calculating the bubble and surface motion with the bubble much closer to the surface than the length of a single boundary integral element (see §5.3). However, numerical experimentation has shown that, provided not too much fluid above the bubble is thrown away, this has little effect on the subsequent bursting motion. It would, in any case, be inappropriate to assume that the irrotational model can accurately predict the fluid flow in the film when it becomes thin. In the case where surfactants are present various physico-chemical phenomena such as surface viscosity may become important so that stress-free interfacial boundary conditions become invalid. It is thus hard to see how the rupture time can be determined based on the calculated thickness of the film other than by matching a modified lubrication layer for the film onto the inviscid model. The rupture-time calculations of Hahn et al (1985) are likewise difficult to implement, firstly because they are inaccurate as indicated in section 5.1.2, but also because of the problem of identifying with any certainty their initial time, when the draining rate of the film above the bubble is independent of radial position. It is suggested, however, that this time will be close to the time that the bubble comes to rest at the surface.

It seems clear, that one of the most important factors determining the motion following

film rupture, in terms of the energy released, is the height of the top of the bubble above the equilibrium free-surface position. The experimental study of Kirkpatrick and Lockett (1974) indicates that bubbles moving at speeds approaching terminal velocity, upon reaching the free-surface, tend to bounce a couple of times before bursting. It has also been observed (see for example Newitt et al 1954 or Allan et al, 1961) that a bubble may rest for a short time at the free-surface before bursting. In any case, we assume that the thinning of the film and the instabilities which eventually rupture it when it reaches a critical thickness are to some extent asynchronous with the bouncing of the bubble and that, on average, a bubble will burst at its static equilibrium position when the buoyancy force is equal to the downward component of surface tension. For a spherical bubble in a pure liquid, the non-dimensional height above the surface of the top of the bubble is approximately

$$h = 1 - \sqrt{1 - E_o/6}. \tag{5.2.3}$$

This is equivalent to the formula given by Allan et al (1961) for the radius of the rim of intersection of the free-surface and the bubble, in terms of the bubble radius. Here, we use a pressure balance to find the equilibrium bubble and meniscus shapes, employing equation (5.2.3) as a first approximation. If σ_{ij} are the surface tensions of the interfaces (i,j), (see figure 5.2) then force balances in the r and z directions give us respectively,

$$\sigma_{13} \cos \theta_c = \sigma_{12} \cos \phi_c + \sigma_{23} \cos \psi_c - \frac{K}{r_c} \tag{5.2.4}$$

and

$$\sigma_{13} \sin \theta_c = \sigma_{12} \sin \phi_c + \sigma_{23} \sin \psi_c, \tag{5.2.5}$$

where K is the line tension from the intersection of the three interfaces. A subscript c denotes evaluation at this contact line. In general, the value of K depends on the geometric configuration of the interfaces as well as the physical properties of the fluids (see Ivanov, Kralchevsky and Nikolov, 1986).
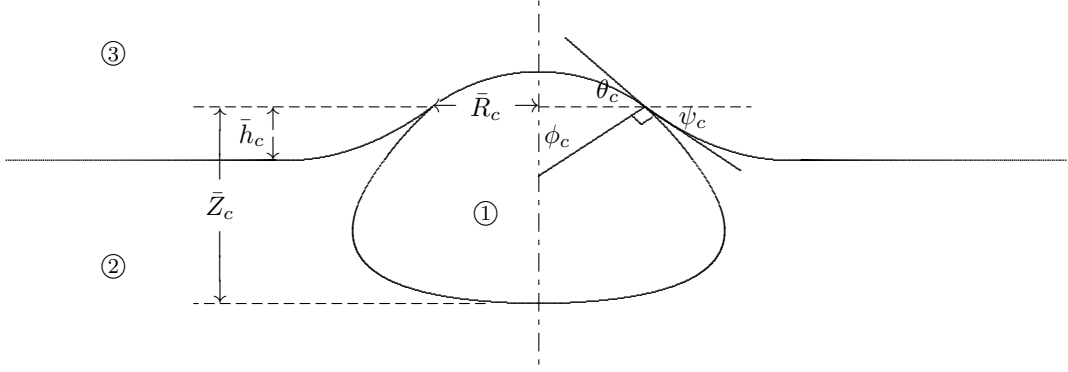
Figure 5.2. Schematic diagram of a bubble at a free-surface in the initial static equilibrium position just prior to film rupture.

It is convenient at this point to follow Ivanov et al (1986) and rescale lengths with respect to the mean radius of curvature, b, of the lowest point of the bubble. Correspondingly scaled quantities will be indicated by an overbar. We also introduce the quantity $\beta = \rho g b^2 / \sigma$ (similar to the Eötvos number, E_o), where $\sigma = \sigma_{12} = \sigma_{23}$. If we write $\bar{\tau} = \sigma_{13}/\sigma$ and $\bar{K} = K/b\sigma$, the experimental evidence of Ivanov et al (1986) suggests that

$$|\bar{\tau} - 2| \ll 1, \quad \text{and} \quad |\bar{K}| \ll 1. \tag{5.2.6}$$

As angles θ_c, ϕ_c and ψ_c must be acute, (5.2.4) and (5.2.5) give approximate solutions, $\theta_c = (\phi_c + \psi_c)/2$ and $\phi_c = \psi_c$, namely $\theta_c = \phi_c = \psi_c$.

Let $(\bar{R}, \bar{Z})$ be the rectangular coordinates of a point in a half-plane containing the axis of symmetry, centred on the lowest point of the bubble crater. A simple consideration of the pressure jump across the interface $(1, 2)$ shows that the shape of the bubble cavity is described by the differential system

$$\frac{d\bar{R}}{d\phi} = \frac{\bar{R} \cos \phi}{(2 + \beta \bar{Z})\bar{R} - \sin \phi}, \tag{5.2.7}$$

$$\frac{d\bar{Z}}{d\phi} = -\tan \phi \frac{d\bar{R}}{d\phi}, \tag{5.2.8}$$

with boundary conditions

$$\bar{R} = \bar{Z} = 0, \quad \text{at} \quad \phi = \pi. \tag{5.2.9}$$

We denote the values of $\bar{R}$ and $\bar{Z}$ at $\phi = \phi_c$ by $\bar{Z}_c$ and $\bar{R}_c$ respectively.

Similarly, the meniscus (interface $(2,3)$) has shape $\bar{z} = \bar{h}(\bar{r})$ which is governed by the second-order equation

$$\bar{h}'' = \left(-\frac{\bar{h}'}{r} + \beta\bar{h}(1 + \bar{h}'^2)^{1/2}\right)(1 + \bar{h}'^2), \tag{5.2.10}$$

with the two-point boundary conditions

$$\bar{h}'(\bar{R}_c) = -\tan\psi_c, \quad \text{and} \quad \bar{h}(\infty) = 0. \tag{5.2.11}$$

Aymptotic solutions for both the bubble cavity and meniscus shapes exist for small values of β and $\bar{R}_c$ respectively (see Ivanov et al, 1986 and Lo, 1983). However, for larger bubbles these expressions are less accurate and so a numerical solution is used here.

The system given by (5.2.10) and (5.2.11) can be solved using a technique similar to that of Princen (1963), by choosing a value for $\bar{h}_c \equiv \bar{h}(\bar{R}_c)$ and performing a simple bisection search depending on whether the solution tends to infinity or dips below the $z = 0$ plane. It is not possible for the interface shape in static equilibrium to have a maximum above or a minimum below the (x, y)-plane: the curvature at such a stationary point would be inconsistent with the hydrostatic pressure difference. Since the meniscus meets the bubble at $\bar{r} = \bar{R}_c$, we have that the bubble position in the fluid is given by

$$\bar{z} = \bar{Z}(\phi) + \bar{h}_c - \bar{Z}_c. \tag{5.2.12}$$

We further assume the film separating the bubble from the atmosphere to be very thin and thus gravity forces negligible compared to the effect of pressure so that the film may be taken to be spherical with radius $\bar{c}$. Using this to equate the pressure in the bubble given in terms of the pressure jump across the spherical film, with that given by the hydrostatic pressure at the bottom plus a corresponding jump due to surface tension there, gives

$$\frac{4}{\bar{c}} = 2 + \beta(\bar{Z}_c - \bar{h}_c). \tag{5.2.13}$$

Since the dome is spherical, $\bar{R}_c = \bar{c}\sin\theta_c$ and, bearing in mind that the critical angles are assumed equal, (5.2.13) can be written as

$$\bar{R}_c\left(1 + \frac{\beta}{2}(\bar{Z}_c - \bar{h}_c)\right) = 2\sin\phi_c. \tag{5.2.14}$$

$$-\ 107\ -$$

Equation (5.2.14) fixes the height of the bubble in the fluid, but we also need an equation to set the volume. The volume of the bubble with the new scalings is

$$\bar{V} = 4\pi(E_o/4\beta)^{3/2}/3. \tag{5.2.15}$$

Note that the volume, $\bar{V}$, is calculated by adding the volume for the region of the bubble below the ring of intersection, $\bar{V}_{12}$, which can be found numerically, to the volume of the spherical dome with radius given by equation (5.2.13), thus

$$\bar{V} = \bar{V}_{12} + \pi\left[\frac{2}{3}\left(\bar{c}^3 - (\bar{c}^2 - \bar{R}_c^2)^{3/2}\right) - \bar{R}_c^2(\bar{c}^2 - \bar{R}_c^2)^{1/2}\right]. \tag{5.2.16}$$

The solution method is to firstly select an approximation for the unknown variables, ϕ_c and β. These are given by the assumption that the bubble is almost spherical, radius a with the top a non-dimensional height above the free-surface given by (5.2.3), so that

$$\bar{R}_c^{(0)} = \sqrt{E_o/6}, \tag{5.2.17}$$

thus

$$\phi_c^{(0)} = \arcsin(\bar{R}_c^{(0)}), \tag{5.2.18}$$

and

$$\beta^{(0)} = E_o/4. \tag{5.2.19}$$

For this initial approximation, we must restrict E_o to be less than 6, which imposes a maximum on the bubble radius of about $0.34cm$. Newton iteration is used to calculate the values of ϕ_c and β subject to the equations (5.2.14) and (5.2.15) with $\bar{V}$ given by (5.2.16).

An alternative bursting mechanism which will work well only for small bubbles, but that illustrates the importance of a physically realistic bursting procedure for larger bubbles can be used for bubbles that have been followed numerically from a distance below the free-surface. This is to simply burst the bubble when its uppermost nodes become closer to the free-surface than some critical distance. Any points on the bursting bubble or free-surface closer together than some other prescribed distance are removed. The remains of the bubble and free-surface are then re-joined to form an indented free-surface.

We assume that the burst takes place in an instant, so that the potentials on the other parts of the bubble are unaffected. Note, however, that when the mth bubble bursts the constant, k_m, must be subtracted from the potentials on that bubble before re-connecting it to the free-surface. To smooth the new surface slightly at the join, a new node is added at the midpoint of the first nodes removed from the old surfaces and the potential at this node is simply taken as the average of the potentials at the old two nodes. The calculation is then allowed to continue. This method of bursting can be anticipated to result in a significant overestimate of the energy release when a large bubble bursts, as shown below.

5.3 Solution by boundary integral method.

The solution method relies on writing Laplace's equation for the potential, ϕ, in the form of an integral equation, which can be solved in a discrete form. Define the surfaces $\partial\Omega$, the boundary of Ω_-, and $C = C_0(R) \cup \tilde{C}_0(R) \cup C_1 \cup \cdots \cup C_M$, where $\tilde{C}_0(R)$ is a spherical arc of radius R, centred at a point $\boldsymbol{x}^\star \in \Omega_- \setminus \partial\Omega$, and take $C_0(R)$ to be the finite portion of C_0 extending as far as $\tilde{C}_0(R)$, in such a way that $\tilde{C}_0(R) \cup C_0(R)$ encloses all of the C_m, $(m = 1, \ldots, M)$. If we now chose a point $\boldsymbol{x}$ on $\partial\Omega$, we may use Green's integral formula written in the form

$$\phi(\boldsymbol{x}^\star) - \phi(\boldsymbol{x}) = \int_C \left(G(\boldsymbol{x}^\star, \boldsymbol{x}') \frac{\partial\phi}{\partial n}(\boldsymbol{x}') - (\phi(\boldsymbol{x}') - \phi(\boldsymbol{x})) \frac{\partial G}{\partial n'}(\boldsymbol{x}^\star, \boldsymbol{x}') \right) dS', \qquad (5.3.1)$$

where

$$G(\boldsymbol{x}^\star, \boldsymbol{x}') = \frac{1}{4\pi|\boldsymbol{x}^\star - \boldsymbol{x}'|}, \qquad (5.3.2)$$

is the fundamental solution of the three-dimensional Laplace equation. As the fluid is at rest at infinity, we assert that $\phi(\boldsymbol{x}) \to 0$ as $|\boldsymbol{x}| \to \infty$ and so for $\boldsymbol{x}' \in \tilde{C}_0(R)$, $dS = O(R^2)$, $\phi = O(1/R)$ and $\partial\phi/\partial n = O(1/R^2)$ as $R \to \infty$. It is clear that the integral over $\tilde{C}_0(R)$ (with the exception of the term in $\phi(\boldsymbol{x})$ which approaches the value $-\phi(\boldsymbol{x})/2$) behaves as $1/R$ and so vanishes when we take the limit $R \to \infty$. We also take the limit $\boldsymbol{x}^\star \to \boldsymbol{x}$, which is trivially done, due to the regularity of the integral. As the principal value integral of the

remaining term in $\phi(\boldsymbol{x})$ is now zero,

$$\frac{1}{2}\phi(\boldsymbol{x}) = \int_{\partial\Omega}\left(G(\boldsymbol{x},\boldsymbol{x}')\frac{\partial\phi}{\partial n}(\boldsymbol{x}') - \phi(\boldsymbol{x}')\frac{\partial G}{\partial n'}(\boldsymbol{x},\boldsymbol{x}')\right)dS', \quad \boldsymbol{x}\in\partial\Omega. \qquad (5.3.3)$$

Finally, substituting f for ϕ as in (5.2.1) and using the fact that $k_0(t) \equiv 0$, gives the expression

$$\frac{1}{2}f(\boldsymbol{x}) = k_m + \int_{\partial\Omega}\left(G(\boldsymbol{x},\boldsymbol{x}')\frac{\partial\phi}{\partial n}(\boldsymbol{x}') - f(\boldsymbol{x}')\frac{\partial G}{\partial n'}(\boldsymbol{x},\boldsymbol{x}')\right)dS', \quad \boldsymbol{x}\in C_m, \quad m=0,\dots,M. \quad (5.3.4)$$

The integral equation (5.3.4) is in a form suitable for use in the program described below which is a modified version of the code of Best and Kucera (1992), which was originally designed for cavitation and explosion bubbles in an infinite fluid.

Initially, nodes are equally spaced by arc length on the bubbles, but on the free-surface, they are placed on the portion $0 \leq r \leq R_{max}$ of B_0, for some large R_{max}, with the non-linear distribution

$$r_0i = \frac{iR_{max}}{2N_0}\left(1 + (i - N_0 - 1)^{-2}\right), \quad i = 0,\dots,N_0, \qquad (5.3.5)$$

so that points are distributed more densely near the axis, where resolution is particularly important. Subsequently, R_{max} is allowed to alter dynamically with the position of the end node on the free-surface, namely $R_{max}(t) = r_{0N_0}$. Similarly we define $Z_{max}(t) = z_{0N_0}$ and $F_{max}(t) = f_{0N_0}$.

In order to evaluate the integral over the infinite free-surface, an approximate expression is required for the quantities in the integrand of (5.3.4). The motion of a bursting bubble may be thought of as a superposition of harmonic modes of which the spherically symmetric mode, corresponding to the isotropic collapse of a cavity due to surface tension may be represented by a potential sink. The potential may therefore be expected to contain a term $-\dot{R}R^2/r$, with the cavity radius, $R(t)$, governed by a differential equation similar to the Rayleigh equation for spherical cavitation bubbles, but driven by surface tension rather than a constant pressure difference. A consideration of the linearised boundary conditions for large r indicates that at $z = 0$, $\partial^2\phi/\partial t^2 \sim -\partial\phi/\partial z$. This condition is not

satisfied by the source or sink alone but is satisfied by a potential that falls off as r^{-3}. Indeed, the solution to the linearised free-surface response to a sink contains a source of equal strength as an image in the free-surface, thus resulting in a dipole far field. For a source of strength $m(t)$ at $\boldsymbol{r} = \boldsymbol{x} = (0, 0, -h)$, using methods similar to those in section 3.3, it can be shown that the potential in this case, in the absence of surface tension, is given by

$$\phi(\boldsymbol{r}) = m(t) \left\{ \frac{1}{|\boldsymbol{r} - \boldsymbol{x}|} - \frac{1}{|\boldsymbol{r} - \boldsymbol{x}'|} \right\} + 2 \int_0^\infty e^{\xi(z-h)} J_0(\xi r) \int_0^t m(\tau) \xi^{1/2} \sin[\xi^{1/2}(t - \tau)] d\tau d\xi,$$

where $\boldsymbol{x}' = (0, 0, h)$ is the position of the image singularity and J_0 is a zeroth order Bessel function. As the source strength in the integrand, $m(t)$, is bounded on the interval $(0, t)$, we can expand the integrand of the time integral in a power series and interchange the order of integration and summation. Upon using the fact that the zeroth order Hankel transform, with respect to r, of a unit source at the origin is $\xi^{-1} e^{\xi z}$ for $z \leq 0$, and differentiating repeatedly with respect to z, we can write the potential in the form (see for example Stoker, 1957, p190)

$$\phi(\boldsymbol{r}) = m(t) \left\{ \frac{1}{|\boldsymbol{r} - \boldsymbol{x}|} - \frac{1}{|\boldsymbol{r} - \boldsymbol{x}'|} \right\} + 2 \sum_{i=1}^\infty \left\{ \frac{\partial^i}{\partial z^i} \left(\frac{1}{|\boldsymbol{r} - \boldsymbol{x}'|} \right) \int_0^t m(\tau) (-1)^{i-1} \frac{(t - \tau)^{2i-1}}{(2i - 1)!} d\tau \right\}.$$

Hence at the free-surface, the dipole term of the summed quantity dominates the potential so that $\phi \sim r^{-3}$ as $r \to \infty$. The assumption of a dipolar far field is also consistent with the fully non-linear boundary conditions and implies that the free-surface elevation is also of order r^{-3} for large r. Thus for the purposes of the numerical computations, we write for $r \geq R_{max}$

$$f_0(r) = F_{max} \left(\frac{R_{max}}{r} \right)^3 \quad \text{and} \quad z_0(r) = Z_{max} \left(\frac{R_{max}}{r} \right)^3. \tag{5.3.6}$$

A similar asymptotic technique was used in the boundary integral method of Oguz and Prosperetti (1989), to calculate the motion of the contact line between a drop and a free-surface.

As described in Chapter 4, cubic splines are used to interpolate the surface nodes. Since the spline for the free-surface only reaches as far as $r = R_{max}$, the end conditions

there are

$$\frac{\partial z_0}{\partial s} = \frac{-3z/r}{(1 + (3z/r)^2)^{1/2}}, \quad \frac{\partial r_0}{\partial s} = \left(1 + (3z/r)^2\right)^{-1/2} \quad \text{and} \quad \frac{\partial f_0}{\partial s} = \frac{-3f/r}{(1 + (3z/r)^2)^{1/2}}, \qquad (5.3.7)$$

thus ensuring continuity of first derivative with the analytic portion of the free-surface. The corresponding asymptotic form for the normal derivative of the potential, for large r is also r^{-3}, thus we assume

$$\psi_0(r) = \Psi_{max} \left(\frac{R_{max}}{r}\right)^3, \qquad (5.3.8)$$

for $r \geq R_{max}$, where $\Psi_{max} = \psi_{0N_0}$.

5.4 Viscous effects.

5.4.1 Boundary layer approximation.

As mentioned in section 5.1, it has been proposed that a possible cause of cell damage is high shear stresses in the boundary layer of a bursting bubble. Independent calculations by Chalmers (1992) suggest that the shear stresses occurring in the downward jet, particularly for small bubbles, may be large enough to cause cell damage. It is therefore of interest to calculate the vorticity development in the downward jet region to try and ascertain the magnitude of stresses there. It is also important to gain information as to the effect of viscosity on the interface motion, particularly on the development of the jet where high rates of strain are expected.

There have been a number of studies where weak viscous effects have been included into otherwise inviscid boundary integral formulations. Miksis, Vanden-Broek and Keller (1982) included a modified boundary condition into calculations of the steady state shape of a rising bubble (see Chapter 4). Their modification took into account only the change in the normal stress at the surface due to viscosity, and ignored the pressure drop across the boundary layer itself which, as they noted, becomes particularly important on the lower part of the bubble.

This was taken a stage further by Lundgren and Mansour (1988), where an analysis of the boundary layer equations resulted in expressions for the pressure difference and normal

component of the velocity perturbation due to the viscous layer. For completeness, we indicate the method of Lundgren and Mansour and then describe a way in which this can be extended so that the tangential component of the boundary layer velocity can be obtained. With this information it is possible to identify approximate initial conditions for the vorticity distribution as the jet is about to form and thus gain greater understanding of the flow in the downward jet.

Lundgren and Mansour's method (referred to as LM) is as follows. The velocity field is written in the form $\boldsymbol{v} = \boldsymbol{u} + \boldsymbol{U}$, where $\boldsymbol{u} = \nabla \phi$ is the usual potential flow field and $\boldsymbol{U} = \nabla \times \boldsymbol{A}$ is the rotational flow. For uniqueness, $\boldsymbol{A}$ is taken to be zero outside the boundary layer. Since the flow is axisymmetric, $\boldsymbol{A} = A\hat{\underset{\sim}{\theta}}$. Likewise, the total pressure may be written as $p^\star = p + P$, where P is the perturbation in pressure due to the boundary layer. The viscous boundary conditions are the usual ones for a free-surface. Firstly, a balance of normal stress on either side of all interfaces is required:

$$-p_m(t) + \kappa = -p^\star + 2Re^{-1}\hat{\boldsymbol{n}} \cdot \nabla \boldsymbol{v} \cdot \hat{\boldsymbol{n}}, \quad m = 0, \dots, M. \tag{5.4.1}$$

Secondly, due to the relatively low dynamic viscosity of the air, there should be no tangential stress at the surfaces:

$$\hat{\boldsymbol{t}} \cdot \nabla \boldsymbol{v} \cdot \hat{\boldsymbol{n}} + \hat{\boldsymbol{n}} \cdot \nabla \boldsymbol{v} \cdot \hat{\boldsymbol{t}} = 0. \tag{5.4.2}$$

Here, $\hat{\boldsymbol{t}}$ and $\hat{\boldsymbol{n}}$ are the tangent and normal to the generator of the axisymmetric bubble. The Reynolds number, Re, is given by $(\sigma a/\rho \nu^2)^{1/2}$.

On assuming that the boundary layer is thin, with thickness δ, and that the variation along a surface is of order unity, LM use the zero tangential stress condition (5.4.2) to make the approximation

$$\frac{\partial U_t}{\partial n} = -2\hat{\boldsymbol{t}} \cdot \nabla \boldsymbol{u} \cdot \hat{\boldsymbol{n}} + O(\delta^2), \tag{5.4.3}$$

which shows that $U_t = O(\delta)$ with $A = O(\delta^2)$ and from mass conservation $U_n = O(\delta^2)$. Here, subscripts n and t refer to normal and tangential components of a local curvilinear coordinate system fitted to the instantaneous interface shape. A consideration of the normal

and tangential components of the Navier-Stokes equations shows that for viscous terms to be retained, the boundary layer thickness must be related to the Reynolds number by $\delta = Re^{-1/2}$. Upon neglecting variations of P across the boundary layer, LM are able to integrate the tangential equation across it and produce an equation for the development of A at the surface. Likewise the normal equation is integrated across the boundary layer to give an expression for P at a surface, in terms of A and the irrotational velocity, $\boldsymbol{u}$. Before giving these expressions it is convenient, for brevity, to introduce the notation:

$$\frac{D\{\boldsymbol{w}\}h}{Dt} \equiv \frac{\partial h}{\partial t} + \boldsymbol{w} \cdot \nabla h. \tag{5.4.4}$$

This is a generalisation of the usual material derivative, where the rate-of-change of a function of the flow field is taken following points that move with a velocity $\boldsymbol{w}$. This notation will prove useful when we consider the calculation of the tangential velocity due to the boundary layer, but is appropriate here. The final boundary conditions found by LM give, in the context of the bubble bursting problem,

$$\frac{D\{\boldsymbol{u} + U_n \hat{\boldsymbol{n}}\}A}{Dt} = -A\left(2\frac{\partial u_t}{\partial s} - 2\kappa^{(t)}u_n + \frac{\boldsymbol{u} \cdot \hat{\boldsymbol{r}}}{r}\right) + 2Re^{-1}\left(\frac{\partial u_n}{\partial s} + \kappa^{(t)}u_t\right) + O(\delta^3), \tag{5.4.5}$$

where $U_n = (\partial(rA)/\partial s)/r$ and $\kappa^{(t)}$ is the curvature of the interface in a plane through the axis of symmetry. For the potential,

$$\begin{aligned}\frac{D\{\boldsymbol{u} + U_n \hat{\boldsymbol{n}}\}\phi}{Dt} =& \frac{1}{2}|(\boldsymbol{u} + U_n \hat{\boldsymbol{n}})|^2 + p_m(0) - p_m(t) - \frac{E_o}{4}(z + \gamma_m) + \kappa - \kappa_m \\ &+ 2A\left(\frac{\partial u_n}{\partial s} + \kappa^{(t)}u_t\right) + 2Re^{-1}\left(\frac{\partial u_t}{\partial s} - \kappa^{(t)}u_n + \frac{\boldsymbol{u} \cdot \hat{\boldsymbol{r}}}{r}\right) + O(\delta^3).\end{aligned} \tag{5.4.6}$$

The modification to the pressure is likewise given by

$$P = 2A\hat{\boldsymbol{t}} \cdot \nabla \boldsymbol{u} \cdot \hat{\boldsymbol{n}} + O(\delta^3). \tag{5.4.7}$$

The model of LM is insufficient if we wish to go on to approximate the flow field after the boundary layer separates from the bubble cavity as the jet is about to form, since it does not include a scheme for calculating the total tangential velocities in the layer: the contribution to the tangential velocities is an order of magnitude higher than to

the normal velocities. To do this, we solve a partial differential equation based on the tangential component of the boundary layer equation (LM's equation (4.18) with a total Lagrangian derivative),

$$\frac{dU_t}{dt} + U_t \hat{\boldsymbol{t}} \cdot \nabla \boldsymbol{u} \cdot \hat{\boldsymbol{t}} = Re^{-1} \frac{\partial^2 U_t}{\partial n^2} + O(\delta^2), \tag{5.4.8}$$

subject to the boundary conditions (5.4.3) at the surface and $U_t \to 0$ outside the thin boundary layer.

Equation (5.4.8) can be solved using a finite difference scheme, by fitting a grid of points to the boundary layer region. If we wish to continue to use the model of LM and the boundary integral scheme, it is possible to use (5.4.8) as an equation for the Lagrangian evolution of particles moving through the fluid in the viscous layer. As the problem is inherently unsteady, these grid points will move in relation to one another and thus it will be difficult to keep track of which nodes are closest to each other for the purpose of calculating derivatives. (For a review of techniques for following closest nodes in such problems see for example Boris, 1989). Alternatively, a scheme could be devised whereby points are re-meshed after each time step to keep them on a more convenient grid. However a technique is used here in which the need to re-position at each time step is removed, except when the usual repositioning of surface nodes is performed in the boundary integral scheme. The idea uses the fact that the bubble or free-surface is a stress-free interface, and consequently a material line that is normal to a surface will remain, locally, orthogonal — see appendix C. Since this orthogonality is only local to the point on the surface, we 'linearise' the Lagrangian time derivative by writing

$$\frac{d}{dt} = \frac{D\{\boldsymbol{v}\}}{Dt} = \frac{D\{\boldsymbol{v}_0 - \eta(\hat{\boldsymbol{n}} \cdot \nabla \boldsymbol{v})|_0\}}{Dt} + (\boldsymbol{v} - \boldsymbol{v}_0 + \eta(\hat{\boldsymbol{n}} \cdot \nabla \boldsymbol{v})|_0) \cdot \nabla, \tag{5.4.9}$$

where η is the normal distance from a point to the surface and the subscript 0 denotes evaluation at the surface. It is clear from (5.4.9) that as $\eta \to 0$ the approximate Lagrangian derivative — following points moving at velocities $\boldsymbol{v}^\star \equiv \boldsymbol{v}_0 - \eta(\hat{\boldsymbol{n}} \cdot \nabla \boldsymbol{v})|_0$ — becomes exact. Writing (5.4.8) in terms of this derivative gives us

$$\frac{D\{\boldsymbol{v}^\star\}U_t}{Dt} = Re^{-1} \frac{\partial^2 U_t}{\partial n^2} - U_t \hat{\boldsymbol{t}} \cdot \nabla \boldsymbol{u} \cdot \hat{\boldsymbol{t}} - (\boldsymbol{v} - \boldsymbol{v}_0 + \eta(\hat{\boldsymbol{n}} \cdot \nabla \boldsymbol{v})|_0) \cdot \nabla U_t + O(\delta^2). \tag{5.4.10}$$

The virtue of this approach is that if we follow mesh points which move with velocities given by $\boldsymbol{v}^\star$, then as this is the exact Lagrangian derivative at the surface where the zero tangential stress condition (5.4.2) is applicable, the mesh lines normal to the surface will remain normal at the surface. The linearisation further ensures that these lines remain straight since the transformation mapping the line to its new position a short time later is linear (as $\hat{\boldsymbol{n}} \cdot \nabla \boldsymbol{v}^\star = (\hat{\boldsymbol{n}} \cdot \nabla \boldsymbol{v})|_0$). The advantages over more usual Lagrangian finite difference schemes are that normal derivatives are always simple to evaluate; there is no need to store the position of the mesh points, only their distances from the surface; and, as mentioned above, there is no need to re-position the points other than occasionally as dictated by the underlying boundary integral scheme (see §5.4.2).

The new term on the right-hand side of (5.4.10) as compared with (5.4.8) can be shown to be of order δ^2 in the boundary layer. As we can assume that the potential flow field changes slowly in the boundary layer, we can view the potential flow part of $\boldsymbol{v}^\star$ as the error in the Taylor expansion of $\boldsymbol{u}$ and so if $\eta = O(\delta)$,

$$(\boldsymbol{v} - \boldsymbol{v}_0 + \eta(\hat{\boldsymbol{n}} \cdot \nabla \boldsymbol{v})|_0) \cdot \nabla U_t = (\boldsymbol{U} - \boldsymbol{U}_0 + \eta(\hat{\boldsymbol{n}} \cdot \nabla \boldsymbol{U})|_0) \cdot \nabla U_t + O(\delta^2). \tag{5.4.11}$$

Splitting the remaining velocities into their normal and tangential components, shows the first two terms to be of order δ^2, leaving

$$\eta \left(\left.\frac{\partial U_t}{\partial n}\right|_0 \hat{\boldsymbol{t}} + \left.\frac{\partial U_n}{\partial n}\right|_0 \hat{\boldsymbol{n}} \right) \cdot \nabla U_t + O(\delta^2). \tag{5.4.12}$$

This is of order $\eta\delta$ which is of order δ^2 in the boundary layer. Knowing U_t to order δ is consistent with calculating A to order δ^2 since $U_t \approx \partial A/\partial n$.

The second term on the right of (5.4.10) can also be approximated. Expanding in a Taylor series,

$$\hat{\boldsymbol{t}} \cdot \nabla \boldsymbol{u} \cdot \hat{\boldsymbol{t}} = (\hat{\boldsymbol{t}} \cdot \nabla \boldsymbol{u} \cdot \hat{\boldsymbol{t}})|_0 - \eta \left[\hat{\boldsymbol{n}} \cdot \nabla(\hat{\boldsymbol{t}} \cdot \nabla \boldsymbol{u} \cdot \hat{\boldsymbol{t}}) \right]\Big|_0 + O(\eta^2). \tag{5.4.13}$$

Since this term is multiplied by U_t, the first order correction in (5.4.13) may be ignored in the boundary layer. The final form of (5.4.10) is thus

$$\frac{D\{\boldsymbol{v}^\star\}U_t}{Dt} = Re^{-1}\frac{\partial^2 U_t}{\partial n^2} - U_t(\hat{\boldsymbol{t}} \cdot \nabla \boldsymbol{u} \cdot \hat{\boldsymbol{t}})|_0 + O(\delta^2). \tag{5.4.14}$$

Derivatives of U_t are calculated by fitting quadratics to nodal values along a normal to the surface, with the value on the surface given by (5.4.3) and U_t assumed zero outside the boundary layer. This is then repeated to give the second derivatives.

The rate-of-change of the distance between the surface node and a corresponding mesh node on the normal to the surface is given by the difference in normal velocity between the surface and the mesh point. Thus if we now view η as a parametrisation of a mesh normal to a surface with the linearised time derivative, we see that

$$\frac{\partial \eta}{\partial t} = \eta (\hat{\boldsymbol{n}} \cdot \nabla \boldsymbol{v})\big|_0 . \hat{\boldsymbol{n}}. \tag{5.4.15}$$

Writing the continuity equation for the potential flow in terms of normal and tangential derivatives, gives

$$\frac{\partial u_n}{\partial n} + \frac{\partial u_t}{\partial s} - \kappa^{(t)} u_n + \frac{\boldsymbol{u} \cdot \hat{\boldsymbol{r}}}{r} = 0, \tag{5.4.16}$$

so that (5.4.15) may be written as

$$\frac{\partial \eta}{\partial t} = -\eta \left(\frac{\partial u_t}{\partial s} - \kappa^{(t)} u_n + \frac{\boldsymbol{u} \cdot \hat{\boldsymbol{r}}}{r} \right) \bigg|_0 + O(\delta^2). \tag{5.4.17}$$

Note that as the linearised derivative matches up with the total derivative at the boundary, the evolution of A and of ϕ can be approximated by using equations (5.4.5) and (5.4.6), however (5.4.6) first needs modifying to take account of the tangential component of the derivative by adding a term $U_t \hat{\boldsymbol{t}} \cdot \nabla \phi$ to both sides. This order δ term simply corrects for the additional tangential motion without otherwise affecting the potential distribution on the surface. We write (5.4.6) as

$$\begin{aligned}\frac{D\{\boldsymbol{v}_0\}\phi}{Dt} =& \frac{1}{2}\left(|\boldsymbol{v}_0|^2 - U_t^2\right) + p_m(0) - p_m(t) - \frac{E_o}{4}(z + \gamma_m) + \kappa - \kappa_m \\ &+ 2A\left(\frac{\partial u_n}{\partial s} + \kappa^{(t)} u_t\right) + 2Re^{-1}\left(\frac{\partial u_t}{\partial s} - \kappa^{(t)} u_n + \frac{\boldsymbol{u} \cdot \hat{\boldsymbol{r}}}{r}\right) + O(\delta^3).\end{aligned} \tag{5.4.18}$$

We assume that the fluid starts off stationary so that all perturbation quantities due to the boundary layer are initially zero. For the case of a bubble bursting, we are thus neglecting any vorticity that would have been created in the boundary layer as the bubble rose to the surface.

Certain limiting cases as $r \to 0$ need to be calculated. By symmetry, u_t, $\partial u_n/\partial s$ and $\partial^2 u_t/\partial s^2$ all vanish on the axis. From this it follows that $\boldsymbol{u} \cdot \hat{\boldsymbol{r}}/r \to \hat{\boldsymbol{t}} \cdot \nabla \boldsymbol{u} \cdot \hat{\boldsymbol{t}}$ as $r \to 0$. For motions starting in a perfect state of rest, $A = 0$ on the axis initially and so equation (5.4.5) will ensure that A remains zero there throughout the motion.

Moore (1963), calculated expressions for the boundary layer on a spherical bubble moving through a liquid. He found the boundary layer approximation to be invalid in a region of width $\delta^{1/3}$ near to the rear of the bubble due to separation. Vorticity in this region is confined to a layer of thickness $\delta^{1/3}$ and so viscous forces are no longer as important as inertial forces. Closer still to the axis of symmetry, the layer thickens further to form a wake, where stream surfaces are eventually cylindrical and parallel to the axis. The wake region has width $\delta^{1/2}$ so that again diffusive viscous effects are negligible, with the movement of vorticity being dominated by advection. We shall assume that a similar, thin wake structure also exists in the case of a non-spherical rising bubble or for a bursting bubble until the jet forms. Jet formation will cause vorticity from a larger region near the underside of the bubble cavity to be advected into the downward jet. From a modelling viewpoint we can correct for this thin wake to a certain extent, provided that the spacing between nodes is not too small, by using an appropriate expression for the perturbation to the normal velocity at the node on the axis beneath the bubble. This normal velocity only directly affects adjacent nodes through the arc-length derivatives taken on a cubic spline for A. Indeed, the radial derivative of A which is, apart from a factor of 2, precisely the normal velocity at the end node, is required here in order to fit the cubic spline to A. In order to calculate U_n here, we can use the vertical component of the Navier-Stokes equations. Moore's estimates indicate that inertial terms dominate both viscous and pressure gradient terms, so that we may write

$$
\begin{aligned}
\frac{d}{dt}\left(\frac{\partial A}{\partial s}\right) &= -\frac{\partial A}{\partial s}\frac{\partial^2 \phi}{\partial n^2} + \frac{1}{Re}\frac{\partial^2 U_n}{\partial s^2} \\
&= 2\frac{\partial A}{\partial s}\left(\frac{\partial u_t}{\partial s} - \kappa^{(t)}u_n\right) + \frac{1}{Re}\frac{\partial^2 U_n}{\partial s^2},
\end{aligned}
\tag{5.4.19}
$$

on using (5.4.16). The highest order viscous term is retained in order to start the calcula-

tions off, as at the time the boundary layer calculations commence, all perturbations are assumed zero.

If calculations also include rising bubbles, for a cubic spline to be fitted to A the value of $\partial A/\partial s$ is also required at the top, on the axis of symmetry. Similar to equation (C2), it can be shown that

$$\frac{\partial}{\partial s}\left(\frac{dA}{dt}\right) = \frac{d}{dt}\left(\frac{\partial A}{\partial s}\right) + \frac{\partial A}{\partial s}\frac{d\lambda}{ds}\frac{d}{dt}\left(\frac{ds}{d\lambda}\right). \tag{5.4.20}$$

From (C2) we also obtain

$$\hat{\boldsymbol{t}}\cdot\nabla\boldsymbol{u}\cdot\hat{\boldsymbol{t}} = \frac{d\lambda}{ds}\frac{d}{dt}\left(\frac{ds}{d\lambda}\right) + O(\delta). \tag{5.4.21}$$

Combining (5.4.20), (5.4.21) and (5.4.5) and taking the limit as $s \to 0$, gives an equation for the time evolution of $\partial A/\partial s$ on the axis above a bubble,

$$\frac{d}{dt}\left(\frac{\partial A}{\partial s}\right) = -4\left(\frac{\partial u_t}{\partial s} - \kappa^{(t)}u_n\right)\frac{\partial A}{\partial s} + \frac{2}{Re}\left(\frac{\partial^2 u_n}{\partial s^2} + \kappa^{(t)}\frac{\partial u_t}{\partial s}\right) + O(\delta^2). \tag{5.4.22}$$

The condition on the slope of A at $r = R_{max}$, is found by a consideration of the limiting form of (5.4.5). Making use of (5.3.6) and (5.3.8), we see that $A = O(1/r^4)$ as $r \to \infty$.

When the walls of the bubble cavity start to move inwards immediately before forming the jet, the vorticity created in the thin boundary layer is advected into the bulk of the liquid. The assumption of a thin boundary layer is violated once this separation takes place, causing the boundary layer calculations using the method described above to break down. However, we can follow this advection of vorticity from the boundary layer using the vorticity equation,

$$\frac{D\{\boldsymbol{u}\}\underset{\sim}{\omega}}{Dt} \approx \frac{d\underset{\sim}{\omega}}{dt} = \underset{\sim}{\omega}\cdot\nabla\boldsymbol{v} + Re^{-1}\nabla^2\underset{\sim}{\omega}. \tag{5.4.23}$$

Since $\underset{\sim}{\omega} = \omega\hat{\underset{\sim}{\theta}}$, (5.4.23) can be written as

$$\frac{D\{\boldsymbol{u}\}\omega}{Dt} \approx \omega\frac{\boldsymbol{u}\cdot\hat{\boldsymbol{r}}}{r} + Re^{-1}\left(\nabla^2\omega - \frac{\omega}{r^2}\right). \tag{5.4.24}$$

We assume that the layer is initially thin enough so that derivatives of the pertubation velocity across it are larger than those taken along it, thus the initial vorticity may be approximated by

$$\omega = \frac{\partial U_t}{\partial n} - \frac{\partial U_n}{\partial s} - \kappa^{(t)}U_t \approx \frac{\partial U_t}{\partial n}. \tag{5.4.25}$$

As the boundary layer separates, viscous terms will become less important, and we may assume that the vorticity development can be described by pure convection together with changes brought about by the stretching of vortex rings moving towards or away from the central axis. Hence by following material points, in the sense defined by the potential flow field, we can calculate an estimate of the vorticity evolution in both the upward and downward jets. We examine *a posteriori* our assumption that the self-induced motion of the vorticity can be neglected when compared to the advection due to the irrotational flow.

<center>*5.4.2 Repositioning and smoothing.*</center>

In order to maintain a good resolution of surfaces, it is necessary to reposition points periodically. Points on bubbles are moved so that they are once again evenly spaced. Points on the free-surface are spaced so that the arc lengths follow a non-linear distribution similar to that in equation (5.3.5). Regular smoothing with the Longuet-Higgins and Cokelet (1976) smoothing formula was also required in order to prevent high frequency surface oscillations.

As was mentioned in section 5.4.1, finite difference points in the boundary layer are repositioned with nodes on the surfaces. Since these points must always lie on normals to the surface, this can be done as follows. The standard repositioning of the surface nodes decides between which two old nodes a new node is to be placed. Values of U_t on the new boundary layer normal are chosen at the same heights as those on the old normal immediately to its left by a simple linear interpolation scheme, based on the assumption that the surface curvature will not change much from one node to the next, so that the three normals meet at a single point. Hence changes in U_t at nodes equi-distant from the surface on the normals will be in the same proportion as the arc lengths along the surface. To do this the value of U_t on the normal immediately to the right of the new normal is also calculated at the same height by quadratic interpolation. This is repeated for all nodes on each normal.

5.5 Results and discussion.

The methods described in the previous sections allow numerical calculation of bubble and interface shapes at various times during bubble rise or burst. A number of cases of bubbles bursting are shown in figures 5.3(a)-(f) for different bubble sizes. It is clear that the smaller bubbles, as their internal pressures are higher, burst from lower in the fluid and thus release a proportionately greater amount of energy in the form of the high-speed liquid jets observed experimentally (see for example, MacIntyre, 1972; Kientzler et al, 1954). The larger bubbles form wider jets and this is observed in Garner et al (1954). The velocity of the central node on the free-surface increases sharply as the jet is formed. In the figures 5.3(a)-(d), there is a noticeable drop in velocity immediately before the jet begins to rise. This can be seen more clearly in a magnification of the motion of figure 5.3(b), shown in figure 5.4. As the cavity walls straighten early on in the burst, the bottom rises slowly and flattens off, creating a ring of high curvature at the 'corner' between the near vertical wall and the horizontal base. The effect of surface tension then pulls this ring inwards. Thus the liquid — which flows from the region of opposite curvature near the highest point of the surface — now flows predominantly towards this ring rather than towards the very lowest part of the cavity. The node on the axis of symmetry is then observed to slow down. As the walls close in further, an axisymmetric cusp almost occurs and the liquid is forced upwards. This high surface curvature and the subsequent large velocities and accelerations suggest possible physical similarities between jet formation and the classes of free-surface flows considered by Longuet-Higgins (1980, 1983).

The jet accelerates for only a short time, and then slows as it rises. For the first three calculations of figure 5.3, the speed of the uppermost point increases very slightly, once more due to the thinning of the jet and the breaking off of a drop, at which point the calculations must stop. As velocities scale with respect to $(\sigma/\rho a)^{1/2}$, it is clear that smaller bubbles result in faster jets.

Compare these calculations with figure 5.5, where a $3mm$ radius bubble is burst from

a completely submerged position. Here, unlike in figure 5.3(f), a high-speed jet is formed. Due to the greater influence of gravity, this jet is wider and not as fast as those produced by smaller bubbles, which burst with similar initial configurations.

The calculated free-surface shapes before jet production are repeated for the $0.75mm$ bubble in figure 5.6 in order to show a comparison with the experimental results of Kientzler et al (1954). Slight differences in the initial motion can be attributed to the fact that the experimental profile starts off slightly lower in the fluid. The jet produced in the experiments is asymmetric and breaks up significantly earlier than calculated, so that the comparison for later times is not so good. This is not shown, due to the difficulty of identifying the surface position of the lower part of the jet which, in the photographs of Kientzler et al (1954), is obscured by the surrounding bubble crater. In addition to the inevitable neglect of asymmetric instabilities, node repositioning and smoothing may cause discrepancy in the jet shapes. Enhancements to the numerical procedure, to the surface representation or so that smoothing is no longer required, may improve this. The effect of a boundary layer on the jet is discussed below.

The existence of a downward jet in the calculation is confirmed by placing a second bubble directly below the bursting bubble. It can be seen in figure 5.7 that the top of the second bubble is firstly pulled up by the effect of the low pressure around the highly curved bursting bubble cavity. Then, just as the jet forms, the top of the lower bubble develops a dimple. The lower bubble then begins to rise and soon starts to form a jet from below, characteristic of bubbles of this size (see Chapter 4). The jet velocity for the bursting bubble reaches a slightly higher peak, but is otherwise largely unaffected by the following bubble. Likewise, the centroid velocity of the following bubble, indicated by the lower trace of the velocity plot for figure 5.7, undergoes a small dip as the jet of the bursting bubble forms.

Using the boundary layer calculations of section 5.4, we find that the surface shapes, up until jet formation, are indistinguishable from those in the figures above. Unfortunately

boundary layer separation over a significant region occurs just before the jet forms (figure 5.8) so that the boundary layer calculation must stop. The dissipative effect of viscosity on the jet can be seen by allowing a boundary layer to develop just after the jet has begun to form (at $t = 0.5$ for the $0.75mm$ case). Calculations run as far as the time when the droplet at the end of the jet begins to develop. Figure 5.9 shows the resulting jet to be very slightly shorter than in the corresponding potential flow case at the same time.

The pressure in the fluid is calculated using the Bernoulli formula (4.3.1) together with the boundary layer modification (5.4.7). To improve resolution near to the surface, where the boundary integral formula for the potential in the fluid is badly behaved due to the weakly singular kernel, the pressure there is given by

$$p^\star - p_\infty = \frac{dk_m}{dt} + \kappa_m - \kappa + \frac{\gamma_m E_o}{4} + \frac{2}{Re} \hat{\boldsymbol{n}} \cdot \boldsymbol{e} \cdot \hat{\boldsymbol{n}}, \tag{5.5.1}$$

where $\boldsymbol{e} = e_{ij}$ is the rate-of-strain tensor. Since the fluid is incompressible,

$$\hat{\boldsymbol{n}} \cdot \boldsymbol{e} \cdot \hat{\boldsymbol{n}} = -\frac{\partial u_t}{\partial s} + u_n \kappa^{(t)} - \frac{\boldsymbol{u} \cdot \hat{\boldsymbol{r}}}{r} + O(\delta). \tag{5.5.2}$$

As cells are more likely to be ripped apart by straining flows than by a strong velocity gradient in one particular direction, when damage can be reduced by the cells rotating with the fluid, the energy dissipation rate, $\Phi = 2\mu e_{ij} e_{ij}$, gives a good indication of the stresses placed on a cell in the fluid, thereby providing a possible measure of the damaging nature of a particular flow field.

In the fluid, outside the boundary layer, the non-zero rates-of-strain are given by

$$e_{rr} = \frac{\partial u_r}{\partial r}; \quad e_{\theta\theta} = \frac{u_r}{r}; \quad e_{zz} = \frac{\partial u_z}{\partial z} \quad \text{and} \quad e_{rz} = \frac{1}{2} \left\{ \frac{\partial u_r}{\partial z} + \frac{\partial u_z}{\partial r} \right\}. \tag{5.5.3}$$

At the surface, by virtue of the stress-free boundary condition, the rates-of-strain are

$$e_{nn} = -\frac{\partial u_t}{\partial s} + u_n \kappa^{(t)} - \frac{\boldsymbol{u} \cdot \hat{\boldsymbol{r}}}{r} + O(\delta); \quad e_{tt} = \frac{\partial u_t}{\partial s} - u_n \kappa^{(t)} + O(\delta) \quad \text{and} \quad e_{\theta\theta} = \frac{\boldsymbol{u} \cdot \hat{\boldsymbol{r}}}{r} + O(\delta), \tag{5.5.4}$$

with all off-diagonal terms zero. By exploiting incompressibility, the corresponding dimensional energy dissipation rate at the surface may be written as

$$\Phi = 4\mu(e_{nn}^2 + e_{tt}^2 + e_{nn} e_{tt}). \tag{5.5.5}$$

The pressures above atmospheric pressure ($dyn\,cm^{-2}$) for the $0.75mm$ and $3mm$ bubbles are plotted in figures 5.10 and 5.11. For the smaller bubble, the initial motion is driven by the very high pressure around the rim of the cavity. This is less dramatic in the $3mm$ case where gravity also plays a significant role in shaping the motion. In frames 11(a) and (b), the low pressure around the underside of the bubble intensifies as a small wave that was initially just below the neck of the bubble crater moves down the bubble increasing in curvature. This wave can also be seen clearly on the second frames of figures 5.3(a)-(c), and moving on figure 5.4. MacIntyre (1972) observed another ripple with a smaller wavelength immediately in front of this as a possible Crapper capillary wave. This is only resolved by the code if a high point density is used, for example when R_{max} is reduced to about 5. However, this results in excessively fast, thin jets.

As the walls of the cavity collapse inwards (figure 5.10(b)) a ring of high pressure can be seen to develop. This then moves downwards until it finally becomes a point of high pressure directly beneath the bubble (figure 5.10(c)). This pushes fluid upward and downward to produce the jets evident in previous figures. The high pressure remains during the early stages of jet formation, further accelerating the jet (figure 5.10(d)). The pressure in the jet is relatively high due to surface tension which acts so as to thin it until one or more drops break off. For the large bubble, the pressure rises only slightly as the much smaller jet is about to form. This can be seen through the slight upward bending of the contour lines of the highly visible hydrostatic pressure.

Figure 5.12 shows that the largest maximum pressures occur for the smallest bubbles. This was expected from the experimental studies on cell damage. However, it seems that the pressures themselves are insufficient to kill cells, being equivalent to the hydrostatic pressure due to only a few centimetres of water.

Figures 5.13 and 5.14 show the energy dissipation rates ($dyn\,cm^{-2}s^{-1}$) for the same times as above. It is seen that the peak energy dissipation rate moves round with the wave of fluid, where the pressure is low, increasing in magnitude until the jet forms.

MacIntyre (1972) indicated that this ripple was a site where high rates of strain were likely. Indeed, high rates of strain are to be expected when the jet is forming due to the extensional flow around a stagnation point near to the pressure maximum. Fluid must be drawn in from the sides towards the axis of symmetry and then rapidly accelerated upwards or downwards into one of the jets. Such flows are potentially lethal to cells which may be stretched and ruptured by the high strain rates. Figure 5.15 shows that the maximum energy dissipation rates, which occur beneath the bubble, immediately before jet formation, increase rapidly with decrease in bubble radius. Again, this is in keeping with the finding that cell damage is greater for smaller bubbles. There is no complete agreement on the strength of cells. Orton and Wang (1990) suggest that stresses of the order of $10^3 dyn\,cm^{-2}$ are sufficient to cause death, whereas Zhang et al (1991) give cell bursting pressures of about $5 \times 10^4 dyn\,cm^{-2}$. The calculated maximum energy dissipation rates for the smallest bubbles are equivalent to stresses of the order of $10^4 dyn\,cm^{-2}$, indicating that bubble bursting can create an hydrodynamic environment which may be deadly for cells.

The boundary layer makes almost no difference to the calculated values of energy dissipation rate. This is mainly because the effect of the boundary layer in ensuring zero tangential stress at the surface, is exploited even when no boundary layer is being used in the calculations, in order to improve resolution in the contouring program.

It was proposed by Orton and Wang (1990) that cell death rates are closely related to the rate of liquid entrainment from bursting bubbles. As it seems reasonable to assume that the underlying cause of cell damage must be some form of hydrodynamic stress, there should be a corresponding relationship between this stress and the entrainment rate. To investigate this, we calculated estimates for the volume of the first drop released. The calculated entrainment rates are compared with the jet drop sizes of Garner et al (1954) in figure 5.16. Note that only the size of the first released drop is calculated and no allowance is made for the volume of fluid entrained by the rupture of the film above the bubble,

which is significant for only the largest bubbles (see Garner et al, 1954). The droplet sizes for the smaller bubbles agree to an order of magnitude. Differences are partly because of the difficulty in predicting the precise time and place of disengagement, but are also due to discrepancies in the jet formation itself pointed out above. Smoothing and repositioning of nodal points in the jets may smooth out small scale instabilities that would otherwise affect drop formation. An interesting point to note is that the calculated entrainment rates seem to be at a maximum for bubbles of radii around $2mm$. Even though the bubble of figure 5.3(d) does not form a long, thin jet, the relative volume of the drop released is much larger than that of the three smallest bubbles studied. When this calculation was allowed to continue past the point where the drop almost disengaged, the code did not break down, but the jet fell back into the fluid. In reality, it would be surely be pinched off by surface tension, before falling back into the fluid. We can therefore conclude that $2mm$ must be close to the bubble radius beyond which no drop is released. Garner et al (1954) suggest that this cut-off point for jet drop formation is at about $2.5mm$. The velocity plot of figure 5.3(d) shows that, at the time of droplet formation, the top of the jet is moving slowly downwards. If this is the case, such large droplets near to the cut-off point may not have been identified as such by the experimentalists whose methods hinged on observations and detection of drops thrown up above the jet. That larger droplets are formed for larger bubbles is noted by Garner et al (1954), but the sizes are still small in comparison with our calculations.

The approximate vorticity distribution (s^{-1}) is shown at three stages of jet formation in figure 5.17. This vorticity was created in a boundary layer by the initial collapse of the crater for the $0.75mm$ bubble and shed prior to jet formation (figure 5.17(a)). Here, it is shown being convected into the bulk of the fluid by the formation of the jets. The sign of the vorticity in figure 5.17(a) can be explained in terms of the dissipative effect of viscosity, which reduces tangential velocity gradients at stress-free surfaces to zero. As the vorticity is dominated by $\partial U_t/\partial n$, it will be negative in sign when $\partial u_t/\partial n$ is positive.

This was verified by examining the values of $\partial u_t/\partial n$ at the time of figure 5.17(a). (In fact $\partial u_n/\partial s + \kappa^{(t)}u_t$ was used as it is easier to calculate accurately, due to the singular nature of the boundary integral formulation. See (C6).) In figure 5.17(a), the sign of the vorticity was observed to be generally opposite to that of the tangential velocity, u_t. Bearing in mind that normals are directed out of the fluid, this implies that at this time the tangential flow speed at the surface is generally faster than nearby in the bulk of the fluid.

It should be emphasised that although the vorticity carried into the jet is positive, large negative curvatures and tangential velocities near the top of the fully developed jet in figure 5.17(c) and at subsequently times ensure that the tangential speed near to the surface is greater than at the surface. There is consequently a net negative vorticity at the surface due to additional vorticity created in the boundary layer of the jet which is not accounted for in these figures. In the jet of figure 5.17(b) and in the lower parts of the jet of figure 5.17(c), the tangential velocity of the surface is higher so that the direction of fluid rotation is as depicted. As a droplet begins to develop, a region of positive curvature is formed. Thus negative surface values of $\partial u_t/\partial n$ and positive vorticities are found in this region. If we move further down the jet, the thinning becomes less noticeable and a further change of the sign of the surface vorticity takes place. More sign changes are observed to occur around the base of the jet. The magnitude of the vorticity suggests that viscous effects make only a very small contribution to the stresses in the downward jet region.
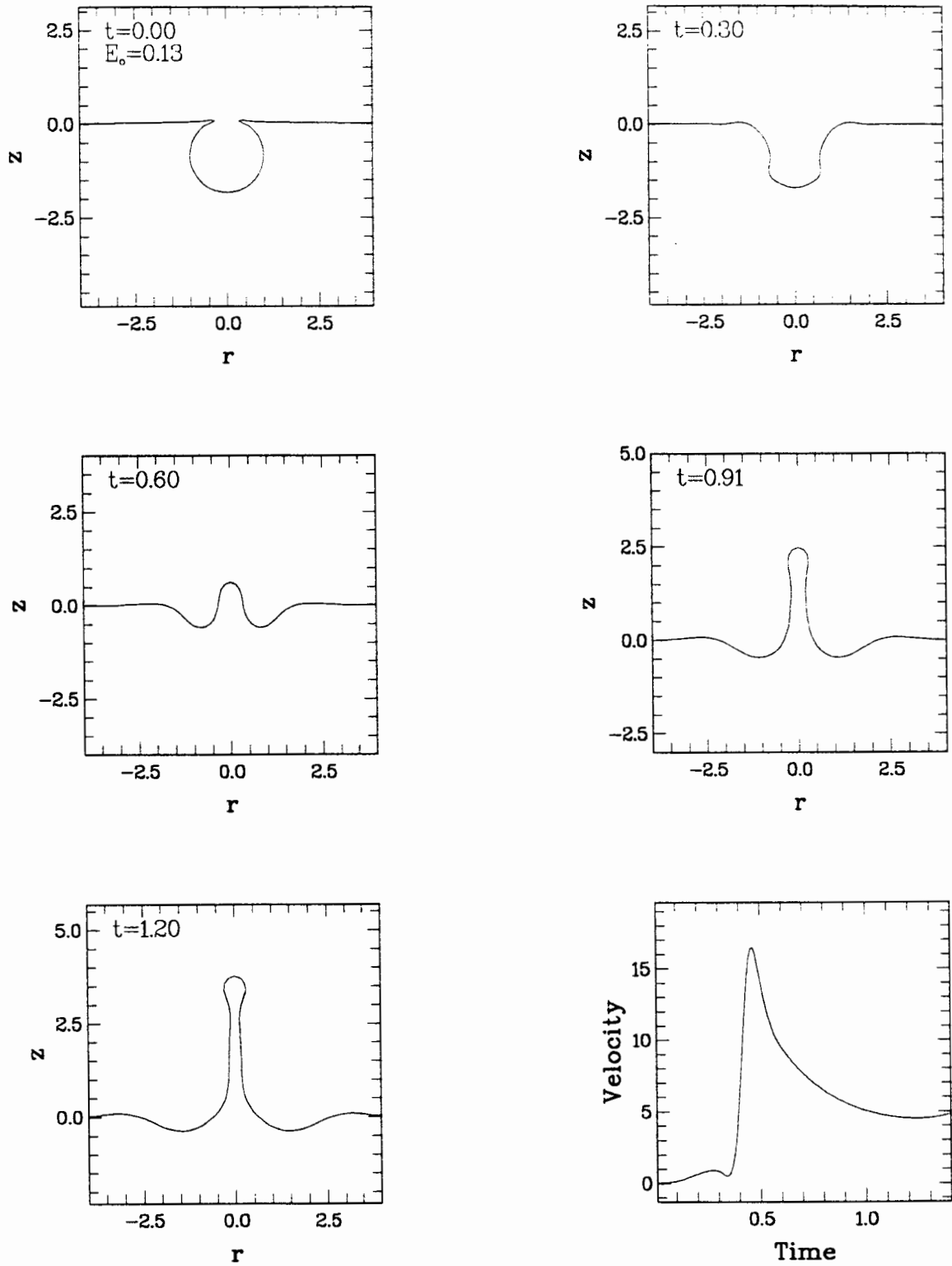
Figure 5.3. Calculated free–surface shapes for different initial bubble sizes, together in each case with the velocity of the node on the central axis. Eötvos numbers are (a) 0.13, (b) 0.30, (c) 0.53, (d) 2.12, (e) 3.31 and (f) 4.77, corresponding to equivalent radii of 0.05, 0.075, 0.1, 0.2, 0.25 and 0.3 centimetres respectively.
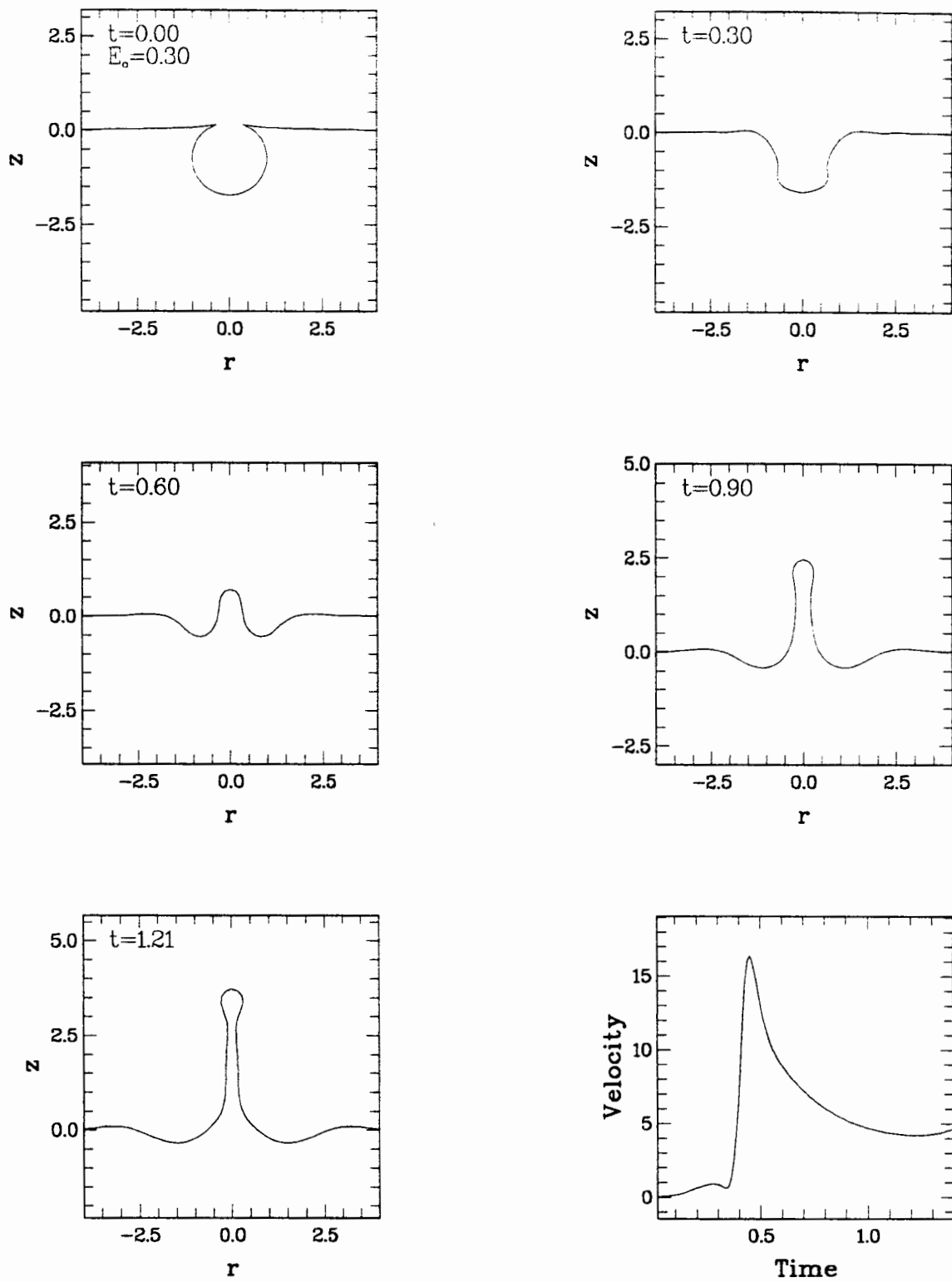
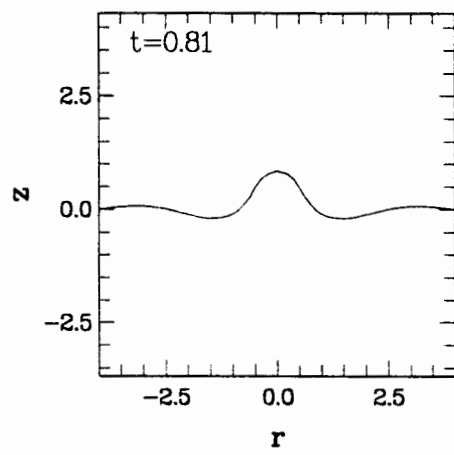Figure 5.3(b)
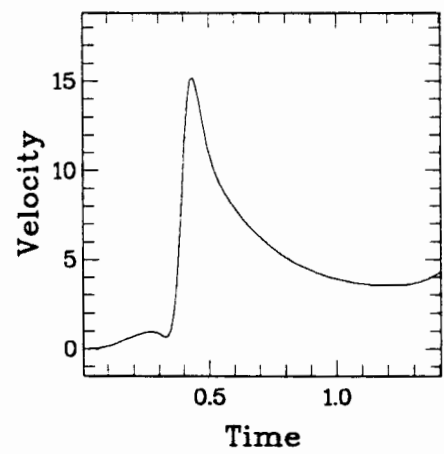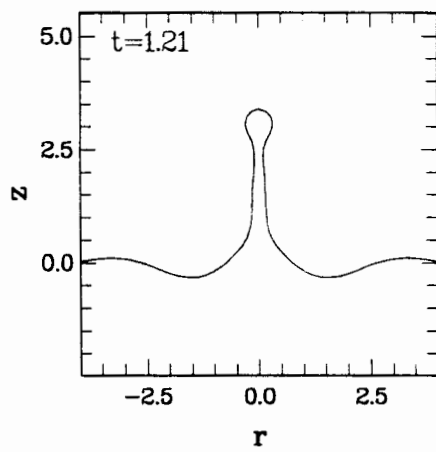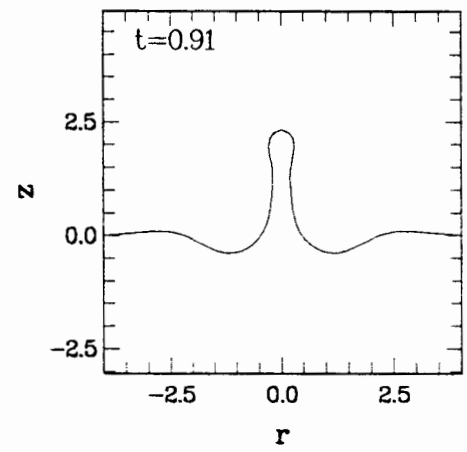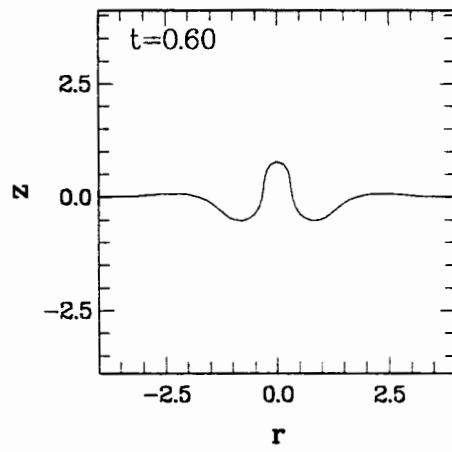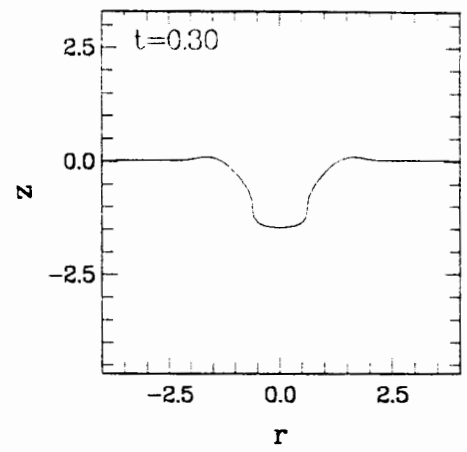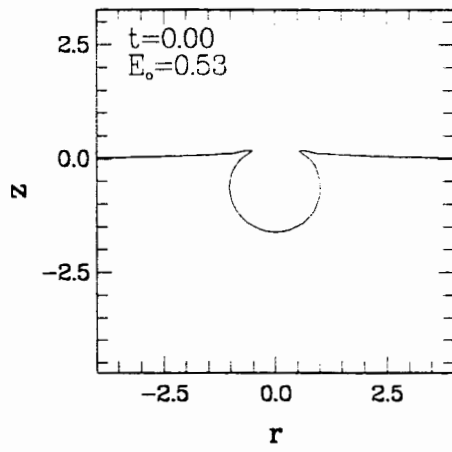
Figure 5.3(c)
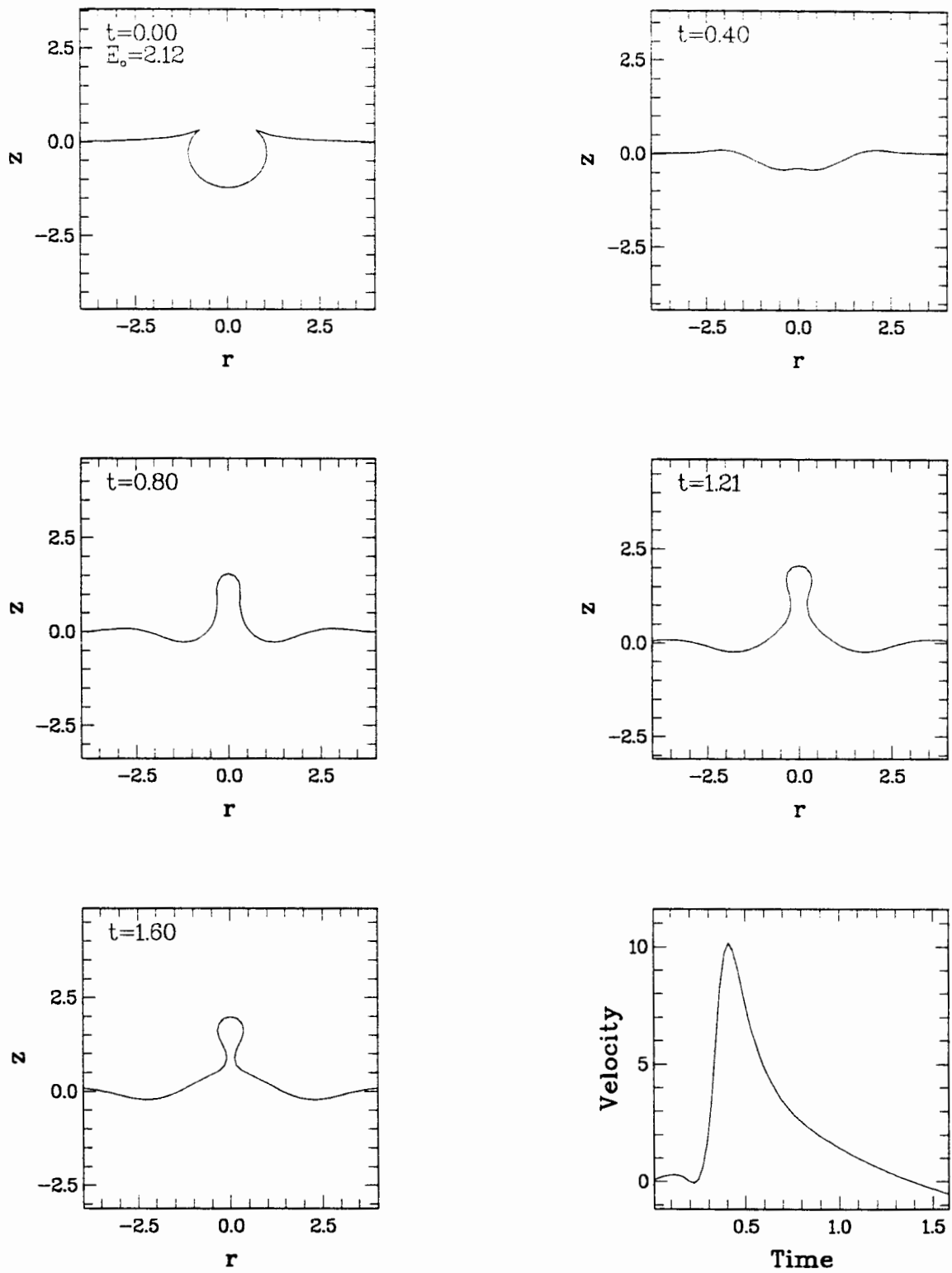
Figure 5.3(d)
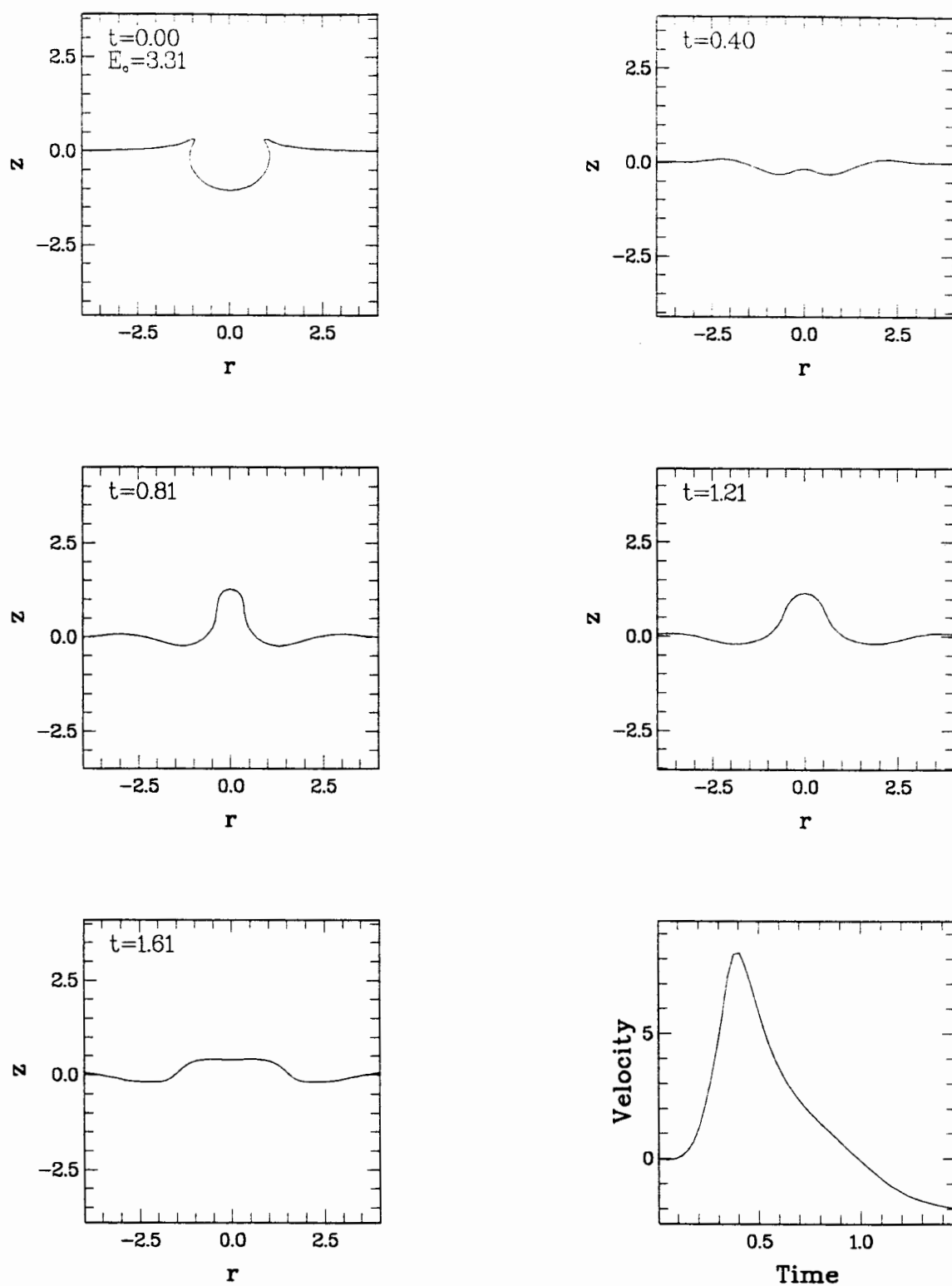
Figure 5.3(e)
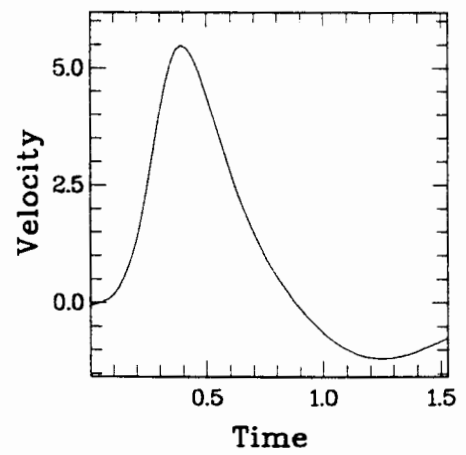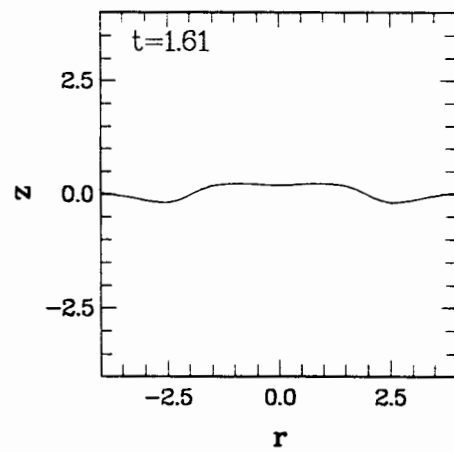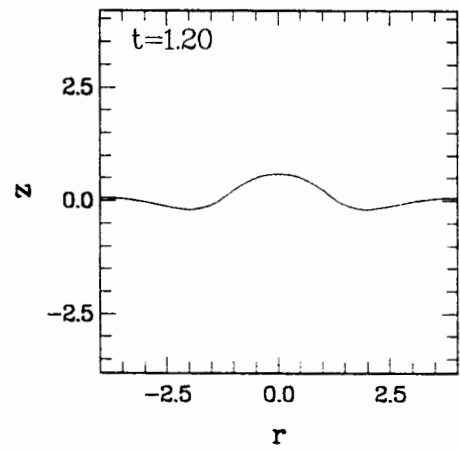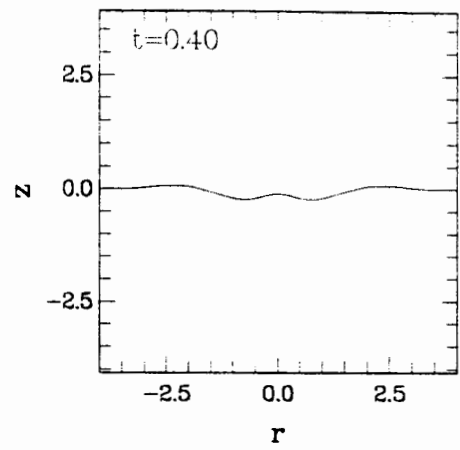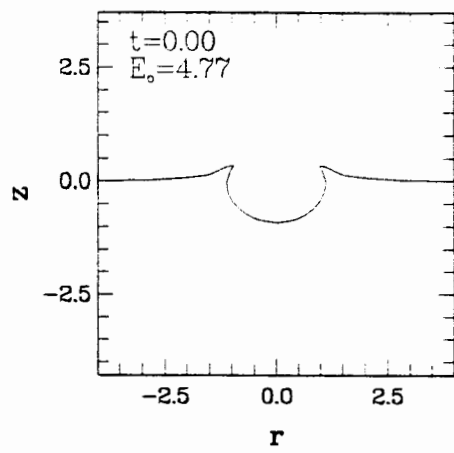
Figure 5.3(f)
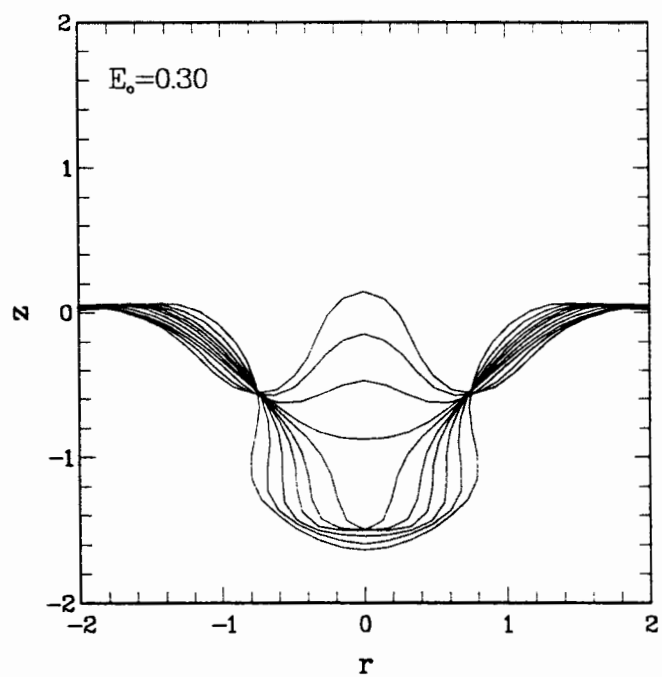
Figure 5.4. A closer look at the motion near to the base of the bubble cavity of Figure 5.3(b) as the jet is about to form. The sharpening of the curvature at the corners can be seen as the base becomes flatter. The time between frames is approximately constant.
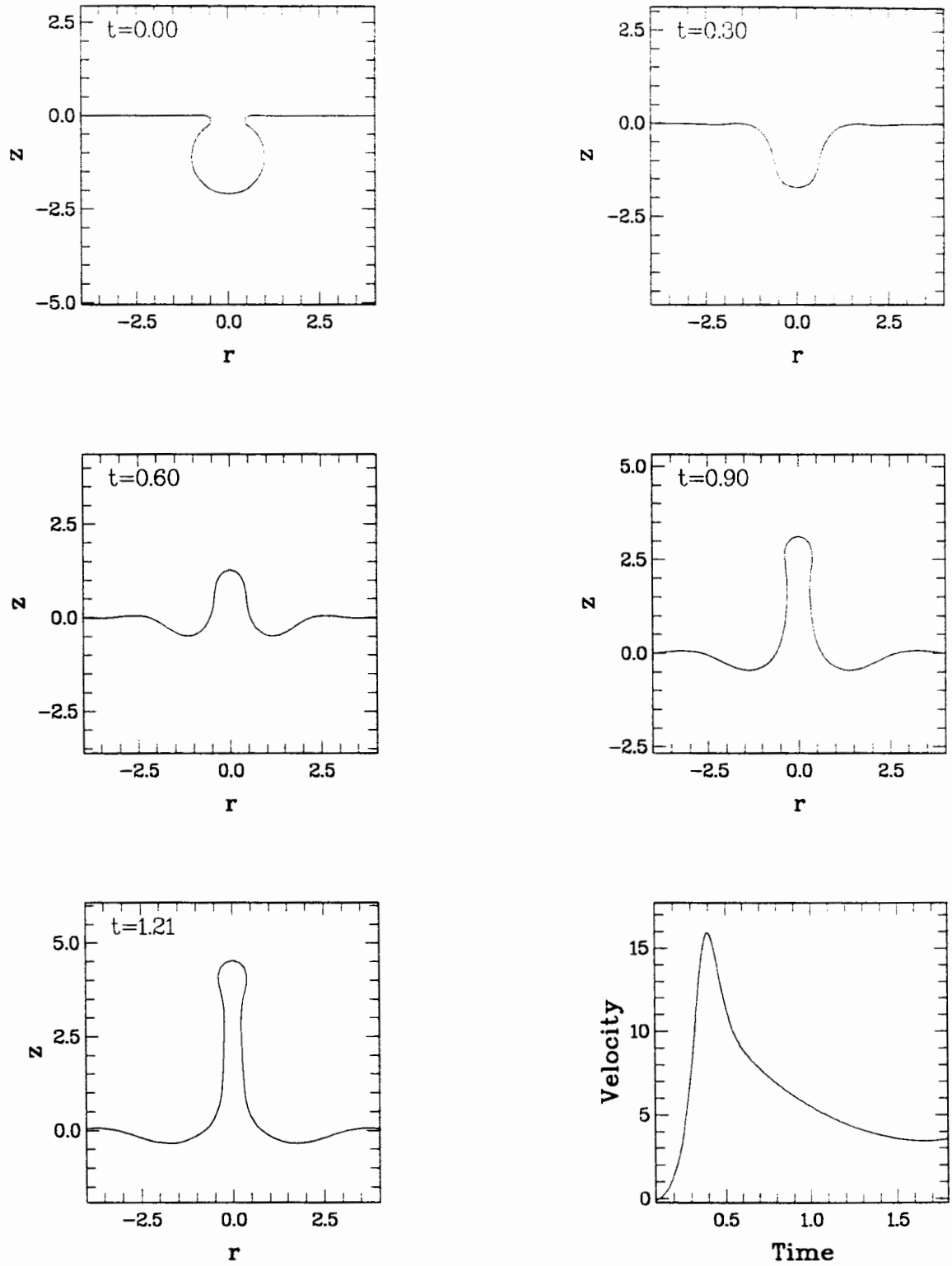
Figure 5.5. A spherical bubble of the same volume as that in figure 4(f), burst from a position just below a flat free–surface. The bursting motion is not greatly affected by the amount of free–surface removed in order to re–join to the bubble. E_o=4.77, γ_i=1.1, a=3cm.
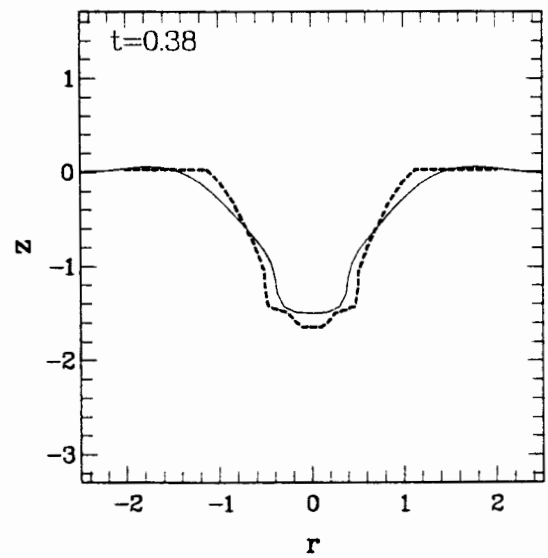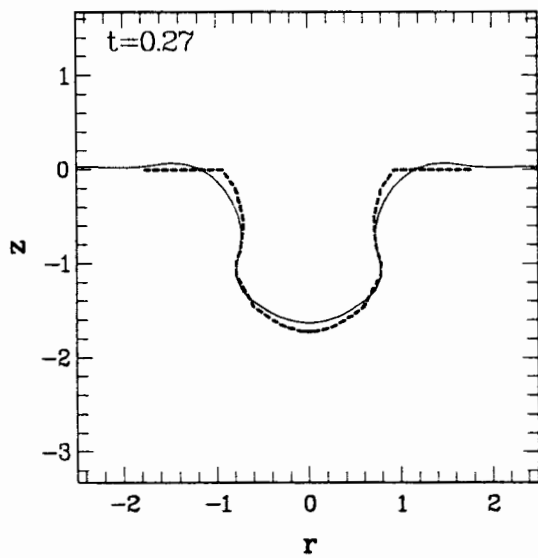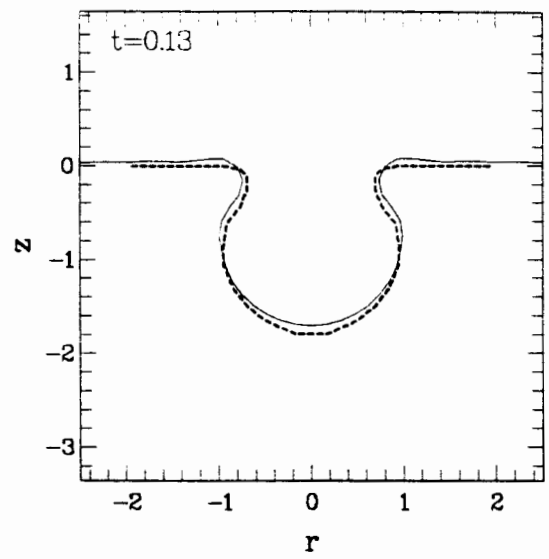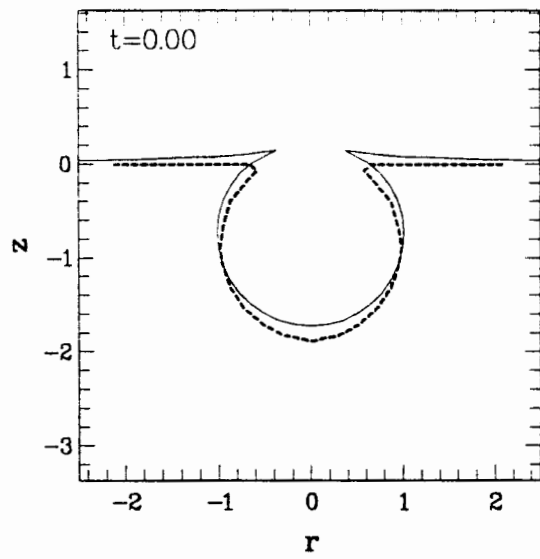
Figure 5.6. Calculated motion of the 0.75mm bubble (solid lines) compared with the experiments of Kientzler et al (1954) (dashed lines). The exact shapes of the experimental bubble craters near to where they joint the free surface are not clear from the photographs in their paper and this may be the cause of some discrepancy.
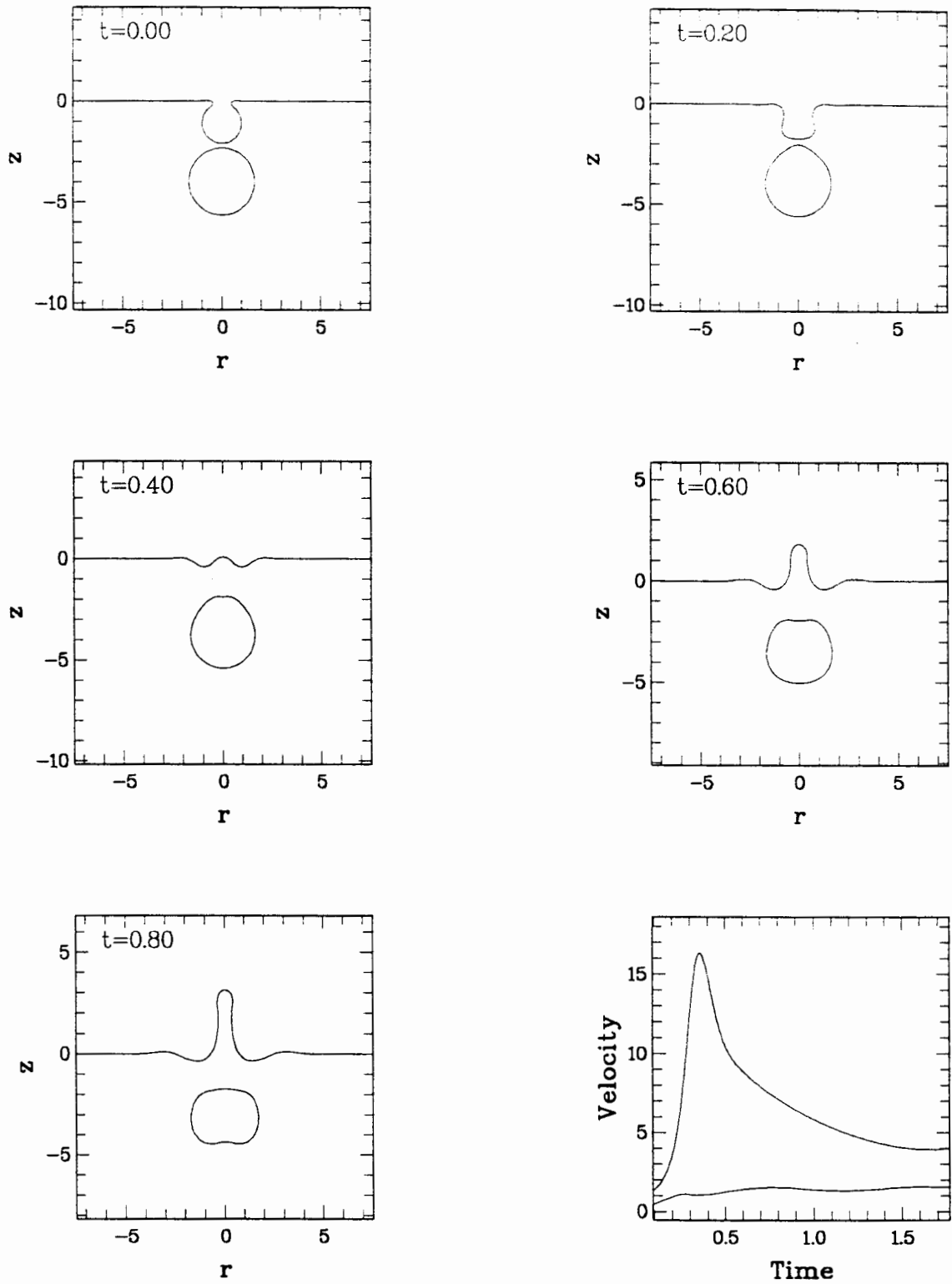
Figure 5.7. The effect of a bursting bubble on a second, larger bubble following close behind, together with a plot of the jet velocity and centroid speed of the lower bubble. $E_o=4.77$, $\gamma_1=1.1$, $\gamma_2=4.0$, $a=0.3$cm, $r_2=1.67$.
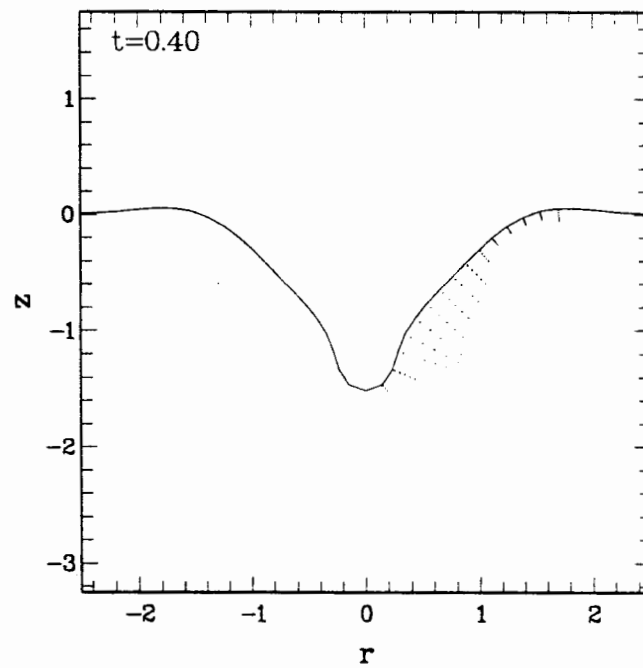
Figure 5.8. Boundary layer separation before jet formation is indicated by the motion of boundary layer nodes away from the rapidly retreating surface.
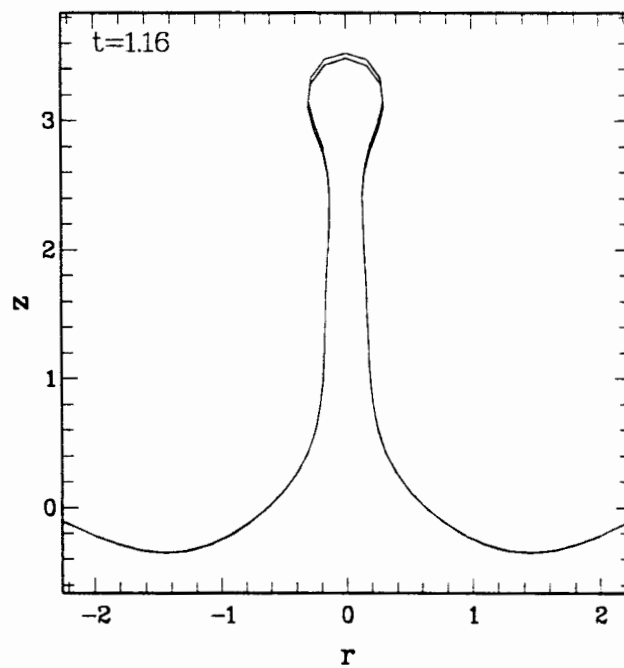
Figure 5.9. Starting the boundary layer calculations just after the jet forms shows the dissipative effect of viscosity, resulting in a slightly shorter jet compared to the purely potential flow case.
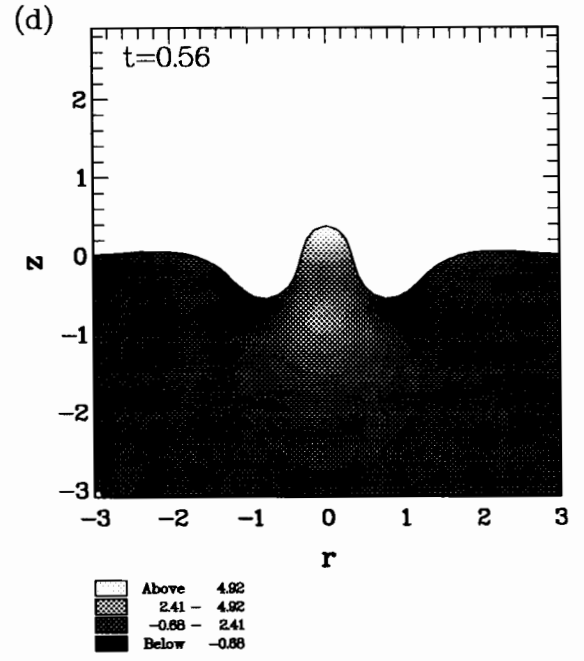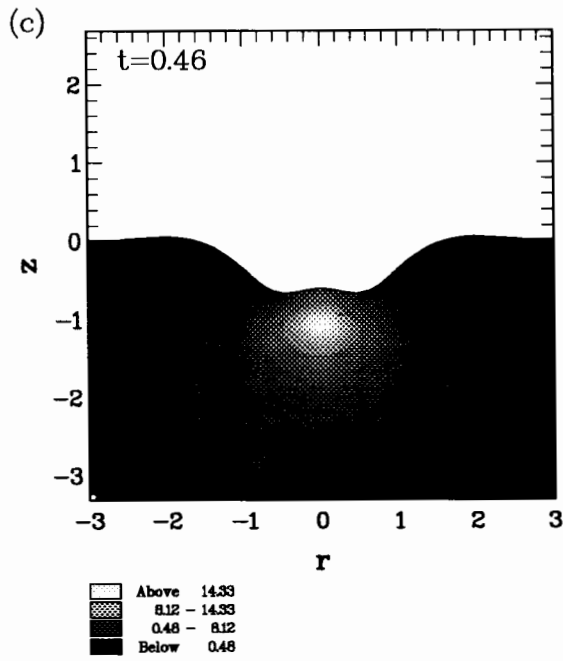
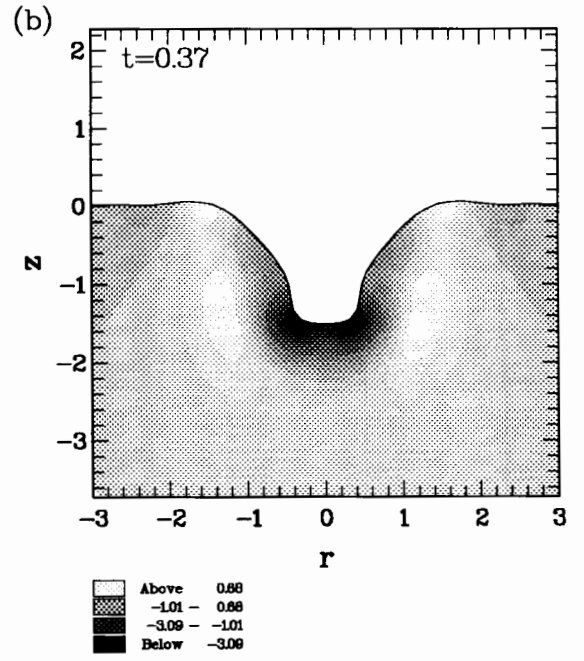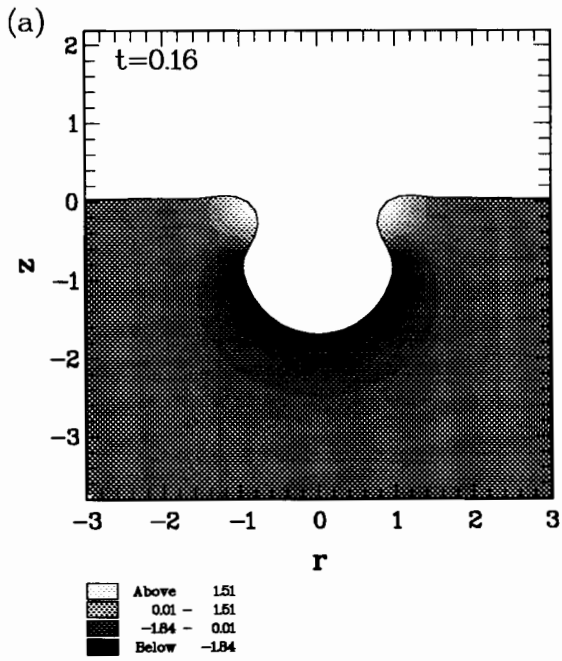Figure 5.10. Pressure above ambient pressure (10^3dyn cm^{-2}) for the 0.75mm bubble of figure 5(b).
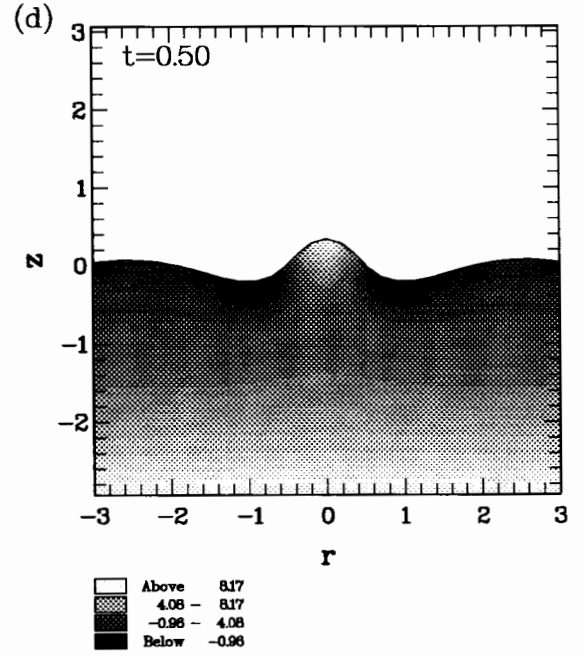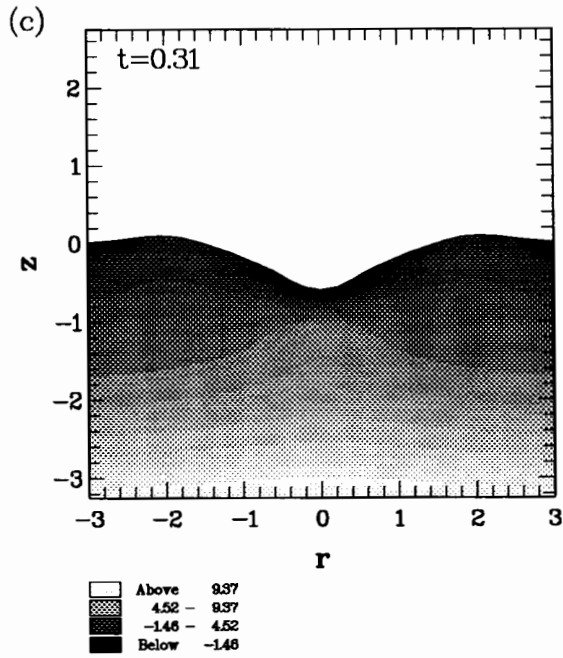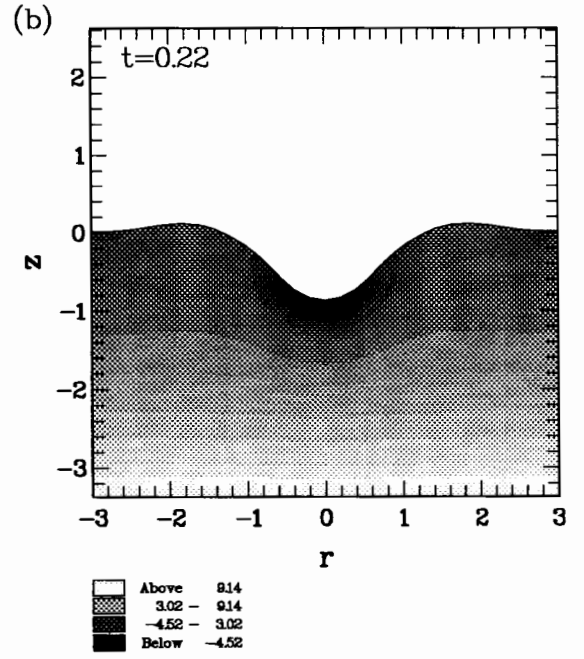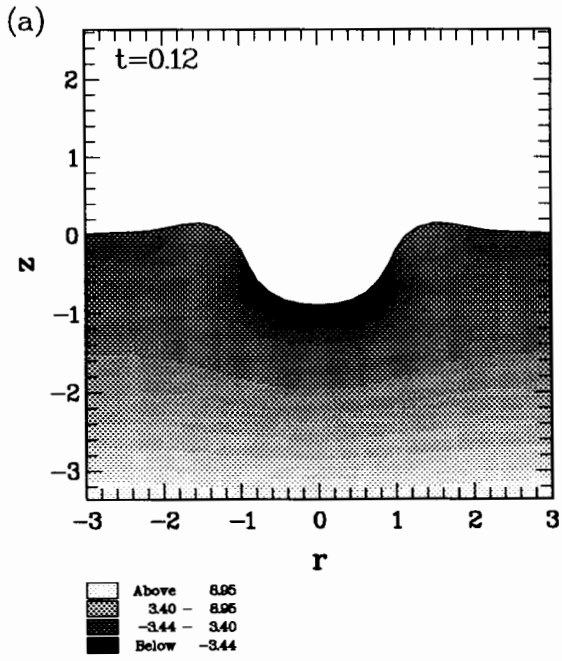
Figure 5.11. Pressures above ambient pressure (10^2dyn cm^{-2}) for the 3mm bubble of figure 5(f).
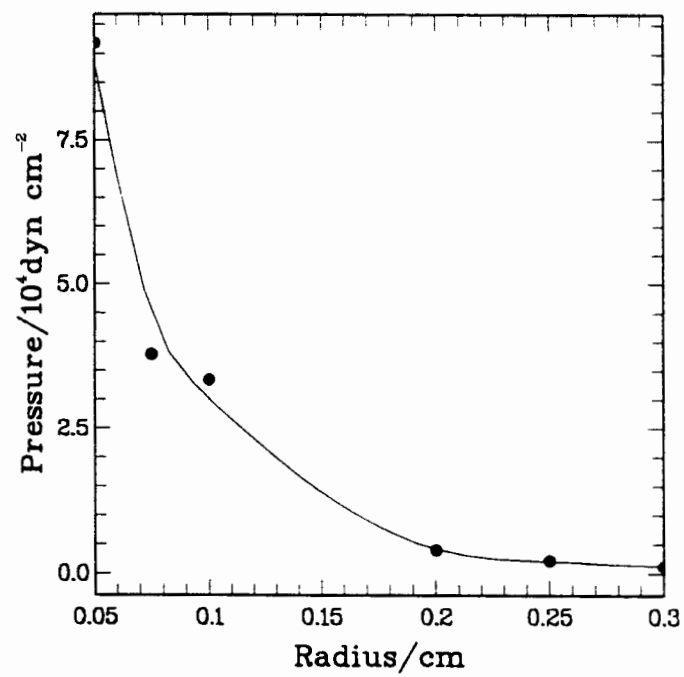
Figure 5.12. Maximum pressures produced throughout the bursting process plotted against bubble radius.
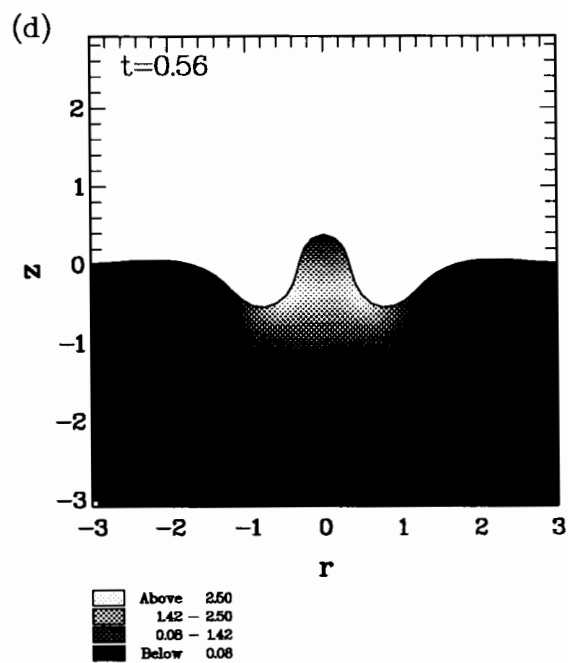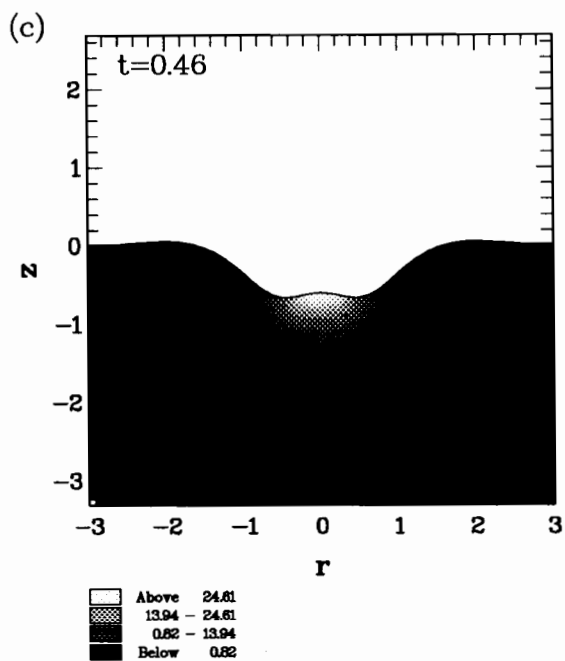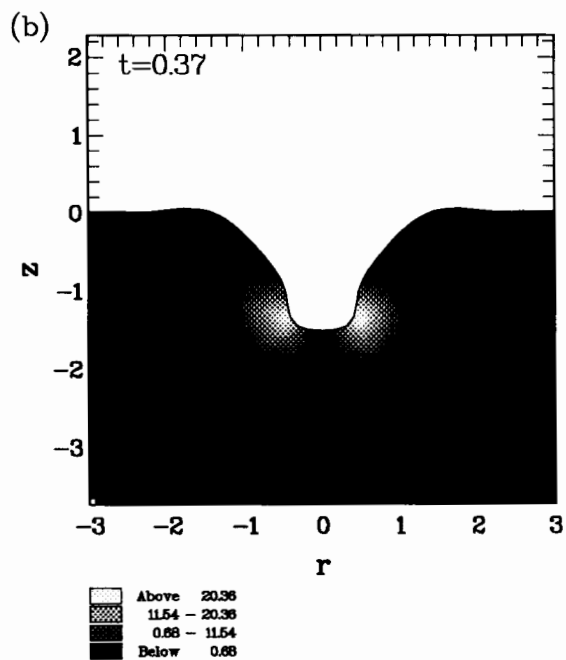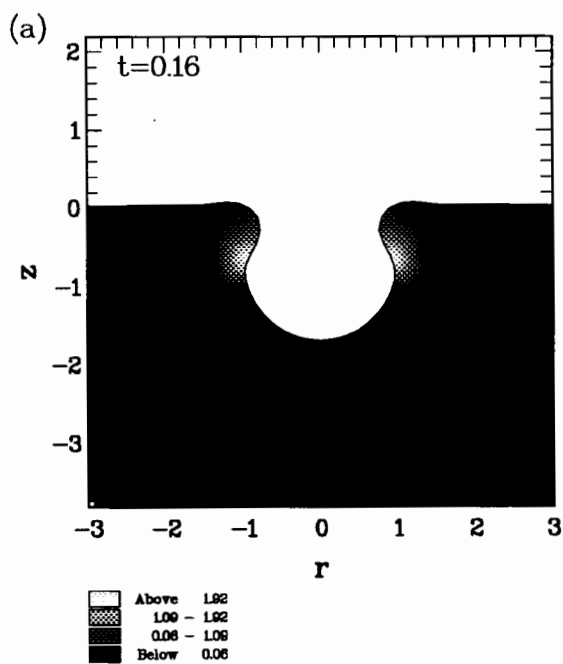
Figure 5.13. Energy dissipation rates (10^6dyn cm^{-2}s^{-1}) corresponding to frames of figure 11.
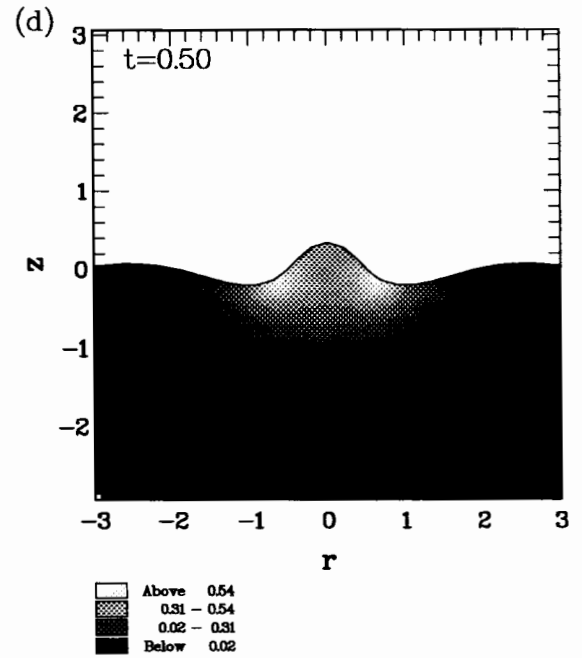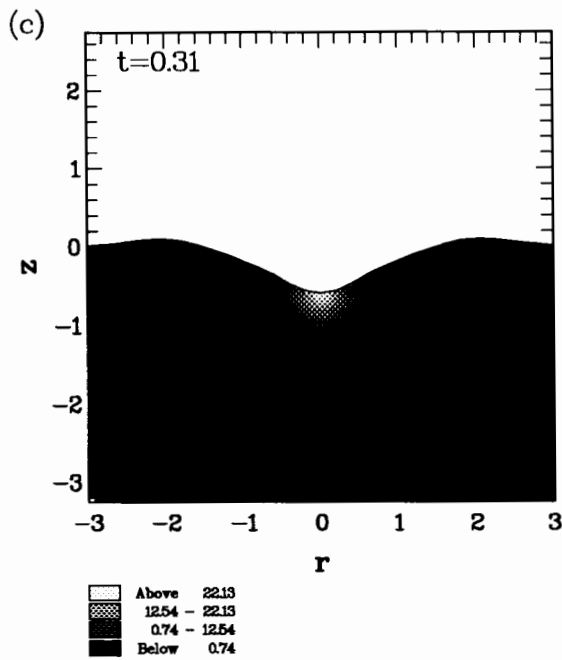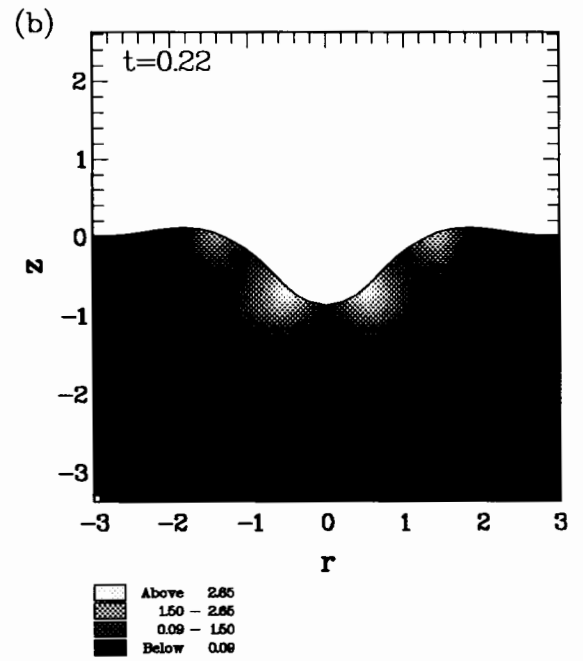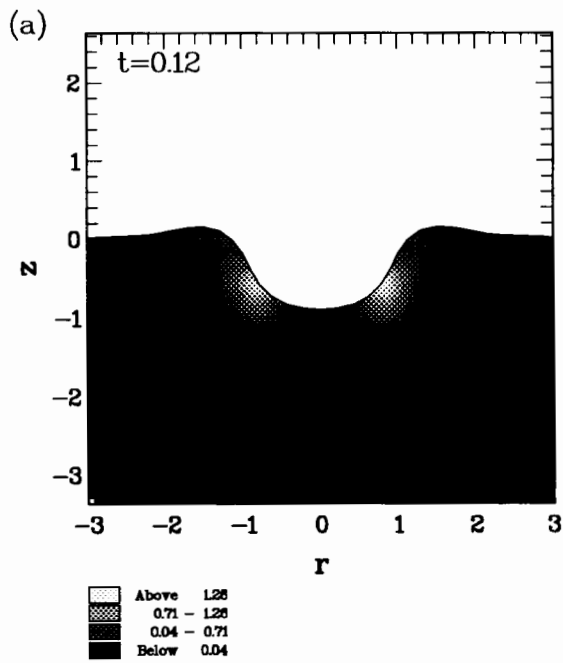
Figure 5.14. Energy dissipation rates (10^3dyn cm^{-2}s^{-1}) corresponding to frames of figure 12.
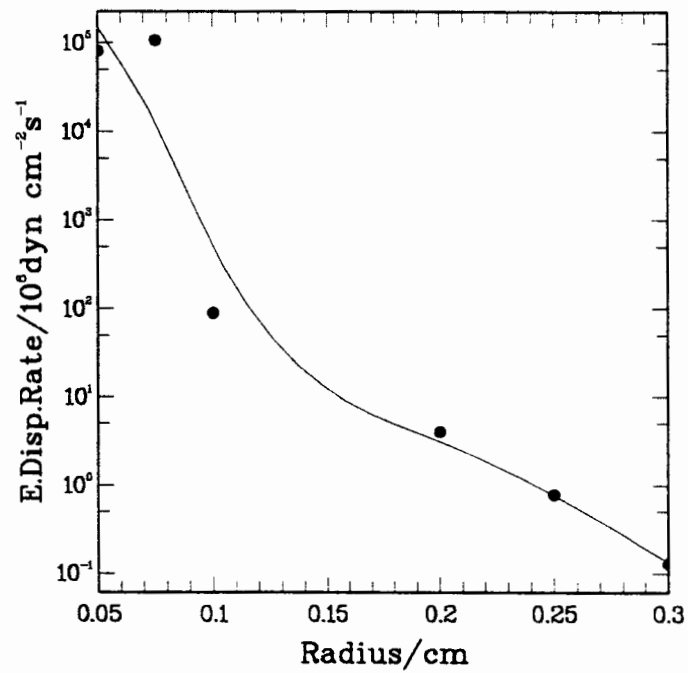
Figure 5.15. Maximum energy dissipation rates produced throughout the bursting process, plotted against bubble radius. The initial rise of the data values for the smallest bubbles may be due to the difficulty in locating the exact place and time of the peak, due to large spatial and temporal gradients beneath the forming jet. The logarithmic scale indicates an exponential dependence of maximum stress on bubble radius for larger bubbles.
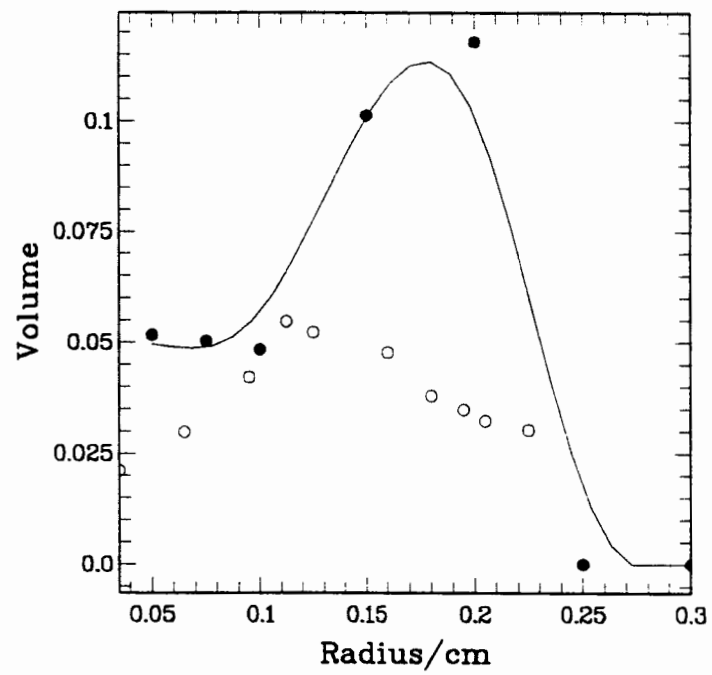
Figure 5.16. Non-dimensional jet drop volumes against bubble radius: calculated (solid discs and line), compared with the experimental values of Garner et al (1954) (circles).
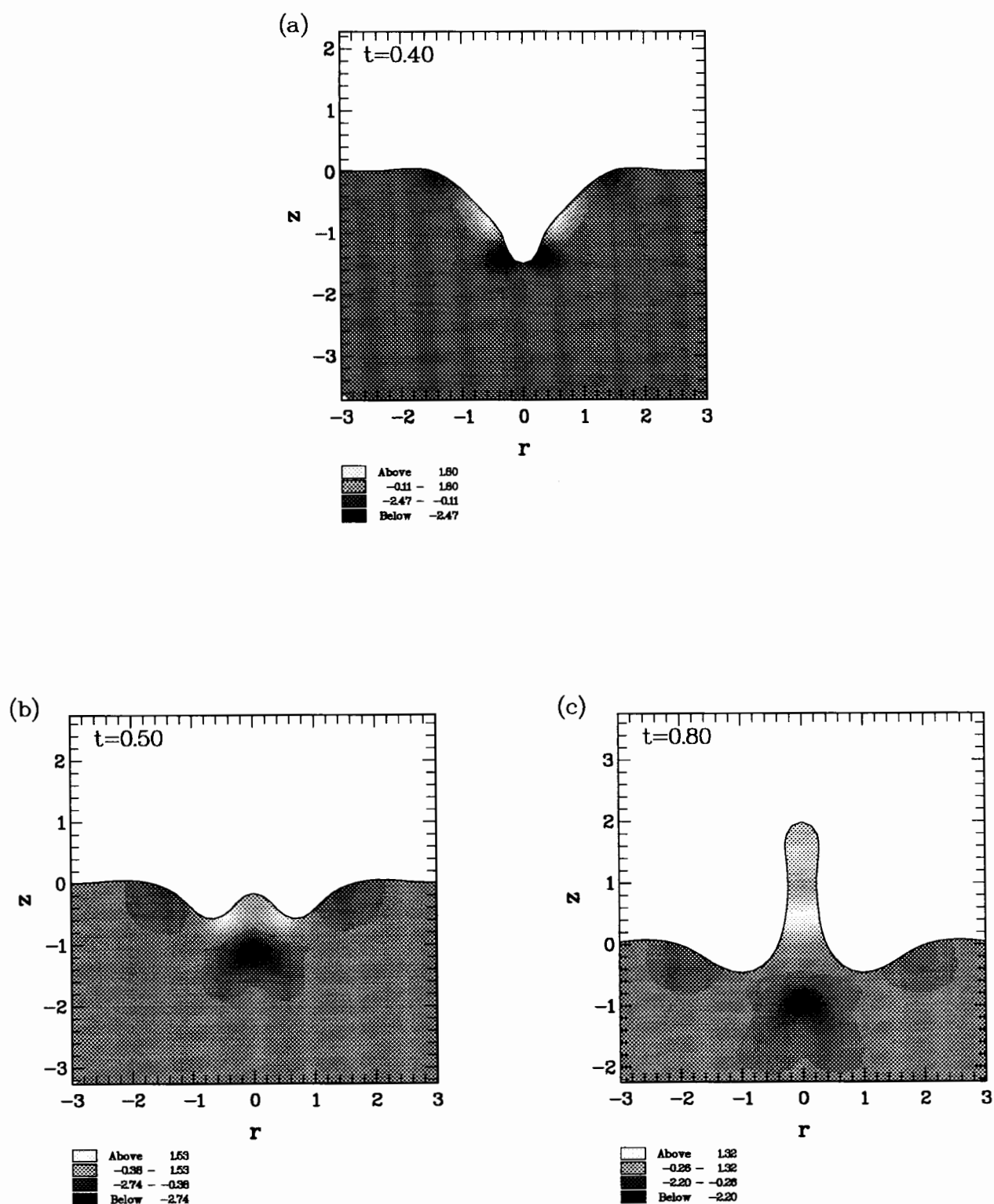
Figure 5.17. The vorticity distribution ($10^2 s^{-1}$) generated in the boundary layer and subsequently advected into the fluid by the upward and downward jets. The 0.75mm bubble of figure 4(b) is shown at times t=0.40, 0.50 and 0.80 respectively.

Chapter 6.

CONCLUDING REMARKS AND
FUTURE DEVELOPMENTS

6.1 Conclusions

In this thesis we develop and utilise powerful boundary integral techniques in order to study unsteady gas bubble rise and burst at high Reynolds number. This was motivated by the problem of cell destruction in bubble aerated bioreactors. In particular, we have focused on the bubble disengagement which experiments highlight as an important damaging factor. A consideration of the effect of a free surface on the motion of bubbles is also of interest. This, together with bubble bursting, is a theme running through a large portion of this work. An examination of the motions of two-dimensional bubbles provides an important introduction both into the types of fluid behaviours that one may expect in three-dimensions and into the numerical methods used to study them. As the axisymmetric boundary integral method is effectively a two-dimensional method with a modified Green's function, the step up from two to three-dimensional bubbles is straightforward. Although, through choice, we use splines for interpolation along the interfaces in the latter case rather than linear elements, the axisymmetric method still affords a simple, easily managed surface representation, when compared to a fully three-dimensional code. The effectiveness of these techniques for solving often complicated, non-linear, unsteady fluid motions is apparent from the previous chapters. At the very heart of the boundary integral methods used is the ability to follow fluid interfaces through time and thus gain an understanding of the physical processes involved which would not have been possible through the use of purely analytical techniques. Useful functions of the flow field such as streamlines, pressures and energy dissipation rates can also be calculated with relative ease.

Several boundary integral methods are compared for solving the problem of a rising two-dimensional bubble. The methods used are in many ways very similar. Unlike Baker et al (1982) and Baker and Moore (1989) who form equations which can be used to directly update singularity strengths for the surface distributions, in each case we retain the same form for the dynamic boundary condition and use this to update surface potentials. This comparison therefore depends mainly upon the relative merits of the underlying integral equations upon which the methods rely. In all of the methods used in Chapter 2, linear elements are used to interpolate surface nodes for integration purposes. The use of quadratic elements affords increased accuracy for the determination of tangential derivatives but is also sometimes necessary in the calculation of integrals over elements adjoining the field point node in order to maintain the regularity of the integrand. Superficially, the results indicate very little difference between the various approaches except for the case of a source distribution method which fails to calculate the motion beyond the first stages of jet formation. Otherwise the bubble profiles agree with independent calculations performed by Baker and Moore (1989). The vortex method seems to conserve energy best, particularly in the final stages of the calculations. The numerical stability of the Green's formula method, based on a first-kind Fredholm equation, is comparatively poor. When using an initial bubble perturbed by just 1%, with a wave number of 18 the top of the bubble develops a severe Rayleigh-Taylor instability within a very short time. The underside of the bubble, where the liquid is accelerated towards the lighter gas phase, is largely unaffected by the initial perturbation as might be expected. This instability seems to be as a result of ill-conditioning of the Green's formula method, which greatly amplifies a slightly altered initial condition.

An investigation of the physical stability of a two-dimensional bubble rising from rest for small times, when an analytical solution for the unperturbed motion is available, shows that a small amount of surface tension can stabilise a bubble, at least for short wavelength perturbations, even though this surface tension has very little effect on the motion of an

unperturbed bubble, where the surface curvatures are much less. This suggests that the Green's formula method may reflect reality better than the other methods.

The reason for the lack of success with the source and modified source methods is not clear — the condition numbers of the modified source method which relies on a second-kind equation are not significantly higher than those for the Green's formula method. It seems that there is an inherent problem with trying to accurately solve a problem with a dipole far-field potential based solely on a distribution of sources.

By employing a conformal map to transform a semi-infinite region onto a bounded domain, the boundary integral methods described in Chapter 2 are extended to allow the modelling of a two-dimensional bubble beneath a free gas/liquid interface. The bubble behaviour is very similar to that for the infinite fluid case, especially when the bubble rises from a distance far below the interface; a fact that gives us confidence in the accuracy of our results. Nearer to the interface, the fluid is less mobile due to the stabilising effect of gravity on the free-surface. Consequently, the jet formed on a bubble rising in close proximity to the surface is appreciably slower and thus broadens earlier. The inclusion of surface tension allows us to model bubbles that do not form jets, but that become flattened as they rise due to the lower pressures around the sides. The pressure at a point in the fluid above the bubble increases as the bubble approaches so that the free-surface rises noticeably when the bubble becomes close. This surface elevation compares well with calculations based on the assumption that a deeply submerged, circular, constant volume bubble may be regarded as a dipole.

Several similarities in the bubble shapes for the two and three-dimensional cases become apparent when we consider the problem of axisymmetric rising bubbles. For low surface tension, a much faster jet is formed which, although initially broader, impacts on the far side of the bubble rather than spreading out. The broadening of the jet tip, which subsequently pinches off a ring bubble leaving a spherical cap, occurs only in the case of non-zero surface tension. Increasing surface tension results in wider jets, until no

secondary, toroidal bubble is released.

The interaction of two axisymmetric bubbles is also considered. The effect on the lower bubble is greater, its top being drawn up with the fluid flowing into the jet of other. This phenomenon is not as marked as in the corresponding situation for two-dimensional bubbles (considered by Robinson, 1992; Robinson et al, 1993), since a proportionately greater volume of the fluid forming the jet originates further from the axis of symmetry in three-dimensions. As the top of the lower bubble is pulled upward, the bubble as a whole thins reducing its added mass so that it rises faster than it would if it were in an infinite fluid. Its jet speed is correspondingly increased.

As an example of an alternative use of boundary integral methods, the problem of a bubble rising steadily due to the balance of viscous drag and buoyancy is considered. This problem is formulated as a large set of non-linear integral and differential equations which when put into a discrete form are solved using Newton iteration. The results match closely those of Miksis, Vanden Broeck and Keller (1982) who first took this approach to this problem.

In the last chapter, we develop a numerical model of bursting bubbles for the time between immediately after the rupturing of the film up until jet and drop formation. The formation of jets is the result of the collapse of the bubble crater towards the axis of symmetry so that fluid is eventually forced both upwards and downwards. High speed jets do not feature in larger (over about $2.5mm$ radius) bubble bursts as there is insufficient potential energy in the initial configuration. This is due to the reduced equilibrium depth of a larger, more buoyant bubble.

High energy dissipation rates prior to jet rise have been identified as a possible indicator of cell damage. The maximum values of energy dissipation rates are reduced exponentially as the bubble radius is increased. With regard to the problem of cell damage in aerated bioreactors, this is very encouraging, particularly as experiments suggest that only the very small bubbles cause damage. However, the full implications can only

become apparent when we know more details of the likely positions of cells in relation to regions of high rates of strain, both around the crater as it collapses and below the bubble as the jets form. The survivability of cells in specific flow environments also needs to be studied in more depth before any concrete conclusions are drawn in this respect.

A technique for including viscous forces in a stress-free boundary layer, based on the method of Lundgren and Mansour, is introduced. This utilises the fact that a linearisation of the velocities in the boundary layer results in material elements that remain straight and perpendicular to the interface. This has the effect of obviating the need to use a complicated boundary layer mesh to calculate numerical values for the first order perturbation to tangential velocities. The only noticeable effect of the boundary layer on the motion is on the jet which is slowed slightly due to viscous dissipation. The onset of boundary layer separation gives initial conditions for an estimate of the vorticity development in the upward and downward jets. This suggests only a small contribution to the total stress placed on cells, and indicates that the potential flow model gives essentially accurate information of the fluid motion subsequent to film rupture.

6.2 Future directions.

Although the work described in Chapter 5 provides an important basis for future mathematical research into cell damage in bubble aerated bioreactors, there remain many unexplored avenues of investigation. In this section, we indicate some of the main topics which need to be analysed further, in order to arrive at a more definite set of damage mechanisms. These topics may be divided into three main areas: bubble/free-surface interactions; film rupture and foam production; cell motion. We consider each in turn below.

6.2.1 Bubble/free-surface interactions.

The available evidence strongly suggests that damage is linked with bubble/cell interactions at the air/medium interface. Small bubbles, less than 5mm diameter, appear to

be the most lethal, but these often burst in clusters (Oh, Nienow, Al-Rubeai and Emery, 1992), rather than singly as was assumed in Chapter 5. This will clearly affect the bursting process. Neighbouring bubbles are likely to inhibit much of the inflow of fluid required to produce the jet, and so one may expect clustering bubbles to cause less damage.

Experimentation so far has been largely confined to studies with actual, scaled-down bioreactors and little attention has been paid to observing the stresses placed on a cell in the vicinity of a bursting bubble. A greater amount of experimental information regarding the behaviour of a cell in a straining flow such as that which is seen to occur at the base of the bursting bubble immediately prior to jet formation, would be of great value in this respect. Placing a cell at the stagnation point of a four-roll mill would be a useful experiment that could be performed as a means of determining the maximum strain which a cell can withstand.

In bioreactors, the medium is rarely a pure liquid. Surface active compounds will often be present and any good model of the flow must take account of surface rigidity and surface tension gradients. So far, qualitative agreement with experiment has been obtained, but the results of the last chapter indicate that it is of tremendous importance to determine accurately the position of the bubble in the fluid when it bursts. This will clearly affect greatly the amount of energy released at burst, a factor critical in deciding whether the burst will be deliterious to nearby cells. It is clear that surface chemistry will play a role in this, as well as altering the ensuing bursting motion.

Mathematically, the addition of surface active compounds to the reactor medium, poses us a number of problems. The amount of surfactant will vary from place to place: there may be a different concentration on the free surface than on the rising bubbles that eventually burst there. Consequently there will be a variation in surface tension so that we need to take into account the associated contribution to tangential particle motions. The advection and diffusion of surfactant also needs to be included in the calculations. If there is sufficient surfactant, the liquid/gas interfaces will be effectively

rigid to tangential motion. The potential flow solution will not be able to take into account a no-slip boundary condition as well as the other boundary conditions. The resulting boundary layer correction for the velocity at the boundary is likely to have a greater effect on the flow than the stress-free case studied in the previous chapter. In any case, as the surface tension gradients exert a force tangentially, the surface will be able to support a non-zero stress and so the techniques used in Chapter 5 will not be applicable.

6.2.2 Film rupture and foam production.

There are two important aspects to this topic. The first of these is based on the proposal of Chalmers and Bavarian (1991) that film rupture occurring at bubble burst is a possible cause of cell damage. This rests on the claim of Culick (1960) that the region of film in front of the rapidly expanding toroidal rim of a rupturing film is almost stationary, thus any cells adsorbed on the film will be struck by the rim with considerable force.

The other important aspect of film rupture is its relationship to foams. Experimentally it has been shown that the cell damage rates are very sensitive to the amount and stability of any foam produced and on the thickness of the lamellae separating bubbles. The production of commercially viable bioreactors depends critically on determining the precise physico-chemical properties of the bioreactor medium that will support a stable foam which, it has been observed (Handa, Emery and Spier, 1987), significantly reduces the cell death rates. The mechanism for the protection afforded by the presence of Pluronic F-68, which itself allows a stable foam to be formed, is also a matter of great debate (Handa, Emery and Spier, 1987; Kowalski, 1991). An understanding of the effects of the various physical and chemical parameters on the bubble drainage times would provide a vital cornerstone for the future success of this research.

6.2.3 Cell motion.

In any complete study of the role of bubbles in damaging cells, there must be a consideration of where the cells are in relation to the bubbles. The work of Blanchard

and Syzdek (1972) shows that certain solid particles in this case bacteria, tend to become adsorbed onto bubble walls as they rise through the liquid. Cells adsorbed onto bubbles are clearly in a position where they are vulnerable to damage from the stresses produced by bubble bursting.

Using similar techniques to those of Stoos and Leal (1990), a boundary integral method can be employed to calculate the motion of a solid particle attached to a gas/liquid interface. In this way it is possible to gain important information about the cell distribution on the bubble at the time of burst. If they tend to congregate near to the base of the bubble as it rises then they are likely to move into the jet during the burst, thus undergoing a period of high stress. The possibility that cells may be dragged up through the fluid in the wake of a rising bubble, leaving them at risk of possible damage by the downward jet (Chalmers, 1992) is also of possible interest.

To conclude, we remark that we have developed boundary integral techniques which have allowed accurate calculations of the unsteady motions of rising and bursting gas bubbles in two and three-dimensional flow domains. By devising a scheme whereby stress-free interface conditions can easily be incorporated into a boundary integral method through a viscous boundary layer, we have been able to approximate the advection of separated vorticity around a bursting bubble. The presence of a free-surface or other nearby bubbles often has a significant effect on the fluid flow near to rising bubbles and this is clearly reflected in the bubble motion. The ratio of surface tension forces to buoyancy forces is of great importance, both in terms of its effect on the deformation rate of rising bubbles and through the ascertainment of initial conditions for bubble burst. The latter being a critical factor in the determination of the energy released during the burst itself.

Appendix A: Derivation of integral equations for chapter 2.

(i) Source formulation.

For the source formulation, we require the normal derivative of the potential which is given for all $\boldsymbol{x}$ by the expression

$$\phi(\boldsymbol{x}) = k + \frac{1}{2\pi} \int_C \sigma(\boldsymbol{x}') \log \frac{1}{|\boldsymbol{x}' - \boldsymbol{x}|} ds'. \tag{A1}$$

Writing $\phi = \Re[W]$, where W is the corresponding complex potential, we have

$$W(z) = k + \frac{1}{2\pi} \int_C \sigma(z'(s)) \log \frac{1}{z'(s) - z} ds$$
$$= k + \frac{1}{2\pi} \int_C \frac{\sigma(z')}{\tau(z')} \log \frac{1}{z' - z} dz',$$

where s is the arc-length and $\tau(z') = dz'/ds$ is the unit tangent at $z' \in C$. The potential defined above is continuous across C (see §2.2.3) and so there is no difficulty evaluating it.

Differentiating and evaluating at $z^\star \in \Omega_\pm$, we get

$$\frac{dW}{dz^\star} = \frac{1}{2\pi} \int_C \frac{\sigma(z')}{\tau(z')} \frac{dz'}{z' - z^\star}.$$

This expression is not continuous across C, and so we write it in terms of a continuous Cauchy principal value integral and a discontinuous term, thus enabling simple evaluation in the limiting cases as $z^\star \to z \in C$.

Writing this last expression in the form

$$\frac{dW}{dz^\star} = \frac{1}{2\pi} \int_C \left(\frac{\sigma(z')}{\tau(z')} - \frac{\sigma(z)}{\tau(z)} \right) \frac{dz'}{z' - z^\star} + \frac{1}{2\pi} \frac{\sigma(z)}{\tau(z)} \int_C \frac{dz'}{z' - z^\star},$$

and using Cauchy's theorem for the second integral, we get

$$\frac{dW}{dz^\star} = \frac{1}{2\pi} \int_C \left(\frac{\sigma(z')}{\tau(z')} - \frac{\sigma(z)}{\tau(z)} \right) \frac{dz'}{z' - z^\star} + \begin{cases} i\sigma(z)/\tau(z), & z^\star \in \Omega_+, \\ 0, & z^\star \in \Omega_-. \end{cases}$$

If σ/τ is piecewise smooth on C then it is Hölder continuous so that the integral term is continuous as $z^\star$ crosses C. We may thus trivially take the limit as $z^\star \to z$. The corresponding complex velocities we denote by $Q_\pm$ for $z^\star \in \Omega_\pm$.

To get the normal (and tangential) derivatives of the real potential, ϕ, note that if n is the normal pointing into the gaseous phase and contours are followed in the usual positive sense, then $n = i\tau$ and so, resolving in normal and tangential directions, we may write, formally

$$Q_\pm = \left(i\frac{\partial\phi}{\partial n_\pm} + \frac{\partial\phi}{\partial s_\pm}\right)\tau = \left(\frac{\partial\phi}{\partial n_\pm} - i\frac{\partial\phi}{\partial s_\pm}\right)n.$$

Hence clearly

$$\frac{\partial\phi}{\partial n_\pm} = \Re[Q_\pm^* n], \quad \text{and} \quad \frac{\partial\phi}{\partial s_\pm} = \Re[Q_\pm^* \tau], \tag{A2}$$

where an asterisk denotes complex conjugation. This gives the normal derivative on the fluid side of the bubble as

$$\frac{\partial\phi}{\partial n} = \frac{1}{2\pi}\int_C \left(\sigma(\boldsymbol{x}')\hat{\boldsymbol{n}}(\boldsymbol{x}) - \sigma(\boldsymbol{x})\hat{\boldsymbol{n}}(\boldsymbol{x}')\right)\cdot\frac{\boldsymbol{x}'-\boldsymbol{x}}{|\boldsymbol{x}'-\boldsymbol{x}|^2}ds', \quad \boldsymbol{x}\in C, \tag{A3}$$

and for the tangential derivative,

$$\frac{\partial\phi}{\partial s} = \frac{1}{2\pi}\int_C \left(\sigma(\boldsymbol{x}')\hat{\boldsymbol{t}}(\boldsymbol{x}) - \sigma(\boldsymbol{x})\hat{\boldsymbol{t}}(\boldsymbol{x}')\right)\cdot\frac{\boldsymbol{x}'-\boldsymbol{x}}{|\boldsymbol{x}'-\boldsymbol{x}|^2}ds', \quad \boldsymbol{x}\in C. \tag{A4}$$

(ii) Dipole formulation.

For the dipole formulation, the potential is given, for all $\boldsymbol{x}$, by

$$\phi(\boldsymbol{x}) = k - \frac{1}{2\pi}\int_C \mu(\boldsymbol{x}')\frac{\partial}{\partial n'}\log\frac{1}{|\boldsymbol{x}'-\boldsymbol{x}|}ds'$$
$$= k + \frac{1}{2\pi}\int_C \mu(\boldsymbol{x}')\hat{\boldsymbol{n}}(\boldsymbol{x}')\cdot\frac{\boldsymbol{x}'-\boldsymbol{x}}{|\boldsymbol{x}'-\boldsymbol{x}|^2}ds'.$$

Recall from the derivation of the dipole formulation (§2.2.3) that ϕ is not continuous, so we aim to write it in a more convenient form. So that the normal and tangential velocities may be derived easily, we first write it in complex form for $z^\star \in \Omega_\pm$, $z \in C$

$$W(z^\star) = k + \frac{1}{2\pi}\int_C \mu(z'(s))\frac{n(z'(s))}{z'(s)-z^\star}ds$$
$$= k - \frac{1}{2\pi i}\int_C \mu(z')\frac{dz'}{z'-z^\star}.$$

This may be written as

$$W(z^\star) = k - \frac{1}{2\pi i}\int_C \left(\mu(z')-\mu(z)\right)\frac{dz'}{z'-z^\star} - \begin{cases} \mu(z), & z^\star\in\Omega_+, \\ 0, & z^\star\in\Omega_-. \end{cases}$$

Taking the limit as $z^\star \to z$ and evaluating the real part for the case $z^\star \in \Omega_-$ gives

$$\phi(\boldsymbol{x}) = k + \frac{1}{2\pi} \int_C \left(\mu(\boldsymbol{x}') - \mu(\boldsymbol{x})\right) \hat{\boldsymbol{n}}(\boldsymbol{x}') \cdot \frac{\boldsymbol{x}' - \boldsymbol{x}}{|\boldsymbol{x}' - \boldsymbol{x}|^2} ds'. \tag{A5}$$

To get the derivative, and hence the complex velocities for $z^\star \in \Omega_\pm$, note that

$$\frac{dW}{dz^\star} = -\frac{1}{2\pi i} \int_C \mu(z') \frac{\partial}{\partial z^\star} \left(\frac{1}{z' - z^\star}\right) dz',$$

where this integral is interpreted as a finite-part integral (see for example Martin and Rizzo, 1989). Integrating by parts over the closed contour, C, gives

$$\frac{dW}{dz^\star} = -\frac{1}{2\pi i} \int_C \frac{d\mu}{dz'} \frac{dz'}{z' - z^\star}.$$

Taking $z \in C$, this may be written as

$$\frac{dW}{dz^\star} = -\frac{1}{2\pi i} \int_C \left(\frac{d\mu}{ds}(z') \frac{1}{\tau(z')} - \frac{d\mu}{ds}(z) \frac{1}{\tau(z)}\right) \frac{dz'}{z' - z^\star} - \begin{cases} d\mu/dz'(z), & z^\star \in \Omega_+, \\ 0, & z^\star \in \Omega_-, \end{cases}$$

which, in the limit $z^\star \to z$ and on use of (A2), immediately gives the velocities on the fluid side of the bubble as

$$\frac{\partial \phi}{\partial n} = -\frac{1}{2\pi} \int_C \left(\frac{d\mu}{ds}(\boldsymbol{x}') \hat{\boldsymbol{t}}(\boldsymbol{x}) - \frac{d\mu}{ds}(\boldsymbol{x}) \hat{\boldsymbol{t}}(\boldsymbol{x}')\right) \cdot \frac{\boldsymbol{x}' - \boldsymbol{x}}{|\boldsymbol{x}' - \boldsymbol{x}|^2} ds', \quad \boldsymbol{x} \in C, \tag{A6}$$

and

$$\frac{\partial \phi}{\partial s} = \frac{1}{2\pi} \int_C \left(\frac{d\mu}{ds}(\boldsymbol{x}') \hat{\boldsymbol{n}}(\boldsymbol{x}) - \frac{d\mu}{ds}(\boldsymbol{x}) \hat{\boldsymbol{n}}(\boldsymbol{x}')\right) \cdot \frac{\boldsymbol{x}' - \boldsymbol{x}}{|\boldsymbol{x}' - \boldsymbol{x}|^2} ds', \quad \boldsymbol{x} \in C. \tag{A7}$$

(iii) Vortex formulation.

For the vortex formulation, the potential is precisely that for the source formulation multiplied by i. Hence from the results of (i), the velocities on the fluid side of the bubble are

$$\frac{\partial \phi}{\partial n} = -\frac{1}{2\pi} \int_C \left(\Gamma(\boldsymbol{x}') \hat{\boldsymbol{t}}(\boldsymbol{x}) - \Gamma(\boldsymbol{x}) \hat{\boldsymbol{t}}(\boldsymbol{x}')\right) \cdot \frac{\boldsymbol{x}' - \boldsymbol{x}}{|\boldsymbol{x}' - \boldsymbol{x}|^2} ds', \quad \boldsymbol{x} \in C, \tag{A8}$$

and

$$\frac{\partial \phi}{\partial s} = \frac{1}{2\pi} \int_C \left(\Gamma(\boldsymbol{x}') \hat{\boldsymbol{n}}(\boldsymbol{x}) - \Gamma(\boldsymbol{x}) \hat{\boldsymbol{n}}(\boldsymbol{x}')\right) \cdot \frac{\boldsymbol{x}' - \boldsymbol{x}}{|\boldsymbol{x}' - \boldsymbol{x}|^2} ds', \quad \boldsymbol{x} \in C. \tag{A9}$$

It can be seen from the form of (A8,9) that Γ here corresponds to $d\mu/ds$ in the dipole formulation.

Appendix B: Details of interpolation scheme
for chapter 2.

This appendix gives the quadratic interpolation used to integrate over elements neighbouring the observation node on the bubble, in the cases indicated in the text. The same interpolation was used to give the directions of normals and tangents at nodes and to give surface derivatives of potentials and dipole strengths.

Since the distance between points is not, in general, uniform, a Lagrangian interpolation polynomial is used, parameterised with respect to a linear arc-length, s. We require the polynomial, $X_i(s)$, to go through $(-d_{i-1}, x_{i-1})$, $(0, x_i)$ and (d_i, x_{i+1}), where $d_j = |\boldsymbol{x}_{j+1} - \boldsymbol{x}_j|$ is the distance between nodes. To avoid lengthy expressions, define the functions $\mathcal{A}_a$, $(a = 1, 2)$, acting on three consecutive members of an ordered set of scalars or vectors, by

$$\mathcal{A}_1(\{x_{i-1}, x_i, x_{i+1}\}) = d_{i-1}^2 x_{i+1} - (d_{i-1}^2 - d_i^2) x_i - d_i^2 x_{i-1},$$

and

$$\mathcal{A}_2(\{x_{i-1}, x_i, x_{i+1}\}) = d_i x_{i-1} - (d_{i-1} + d_i) x_i + d_{i-1} x_{i+1}.$$

For convenience, write these as $\mathcal{A}_1(x_i)$ and $\mathcal{A}_2(x_i)$ respectively. It turns out that X_i is given by

$$X_i(s) = \frac{1}{D_i} \left(s^2 \mathcal{A}_2(x_i) + s \mathcal{A}_1(x_i) \right) + x_i,$$

where $D_i = d_i d_{i-1}(d_i + d_{i-1})$.

In particular, we have that

$$\boldsymbol{q}_i(s) = \frac{1}{D_i} \left(s^2 \mathcal{A}_2(\boldsymbol{x}_i) + s \mathcal{A}_1(\boldsymbol{x}_i) \right) + \boldsymbol{x}_i.$$

From this, we immediately see that the tangent at node i is in the direction $\mathcal{A}_1(\boldsymbol{x}_i)$ and hence the normal, which we denote by $\mathcal{A}_1^\perp(\boldsymbol{x}_i)$, may be found. We are now in a position to express the integrals in terms of the interpolation polynomials.

(i) Integrals of the form -

$$\int_C \left(f(\boldsymbol{x}')\hat{\boldsymbol{n}}(\boldsymbol{x}) - f(\boldsymbol{x})\hat{\boldsymbol{n}}(\boldsymbol{x}') \right) \cdot \frac{\boldsymbol{x}' - \boldsymbol{x}}{|\boldsymbol{x}' - \boldsymbol{x}|^2} ds',$$

where f represents some quantity such as the dipole strength. For the interval of integration where $\boldsymbol{x}' \in [\boldsymbol{x}_{i-1}, \boldsymbol{x}_{i+1}]$, we get

$$\int_{-d_{i-1}}^{d_i} \left\{ \left[\frac{s^2 \mathcal{A}_2(f_i)}{D_i} + \frac{s \mathcal{A}_1(f_i)}{D_i} + f_i \right] \frac{\mathcal{A}_1^\perp(\boldsymbol{x}_i)}{|\mathcal{A}_1(\boldsymbol{x}_i)|} - f_i \left[\frac{2s \mathcal{A}_2^\perp(\boldsymbol{x}_i) + \mathcal{A}_1^\perp(\boldsymbol{x}_i)}{|2s \mathcal{A}_2(\boldsymbol{x}_i) + \mathcal{A}_1(\boldsymbol{x}_i)|} \right] \right\}$$
$$\cdot D_i \left[\frac{s^2 \mathcal{A}_2(\boldsymbol{x}_i) + s \mathcal{A}_1(\boldsymbol{x}_i)}{|s^2 \mathcal{A}_2(\boldsymbol{x}_i) + s \mathcal{A}_1(\boldsymbol{x}_i)|^2} \right] \left| \frac{d\boldsymbol{q}}{ds} \right| ds.$$

Noting that $\mathcal{A}_a(\boldsymbol{x}_i) \cdot \mathcal{A}_a^\perp(\boldsymbol{x}_i) = 0$, $(a = 1, 2)$, a factor of s^2 cancels and we are left with

$$\int_{-d_{i-1}}^{d_i} \frac{|2s \mathcal{A}_2(\boldsymbol{x}_i) + \mathcal{A}_1(\boldsymbol{x}_i)|}{D_i |s \mathcal{A}_2(\boldsymbol{x}_i) + \mathcal{A}_1(\boldsymbol{x}_i)|^2} \left[\left(s^2 \mathcal{A}_2(f_i) + s \mathcal{A}_1(f_i) + D_i f_i \right) \frac{\mathcal{A}_1^\perp(\boldsymbol{x}_i) \cdot \mathcal{A}_2(\boldsymbol{x}_i)}{|\mathcal{A}_1(\boldsymbol{x}_i)|} \right.$$
$$\left. - f_i \left[\frac{2 \mathcal{A}_2^\perp(\boldsymbol{x}_i) \cdot \mathcal{A}_1(\boldsymbol{x}_i) + \mathcal{A}_1^\perp(\boldsymbol{x}_i) \cdot \mathcal{A}_2(\boldsymbol{x}_i)}{|s \mathcal{A}_2(\boldsymbol{x}_i) + \mathcal{A}_1(\boldsymbol{x}_i)|^2} \right] \right] ds.$$

Substituting the values for the $\mathcal{A}$'s into this, the integrand and hence the integral's value may be calculated.

(ii) Integrals of the form -

$$\int_C \left(f(\boldsymbol{x}')\hat{\boldsymbol{t}}(\boldsymbol{x}) - f(\boldsymbol{x})\hat{\boldsymbol{t}}(\boldsymbol{x}') \right) \cdot \frac{\boldsymbol{x}' - \boldsymbol{x}}{|\boldsymbol{x}' - \boldsymbol{x}|^2} ds'.$$

This integral is slightly more difficult in that the factor of s^2 does not explicitly cancel, though the integrand is still bounded as $s \to 0$. For the interval of integration where $\boldsymbol{x}' \in [\boldsymbol{x}_{i-1}, \boldsymbol{x}_{i+1}]$, we write it as

$$\int_{-d_{i-1}}^{d_i} \left\{ \left[\frac{s^2 \mathcal{A}_2(f_i)}{D_i} + \frac{s \mathcal{A}_1(f_i)}{D_i} + f_i \right] \frac{\mathcal{A}_1(\boldsymbol{x}_i)}{|\mathcal{A}_1(\boldsymbol{x}_i)|} - f_i \left[\frac{2s \mathcal{A}_2(\boldsymbol{x}_i) + \mathcal{A}_1(\boldsymbol{x}_i)}{|2s \mathcal{A}_2(\boldsymbol{x}_i) + \mathcal{A}_1(\boldsymbol{x}_i)|} \right] \right\}$$
$$\cdot D_i \left[\frac{s^2 \mathcal{A}_2(\boldsymbol{x}_i) + s \mathcal{A}_1(\boldsymbol{x}_i)}{|s^2 \mathcal{A}_2(\boldsymbol{x}_i) + s \mathcal{A}_1(\boldsymbol{x}_i)|^2} \right] \left| \frac{d\boldsymbol{q}}{ds} \right| ds.$$

The term in the first factor that does not contain an s in the numerator is equal to

$$\frac{f_i}{D_i} \mathcal{A}_1(\boldsymbol{x}_i) \left| \frac{d\boldsymbol{q}}{ds} \right|^{-1} \left[\frac{|2s \mathcal{A}_2(\boldsymbol{x}_i) + \mathcal{A}_1(\boldsymbol{x}_i)|}{|\mathcal{A}_1(\boldsymbol{x}_i)|} - 1 \right],$$

and is clearly of order s as $s \to 0$, since the tangents at the observation point and the integration point become equal at $s = 0$. If the quadrature routine evaluates the integrand at very small values of s, it would be worthwhile expanding this difference in powers of s in order to avoid division by small quantities.

Appendix C: Identities for chapter 5.

(i)

We may easily show that a material curve that is locally normal to a stress-free surface will remain so. First, consider a general material curve indexed by the Lagrangian parameter λ. If the unit tangent to the curve is $\hat{\boldsymbol{m}}$ then

$$
\begin{aligned}
\hat{\boldsymbol{m}} \cdot \nabla \boldsymbol{v} &= \frac{\partial}{\partial s}\left(\frac{d\boldsymbol{x}}{dt}\right) \\
&= \frac{d\lambda}{ds}\frac{\partial}{\partial\lambda}\left(\frac{d\boldsymbol{x}}{dt}\right).
\end{aligned}
\tag{C1}
$$

As both derivatives are taken in a Lagrangian sense, they may be interchanged to give

$$
\begin{aligned}
\hat{\boldsymbol{m}} \cdot \nabla \boldsymbol{v} &= \frac{d\lambda}{ds}\frac{d}{dt}\left(\frac{ds}{d\lambda}\frac{\partial\boldsymbol{x}}{\partial s}\right) \\
&= \frac{d\hat{\boldsymbol{m}}}{dt} + \hat{\boldsymbol{m}}\frac{d\lambda}{ds}\frac{d}{dt}\left(\frac{ds}{d\lambda}\right).
\end{aligned}
\tag{C2}
$$

Thus if $\hat{\boldsymbol{m}}$ is chosen to be the normal or tangent to the surface, then

$$
\hat{\boldsymbol{n}} \cdot \nabla \boldsymbol{v} \cdot \hat{\boldsymbol{t}} = \frac{d\hat{\boldsymbol{n}}}{dt}\cdot\hat{\boldsymbol{t}} \quad \text{or} \quad \hat{\boldsymbol{t}} \cdot \nabla \boldsymbol{v} \cdot \hat{\boldsymbol{n}} = \frac{d\hat{\boldsymbol{t}}}{dt}\cdot\hat{\boldsymbol{n}}.
\tag{C3}
$$

By using (5.4.2) and adding the equations of (C3), we see that for a stress-free surface,

$$
\frac{d\hat{\boldsymbol{n}}\cdot\hat{\boldsymbol{t}}}{dt} = 0.
\tag{C4}
$$

(ii)

In order to calculate normal derivatives of the tangential velocity, u_t, we use the fact that $\boldsymbol{u}$ is irrotational to re-write it in terms of tangential derivatives of the normal velocity, u_n, which can be calculated more accurately. As the tangent vector is fixed with respect to small changes in the normal direction,

$$
\frac{\partial u_t}{\partial n} = \hat{\boldsymbol{n}} \cdot \nabla \boldsymbol{u} \cdot \hat{\boldsymbol{t}}.
\tag{C5}
$$

Since $\boldsymbol{u}$ is irrotational, the rank-2 tensor $\nabla\boldsymbol{u}$ is symmetric, so that the right-hand side of (C5) can be re-ordered, giving

$$
\begin{aligned}
\frac{\partial u_t}{\partial n} &= \hat{\boldsymbol{t}} \cdot \nabla \boldsymbol{u} \cdot \hat{\boldsymbol{n}} \\
&= \frac{\partial u_n}{\partial s} + \kappa^{(t)} u_t.
\end{aligned}
\tag{C6}
$$

References

Allan, R.S., Charles, G.E. & Mason, S.G. 1961 The approach of gas bubbles to a gas/liquid interface. *J. Coll. Sci.*, **16** pp 150–165.

Al-Rubeai, M. Chalder, S. & Emery, A.N. 1990 Dynamic assay of synthetic activities in single hybridoma cells. In *Production of Biologicals from Animal Cells in Culture.* (Eds. Spier, R.E., Griffith, J.B. & Meigner, B.) pp 587–593. Butterworth Heinemann.

Atkinson, K. Graham, I. & Sloan, I. 1983 Piecewise continuous collocation for integral equations. *SIAM J. Numer. Anal.* **20(1)** pp 172–186.

Baker, G.R., Meiron, D.I. & Orszag, S.A. 1982 Generalised vortex methods for free-surface flow problems. *J. Fluid Mech.*, **123** pp 477–501.

Baker, G.R. & Moore, D.W. 1989 The rise and distortion of a two-dimensional bubble in an inviscid liquid. *Phys. Fluids A*, **1(9)** pp 1451–1459.

Batchelor, G.K. 1987 The stability of a large gas bubble rising through liquid. *J. Fluid Mech.*, **184** pp 399–422.

Batchelor, G.K. 1967 *An Introduction to Fluid Dynamics.* Cambridge University Press.

Baumel, R.T., Burley, S.K., Freeman, D.F., Gammel, J.K. & Nuttall, J. 1982 The rise of a cylindrical bubble in an inviscid liquid. *Can J. Phys.*, **60** pp 999–1007.

Bavarian, F., Fan, L.S. & Chalmers, J.J. 1991 Microscopic visualization of insect cell-bubble interactions I: Rising bubbles, air-medium interface, and the foam layer. *Biotech. Prog.*, **7(2)** pp 140–150.

Best, J.P. & Kucera, A. 1992 A numerical investigation of nonspherical rebounding bubbles. *J. Fluid Mech.*, **245** pp 137–154.

Bikerman, J.J. 1973 *Foams.* Springer-Verlag.

Bhaga, D. & Weber, M.E. 1981 Bubbles in viscous liquids: shapes, wakes and velocities. *J. Fluid Mech.*, **105** pp 61-85.

Blake, J.R. 1988 The Kelvin impulse: application to cavitation bubble dynamics. *J. Austral. Math. Soc. B*, **30** pp 127-146.

Blake, J.R. & Gibson, D.C. 1981 Growth and collapse of a vapour cavity near a free surface. *J. Fluid Mech.*, **111** pp 123–140.

Blake, J.R. & Kucera, A. 1988 Coning in oil reservoirs *Math. Sci.*, **13** pp 36–47.

Blake, J.R., Taib, B.B. & Doherty, G. 1986 Transient cavities near boundaries. Part I. Rigid Boundary. *J. Fluid Mech.*, **170** pp 479–497.

Blake, J.R., Taib, B.B. & Doherty, G. 1987 Transient cavities near boundaries. Part II. Free Surface. *J. Fluid Mech.*, **181** pp 197–212.

Blanchard, D.C. & Syzdek, L.D. 1972 Concentration of bacteria in jet drops from bursting bubbles. *J. Geophys. Res.*, **77(27)** pp 5087–5099.

Boris, J.P. 1989 New directions in computational fluid dynamics. *Ann. Rev. Fluid Mech.*, **21** pp 345–38

Brebbia, C.A. & Walker, S.J. 1980 *Boundary Element techniques in Engineering.* Butterworths.

Chahine, G.L. 1991 Dynamics of the interaction of non-spherical cavities. In *Mathematical approaches in hydrodynamics*, (Ed. Miloh, T.), SIAM Philadelphia, pp 51–67.

Chalmers, J.J. 1992 Private communication.

Chalmers, J.J. & Bavarian, F. 1991 Microscopic visualization of insect cell-bubble interactions II: The film and bubble rupture. *Biotech. Prog.*, **7(2)** pp 151–159.

Clift, T, R., Grace, J.R. & Weber, M.E. 1978 *Bubbles, Drops, and Particles.* Academic

Press.

Culick, F.E.C. 1960 Comments on a ruptured soap film. *J. Appl. Phys.*, **31I** pp 1128–1129.

Fink, P.T. & Soh, W.K. 1978 A new approach to roll-up calculations of vortex sheets. *Proc. Roy. Soc. Lond. A*, **362** pp 195–209.

Forbes, L.K. & Hocking, G.C. 1990 Flow caused by a point sink in a fluid having a free surface. *J. Austral. Math. Soc. B*, **32** pp 231–249.

Garner, F.H., Ellis, S.R.M. & Lacey, J.A. 1954 The size distribution and entrainment of droplets. *Trans. Instn. Chem. Engrs.*, **32** pp 222–235.

Guerri, L., Lucca, G. & Prosperetti, A. 1981 A numerical method for the dynamics of non-spherical cavitation bubbles. *Proc. 2nd Int. Colloq. on drops and bubbles. California.* pp 175–181.

Hahn P.-S., Chen, J.-D. & Slattery, J.C. 1985 Effects of London-van der Waals forces on the thinning and rupture of a dimpled liquid film as a small drop or bubble approaches a fluid-fluid interface. *AIChE. J.*, **31(12)** pp 2026–2038.

Handa, A. 1986 *Gas-Liquid Interfacial Effects on the Growth of Hybridomas and Other Suspended Mammalian Cells.* Ph.D. Thesis. University of Birmingham, UK.

Handa, A., Emery, A.N. & Spier, R.E. 1987 On the evaluation of gas-liquid interfacial effects on hybridoma viability in bubble column bioreactors. *Dev. Biol. Standard.*, **66** pp 241–253.

Harper, J.F. 1972 The motion of bubbles and drops through liquids. *Adv. Appl. Mech.*, **12** pp 59-129.

Harris, P. 1992 A numerical model for determining the motion of a bubble close to a fixed rigid structure in a fluid. *Int. J. Numer. Meth. Engng.*, **33(9)** pp 1813-1822.

Hastings, C. 1955 *Approximations For Digital Computers.* Princeton University Press, Princeton, N.J.

Havelock, T.H. 1927 The method of images in some problems of surface waves. *Proc. Roy. Soc. Lond. A*, **115** pp 268–280.

Ivanov, B.I., Kralchevsky, P.A. & Nikolov, A.D. 1986 Film and line tension effects on the attachment of particles to an interface. Parts I–IV. *J. Coll. Int. Sci.*, **102(1)** pp 97–143.

Jaswon, M.A. & Symm, G.T. 1963 Integral equation methods in potential theory. Parts I and II. *Proc. Roy. Soc. Lond. A*, **275** pp 23–46.

Jaswon, M.A. & Symm, G.T. 1977 *Integral Equation Methods in Potential Theory and Elastostatics.* Academic Press.

Kientzler, C.F., Arons, A.B., Blanchard, D.C. & Woodcock, A.H. 1954 Photographic investigation of the projection of droplets by bubbles bursting at a water surface. *Tellus*, **6(1)** pp 1–7.

King, A.C. & Bloor, M.I.G. 1988 A note on the free surface induced by a submerged source at infinite Froude number. *J. Austral. Math. Soc. B*, **30** pp 147–156.

Kioukia, N. 1990. *Physical and Chemical Factors Affecting Hybridoma Growth.* M.Sc. Dissertation. University of Birmingham, UK.

Kirkpatrick, R.D. & Lockett, M.J. 1974 The influence of approach velocity on bubble coalescence. *Chem. Eng. Sci.*, **29** pp 2363–2373.

Kowalski, A.J. 1991 *Microscale fluid dynamic effects in suspension processing and attrition of cell cultures.* Ph.D. Thesis. University of Birmingham, UK.

Kreβ, R. & Spassov, W.T. 1983 On the condition number of boundary integral operators for the exterior Dirichlet problem for the Helmholtz equation. *Numer. Math.*, **42** pp 77–95.

Kucera, A. 1991 A boundary integral method applied to the growth and collapse of bubbles near a rigid boundary. To appear in *J. Comp. Phys.*

Kunas, K.T. & Papoutsakis, E.T. 1989 Increasing serum concentrations decrease cell death and allow cell growth of hybridoma cells at higher agitation rates. *Biotech. Letts.*, **11(8)** pp 525–530.

Kunas, K.T. & Papoutsakis, E.T. 1990 Damage mechanisms of suspended animal cells in agitated bioreactors with and without bubble entrainment. *Biotech. and Bioeng.*, **36** pp 476–483.

Lamb, H. 1932 *Hydrodynamics.* Dover.

Levich, V.G. 1949 Motion of gaseous bubbles with high Reynolds numbers. *Zhn. Eksp. Teor. Fiz.*, **19** pp 18–24.

Levich, V.G. 1962 *Physicochemical Hydrodynamics.* Prentice-Hall, New Jersey.

Lighthill, M.J. 1986 *An Informal Introduction to Fluid Mechanics.* Oxford.

Lo, L.L. 1983 The meniscus on a needle — a lesson in matching. *J. Fluid Mech.*, **132** pp 85–78.

Longuet-Higgins, M.S. 1980 On the forming of sharp corners at a free surface. *Proc. Roy. Soc. Lond. A*, **371** pp 453–478.

Longuet-Higgins, M.S. 1983 Bubbles, breaking waves and hyperbolic jets at a free surface. *J. Fluid Mech.*, **127** pp 103–121.

Longuet-Higgins, M.S. & Cokelet, E.D. 1976 The deformation of steep surface waves on water. I. A numerical method of computation. *Proc Roy. Soc. Lond. A*, **350** pp 1–26.

Lundgren, T.S. & Mansour, N.N. 1988 Oscillations of drops in zero gravity with weak viscous effects. *J. Fluid Mech.*, **194** pp 479–510.

Lundgren, T.S. & Mansour, N.N. 1991 Vortex ring bubbles. *J. Fluid Mech.*, **224** pp 177–196.

MacIntyre, F. 1972 Flow patterns in breaking bubbles. *J. Geophys. Res.*, **77(27)** pp 5211–5228.

Martin, P.A. & Rizzo, F.J. 1989 On boundary integral equations for crack problems. *Proc. Roy. Soc. Lond. A*, **421** pp 341–355.

McQueen, A. & Bailey, J.E. 1989 Influence of serum level, cell line, flow type and viscosity on flow-induced lysis of suspended mammalian cells. *Biotech. Letts.*, **11(8)** pp 531–536.

Mikhlin, S.G. 1957 *Integral Equations.* Pergamon.

Miksis, M., Vanden Broeck, J.-M. & Keller, J.B. 1981 Axisymmetric bubble or drop in a uniform flow. *J. Fluid Mech.*, **108** pp 89–100.

Miksis, M., Vanden Broeck, J.-M. & Keller, J.B. 1982 Rising bubbles. *J. Fluid Mech.*, **123** pp 31–41.

Moore, D.W. 1963 The boundary layer on a spherical gas bubble. *J. Fluid Mech.*, **16** pp 161–176.

Moore, D.W. 1965 The velocity of rise of distorted gas bubbles in a liquid of small viscosity. *J. Fluid Mech.*, **23(4)** pp 749–766.

Moore, D.W. 1973 A numerical study of the roll-up of a finite vortex sheet. *J. Fluid Mech.*, **63(2)** pp 225–235.

Moore, D.W. 1981 On the point vortex method. *J. Sci. Stat. Comp.*, **2(1)** pp 65–84.

Muskhelishvili, N.I. 1953 *Singular Integral Equations.* Noordhoff.

Newitt, D.M., Dombrowski, N. & Knelman, F.H. 1954 Liquid entrainment 1. The mechanism of drop formation from gas or vapour bubbles. *Trans. Instn. Chem. Engrs.*, **32**

pp 244–261.

Oguz H.N. & Prosperetti, A. 1989 Surface tension effects in the contact of liquid surfaces. *J. Fluid Mech.*, **203** pp 149–171.

Oguz H.N. & Prosperetti, A. 1990a A generalization of the impulse and virial theorems with an application to bubble oscillations. *J. Fluid Mech.*, **218** pp 143-162.

Oguz H.N. & Prosperetti, A. 1990b Bubble entrainment by the impact of drops on liquid surfaces. *J. Fluid Mech.*, **219** pp 143–179.

Oh, S.K.W., Nienow, A.W., Al-Rubeai, M. & Emery, A.N. 1989 The effects of agitation intensity with and without continuous sparging on the growth and antibody production of hybridoma cells. *J. Biotech.*, **12** pp 45–62.

Oh, S.K.W., Nienow, A.W., Al-Rubeai, M. & Emery, A.N. 1992 Further studies of the culture of mouse hybridomas in an agitated bioreactor with and without continuous sparging. *J. Biotech.*, **22** pp 245–270.

Orton, D.R. & Wang, D.I.C. 1990 Effects of gas interfaces on animal cells in bubble aerated bioreactors. Paper No. 103B presented at AIChE Annual Meeting, Chicago.

Princen, H.M. 1963 Shape of a fluid drop at a liquid-liquid interface. *J. Coll. Sci.*, **18** pp 178–195.

Ranz, W.E. 1959 Some experiments on the dynamics of liquid films. *J. Appl. Phys.*, **30(12)** pp 1950-1955.

Rayleigh, Lord 1878 On the instability of jets. *Proc. Lond. Math. Soc.*, **10** pp 4-13.

Rayleigh, Lord 1891 Some applications of photography. *Nature.*, **44** pp 249–254.

Resch, F.J., Darrozes, J.S. & Afeti, G.M. 1986 Marine liquid aerosol production from bursting of air bubbles. *J. Geophys. Res.*, **91(C1)** pp 1019-1029.

Robinson, P.B. 1992 *The numerical modelling of bubble interactions.* M.Sc. Thesis, University of Birmingham, U.K.

Robinson, P.B., Boulton-Stone, J.M. & Blake, J.R. 1993 The interaction of two-dimensional gas bubbles. Submitted to *J. Eng. Math.*

Ryskin, G. & Leal, L.G. 1984 Numerical solution of free-boundary problems in fluid mechanics. Part 2. Buoyancy-driven motion of a gas bubble through a quiescent liquid. *J. Fluid Mech.*, **148** pp 19–35.

Scheludko, A. 1962 Certain particulars of foam layers. II Kinetic stability, critical thickness and equilibrium thickness. *Proc. K. Ned. Akad. Wetensch B*, **65(1)** 87–96.

Soh, W.K. 1987 Boundary element technique for flow vizualization studies of nonlinear water waves. *Eng. Anal.*, **4(2)** pp 106–112.

Stoker, J.J. 1957 *Water Waves. The Mathematical Theory with Applications.* Interscience Publishers.

Stoos, J.A. & Leal, L.G. 1990 A spherical particle straddling a fluid/gas interface in an axisymmetric straining flow. *J. Fluid Mech.*, **217** pp 263-298.

Taib, B.B. 1985 *Boundary Element Method Applied to Cavitation Bubble Dynamics.* Ph.D. Thesis. University of Wollongong, Australia.

Taylor, G.I. & Michael, D.H. 1973 On making holes in a sheet of fluid. *J. Fluid Mech.*, **58(4)** pp 625–639.

Taylor, T.D. & Acrivos, A. 1964 On the deformation and drag of a falling viscous drop at low Reynolds number. *J. Fluid. Mech.*, **18** pp 466-476.

Tramper, J., Williams, J.B. & Joustra, D. 1986 Shear sensitivity of insect cells in suspension. *Enzyme Microb. Technol.*, **8** pp 33–36.

Tryggvason, G. 1988 Deformation of a free surface as a result of vortical flows. *Phys.*

Fluids, **31(5)** pp 955–957.

Tuck, E.O. & Vanden Broeck, J.-M. 1984 A cusp-like free-surface flow due to a submerged source or sink. *J. Austral. Math. Soc. B*, **25** pp 443–450.

Unverdi, S.O. & Tryggvason, G 1992 A front-tracking method for viscous, incompressible, multi-fluid flows. J. Comp. Phys., **100(1)** pp 25–37.

Vanden Broeck, J.-M., Schwartz, L.W. & Tuck, E.O. 1978 Divergent low-Froude-number series expansions of nonlinear free-surface flow problems. *Proc. Roy. Soc. Lond. A*, **361** pp 207–224.

Vrij, A. 1966 Possible mechanism for the spontaneous rupture of thin, free liquid films. *Disc. Faraday Soc.*, **42** pp 23–33.

Walters, J.K. & Davidson, J.F. 1962 The initial motion of a gas bubble in an inviscid liquid. Part I. The two-dimensional bubble. *J. Fluid Mech.*, **12** pp 408–417.

Wehausen, J.V & Laitone, E.V. 1960 Surface waves. *Handbuch der Physik*, **9(3)** pp 446–778.

Yang, J.-D., Wang, N.S., Chang, K.-C. & Calabrese, R.V. 1990 Hybridoma cell inactivation by air sparging in a mechanically agitated bioreactor. Submitted for publication.

Zhang, Z., Ferenczi, M.A., Lush, A.C. & Thomas, C.R. 1991 A novel micromanipulation technique for measuring the bursting strength of single mammalian cells. *Appl. Microbiol. Biotechnol.*, **36** pp 208–210.